# The Initial Conditions of Clustered Star Formation: An Observational Study of Dense Gas in the Ophiuchus Molecular Cloud

by

Rachel Katherine Friesen
B.Sc.H, Queen's University, 2002
M.Sc., University of Victoria, 2005

A Dissertation Submitted in Partial Fulfillment of the
Requirements for the Degree of

DOCTOR OF PHILOSOPHY

in the Department of Physics and Astronomy

The Initial Conditions of Clustered Star Formation:
An Observational Study of Dense Gas in the Ophiuchus Molecular Cloud

by

Rachel Katherine Friesen
B.Sc.H, Queen's University, 2002
M.Sc., University of Victoria, 2005

Supervisory Committee

Dr. J. Di Francesco, Co-Supervisor
(Herzberg Institute of Astrophysics)

Dr. C. J. Pritchet, Co-Supervisor
(Department of Physics and Astronomy)

Dr. K. A. Venn, Departmental Member
(Department of Physics and Astronomy)

Dr. R. G. Hicks, Outside Member
(Department of Chemistry)

**Supervisory Committee**

Dr. J. Di Francesco, Co-Supervisor
(Herzberg Institute of Astrophysics)

Dr. C. J. Pritchet, Co-Supervisor
(Department of Physics and Astronomy)

Dr. K. A. Venn, Departmental Member
(Department of Physics and Astronomy)

Dr. R. G. Hicks, Outside Member
(Department of Chemistry)

## ABSTRACT

In this dissertation I present a detailed survey of molecular line emission (including $NH_3$, $C_2S$, $HC_5N$, $N_2H^+$, $N_2D^+$ and $H_2D^+$) towards clustered star forming Cores in the nearby Ophiuchus molecular cloud, with the aim of characterizing the distribution and kinematics of the dense gas within a clustered star forming environment and compare these results with those found in more isolated star forming regions. I show that the dense Oph Cores present characteristics of both isolated and clustered star forming regions in several key parameters, including Core kinematics, temperatures and chemistry. At the higher gas densities where the $N_2H^+$ emission is excited, I show that the presence of an embedded protostar is correlated with increased gas motions. I additionally present evidence of $N_2H^+$ depletion from the gas phase, suggesting that in higher density, clustered environments $N_2H^+$ may not accurately trace the physical conditions of the densest core gas. I present the distribution of $H_2D^+$ and $N_2D^+$ across the Oph B Core, and show the distribution is not simple or easily explained by chemical models of evolving, isolated cores. Finally, I summarize the results of this dissertation, the questions it raises concerning the exploration of how stars form in clusters, and discuss how these questions may be answered through upcoming observational surveys and by new telescope facilities.

# Contents

# List of Tables

# List of Figures

# ACKNOWLEDGEMENTS

There are many people I would like to offer my thanks for their support during my time at the University of Victoria. Without all of you, this dissertation could not have been completed.

First, I want to thank my supervisor, James Di Francesco, for taking me on as a PhD student and providing much advice and encouragement, as well as a sense of humour, as we worked through this thesis. Thanks also to my supervisory committee for their support and advice.

To my scientific collaborators for stimulating conversations, and providing useful comments on my many, many observing proposals and the resulting papers, which improved them all greatly.

To my fellow grad students and friends near and far, for being such a fantastic group of people. Thanks for scientific discussions, advice of all kinds and so many great events, hikes and camping trips that helped me remember the big picture. Thanks especially to Helen Kirk, for several years my sole partner in star formation crime, and provider of all things submillimetre continuum (we'll collaborate one of these days).

To my family, for your love and support even when it probably seemed like I'd never leave school. I love you all.

# DEDICATION

*for Grandpa Penner*

# Chapter 1

# The Formation of Stars in Clusters

The process by which dense cores of gas and dust form and evolve within their natal molecular clouds is a key question in the study of star formation. Sensitive measurements of temperatures, densities, gas kinematics and degree of fragmentation within a dense core are necessary to construct and constrain realistic models of core evolution. Recently, observations of systematic depletion of molecular species within dense cores has led to the proposed use of the chemical differentiation of a dense core as an indicator of its evolutionary status. In this Chapter, I present a detailed background and discuss the aims of this thesis, namely, to study the fragmentation and evolution of starless, possibly prestellar cores out of dense gaseous filaments in the clustered star forming environment of the Ophiuchus molecular cloud. In particular, I focus on the use of the chemical structure of the cores to explore their evolutionary status, and compare the evolution of dense cores in clustered environments, through analysis of both kinematics and chemistry revealed by molecular line observations, with that of isolated regions. First, I discuss the general structure of molecular clouds and embedded dense cores of gas which form the precursors to young stars and stellar clusters, and next describe the observational methods used to determine the physical conditions in dense gas. Next, I discuss the observational differences between isolated and clustered star forming environments and the ramifications for theories of clustered star formation. Lastly, I discuss the current star formation in the nearby Ophiuchus molecular cloud.

## 1.1 Molecular Clouds, Cores and Clumps

In the Milky Way, giant molecular cloud (GMC) complexes contain $\sim 10 - 20\%$ of the mass in the inner galactic disk (Shull & Beckwith 1982). Individual GMC masses range from $M \sim 10^3\,\mathrm{M}_\odot$ - $10^6\,\mathrm{M}_\odot$ ($\mathrm{M}_\odot = 1.99 \times 10^{33}\,\mathrm{g}$ is a single solar mass) within linear extents of several parsecs ($1\,\mathrm{pc} = 3.1 \times 10^{18}\,\mathrm{cm}$). While thus characterized by moderate mean densities, $n \sim 10^2\,\mathrm{cm}^{-3}$ - $10^3\,\mathrm{cm}^{-3}$, a wide range of observed inhomogenous structures, including filamentary gas streamers and fragmented 'clumpy' gas cores, are found within all GMCs. These dense gas cores and filaments are found with masses $M \sim \mathrm{few} \times 10\,\mathrm{M}_\odot$ within linear sizes of a few tenths of a parsec, leading to densities $n \sim 10^4\,\mathrm{cm}^{-3}$ or more. When observed with higher resolution, these structures often further resolve into small, dense clumps with masses similar to that of the Sun, and temperatures that can reach extremely low values, $T < 10\,\mathrm{K}$.

Some of these small, dense cores appear starless, while others contain compact sources seen in the infrared by space-borne telescopes such as the InfraRed Astronomical Satellite (IRAS), and more recently, the Spitzer Space Telescope. These infrared detections are signposts of young stellar objects (YSOs) still deeply embedded in the surrounding gas and dust of their natal cloud. The dust absorbs much of the ultraviolet and optical light of the YSO, thermally reradiating it at longer wavelengths that escape the envelope. The evolutionary link between dense cores and YSOs is dependent on the mechanisms responsible for the formation, fragmentation and collapse of a dense core within the global structure of a GMC.

Proposed physical theories tend to fall into one of two favoured regimes. One mechanism is that of magnetic-field mediated dense core growth and subsequent collapse. Here, the magnetic field within a molecular cloud provides support against the cloud's gravity through the coupling of the ions within the GMC to the magnetic field lines. Neutral atoms and molecules are able to diffuse slowly through the magnetic field towards regions of higher density, slowly building up greater mass until the self-gravity of the forming core overcomes the magnetic field support and collapse begins. This neutral-ion drift is called ambipolar diffusion (Mestel & Spitzer 1956). Ambipolar diffusion tends to be a slow process, with the timescale, $\tau_{AD}$, dependent on the strength of the magnetic field $B$ in the cloud and the ion density, $n_i$, according to $\tau_{AD} \propto n_i^{-1} B^{-2}$ (Shu et al. 1987). For typical core conditions, core lifetime

predictions are an order of magnitude longer than the free-fall time on average, or about $t \sim 10^7$ yr. The second mechanism, in contrast to the quasi-static ambipolar diffusion model, is a more rapid, turbulence-driven formation route. There are several flavours to this theory. On one hand, if GMCs are long-lived, turbulence is invoked to provide support to the cloud and prevent its global, rapid collapse. The dissipation of turbulence in localized regions removes support against gravity in dense cores within the GMC, which will then evolve under the influence of gravity (see, e.g., Mac Low & Klessen 2004). On the other hand, another popular theory proposes that GMCs are actually short-lived objects, and dense cores are created at the intersection of turbulent flows within the molecular cloud, and subsequently collapse under their own gravity. In both cases, core evolution is dynamic, and the lifetimes of the dense cores are of the order of the free-fall time, $t_{ff} \sim 10^6$ yr.

Through systematic observations of emission from thermal dust continuum emission and various molecular lines well matched to the excitation conditions at high densities and low temperatures, the physical conditions of dense, starless and protostellar cores have been studied with great success, discussed in detail below. These studies have enabled the creation of detailed physical and chemical models (the extreme chemistry of cold, dense cores is an emerging field of research which combines the astronomy and chemistry disciplines) to probe the formation of isolated cores and subsequent evolution to form a single star or stellar binary. In isolated regions, such combined physical and chemical models of dense cores have made much progress in using observed molecular line emission to probe the physics and timescales of core evolution and collapse.

While astronomers have thus come to a detailed understanding of the structure of dense cloud cores and potential evolutionary stages, most stars form in groups and associations in a more clustered mode (Lada & Lada 2003), where through fragmentation into smaller dense clumps, a single core may form multiple stars. In these regions, a star-forming core rarely evolves in isolation, and is instead impacted by the ongoing star formation in its natal environment. A YSO, for example, in close proximity to a starless core may radically influence the chemical differentiation, the physical structure, and consequently the entire evolution of the core. Creating combined physical and chemical models for such complex regions is extremely difficult, as clustered regions cannot be described by some simplifying assumptions, such as sphericity, used for isolated cores. We may combine, however, model results for iso-

lated cores with extensive, multi-wavelength observations to further our knowledge of the structure and evolution of clustered star forming regions.

## 1.2 Tracing Physical Conditions

The primary constituent of the interstellar medium (ISM) is hydrogen. At low to intermediate densities ($n_H < 10^2\,cm^{-3}$) and temperatures, most hydrogen is in its atomic, gas-phase form, HI. The physical properties and kinematics of the interstellar gas can be probed through emission line observations of its spin-flip transition, observable in the radio regime at a wavelength of 21 cm. Within molecular clouds, however, nearly all hydrogen is in its molecular form, $H_2$, whose rotational emission requires higher excitation conditions within clouds (such emission can trace highly localized shocks, e.g., from outflows on ambient material). Astronomers must therefore turn to other methods, such as the thermal emission from dust, and lower excitation lines of less abundant molecules, to investigate the structure and dynamics of dense gas in giant molecular clouds.

### 1.2.1 Thermal continuum emission from cold dust

In the ISM, the ratio of dust to gas mass is believed to be approximately 0.01 (Goldsmith et al. 1997). Although dust accounts for a small fraction of the total mass of a molecular cloud, it plays a large role in the cloud by the extinction of the light emitted by young stars embedded in the cloud (through absorption and the preferential scattering of short-wavelength radiation), and as an efficient cooling mechanism at high densities through its thermal continuum radiation. The magnitude of extinction of starlight is proportional to the dust column density, and the spatial extent of GMCs can be determined by mapping the extinction of starlight over large areas of sky (Lada et al. 1994; Cambrésy 1999; Alves et al. 2001). For temperatures typical of dense filaments and cores within GMCs ($T \sim 10-30\,K$), dust thermal radiation peaks at wavelengths $\lambda \sim 100 - 300\,\mu m$, and can be observed through several atmospheric windows in the submillimetre regime by terrestrial telescopes.

At typical single dish resolutions [e.g., 15″at 850 $\mu$m for the 15 m diameter James

Clerk Maxwell Telescope (JCMT)], submillimetre continuum emission reveals high column density dust condensations within the cloud, indicating where material has condensed and where star formation is most likely to proceed. Information on the global cloud structures is lost due to the necessity of removing the bright emission from the Earth's atmosphere at submillimetre wavelengths. These observations have provided information on the physical structure of dense starless and protostellar cores at scales of 0.01 pc (clouds such as Ophiuchus and Taurus, 120 pc and 160 pc distant respetively), to 0.03 pc (Orion, 450 pc distant) for major nearby star forming regions.

At submillimetre wavelengths, dust is generally assumed to radiate as a modified blackbody at some average temperature $T_d$. The continuum emission from dust is then given by $S_\nu \propto \kappa_\nu B_\nu(T_d)$, where $\kappa_\nu$ is the dust opacity, and $B_\nu(T_d)$ is the Planck blackbody function at frequency $\nu$ for dust at a temperature $T_d$. At submillimetre wavelengths, the optical depth $\tau$ due to dust is generally much less than one, so the dust emission is optically thin. Submillimetre observations thus sample all the dust emission within the cloud along the line of sight, and can be used to determine the column density and mass of material present within the beam (Hildebrand 1983). Molecular abundances can be determined through comparison of $H_2$ column densities derived from dust emission observations and molecular column densities derived from emission lines (discussed further below). From dust emission observations, physical models of individual cores are created which have been used to probe their density structures and thus their nature as pre-stellar objects.

Interpretation of the observations depends in part on the assumed dust temperature, $T_d$, and additionally on the dust grain composition and size distribution, which are folded into the opacity $\kappa_\nu$. The opacity has been calculated theoretically for multiple models of dust grains (Draine & Lee 1984; Ossenkopf & Henning 1994; Pollack et al. 1994). For dense cores, dust opacity models from Ossenkopf & Henning (1994) which incorporate accreted ice mantles are found to fit the observed dust continuum well (Shirley et al. 2002). Constraining $\kappa_\nu$ is a difficult task, however, as traditionally observations at multiple wavelengths have been required to determine its dependence on wavelength, which can then be compared with model predictions. The dust temperature can also be difficult to constrain, requiring either multiple observations at well-separated wavelengths to sample well the blackbody emission, or observations of molecular emission lines, such as $NH_3$, from which can be calculated the gas kinetic temperature, $T_K$ (discussed further below). In high density regions, it is expected

that $T_K \sim T_d$ due to good coupling between dust and gas, but few direct comparisons have been made.

Over the past two decades, telescopes operating at submillimetre and millimetre wavelengths and equipped with array receivers have enabled the mapping of the thermal emission from cold dust over relatively large regions of molecular clouds, such as in Serpens (Enoch et al. 2008), Perseus (Kirk et al. 2006; Hatchell et al. 2005; Enoch et al. 2006), Ophiuchus (Young et al. 2006; Nutter et al. 2006; Stanke et al. 2006; Johnstone et al. 2004, 2000b; Motte et al. 1998), and Orion (Johnstone et al. 2001; Johnstone & Bally 2006; Johnstone et al. 2006). For nearby regions (distances of 120 pc - 450 pc) these observations have provided information on the physical structure of dense starless and protostellar cores at scales of 0.01 pc - 0.03 pc. Information on the global cloud structures are lost, however, due to the necessity of removing the bright emission from the Earth's atmosphere at submillimetre wavelengths.

Several structure-finding algorithms have been developed to identify rigourously dense cores and clumps in both continuum and line emission observations. The physical properties of the objects, such as size, shape and mass, can then be analysed. These algorithms assign observed emission to individual clumps and cores in different ways. The CLUMPFIND algorithm (Williams et al. 1994) identifies emission peaks in the data at specified brightness intervals (in two dimensions for continuum data, and in three dimensions for molecular line data), and includes in the 'clump' emission in adjacent pixels down to a minimum intensity threshold or until the outer edges of two separate clumps meet. In CLUMPFIND, no limits are placed otherwise on clump shapes. The Gaussclumps method (Stutzki & Guesten 1990) iteratively fits a Gaussian-shaped clump to the observed brightness peak in the map, substracts it and repeats the procedure to a specified minimum threshold. Other techniques involve multiresolution wavelet analysis (Motte et al. 1998), and more recently the identification of structure trees (i.e., nested families of objects) which illustrate the hierarchical nature of the molecular cloud (dendrograms, Rosolowsky et al. 2008b). Studies using different structure-finding techniques often find similar average properties of the identified objects, but their individual objects do not necessarily correlate well (see, e.g., Motte et al. 1998; Johnstone et al. 2000b, for different catalogues of continuum clumps in Ophiuchus).

The deconstruction of molecular clouds into their embedded cores and clumps

enables study of molecular cloud fragmentation, and allows the creation of a 'core mass function' (CMF), analogous to stellar mass functions. Over multiple molecular clouds, the CMFs thus determined from continuum observations appear to follow closely the stellar initial mass function (IMF) shifted to slightly higher masses (Motte et al. 1998; Testi & Sargent 1998; Johnstone et al. 2000b; Kirk et al. 2006; Enoch et al. 2007) suggesting that there is a simple mapping, including an efficiency factor ($\gtrsim 25\%$ based on continuum studies of Perseus, Serpens and Ophiuchus by Enoch et al. 2008) from the observed clumps to the stars they will presumably form. This analysis depends, however, on the identification of nearly *all* clumps as prestellar objects, i.e., clumps that are gravitationally bound and will eventually form a star. This distinction requires additional kinematic information on the cores which must be provided by molecular line observations, described further below.

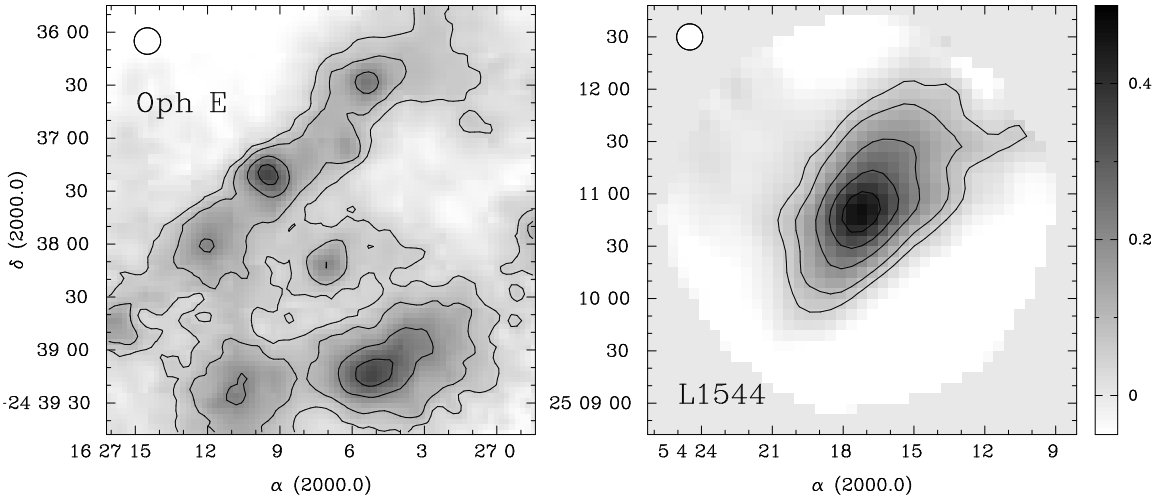


Figure 1.1 A comparison of cores in a clustered (Ophiuchus E, left) and isolated region (L1544 in Taurus, right) observed in submillimetre continuum emission ($\mathrm{Jy\,beam^{-1}}$) with the JCMT. Contours show $0.05\,\mathrm{Jy\,beam^{-1}}$, $0.1\,\mathrm{Jy\,beam^{-1}}$, $0.2\,\mathrm{Jy\,beam^{-1}}$, $0.3\,\mathrm{Jy\,beam^{-1}}$ and $0.4\,\mathrm{Jy\,beam^{-1}}$. Oph E and L1544 are at similar distances (120 pc and 140 pc, respectively) and the 15″ FWHM beam thus subtends similar physical scales. The clustered cores are smaller and more closely spaced than found in more isolated environments.

Submillimetre continuum observations have also revealed differences in the physical characteristics of starless and protostellar cores correlated with their environment. Cores in relatively isolated regions, such as the Taurus molecular cloud, are found to have average densities of $n \gtrsim 10^5 \mathrm{cm^{-3}}$, and linear sizes of $D \sim 0.1\,\mathrm{pc}$. In clustered environments, however, individual cores are systematically denser ($n \gtrsim 10^6 - 10^7\,\mathrm{cm^{-3}}$)

and more compact ($D \sim 0.02 - 0.03\,\mathrm{pc}$). They also tend to be more closely spaced (Ward-Thompson et al. 2007a). These differences can be clearly seen in Figure 1.1, which shows millimetre maps of isolated and clustered cores made with the same resolution. These substantial differences indicate that the formation and evolution of dense cores are strongly influenced by their environment. Also, in clustered environments, high resolution is needed to understand the physical conditions of individual cores.

### 1.2.2 Molecules

Submillimetre observations of dust continuum emission are an efficient tool to study the structure of molecular clouds and embedded dense cores, but no kinematic information can be recovered from these data. Understanding the dynamics of individual dense cores, and of an ensemble of cores within a given molecular cloud, is essential to determine the stability of an object to collapse or fragmentation, and to constrain core formation mechanisms through analysis of their relative and internal motions.

Observations of molecular emission lines can thus be excellent probes of both the physical conditions within molecular clouds and of their kinematics if the transitions are chosen wisely. For example, the choice of molecular line depends on the specific part of the molecular cloud being studied. After molecular hydrogen, CO is the second most abundant species in molecular clouds. CO is therefore often used as a surrogate for $H_2$, and can trace large-scale gas distributions and velocity patterns. Since its discovery in the Orion molecular cloud in 1970 (Wilson et al. 1970), CO has been historically used to find molecular clouds and determine their extents. The millimetre $J = 1 - 0$ rotational emission line of CO has a critical density $n_{cr} \sim 3 \times 10^3\,\mathrm{cm}^{-3}$ and is thus a good tracer of the less dense, large scale features of GMCs. In lines of sight with high column density, however, the CO emission becomes optically thick. Observed emission then only probes the outer layers of the cloud, and an accurate measure of the column density of the line of sight can't be determined. Emission from rarer CO isotopologues, such as $C^{18}O$ and $^{13}CO$, are often used to probe deeper into and through the molecular cloud, but even these can have high optical depths.

Complications also arise in the cold and dense environments of starless, possibly prestellar cores. At moderate densities ($n_{cr} \gtrsim 10^4\,\mathrm{cm}^{-3}$), CO is depleted from the

gas-phase by 'freezing out' onto dust grains. In fact, cores are often largely depleted in C-bearing molecules, precluding the use of their rotational lines as effective tracers of dense material (e.g., Tafalla et al. 2004; Bergin et al. 2002; Jørgensen et al. 2005). We must then turn to other molecules which are more resilient to depletion when studying the densest cores that are presumably on the verge of collapse, discussed further below.

To probe effectively dense molecular cores, molecules must be excited at the high densities ($n \gtrsim 10^4\,\mathrm{cm}^{-3}$, up to $n > 10^7\,\mathrm{cm}^{-3}$ in some objects) and low temperatures ($T \lesssim 20\,\mathrm{K}$) characteristic of these potential seeds of star formation. The disappearance of the CO molecule, along with most C-bearing molecules, from the gas phase in cold, dense regions makes CO a poor choice of probe of the physical characteristics and kinematics of significantly evolved starless cores. Particularly good tracers of quiescent, dense gas in star forming regions are nitrogen-based species, such as $NH_3$ (ammonia), and $N_2H^+$ (diazenylium), which form from the same parent molecule, $N_2$. Both species are collisionally excited at the high densities found in many starless cores [critical densities of $n_{cr} \sim 10^4\,\mathrm{cm}^{-3}$ for the $(J,K) = (1,1)$ and $(2,2)$ inversion transitions of $NH_3$, and $n_{cr} \sim 10^5\,\mathrm{cm}^{-3}$ for $N_2H^+$ (1-0)]. I discuss below the effectiveness of $NH_3$ and $N_2H^+$ in tracing the physical conditions of cores at high densities and low temperatures, and further comment on the use of deuterated species as probes of core environments where most molecules are expected to deplete from the gas phase.

### $NH_3$ and $N_2H^+$

$NH_3$ is a symmetric top molecule, with its N atom at the apex of a pyramid formed with three H atoms as the base. Symmetric top molecules are well understood both theoretically and in the laboratory (e.g., Townes & Schawlow 1975). In the radio regime, the rotation inversion transitions of $NH_3$ have proven useful in probing the physical characteristics of cold gas in the interstellar medium and molecular clouds (Ho & Townes 1983; Walmsley & Ungerechts 1983).

Rotational states of $NH_3$ are described by the two principal quantum numbers $J$ and $K$, respectively the total angular momentum of the molecule and the projection of the total angular momentum along the molecular axis. The lowest $NH_3$ $(J,K)$ rotational states (where $J = K$) are called metastable as they have a long timescale

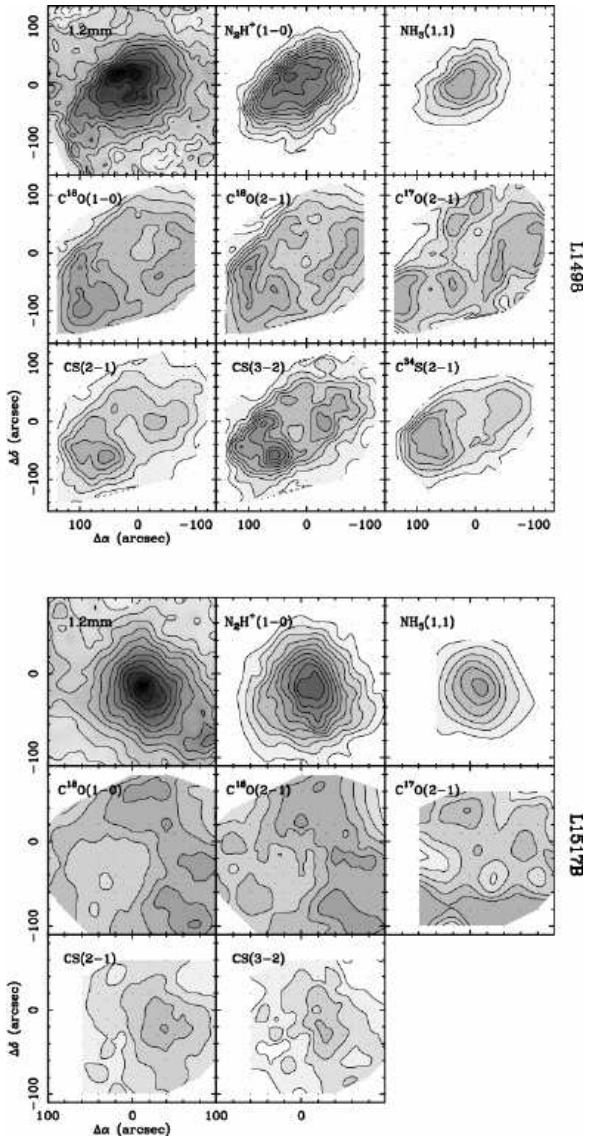


Figure 1.2 Integrated intensity maps for continuum and $NH_3$, $N_2H^+$, CO and CS lines observed by Tafalla et al. (2004) toward L1498 and L1517B. Note the systematic dichotomy between centrally-peaked and centrally-depressed morphologies. For each core, the top row shows the maps of centrally-peaked tracers, 1.2 mm continuum, $N_2H^+$, and $NH_3$, and the two lower rows present the maps of centrally-depressed species, isotopomers of CO (middle row) and isotopomers of CS (bottom row). In each map, the lowest contour and the contour interval are equal, and for each line, the same contour choice has been used for both L1498 and L1517B. Lowest contours are (in $\mathrm{K\,km\,s^{-1}}$): 0.15 for $C^{18}O$(1-0) and (2-1), 0.05 for $C^{17}O$(2-1), 0.25 for $N_2H^+$ (1-0), 1.5 for $NH_3$ (1, 1), 0.15 for CS (2-1), 0.1 for CS (3-2), and 0.05 for $C^{34}S$ (2-1). The $C^{17}O$ (2-1) data have been convolved with a 35″ FWHM Gaussian to improve S/N.

for decay, whereas rotational states where $J \geq K$ decay rapidly to the $J = K$ metastable state. The selection rules for radiative transitions are $\Delta K = 0$ and $\Delta J = 0, \pm 1$. Therefore transitions between states with different $K$ values - or $K$-ladders - is forbidden radiatively and they are populated solely via collisions. This allows the determination of the gas kinetic temperature, $T_K$, through observations of emission from different K-ladder states.

Each $(J, K)$ rotational state is split into inversion doublets, due to the ability of the N atom to tunnel quantum mechanically through the plane made by the three H atoms. These transitions are characterized by $(\Delta J = 0, \Delta K = 0)$. Furthermore, inversion spectra contain hyperfine structure due to both electric dipole and magnetic quadrupole moments. Given the expected frequencies and line strengths for the hyperfine components, the total line opacity and excitation temperature can be derived through fitting of the $(J, K)$ hyperfine structure (see, e.g., Ho & Townes 1983; Mangum et al. 1992), which can then be used to calculate directly the total $NH_3$ column density, $N(NH_3)$. $NH_3$ emission is found to correlate well with millimetre and submillimetre continuum emission in isolated cores, indicating that they trace the same material (Caselli et al. 2002a; Tafalla et al. 2002, 2004).

In particular, $NH_3$ may even be enhanced in dense cores with severe CO depletion (Tafalla et al. 2002, 2004). The reasons for this behaviour are not completely understood at present. It was thought that the binding energy of $N_2$, the parent molecule of both $NH_3$ and $N_2H^+$, was sufficiently different from CO to account for the differences in depletion from the gas phase in cold, dense regions. Recent work, however, has shown that the binding energies of the two species are similar (Bisschop et al. 2006). New models of the chemistry in isolated, evolving prestellar cores have made steps towards resolving this issue, with possible solutions discussed by Di Francesco et al. (2007).

To date, $NH_3$ has been detected in many dark clouds and molecular cloud cores, mainly through single pointings or small maps of select regions. In an extensive database of all pre-1999 $NH_3$ observations of dense cloud cores, Jijina et al. (1999) found that the effect of environment (i.e., within clustered compared to isolated regions) on observed core properties (such as the non-thermal line width, $\Delta v_{nt}$, kinetic gas temperature $T_k$, and linear size $D$) is statistically larger than effects due to the presence or absence of an embedded YSO. Cores in clustered environments tend to be

hotter, larger, and have larger, more turbulent $\Delta v_{nt}$ than isolated cores. This finding, however, contradicts the conclusions based on dust observations that clustered cores are smaller than isolated cores.

The difference between line and continuum observations of cores is one of linear resolution. Most $NH_3$ observations have been made with single dish telescopes with angular resolutions of $\sim 1'$ (Jijina et al. 1999). Also, most objects in the Jijina et al. (1999) sample are at distances $\gtrsim 300\,\mathrm{pc}$. At these distances, the linear scales probed are $\gtrsim 0.1\,\mathrm{pc}$. Since submillimetre continuum emission studies find dense cores with typical radii of 0.02 - 0.03 pc in clustered regions, these observations are not resolving individual core structures. Most cores identified in $NH_3$ emission at $1'$ scales certainly contain significant unresolved substructure. For example, while the nearby Ophiuchus cloud was largely not included in the sample, at 125 pc, $1'$ still corresponds to a spatial distance of 0.04 pc. Consequently, higher spatial resolution, such as that provided by interferometers, is essential to studies of the formation and evolution of dense cores in clustered regions.

Rotational transitions of $N_2H^+$ also contain hyperfine structure, from which can be derived $T_{ex}$ and $\tau$ of the line transition. These transitions are found at higher frequencies than the low-lying $NH_3$ inversion transitions. Single dish $N_2H^+$ observations can potentially have higher spatial resolution than single-dish $NH_3$ observations, depending on the telescope diameter. If these resolutions allow, estimates of $H_2$ column density can be made, allowing calculation of the fractional $N_2H^+$ abundance, $X(N_2H^+) = N(N_2H^+)/N(H_2)$.

In isolated cores, $NH_3$ and $N_2H^+$ emission correlate well with each other and the (sub)millimetre continuum emission, indicating that all three trace the same material (Caselli et al. 2002a; Tafalla et al. 2002, 2004). In very cold, dense isolated cores where molecules such as CO are depleted, both species have been predicted (Aikawa et al. 2005; Lee et al. 2004; Bergin & Langer 1997) and observed (Tafalla et al. 2002, 2004) to remain abundant. These trends can be seen in Figure 1.2 (Tafalla et al. 2004), which shows the distribution of millimetre continuum emission and line emission from four different molecular species ($NH_3$, $N_2H^+$, CO, and CS) in the isolated, starless L1498 and L1517B cores. In both cores, $NH_3$ and $N_2H^+$ integrated intensity contours follow closely the continuum emission while CO and CS appear to avoid the core centres.

Similar good correlation between dense gas tracers and continuum emission has

been found in the NGC 1333 cluster forming region (Walsh et al. 2007). Clump mass functions determined through structure identification in 3D data cubes of dense gas tracers also resemble the stellar IMF, suggesting that the form of the IMF is determined through some fragmentation process in the larger dense cores.

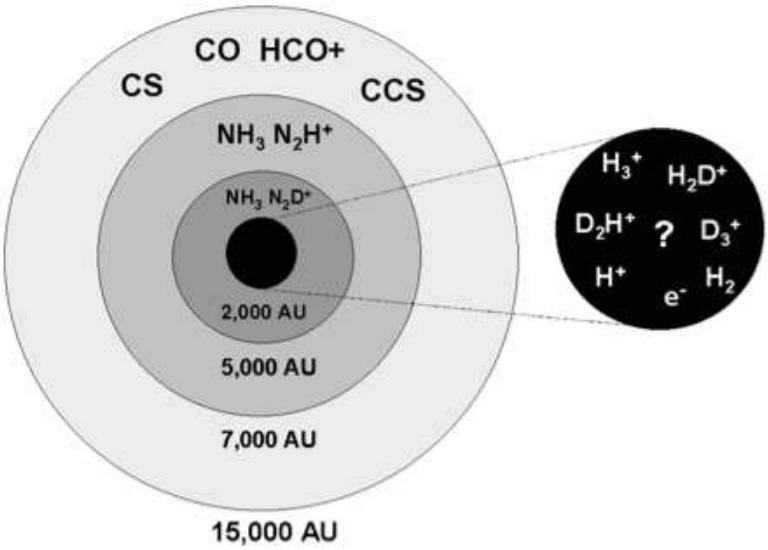


Figure 1.3 Proposed chemical differentiation of an evolved, isolated starless core (Di Francesco et al. 2007). At decreasing core radii and increasing core density, the depletion from the gas phase of species onto dust grains ('freeze out') leads to the core becoming extremely chemically differentiated. The figure shows the dominant molecular species of each layer. At core centres, it is currently unclear what species remain in the gas phase to be used as physical tracers of the physical conditions at the highest densities.

### Deuterated Species

Recent $N_2H^+$ observations (Bergin et al. 2002; Belloche & André 2004), and chemical models of star forming cores (Aikawa et al. 2005)have suggested that the resistance of $NH_3$ and $N_2H^+$ to depletion from the gas phase is limited to central core densities $n \lesssim 10^{6-7}\,\mathrm{cm}^{-3}$. The lack of heavy molecules in the gas phase at high densities leads to an increased abundance of deuterated molecules, where H atoms have been replaced through chemical reactions with D atoms. The chemical differentiation of a

dense core may thus look something like Figure 1.3 (Di Francesco et al. 2007), where the best tracers of central core conditions are deuterated forms of the trihydrogen ion, $H_3^+$.

The systematic depletion of species from the gas phase in dense cores is problematic, as this differentiation of chemical abundance likely becomes more extreme as cores condense. All heavy molecules may deplete from the gas phase in the densest cores. In clustered environments, the chemical differentiation could be even more pronounced given the higher densities, and more difficult to understand given the complexities of these regions. Chemical differentiation could lead, however, to a method of assaying the 'age' of a core by studying the distributions of the various molecular emission lines in and around the core, and comparing their emission (or lack thereof) with models of the chemistry in star forming regions. Since the timescale of core evolution strongly affects the resulting core chemistry, the observed chemical differentiation of a dense core could be an excellent indicator of its evolutionary status, and of the relevant timescales, when compared to predictions from chemical reaction models combined with physical models of core formation and evolution.

Within 1 kpc of the Sun, the observed D/H ratio $\gtrsim (2.3 \pm 0.2) \times 10^{-6}$ (Linsky et al. 2006). In dense cores, the depletion of many molecular species discussed above leads to radically different abundances of deuterated molecules than in the more distributed gas of the molecular cloud as a whole. This is due to the exothermic nature in the forward direction of the reaction

$$H_3^+ + HD \rightleftharpoons H_2D^+ + H_2 \tag{1.1}$$

where the backward, endothermic reaction does not proceed at temperatures $T < 20\,\mathrm{K}$, while the main $H_2D^+$ destruction route, through reactions with CO, is disrupted due to the depletion of CO from the gas phase. The isotope exchange equilibrium reaction in Equation 1.1 begins a chain of deuterium transfer reactions, which increases the deuteration fractionation in a variety of molecules and molecular ions, including $HCO^+$, $NH_3$ and $N_2H^+$. In fact, singly, doubly and triply deuterated $NH_3$ have been observed in dense cores, such as L134N and Barnard 1; see, e.g., Roueff et al. (2000); Lis et al. (2002). These results imply deuterium abundances of orders of magnitude above the $\sim 10^{-6}$ D/H ratio typical of the solar neighbourhood are

reached in star forming cores. Observations of $H_2D^+$ itself in dense cores can thus probe physical conditions of the innermost core environments, and provide insight into the core chemical state.

Like $H_2$, $H_2D^+$ exists in both ortho (hydrogen spins are parallel) and para (hydrogen spins are antiparallel) states. The lowest ortho-$H_2D^+$ $1_{11} - 1_{10}$ transition has a critical density $n_{cr} \sim 2 \times 10^5\,\mathrm{cm}^{-3}$ (van Dishoeck et al. 1992), and is thus an excellent tracer of the physical conditions of cores otherwise depleted in heavy molecules. While enhancements in the abundance ratios of $DCO^+/HCO^+$ and other species have been noted in molecular clouds for several decades (Loren et al. 1990), the first detection of $H_2D^+$ was made by Stark et al. (1999) towards the NGC 1333 IRAS 4A protostellar core. The transition, however, occurs at a frequency 372 GHz near the edge of a strong telluric water line, making it extremely difficult to observe from ground-based telescopes. Recent detector advances at submillimetre telescopes, such as the JCMT, have improved receiver sensitivities such that multiple detections have been recently presented (Caselli et al. 2003, 2008; Harju et al. 2008; Pagani et al. 2009). Analysis of $H_2D^+$ emission has been used to model in detail core chemistry and probe core ages independently of number statistics. In L183, for example, Pagani et al. used $H_2D^+$ observations in conjunction with a chemical/physical core model to constrain the ortho- to para-$H_2$ ratio in the core, which in turn constrained the core age to $\gtrsim 1.5 - 2 \times 10^5$ years.

Most of these detections are single pointings or small maps of $\sim 1'$ in extent only towards isolated starless and protostellar cores. It is unclear whether similar deuteration processes occur in more complex, clustered environments. The higher densities in clustered cores should favour deuteration, but the warmer core temperatures could allow the reaction in Equation 1.1 to proceed in both directions and therefore produce less $H_2D^+$. Additionally, different timescales in the condensation and collapse of clustered cores compared with starless cores will have an impact on the core chemistry.

### 1.2.3 The Ophiuchus Molecular Cloud

The Ophiuchus molecular cloud is one of the closest active star forming regions at a distance of only $\sim 120$ pc (see Chapter 2 for a discussion of various distance estimates),

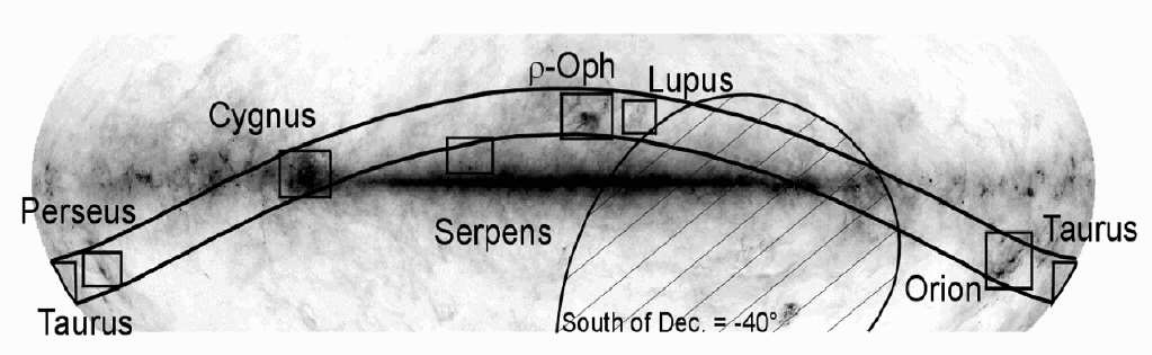


Figure 1.4 Locations of nearby molecular clouds, including Ophiuchus, overlaid on an $100\,\mu$m map of the galactic plane made with IRAS. The Gould Belt is identified in the figure by the doubled solid lines. Image from www.jach.hawaii.edu/JCMT/surveys/gb/

and resides in the Gould Belt, originally identified as a system of bright stars residing in a belt inclined $\sim 20\,^\circ$ from the Galactic plane (Gould 1879; Herschel 1847) and now recognized as a local ring of ongoing star formation. Figure 1.4 shows the location of nearby molecular clouds, including Ophiuchus, overlaid on an IRAS $100\,\mu$m map of the galactic plane.

Towards central Ophiuchus, extremely high column densities of gas and dust lead to the extinction of visual starlight by up to $\sim 100$ magnitudes (Casanova et al. 1995). I show in Figure 1.5 the visual extinction measured using star counts and an adaptive grid technique by Cambrésy (1999). The region in Ophiuchus with the greatest extinction, labelled $\rho$ Oph in the image, is also identified as the Lynds 1688 dark cloud (L1688, Lynds 1962), while L1689 streams to the southeast. The total cloud mass $M \sim 25400\,\mathrm{M}_\odot$ determined through near-infrared extinction measurements, with $M \sim 8300\,\mathrm{M}_\odot$ at K-band extinctions $A_K > 0.2\,$mag (Lombardi et al. 2008), of which several thousand $M_\odot$ is found in the L1688 region alone (Johnstone et al. 2004).

Ongoing star cluster formation is occurring in L1688, where the first deeply embedded stellar cluster was discovered using single-channel infrared photometers (Grasdalen et al. 1973; Wilking & Lada 1983). Several authors have suggested that star formation in L1688 was triggered by compression from the nearby Sco-Cen OB association (e.g., Vrba 1977). The median age of the YSOs associated with the L1688 dense cores is 0.3 Myr. An extended population, however, of older YSOs may predate

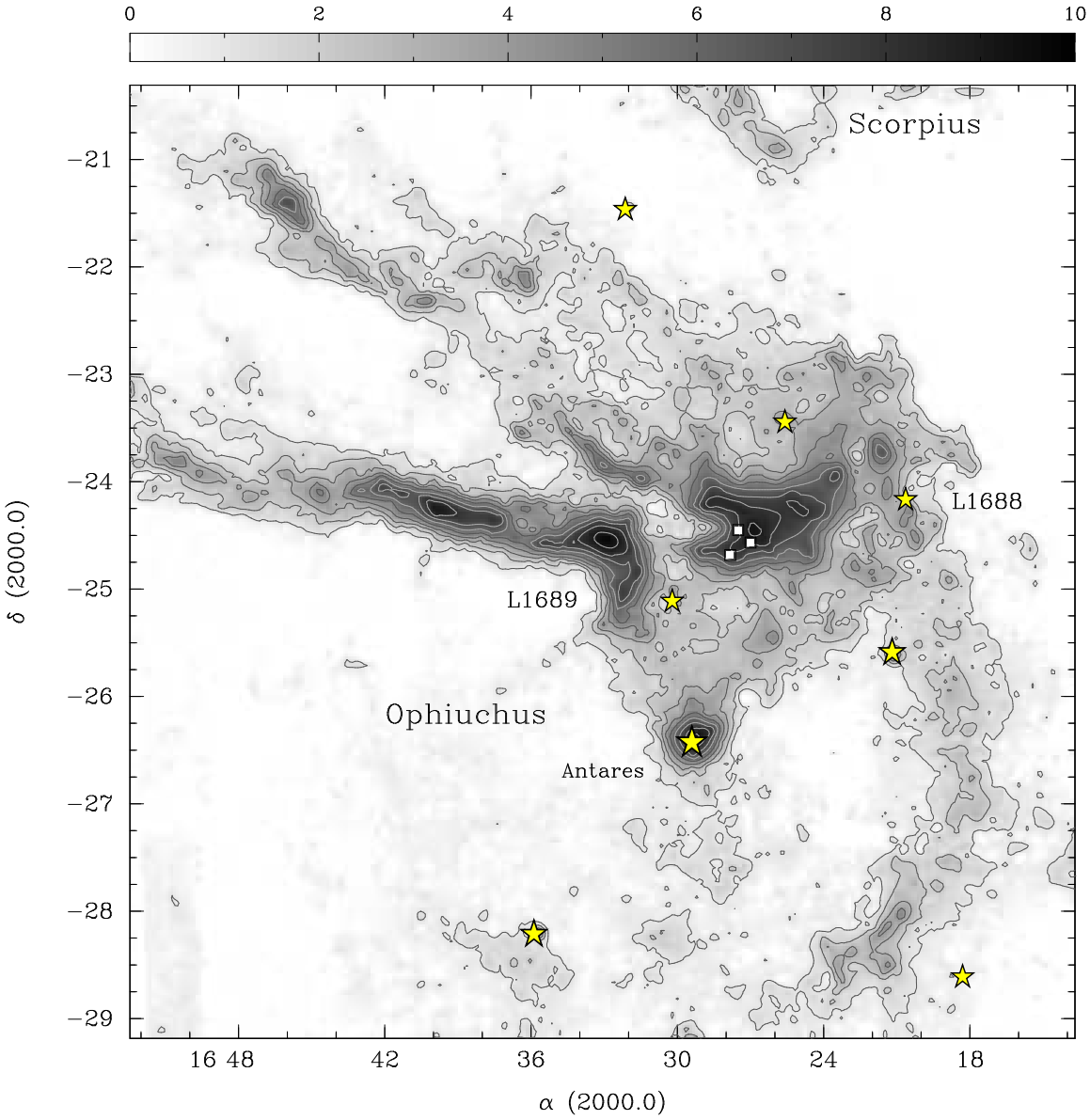


Figure 1.5 Visual extinction, based on star counts, towards the Ophiuchus molecular cloud from public data described in Cambrésy (1999). The southern tip of the Scorpius molecular cloud is also shown. In Ophiuchus, the two major extincted regions, Lynds 1688 and Lynds 1689, are labelled. Stars indicate positions of stars brighter than $5^{th}$ magnitude. Note that bright stars create artificial peaks in extinction with this method due to the inability to see additional nearby stars. The extinction peak towards the brightest star in the field, Antares ($\alpha$ Sco, $V = 1.1$), is an example of this effect. The resolution is variable based on the number of background stars visible, and can be $\sim 10'$ in the most extincted regions. The locations of the Oph B, C and F Cores are indicated by the white squares in L1688.

the interaction (Wilking et al. 2008) and connect the star formation in Oph with that of the low mass Upper Scorpius subgroup (Wilking et al. 2005).

The development and launch of space-based infrared observatories, such as IRAS and the Spitzer Space Telescope, have greatly improved our sensitivity to deeply embedded YSOs in molecular clouds. In Figure 1.6, I show the Lynds 1688 dark cloud in Ophiuchus as seen by Spitzer's InfraRed Array Camera (IRAC) and Multiband Imaging Photometer for Spitzer (MIPS). The most deeply embedded objects are red in this image (red colours show $24\,\mu$m emission), while more evolved stars which have lost their natal envelopes appear blue (blue colours show $3.6\,\mu$m emission). The infrared data allow the cataloguing and placing of the embedded population of the cloud in an evolutionary progression. Recent work has shown that most of the embedded YSOs in Ophiuchus are Class I objects or later (Enoch et al. 2008; Jørgensen et al. 2008; Enoch et al. 2009), meaning the embedded protostars have begun to remove their natal gas envelope through accretion and outflow processes. Only a few YSOs are surrounded by a substantial gas envelope. Note, however, that large areas of the central Oph regions remain dark even at $24\,\mu$m, revealing areas of extremely high $H_2$ column density which may shroud YSOs from view, even with Spitzer's sensitivity. Nevertheless, infrared observations show that the L1688 region is forming stars with a higher efficiency (star formation efficiency $SFE = M_{YSO}/(M_{gas+dust} + M_{YSO}) \sim 9 - 14\%$, Jørgensen et al. 2008) than in other, smaller star forming regions ($SFE \sim$ few %).

Central Oph (L1688) has been surveyed extensively in (sub)millimetre continuum emission from cold dust, revealing a highly fragmented and clumped complex containing both starless and protostellar cores (Johnstone et al. 2000b; Motte et al. 1998). Figure 1.7 shows $850\,\mu$m continuum emission in central L1688 observed with the James Clerk Maxwell Telescope (JCMT) at $15''$ resolution (first published by Johnstone et al. 2000b; Di Francesco et al. 2008, re-reduced and coadded all available data in the region). The cloud's central region contains several bright irregularly shaped filaments up to a few arcminutes in diameter, along with numerous smaller cores and structures. The larger filaments have masses of up to several tens of solar masses, and themselves fragment into multiple smaller continuum clumps with $M \lesssim 1 M_\odot$ determined from the dust emission. These regions of high column density all lie within the high extinction contours of Figure 1.5, with $A_v \gtrsim 10$ (Johnstone et al. 2004). Of the larger filaments, several are associated with known YSOs, while others appear

Figure 1.6 Spitzer Space Telescope IRAC and MIPS image of the Lynds 1688 region of the Ophiuchus molecular cloud. Blue colours show 3.6 $\mu$m emission, green shows 8 $\mu$m emission, and red shows 24 $\mu$m emission. Image Credit: NASA/JPL-Caltech/Harvard-Smithsonian CfA.

starless (Jørgensen et al. 2008; Enoch et al. 2009). Physical parameters of the large cores are given in Table 1.1 based on millimetre continuum observations by Motte et al. (1998).

On large scales, observed $^{13}$CO line widths (average $\Delta v = 1.5\,\mathrm{km\,s^{-1}}$ $\pm 0.25\,\mathrm{km\,s^{-1}}$ in L1688, Loren 1989) show that the region is dominated by supersonic non-thermal motions given the observed gas temperature $T$, where $\sigma^2_{NT} = \sigma^2_{obs} - \sigma^2_T$, and the thermal velocity dispersion $\sigma^2_T = kT/(\mu\, m_{\rm H})$. These large non-thermal motions are reduced on smaller scales and at higher densities, shown by recent $N_2H^+$ 1-0 obser-

| Filament | $T_d$ (K) | $N_{H_2}$ ($10^{22}\,\mathrm{cm^{-2}}$) | $n_{H_2}$ ($\mathrm{cm^{-3}}$) | $M$ ($M_\odot$) | YSO surf. dens. [stars/(0.1 pc)$^2$] |
|---|---|---|---|---|---|
| A | 20 | 78 | $4.0 \times 10^6$ | 23 | $2.4 - 4.4$ |
| B1 | 12 | 12 | $4.6 \times 10^5$ | 7.2 | 0.45 |
| B2 | 12 | 41 | $1.2 \times 10^6$ | 42 | 0.55 |
| C | 12 | 22 | $5.3 \times 10^5$ | 44 | 0.65 |
| F | 15 | 10 | $3.7 \times 10^5$ | 8.1 | $2.9 - 4.6$ |

Table 1.1 Parameters of Ophiuchus Cores from 1.3 mm continuum (11″ resolution) observations by Motte et al. (1998).

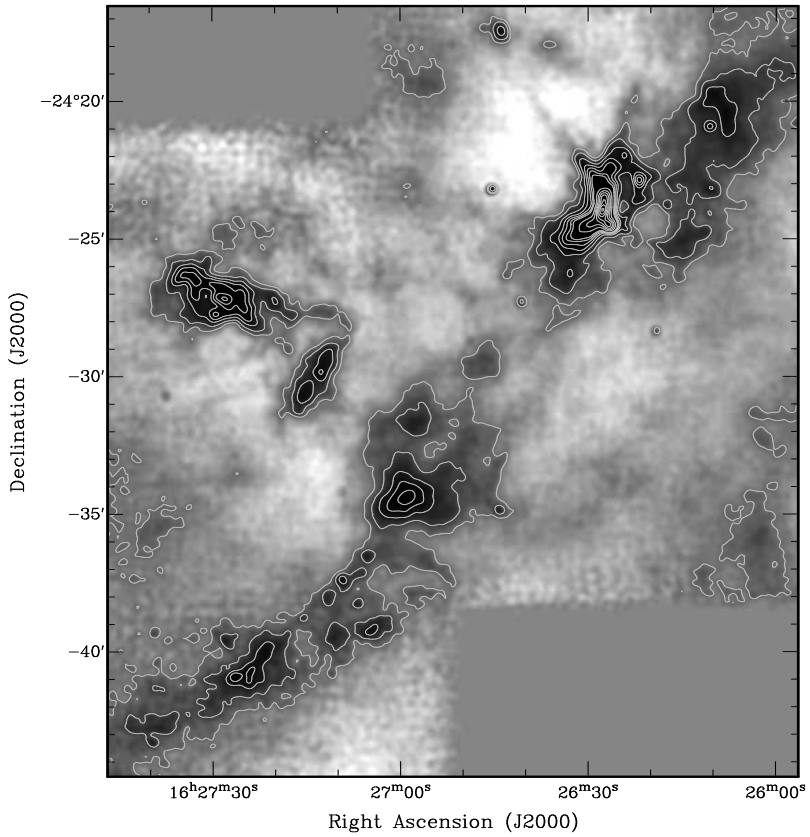


Figure 1.7 850 $\mu$m continuum emission towards the central L1688 cloud in Ophiuchus observed with 15″ FWHM angular resolution at the James Clerk Maxwell Telescope. Contours are in increments of 0.1 Jy beam$^{-1}$.

vations towards the continuum cores (André et al. 2007, at 26″ angular resolution). André et al. also found that most of the continuum clumps were consistent with being gravitationally bound and thus prestellar.

## 1.3 Characterizing Cluster-Forming Cores Through Multi-Molecular Observations

The proximity of Ophiuchus makes it an ideal target for the characterization of dense gas in a clustered star forming environment. Prior to this work, few studies of the molecular line emission from dense gas tracers at the high resolution needed to probe the small scale structure observed in clustered environments have been performed, possibly due to its low declination (-24°). The goal of this dissertation is to probe the physical conditions of dense cores within the nearby Ophiuchus molecular cloud which are currently forming small stellar clusters, and compare them with the results of previously published studies of isolated star forming regions. In this thesis, I present observations and interpretation of the line emission from multiple molecular species which are both abundant and excited in cold molecular clouds over space densities $n \sim 10^4 - 10^6\,\mathrm{cm}^{-3}$. These data complement studies of thermal continuum emission from cold dust, which is a sensitive probe of the column density of material along the line of sight but cannot provide information on the gas kinematics or chemical abundances.

### 1.3.1 Chapter Summaries

In Chapter 2 (published in the Astrophysical Journal, Friesen et al. 2009b), I present combined interferometer and single dish telescope data of $NH_3$ $(J,K) = (1,1)$ and (2,2) emission towards the clustered, low mass star forming Ophiuchus B, C and F Cores at high spatial resolution ($\sim 1200\,\mathrm{AU}$) using the Australia Telescope Compact Array, the Very Large Array, and the 100 m Green Bank Telescope. I show that the dense gas traced by the $NH_3$ emission is highly fragmented, as expected for a cluster-forming Core, in Oph B and Oph F, but less so in Oph C. Significant and unexpected offsets were found between the locations of $NH_3$ 'clumps' and those identified in continuum emission, in direct contrast with most results in isolated star forming environments. The variation of the local standard of rest (LSR) line-of-sight velocity of the gas varies little between all three Cores. $NH_3$ line widths in Oph B and F tend to be mildly supersonic, while Oph C is characterized by narrow line widths which decrease to values indicative of purely thermal motions.

I use the intensity ratio of the collisionally excited $NH_3$ (1,1) and (2,2) inversion transitions to determine the kinetic temperature $T_K$ of the gas, and find that Oph B and F are warmer on average than typically found in isolated regions. Oph C, in contrast, is significantly colder with temperatures that decrease towards the column density peak.

I calculate the $NH_3$ column density across the Cores, and use publicly available submillimetre continuum emission to determine the $H_2$ column density and consequently the fractional $NH_3$ abundance within the Cores. I find a general trend where the $NH_3$ abundance decreases towards the greatest $H_2$ column densities, suggestive of the depletion of $NH_3$ from the gas phase in the densest central regions of the Cores. Because of this decrease in $NH_3$ abundance with increasing $H_2$ column density, most clumps identified in continuum emission are thus locations of $NH_3$ abundance minima. This is in direct contrast with studies of isolated cores which find central $NH_3$ abundance enhancements.

In summary, in contrast to previous studies which suggest association with a young stellar cluster has a greater impact on core physical properties than the presence within a core of an embedded young stellar object, the derived properties of the Oph B, C and F cores suggest that both 'isolated'- and 'clustered'-type cores can coexist in the same environment. Additionally, the evidence that $NH_3$ may itself be depleted at the high densities found in the Oph Cores implies that observations of molecular line emission from species and transitions with greater critical densities may be better probes of the physical conditions of dense core interiors.

In Chapter 3 (submitted to the Astrophysical Journal, Friesen et al. 2009a), I present Nobeyama 45 m Radio Telescope maps and Australia Telescope Compact Array pointed observations of $N_2H^+$ 1-0 emission towards the Ophiuchus B Core, and determine the velocity, density and $N_2H^+$ abundance distribution. I compare these data with the results of $NH_3$ observations presented in Chapter 2. The locations of $N_2H^+$ clumps identified in the single-dish emission match well those identified in $NH_3$ (1,1) emission, but are similarly offset from clumps identified in continuum emission. This result is again in contrast with the close correlation between $N_2H^+$ and continuum emission typically found in isolated cores.

Oph B can be divided into subCores, labelled B1, B2 and B3. $N_2H^+$ 1-0 line widths in Oph B2 indicate non-thermal motions dominate the Core kinematics, and

remain transonic at densities $n \sim 3 \times 10^5\,\mathrm{cm}^{-3}$ with large scatter and no trend with $N(\mathrm{H_2})$. In contrast, non-thermal motions in Oph B1 and B3 are subsonic with little variation, but also show no trend with $\mathrm{H_2}$ column density. Over all Oph B, non-thermal $\mathrm{N_2H^+}$ line widths are substantially narrower than those traced by $\mathrm{NH_3}$, making it likely $\mathrm{NH_3}$ and $\mathrm{N_2H^+}$ trace different regimes, but the $v_{\mathrm{LSR}}$ of transitions from both species agree well, and their emission have strong spatial correspondence.

I find evidence for recent accretion in Oph B1 from the surrounding ambient gas. The $\mathrm{NH_3}$ / $\mathrm{N_2H^+}$ abundance ratio is larger towards Oph B1 than towards Oph B2, similar to recent observational results towards starless and protostellar cores, but with values substantially smaller than previously observed. The interferometer observations reveal small-scale structure in $\mathrm{N_2H^+}$ 1-0 emission, which is again offset from continuum emission. No continuum clumps observed were found to be coincident with interferometric $\mathrm{N_2H^+}$ emission peaks, including the $\sim 1\,\mathrm{M}_\odot$ B2-MM8 clump which is associated with a $\mathrm{N_2H^+}$ emission hole and surrounding broken ring-like emission structure, suggestive of $\mathrm{N_2H^+}$ depletion. I find a general trend of decreasing $\mathrm{N_2H^+}$ abundance with increasing $N(\mathrm{H_2})$ in B2 which matches that found for $\mathrm{NH_3}$.

In Chapter 4, I present $\mathrm{N_2D^+}$ 3-2 and $\mathrm{H_2D^+}$ $1_{11} - 1_{10}$ and $\mathrm{N_2H^+}$ 4-3 maps of the Oph B2 Core. The $\mathrm{N_2D^+}$ observations were performed at the Institut de Radio Astronomie Millimetrique 30 m Telescope, while the $\mathrm{H_2D^+}$ and $\mathrm{N_2H^+}$ observations were performed at the 15 m James Clerk Maxwell Telescope. The $\mathrm{H_2D^+}$ data in particular form the largest ($\sim 4' \times 3'$) $\mathrm{H_2D^+}$ map yet observed. In conjunction with the $\mathrm{N_2H^+}$ observations presented in Chapter 3, the $\mathrm{N_2D^+}$ data reveal the deuterium fractionation, or enhancement of deuterated species relative to their normal counterparts, in the high density gas across Oph B2. I show that the average deuterium fractionation value over the Core is several orders of magnitude above the interstellar D/H ratio, but is low relative to previous results in isolated starless cores and consistent with previous results in protostellar cores. The column density distributions of both $\mathrm{H_2D^+}$ and $\mathrm{N_2D^+}$ show no correlation with total $\mathrm{H_2}$ column density. I find, however, an anticorrelation in deuterium fractionation with proximity to the embedded protostars in the Oph B2 Core to distances $\gtrsim 0.04\,\mathrm{pc}$. I explore the mechanisms by which protostars may impact the core chemistry over such distances, which require temperatures greater than determined in Chapter 2 to proceed. This result implies that either the gas temperatures determined in Chapter 2 are not applicable to the higher density gas in which the deuterated species are formed and excited, or a new

mechanism of interrupting the deuterium fractionation reactions must be explored. I present a new method of calculating gas temperatures through the equating of non-thermal line widths for molecules expected to trace the same core regions, but the complex line structure in B2 precludes finding a reasonable result in many locations. This method may, however, work well in isolated cores with less complicated velocity structures. Finally, I show how $N_2D^+$ and $H_2D^+$ observations may be used to set a lower limit on the ionization fraction of a star forming core, informing discussion of the possible timescales for core evolution in the presence of a magnetic field.

In Chapter 5, I summarize briefly the implications of the results of this dissertation to the study and understanding of the physical and chemical structure of clustered star forming environments. I also discuss current and future observational initiatives which will greatly impact star formation astronomy and possible future work which can build on the work presented here.

# Chapter 2

# $NH_3$ Observations of Dense Cores in Ophiuchus

## 2.1 Introduction

Stars form out of the gravitational collapse of centrally condensed clumps[1] of dense molecular gas. Recent years have seen leaps forward in our understanding of the structure and evolution of isolated, star forming clumps. Most star formation, however, occurs in clustered environments (Lada & Lada 2003). These regions are more complex, with complicated observed geometries, and contain clumps which tend to have higher densities and more compact sizes than those found in isolation (Motte et al. 1998; Ward-Thompson et al. 2007a). It is likely that due to these differences the star formation process in clustered regions proceeds differently than in the isolated cases. Characterizing the physical and chemical structures of these more complicated regions are thus the first steps towards a better understanding of the process of clustered star formation.

It is now clear that molecular clumps become extremely chemically differentiated, as many molecules commonly used for tracing molecular gas, such as CO, become severely depleted in the innermost regions through adsorption onto dust grains [see, e.g., Di Francesco et al. (2007) for a review]. An excellent probe, therefore, of dense

[1]In this paper, we call prestellar objects 'clumps' instead of 'cores' to avoid confusion with the Ophiuchus 'Cores' discussed here.

clump interiors is the ammonia molecule ($NH_3$), with a relatively high critical density ($n_{cr} \sim 10^4\,\mathrm{cm}^{-3}$ for the (1,1) and (2,2) inversion transitions) and apparent resistance to depletion until extreme densities and low temperatures are reached in a starless core's evolution (Tafalla et al. 2004; Aikawa et al. 2005; Flower et al. 2006). The additional kinematic information provided by line observations are complementary to continuum observations of emission from cold dust, and the ammonia molecule in particular allows the determination of the gas kinetic temperature and density structure due to hyperfine transitions of its metastable states (Ho & Townes 1983).

The nearby Ophiuchus molecular cloud, containing the dark L1688 region, is our closest example of ongoing, clustered star formation. The central Ophiuchus cloud has been surveyed extensively in millimeter (Young et al. 2006; Stanke et al. 2006; Motte et al. 1998) and submillimeter (Johnstone et al. 2004, 2000b) continuum emission. These observations have revealed a highly fragmented complex of star forming clumps with masses $M \sim 0.2 - 6\,M_\odot$, the majority of which are embedded within larger, highly fragmented structures, called 'Cores' for historical reasons (Loren et al. 1990) and named A through I, which reside only in areas of high extinction (Johnstone et al. 2004; Young et al. 2006; Enoch et al. 2007). The total mass of the distinct (sub)millimeter clumps, $\sim 40-50\,M_\odot$, makes up only $0.5-3\,\%$ of the total $\sim 2000\,M_\odot$ mass of the molecular cloud (Young et al. 2006; Johnstone et al. 2004).

Most recent estimates put the distance to the central L1688 cloud region (often also called '$\rho$ Oph') at 120 pc (Loinard et al. 2008; Lombardi et al. 2008; Knude & Hog 1998), in agreement with some older results (de Geus et al. 1989), but a clear consensus has not yet been reached. Mamajek (2008), for example, find a distance of 135 pc towards the cloud using Hipparchos parallax data, while VLBA observations by Loinard et al. (2008) suggest that the Ophiuchus B core may be further distant than the rest of the cloud, at 165 pc (we also note that Oph B consists of three sub-Cores, B1, B2 and B3, described further in §3). This distance is outside the range in median cloud thickness determined by Lombardi et al. (2008) of $28^{+29}_{-19}$ pc, but in agreement with an older result by Chini (1981). The stars used to determine the distance to Oph B may, however, be background stars (Lombardi et al. 2008). In the following, we adopt the 120 pc distance to the entire central Ophiuchus region.

In this work, we discuss the results of high resolution observations of $NH_3$ (1,1) and (2,2) in the Ophiuchus B, C and F Cores to study the distribution, kinematics

Table 2.1. Rest frequencies of all observed spectral lines

| Molecule | Transition | Rest Frequency GHz | Source |
|---|---|---|---|
| $C_2S$ | $(2_1 - 1_0)$ | 23.3440330 | Pickett et al. (1998) |
| $NH_3$ | $(1,1)$ | 23.694495 | Ho & Townes (1983) |
| $NH_3$ | $(2,2)$ | 23.722633 | Ho & Townes (1983) |
| $HC_5N$ | $(9-8)$ | 23.963888 | Myers et al. (1979) |

and abundance patterns of the Cores and associated embedded clumps. We find that although the Cores are embedded in the same physical environment, they present very different physical characteristics. We discuss the observations and the combination of interferometer and single dish data in §2. In §3, we present the data, and detail the hyperfine line fitting procedure and derivations of kinetic temperature $T_K$, $NH_3$ column $N(NH_3)$ and space density $n(H_2)$ in §4 (see also Appendix A). We discuss the results in §5 and summarize our findings in §6.

## 2.2 Observations and Data Reduction

Figure 2.1 shows the central Ophiuchus region in 850 $\mu$m continuum emission first mapped with the Submillimetre Common User Bolometer Array (SCUBA) at the James Clerk Maxwell Telescope (JCMT) by Johnstone et al. (2000b) and recently re-reduced and combined with all other SCUBA archive data in the region by Jørgensen et al. (2008), following the description in Kirk et al. (2006). The Oph B, C and F Cores are labelled, and boxes show the approximate areas we mapped at the Green Bank Telescope (GBT), the Australia Telescope Compact Array (ATCA) and the Very Large Array (VLA). The details of all astronomical observations are described below. Table 2.1 lists the lines observed and their rest frequencies.

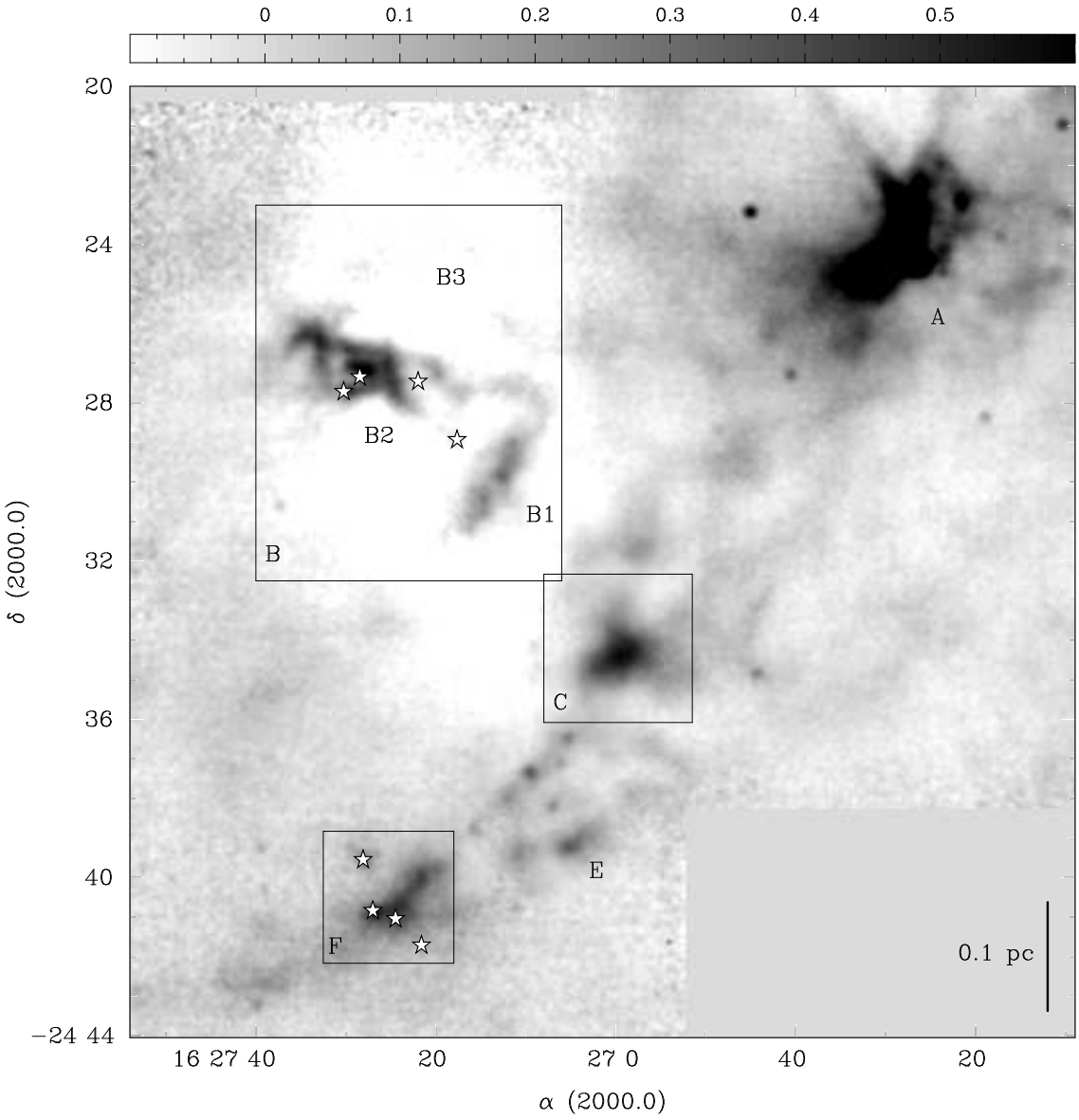


Figure 2.1 The central region of the Ophiuchus molecular cloud in 850 $\mu$m continuum emission originally mapped at the JCMT by Johnstone et al. (2000b). Colour scale units are Jy beam$^{-1}$, where the beam FWHM $\approx 15''$. The B, C and F Cores are labelled (Oph B3 is not well detected in 850 $\mu$m continuum). Rectangles show areas mapped in $NH_3$ (1,1) and (2,2) emission, as well as $C_2S$ ($2_1 - 1_0$) and $HC_5N$ (9 - 8) at the GBT. Stars indicate locations of protostars identified in the infrared with Spitzer (Enoch et al. 2008). VLA and ATCA pointings were placed to provide Nyquist-sampled mosaicing of the indicated regions, with multiple beam overlap in the areas of bright continuum emission.

### 2.2.1 Green Bank Telescope

Single-dish observations of emission from the $NH_3$ $(J,K) = (1,1)$ and $(2,2)$ inversion lines, $C_2S$ $J_N = 2_1 - 1_0$ and $HC_5N$ $J = 9 - 8$ in the Ophiuchus Cores were obtained using the 100 m Robert C. Byrd Green Bank Telescope (GBT), located near Green Bank, WV, USA. The observations were done in frequency-switching mode, using the GBT K-band (upper) receiver as the front end, and the GBT spectrometer as the back end. This setup allowed the simultaneous observation of all lines in four 50 MHz-wide IFs, each with 8192 spectral channels, giving a frequency resolution of 6.104 kHz, or 0.077 $\mathrm{km\,s^{-1}}$ at 23.694 GHz.

The data were taken using the GBT's On-The-Fly (OTF) mapping mode, using in-band frequency switching with a throw of 4 MHz. In OTF mode, a map is created by having the telescope scan across the target in Right Ascension (R.A.) at a fixed Declination (Dec.), or in Dec. at a fixed R.A., writing data at a predetermined integration interval. The maps of Oph B1 and B2 were made while scanning only in R.A. at a fixed Dec., while for subsequent targets (Oph B3, C and F) the scanning mode was alternated to avoid artificial striping in the final data cubes. No striping, however, is apparent in the final B1 or B2 images. At the observing frequency of 23 GHz, the telescope beam was approximately $32''$ FWHM. Subsequent rows or columns were spaced by $13''$ in Dec. or R.A. to ensure Nyquist sampling. Scan times were determined to ensure either one or two full maps of the observed region could be made between pointing observations. For all observations, pointing updates were performed on the point source calibrator 1622-254 every 45 - 60 minutes, with corrections approximately $2-3''$. The average telescope aperture efficiency $\eta_A$ and main beam efficiency $\eta_{mb}$ were $0.59 \pm 0.05$ and $0.78 \pm 0.06$ respectively, determined through observations of 3C286 at the start of each shift. The absolute flux accuracy is thus $\sim 8\,\%$. The average elevation of Ophiuchus for all observations was approximately 26 degrees.

System temperatures ($T_{sys}$) varied between 48 K and 92 K over the observation dates with an average $T_{sys} \sim 62$ K. Table 2.2 gives the area mapped in each region and the final rms sensitivity in K ($T_{MB}$).

Initial data reduction and calibration were done using the GBTIDL[2] package.

[2]GBTIDL is an interactive package for reduction and analysis of spectral line data taken with

Table 2.2. GBT Observation Details by Region

| Core | Area Mapped *arcmin* × *arcmin* | rms K ($T_{MB}$) |
|---|---|---|
| Oph B1 | $3 \times 3$ / $4 \times 5.5$ [a] | 0.05 / 0.07 [b] |
| Oph B2 | $5 \times 4$ | 0.08 |
| Oph B3 | $3 \times 3$ | 0.07 |
| Oph C | $3 \times 3$ / $4 \times 4$ [a] | 0.05 / 0.07 [b] |
| Oph F | $3 \times 3$ | 0.06 |

[a]First values indicate the original OTF map size. Second values are the final map sizes, increased due to observed extent of emission.

[b]First rms value is calculated over the central region where all observations overlap. Second value is calculated over the entire map.

Zenith opacity values for each night were obtained using a local weather model, and the measured main beam efficiency was used to convert the data to units of main beam temperature, $T_{MB}$. The two parts of the in-band frequency switched data were aligned and averaged, weighted by the inverse square of their individual $T_{sys}$. The data were then converted to AIPS[3] SDFITS format using the GBT local utility idlToSdfits. In AIPS, the data were combined and gridded using the DBCON and SDGRD procedures. Finally, the data cubes were written to FITS files using FITTP.

### 2.2.2 Australia Telescope Compact Array

Maps of $NH_3$ (1,1) and (2,2) inversion line emission of the Ophiuchus B1, B2, C and F Cores were made over two separate observing runs at the Australia Telescope Compact Array (ATCA). The ATCA is located near the town of Narrabri in New South Wales, Australia, and consists of six antennas, each 22 m in diameter. Five of

the GBT.

[3]The NRAO Astronomical Image Processing System

the six antennas are movable along the facility's east-west line and small north line, while the sixth antenna is permanently placed along the east-west line at a distance of 6 km from the other antennas. An 8 MHz bandwidth with 1024 channels was used, which provided a spectral resolution of 7.81 kHz (0.1 km s$^{-1}$ at 23.694 GHz). This configuration enabled in-band frequency switching for the observations. The Oph B Cores were observed over four 9-hour tracks of the array (August 5 - 8, 2004), and the Oph C and F Cores were observed over three 9-hour tracks of the array (May 5 - 7, 2005). Both sets of observations were done with the array in its H168 configuration. This is a compact, hybrid configuration, where three of the movable antennas are placed along the east-west line and two antennas are located on the north spur. Baselines ranged from 61.2 m to 184.9 m ($\sim$ 4.7 k$\lambda$ - 14.2 k$\lambda$) with five antennas. At 23.7 GHz, these observations provided a primary beam (field-of-view) of 2′.

Maps were made of the Cores using individual pointings spaced by an angle $\Theta_N$, where $\Theta_N = (2 / \sqrt{3})\, \lambda / 2D \sim 1.1'$ at 23.7 GHz for Nyquist sampling on a hexagonal grid. Table 2.3 gives the number of individual pointings required to cover each Core, the multiple-beam overlap area observed, and the final rms sensitivity achieved towards each Core for both the ATCA and the VLA observations (described below).

Observations cycled through each individual pointing between phase calibrator observations to maximize *uv*-coverage and minimize phase errors. The phase calibrator, 1622-297, was observed every 20 minutes, and was also used to check pointing every hour. Flux and bandpass calibration observations were performed every shift on the bright continuum sources 1253-055, 1934-638 and 1921-293.

The ATCA data were reduced using the MIRIAD data reduction package (Sault et al. 1995). The data were first flagged to remove target observations unbracketed by phase calibrator measurements, data with poor phase stability or anomalous amplitude measurements. The majority of the data were good, as the weather was stable during the observations. Much of the data from baselines involving the 6 km antenna, however, were flagged due to poor phase stability. The bandpass, gains and phase calibrations were applied, and the data were then jointly deconvolved. First, the data were transformed from the spatial frequency $(u, v)$ plane into the image plane using the task INVERT and natural weighting to maximize signal to noise. The data were then deconvolved and restored using the tasks MOSSDI and RESTOR to remove the

Table 2.3. ATCA and VLA Observation Details by Region

| Core | Overlap Extent *arcmin* × *arcmin* | ATCA $N_{mos}$[a] | ATCA rms mJy beam$^{-1}$ | VLA $N_{mos}$[a] | VLA rms mJy beam$^{-1}$ |
|---|---|---|---|---|---|
| Oph B1 | 2 × 3 | 3 | 20 | 7 [b] | 13 |
| Oph B2 | 5 × 4 | 10 | 20 | 16[c] | 12 |
| Oph C | 4 × 4 | 7 | 30 | 7 | 10 |
| Oph F | 3 × 2 | 3 | 30 | 5 | 15 |

Note. — The spectral resolution of the observations is 0.1 km s$^{-1}$ (ATCA) and 0.3 km s$^{-1}$ (VLA).

[a]Number of individual pointings in mosaic observations.

[b]Pointings for B1 were aligned and spaced to provide continuous coverage between B1 and B2.

[c]Additional pointings added to the B2 core to include B3 in the overlap region.

beam response from the image. MOSSDI uses a Steer-Dewdney-Ito CLEAN algorithm (Steer et al. 1984). The cleaning limit was set at twice the rms noise level in the beam overlap region for each object. Clean boxes were used to avoid cleaning noise in the outer regions with less beam overlap. Applying natural weighting provided a final synthesized beam of $\sim 8'' \times 10''$ FWHM.

### 2.2.3 Very Large Array

Maps of $NH_3$ (1,1) and (2,2) emission were made at the Very Large Array (VLA) near Socorro, NM, USA over the period of 2007 January 20 through 2007 February 11. Nine observing shifts were allotted to the project in the array's DnC configuration, each five hours in duration covering the LST range 14:00 - 19:00. The DnC configuration is a hybrid of the most compact D configuration with the next most compact C configuration. This setup ensures a more circular beam shape for southern sources like Ophiuchus while retaining the sensitivity of the D configuration.

For these observations, we used a correlator setup with two IFs, each with a bandwidth of 3.125 MHz with 24.414 kHz spectral resolution ($0.3\,\mathrm{km\,s^{-1}}$). While not providing the same high spectral resolution obtained at the ATCA, this setup enabled simultaneous observations of the (1,1) and (2,2) lines, and allowed the main hyperfine component and the two middle satellite components of the (1,1) line to be contained within the band. Mosaic maps were made with Nyquist-spaced ($\sim 1.0'$ at 23 GHz) individual pointings. Observations cycled through pointings between phase calibrator observations. Table 2.3 gives the pointing and rms sensitivity information for each Core.

During these observations, several antennas in the array had been upgraded as part of the Expanded VLA (EVLA) project. Online Doppler tracking at this time was not yet available, and the observations were thus obtained in a fixed frequency mode, with line sky frequencies calculated using the NRAO's online Dopset tool. The observing frequencies were updated frequently, with phase calibrator observations on 1625-254 before and after a frequency change to avoid phase jump problems. Bandpass and absolute flux calibration were done for each shift using observations of 1331+305.

The data were checked, flagged and calibrated using the NRAO Astronomical Image Processing System (AIPS), following the procedures outlined in the AIPS Cookbook[4]. In addition, special processing was required to account for differences in bandpass shape and antenna sensitivity between the VLA and EVLA antennas. System temperatures were lacking for EVLA antennas, so the VLA back-end $T_{sys}$ values were used when reading the data into an AIPS *uv*-database. A bandpass table was then created from the line dataset and applied to a spectrally averaged 'channel 0' dataset. The normal VLA calibration steps were then followed.The calibrated *uv* files were then written to FITS format and imported to MIRIAD, where the data were deconvolved and restored. Applying natural weighting and a taper of $8'' \times 6''$ provided a final synthesized beam of $\sim 10.5'' \times 8.5''$ FWHM.

### 2.2.4 Combining Single Dish and Interferometer Data Sets

Since none of the antennas in the ATCA and the VLA can act as single radio dishes, there is necessarily an upper limit to the size of structure to which each is sensitive.

[4]http://www.aips.nrao.edu/CookHTML/CookBook.html

This upper scale limit is dependent on the shortest spacing between two antennas in the array, and the missing information is thus referred to as the short- or zero-spacing problem. Mosaicing helps to recover short spacing information. For complex sources with emission on many scales, however, combining interferometer data with single-dish observations provides more complete coverage of the *uv* plane and thus creates a more accurate representation of the true source emission structure. Ideally, the single dish diameter should be larger than the minimum interferometer baseline to ensure maximal overlap in the *uv*-plane and determine accurately flux calibration factors between the observations.

Data from each interferometer were first combined separately with the single dish observations. The GBT data were regridded to match the interferometer data in pixel scale and spectral resolution. The data were then converted to units of $\mathrm{Jy\,beam^{-1}}$ for combination with the interferometer data using the average beam FWHM measured at the GBT during the observations. Combination of the data was done using MIRIAD's IMMERGE task. IMMERGE combines deconvolved interferometer data with single-dish observations by Fourier transforming both datasets and combining them in the Fourier domain, applying tapering functions such that at small spacings (low spatial frequencies) the single-dish data are more highly weighted than the interferometer data, while conversely at high spatial frequencies the interferometer data are weighted more highly. The flux calibration factor between the two datasets was calculated in IMMERGE by specifying the overlapping spatial frequencies between the GBT and the interferometers. We took the overlap region in both cases to be 35 m - 100 m (2.7 k$\lambda$ - 7.7 k$\lambda$), yielding a flux calibration factor of $\sim$ 1.4 between the GBT and ATCA datasets, and $\sim$ 1.0 between the GBT and VLA datasets in the $NH_3$ (1,1) line emission. These factors were then applied to the $NH_3$ (2,2) datasets. The final resolution of the combined data is the same as that of the interferometer data.

To combine all three datasets, the ATCA and VLA data were imaged together using the INVERT task, applying natural weighting and taper as described for the VLA imaging. The interferometer data were then cleaned and combined with the GBT data as described above. The overlap region was taken to be 35 m - 100 m, yielding a flux calibration factor of $\sim$ 1.3. By convolving the combined data to match the $32''$ resolution of the GBT data, we estimate the total flux of the combined image recovers nearly all ($\sim$ 98 %) the flux in the single-dish image. These data were used to identify structures in the $NH_3$ data cubes using an automated structure finding

algorithm (see §3). The data were also tapered to a slightly lower resolution of 15″ FWHM to provide higher signal-to-noise ratios for a multiple component hyperfine line fitting routine.

## 2.3 Results

### 2.3.1 Comparison with submillimeter dust continuum emission

We first discuss the $NH_3$ (1,1) intensity in the combined datasets, and compare the distribution of $NH_3$ emission and 850 $\mu$m continuum emission in the Oph Cores as shown in Figure 2.1. Figures 2.2a, 2.3a and 2.4a show the combined $NH_3$ (1,1) line emission at $\sim$ 10.6″ $\times$ 8.5″ FWHM resolution. The emission has been integrated over the central hyperfine components in the Oph B, C and F Cores, respectively, with a clip of $\sim 2\times$ the map rms noise level. (Since the outer edge of the combined maps have higher rms noise levels, integrating only over, i.e., the 'main component' of $NH_3$ reduced the amount of signal included in the noisy outer regions.) The respective 850 $\mu$m emission for each Core at $\sim$ 15″ FWHM resolution, i.e., lower than the resolution of the combined $NH_3$ data, is shown in Figures 2.2b, 2.3b and 2.4b. We also show locations of submillimeter clumps identified with the 2D version of CLUMPFIND (Jørgensen et al. 2008). In Figure 2.2b, we additionally label the $\sim 1\,M_\odot$ continuum object MM8 (Motte et al. 1998).

Figures 2.2, 2.3 and 2.4 also show locations and labels of 'cold' YSOs (based on bolometric temperatures derived from fitting their spectral energy distributions) detected and classified through Spitzer infrared observations (Enoch et al. 2008) overlaid on the submillimeter and $NH_3$ emission. The objects plotted were all identified as Class I protostars (no Class 0 protostars have been associated with Oph B, C or F). Oph B2 is associated with three YSOs. Of these, two are previously known (IRS45/GY273 and IRS47/GY279). Based on association with a continuum emission object (Enoch et al. 2008) and observed infrared colours (Jørgensen et al. 2008), either three or two protostars in Oph B2 are embedded in gas and dust. One additional Class I protostar is located between B1 and B2, and is only associated with diffuse $NH_3$ emission. Oph B1 and B3 appear starless. No embedded protostars are asso-

ciated with Oph C by Enoch et al. (2008), but a "Candidate YSO" is identified by (Jørgensen et al. 2008) 30″ south of the Core continuum peak (R.A. 16:26:59.1, Dec. -24:35:03). Based on the different classifications by the two papers, the significant offset from the continuum emission peak, and the lack of any clear influence on the gas in our data, we will discuss Oph C assuming it is not associated with a deeply embedded object. Four protostars are associated with Oph F, all of which have been previously identified (see Figure 2.4 for object names). Three are likely embedded in the Core.

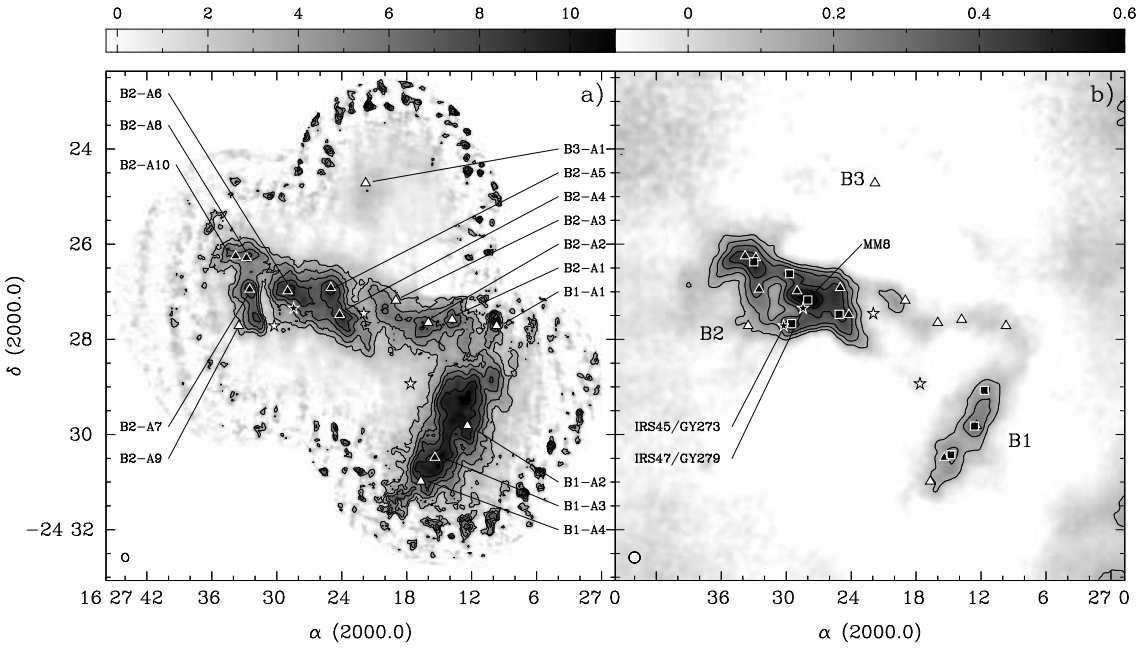


Figure 2.2 Observations of the Oph B Core (including B1, B2 and B3). At lower left in each panel, ovals show the respective resolutions of the data. a) Integrated $NH_3$ (1,1) main component intensity obtained with the GBT, ATCA and VLA telescopes with a synthesized beam FWHM 10.5″ × 8.5″. Emission was integrated over spectral channels with intensities $\geq \pm 2\,\sigma$ rms. The colour scale is in $\mathrm{K\,km\,s^{-1}}$ ($T_B$). Contours begin at $3\,\mathrm{K\,km\,s^{-1}}$ and increase by $1.5\,\mathrm{K\,km\,s^{-1}}$. In both plots, stars denote locations of Class I protostars (Enoch et al. 2008), while triangles indicate the positions of $NH_3$ clumps as identified by CLUMPFIND. (b) Continuum emission at 850 $\mu$m in Oph B at 15″ resolution as in Jørgensen et al. (2008). The colour scale is in $\mathrm{mJy\,beam^{-1}}$. Contours begin at $50\,\mathrm{mJy\,beam^{-1}}$ and increase by $100\,\mathrm{mJy\,beam^{-1}}$. Squares show locations of submillimeter clumps (Jørgensen et al. 2008). We also label the millimeter clump MM8 (Motte et al. 1998) and protostars identified previous to Enoch et al. (2008).

Peaks of $NH_3$ integrated intensity can be used to surmise the presence of 'ob-

jects', but such identifications can ignore any differences in velocity between adjacent dense gas. We therefore used the 3D version of the automated structure-finding routine CLUMPFIND (Williams et al. 1994) to identify distinct $NH_3$ emission objects in the combined $NH_3$ (1,1) data cube, which we will henceforth call "$NH_3$ clumps". CLUMPFIND uses specified brightness contour intervals to search through the data cube for distinct objects identified by closed contours. The size of the identified clumps are determined by including adjacent pixels down to an intensity threshold, or until the outer edges of two separate clumps meet. The clump location is defined as that of the emission peak. CLUMPFIND was used only on the main emission component, where multiple hyperfine components are sufficiently blended to present effectively a single line given the $0.3\,\mathrm{km\,s^{-1}}$ spectral resolution and typically wide line widths found. The standard interval of $2\times$ the data rms between contours, with a slightly larger threshold value worked well to separate distinct emission components in all clumps. A lower limit of 1 K with intervals of 0.4 K, $\sim 2\times$ the cube rms, identified separate emission peaks sufficiently for Oph B and C. Oph F was sufficiently fit using a lower limit of 1.2 K and intervals of 0.65 K, as the rms of the combined data was slightly higher. Even so, some identified clumps appeared by eye to be noise spikes at the map edges, and these were culled from the final list, as well as any clumps which contained fewer pixels than in the synthesized beam. Table 2.4 lists the locations, FWHMs, effective radii and peak brightness temperatures for CLUMPFIND-identified cores in Oph B, C and F, and the clump locations are overlaid on Figures 2.2 - 2.4. The centroid velocities and line widths of the $NH_3$ clumps were determined through spectral line fitting (described further in §4), which provided more accurate measures of $v_{LSR}$ and $\Delta v$ given the hyperfine structure of the $NH_3$ lines.

In Oph B, Figure 2.2 shows that the large-scale structure of the Core is similar in both line and continuum emission, but some significant differences are also apparent. For example, the integrated line emission displays a less pronounced division between the B1 and B2 Cores seen in the continuum, and indeed shows significant filamentary structure in the region connecting B1 and B2 where little to no continuum emission is observed. Similarly, strong line emission is present in the south-eastern edge of B2 where the continuum map shows relatively little emission. Additionally, while B2 is the stronger continuum emitter, B1 is significantly brighter in integrated line emission. Strong $NH_3$ emission in the northern half of B1 extends beyond the continuum contours, and becomes significantly offset from the bulk of the continuum emission to

Table 2.4. $NH_3$ (1,1) clumpfind peaks and parameters

| ID | RA J2000 | Dec. J2000 | FWHM$_x$ × FWHM$_y$[a] (AU) | Peak (K) |
|---|---|---|---|---|
| B1-A1 | 16 27 9.7 | -24 27 43.0 | 3900 × 6700 | 4.90 |
| B1-A2 | 16 27 12.4 | -24 29 49.0 | 6800 × 7800 | 5.10 |
| B1-A3 | 16 27 15.4 | -24 30 29.1 | 5300 × 5000 | 5.60 |
| B1-A4 | 16 27 16.7 | -24 30 59.1 | 3700 × 2900 | 4.90 |
| B2-A1 | 16 27 13.8 | -24 27 35.0 | 2300 × 2500 | 5.20 |
| B2-A2 | 16 27 16.0 | -24 27 39.0 | 5600 × 6100 | 5.10 |
| B2-A3 | 16 27 19.0 | -24 27 11.0 | 4700 × 6700 | 3.90 |
| B2-A4 | 16 27 24.2 | -24 27 29.0 | 6400 × 6000 | 5.10 |
| B2-A5 | 16 27 25.0 | -24 26 55.0 | 5300 × 4700 | 5.00 |
| B2-A6 | 16 27 29.0 | -24 26 59.0 | 3800 × 6700 | 5.70 |
| B2-A7 | 16 27 32.5 | -24 26 57.0 | 3800 × 5200 | 6.70 |
| B2-A8 | 16 27 32.8 | -24 26 17.0 | 3600 × 3600 | 4.00 |
| B2-A9 | 16 27 33.5 | -24 27 43.0 | 5000 × 3600 | 3.60 |
| B2-A10 | 16 27 33.8 | -24 26 14.9 | 2700 × 3700 | 4.00 |
| B3-A1 | 16 27 21.8 | -24 24 42.9 | 3900 × 6100 | 3.60 |
| C-A1 | 16 26 59.0 | -24 34 14.8 | 5000 × 5600 | 5.40 |
| C-A2 | 16 26 59.1 | -24 32 54.8 | 4500 × 4400 | 4.30 |
| C-A3 | 16 27 1.2 | -24 34 34.8 | 6000 × 5400 | 5.50 |
| F-A1 | 16 27 21.9 | -24 39 52.0 | 3600 × 3200 | 4.50 |
| F-A2 | 16 27 24.2 | -24 40 52.1 | 4400 × 5900 | 4.90 |
| F-A3 | 16 27 27.1 | -24 40 58.1 | 2400 × 5000 | 5.50 |

[a]FWHM values calculated by CLUMPFIND have not been deconvolved with the synthesized beam of the combined data.

the east. The $NH_3$ (1,1) observations of the Oph B core region also reveal a narrow-line emission peak north of the western edge of B2, which is coincident with a $DCO^+$ object, Oph B3 (Loren et al. 1990). B3 is just visible at the lowest contour in the $NH_3$ integrated intensity map but is not visible in the continuum map.

Furthermore, although the peaks of continuum emission and line emission are often located in the same vicinity in B1 and B2, the brightest continuum peaks and the integrated line emission maxima are typically non-coincident. Overall, the mean separation between an $NH_3$ integrated intensity peak and the nearest 850 $\mu$m continuum peak in B1 and B2 is $\sim 22''$ (2600 AU), or $\sim 2\times$ the $NH_3$ FWHM resolution. Fifteen CLUMPFIND-identified $NH_3$ clumps are identified in the combined Oph B map, with an average minimum separation between $NH_3$ clumps of $47''$ (5600 AU, or $40''$ (4800 AU), if Oph B3 is not included). The mean minimum distance between $NH_3$ clumps and submillimeter continuum clumps is $44''$ (5300 AU), or $\sim 4\times$ the $NH_3$ FWHM resolution. Only five of the fifteen $NH_3$ clumps are located within $30''$ (3600 AU) of a submillimeter continuum clump.

No protostars in Oph B are found at positions of $NH_3$ (1,1) integrated intensity maxima nor are they associated with identified $NH_3$ clumps. One protostar, IRS47/GY279, is located south of the $NH_3$ clump we identify as B2-A6. The offset between the $NH_3$ clump peak and the protostar, however, is $\sim 30''$, or approximately $3\times$ the angular resolution of the combined $NH_3$ data. A second protostar, IRS45/GY273, is coincident with a submillimeter continuum peak but has little associated $NH_3$ emission. Either of these protostars may be the source of an east-west aligned outflow recently proposed by Kamazaki et al. (2003) from CO observations of B2. The third, previously unidentified protostar, seen west of $NH_3$ clump B2-A4, is located within a narrow ($\sim 30''$) $NH_3$ integrated intensity *minimum* between the B2 core and the filament connecting Oph B1 and B2.

Figure 2.3 shows that Oph C has more similar overall structure when traced by the continuum and integrated $NH_3$ (1,1) line emission than Oph B. Extended emission in Oph C is elongated along a southeast-northwest axis and contains a single integrated intensity peak. A thin ($\sim 30''$) filament of faint emission extends to the north of the central peak. The submillimeter continuum emission is largely coincident with the integrated $NH_3$ contours, but the continuum emission peak is offset to the $NH_3$ integrated intensity peak by $\sim 20''$. CLUMPFIND separates the

central $NH_3$ emission into two cores, C-A1 and C-A3, and finds a third object, C-A2, at the tip of the northern emission extension. C-A1 and C-A3 are found to the northwest and southeast (30″ offset and 15″ offset, respectively) of the centres of both the $NH_3$ integrated intensity and of the continuum emission. Continuum emission also extends in the direction of the faint $NH_3$ northern extension, but there is no secondary peak present.

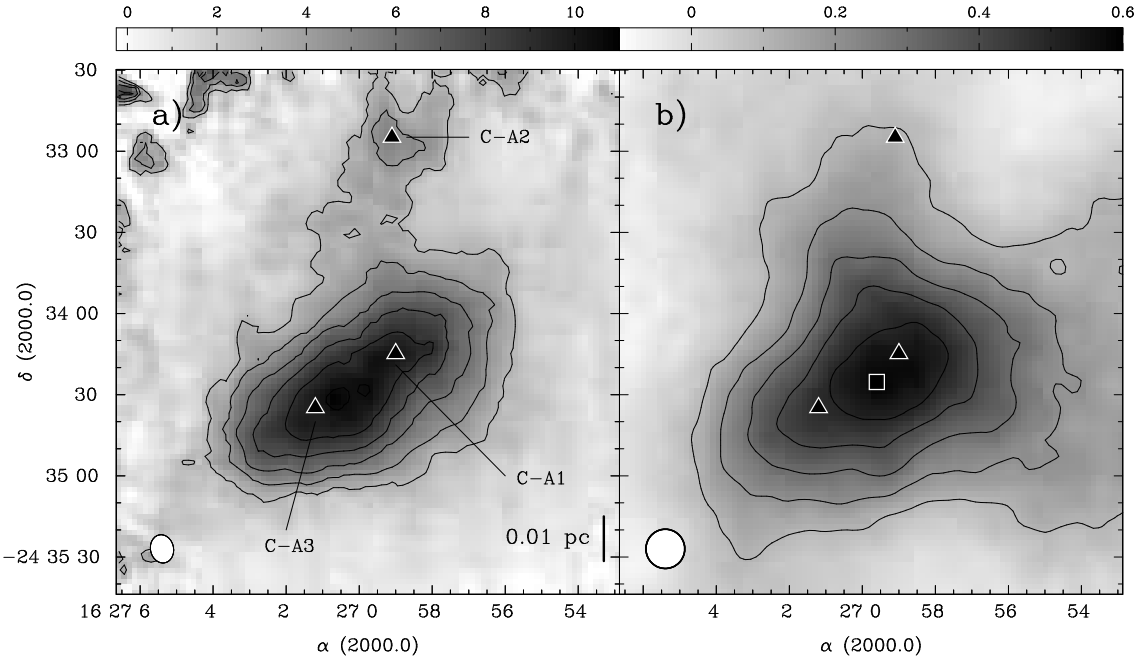


Figure 2.3 Observations of the Oph C Core. At lower left in each panel, ovals show the respective resolutions of the data. a) Integrated $NH_3$ (1,1) main component intensity obtained with the GBT, ATCA and VLA telescopes, summed over spectral channels with intensities $\geq 2\,\sigma$ rms. The colour scale is in units of $\mathrm{K\,km\,s^{-1}}$ ($T_B$). Contours begin at $3\,\mathrm{K\,km\,s^{-1}}$ ($T_B$) and increase by $1.5\,\mathrm{K\,km\,s^{-1}}$. In both plots, triangles indicate the positions of $NH_3$ clumps as identified by CLUMPFIND. b) Continuum emission at $850\,\mu$m in Oph C at 15″ resolution as in Jørgensen et al. (2008). Contours and colour range as in Figure 2.2. Squares show locations of submillimeter clumps (Jørgensen et al. 2008).

Like Oph C (but unlike Oph B), Figure 2.4 shows that Oph F also has very similar structure when traced by either the submillimeter continuum emission or integrated $NH_3$ intensity. Unlike both Oph B and C, the CLUMPFIND-identified $NH_3$ clumps are coincident with the integrated intensity peaks. F-A3 is nearly coincident (within a beam FWHM) with a submillimeter continuum clump and is additionally coincident with an embedded protostar, IRS43/GY265. F-A2 is associated with a

second embedded protostar (CRBR65) and continuum emission, but not an identified continuum clump. A thin filament ($\sim 15''$) extends to the northwest and the third $NH_3$ clump, F-A1, which is also coincident with extended continuum emission but no identified clump. A third embedded protostar (IRS44/GY259) in the north-east is coincident with a continuum peak, but has no associated $NH_3$ emission. A fourth protostar, in the south-west, may be coincident with some unresolved $NH_3$ emission, but is located in a section of the map with larger rms values and consequently the small integrated intensity peak seen at that location may be simply noise.

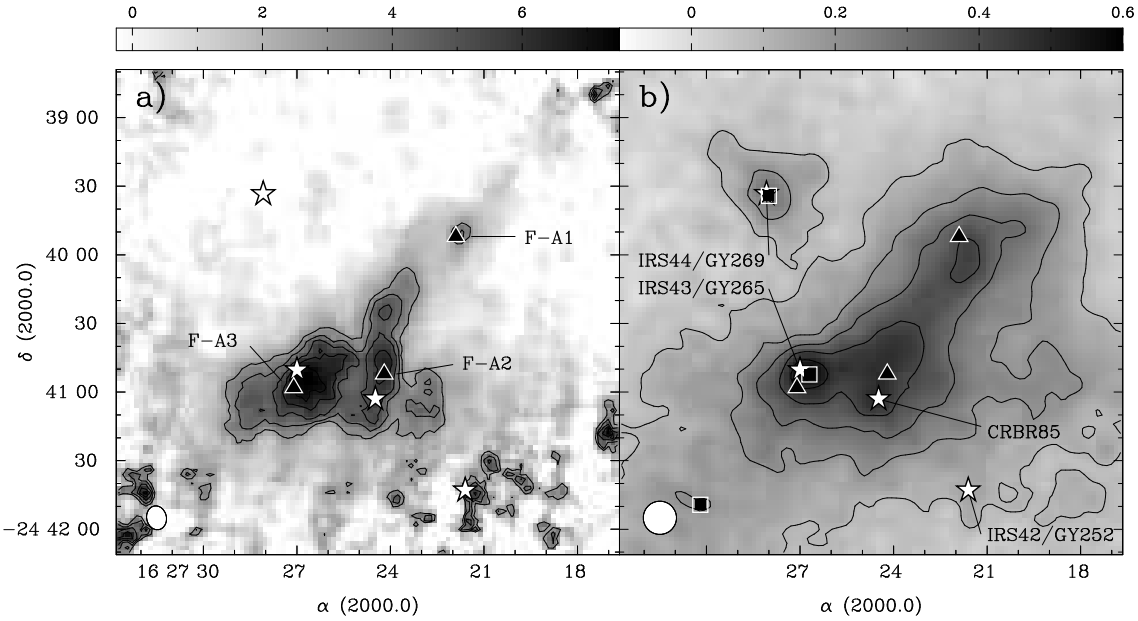


Figure 2.4 Observations of the Oph F Core. At lower left in each panel, ovals show the respective resolutions of the data. a) Integrated intensity $NH_3$ (1,1) main component intensity obtained with the GBT, ATCA and VLA telescopes, summed over spectral channels with intensities $\geq 2\,\sigma$ rms. The colour scale is in units of $\mathrm{K\,km\,s^{-1}}$ ($T_B$). Contours begin at $3\,\mathrm{K\,km\,s^{-1}}$ ($T_B$) and increase by $1\,\mathrm{K\,km\,s^{-1}}$. In both plots, stars denote locations of Class I protostars (Enoch et al. 2008), while triangles indicate the positions of $NH_3$ clumps as identified by CLUMPFIND. b) Continuum emission at $850\,\mu$m in Oph F at $15''$ resolution as in Jørgensen et al. (2008). Contours and colour range as in Figure 2.2. Squares show locations of submillimeter clumps (Jørgensen et al. 2008). We also label protostars identified previous to Enoch et al. (2008).

The discrepancies between $NH_3$ and submillimeter continuum emission in Oph B are in contrast to earlier findings of extremely high spatial correlation between the two gas tracers in isolated, low-mass starless clumps. For example, Tafalla et al. (2002) found that both the millimetre continuum and integrated $NH_3$ (1,1) and (2,2) line

Table 2.5. GBT $C_2S$ $2_1 - 1_0$ and $HC_5N$ $9 - 8$ Peak Parameters

| ID | RA J2000 | Dec. J2000 | FWHM AU | $V_{lsr}$ $\mathrm{km\,s^{-1}}$ | $\Delta v$ $\mathrm{km\,s^{-1}}$ | $T_{MB}$ K | $N$ $10^{12}$ $\mathrm{cm^{-2}}$ | $X$ $10^{-10}$ |
|---|---|---|---|---|---|---|---|---|
| B1-$C_2S$ | 16 27 13.1 | -24 30 50 | 5100 | 3.67(2) | 0.33(5) | 0.36(3) | 4.3(7) | 3.1(7) |
| C-$C_2S$ | 16 26 59.8 | -24 34 13 | 9200 | 3.95(1) | 0.33(2) | 1.12(4) | 10.6(8) | 1.5(1) |
| C-$HC_5N$ | 16 26 58.8 | -24 34 30 | 5800 | 3.94(1) | 0.35(2) | 0.68(3) | 4.0(3) | 0.46(4) |

intensity were compact and centrally concentrated in a survey of five starless clumps, including L1544 in the Taurus molecular cloud. In these clumps, the integrated intensity maxima of both transitions are approximately coincident (within the 40″ angular resolution of the $NH_3$ observations) with the continuum emission peaks. This same coincidence between $NH_3$ and millimeter continuum was found in B68 (Lai et al. 2003). When observed at higher angular resolution, $NH_3$ emission in L1544 remained coincident with the continuum but the line integrated intensity peak was offset by $\sim 20''$. This offset was explained, however, as being due to the the $NH_3$ emission becoming optically thick (Crapsi et al. 2007).

It is also possible that different methods of identifying structure in molecular gas (such as the GAUSSCLUMP method of Stutzki & Guesten 1990, or using dendrograms as in Rosolowsky et al. 2008b, for example) would create a different 'core' list than presented here. We have additionally compared our results in Oph B with the locations of millimeter objects identified using multi-wavelet analysis by Motte et al. (1998), and find a smaller yet still significant mean minimum distance of 27″ between $NH_3$ clumps and millimeter objects. Given the severe positional offsets in some locations between the $NH_3$ emission and submillimeter continuum, it is unlikely that different structure-finding methods would provide substantially different results.

### 2.3.2 Single Dish $C_2S$ and $HC_5N$ Detections

The GBT observations of $C_2S$ $2_1 - 1_0$ emission only resulted in single, localized detections in Oph B1 and Oph C, while only Oph C had a single, localized detection in $HC_5N$ (9-8). The $C_2S$ emission in B1 was confined to a single peak at its southern tip. The single-dish spectra of all observed species at the $C_2S$ peak locations in

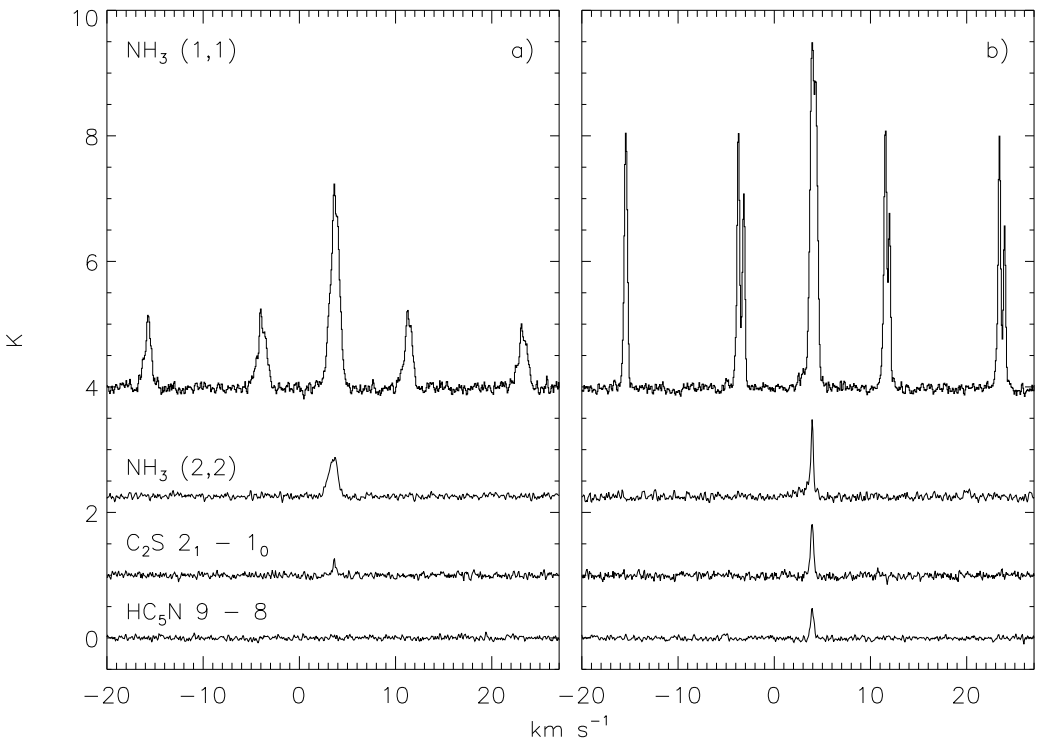


Figure 2.5 a) Spectra of all species observed at the GBT at the integrated intensity $C_2S$ ($2_1 - 1_0$) peak in Oph B1. The $NH_3$ (1,1) and (2,2) and $C_2S$ baselines are offset from 0 for clarity. b) Spectra of all species observed at the GBT at the integrated intensity $C_2S$ ($2_1 - 1_0$) peak in Oph C. The $NH_3$ (1,1) and (2,2) and $C_2S$ baselines are offset for clarity.

B1 and C are presented in Figure 2.5 (note that in Figure 2.5, the $NH_3$ line is so narrow in Oph C that we are detecting the hyperfine structure of the (1,1) line). The integrated intensity GBT maps of all molecules observed in Oph C are shown in Figure 2.6. Within the $\sim 30''$ resolution limits of the GBT data, the $NH_3$, $C_2S$ and $HC_5N$ spectral line integrated intensity peaks overlap with the local $850\,\mu$m continuum emission peak in Oph C. We fit the spectra of the two $C_2S$ and single $HC_5N$ detections with single Gaussians to determine their respective $v_{LSR}$, line width $\Delta v$, and peak intensity of the line in $T_{MB}$ units. We additionally fit a 2D Gaussian to the integrated intensity maps to determine the FWHMs of the emitting regions. We find a beam-deconvolved FWHM = 9200 AU and 5800 AU for the $C_2S$ and $HC_5N$ emission, respectively, in Oph C. The $C_2S$ emission in Oph B1 is elongated, with a FWHM = 9400 AU in R.A. but only 3700 AU in Dec. for an effective FWHM =

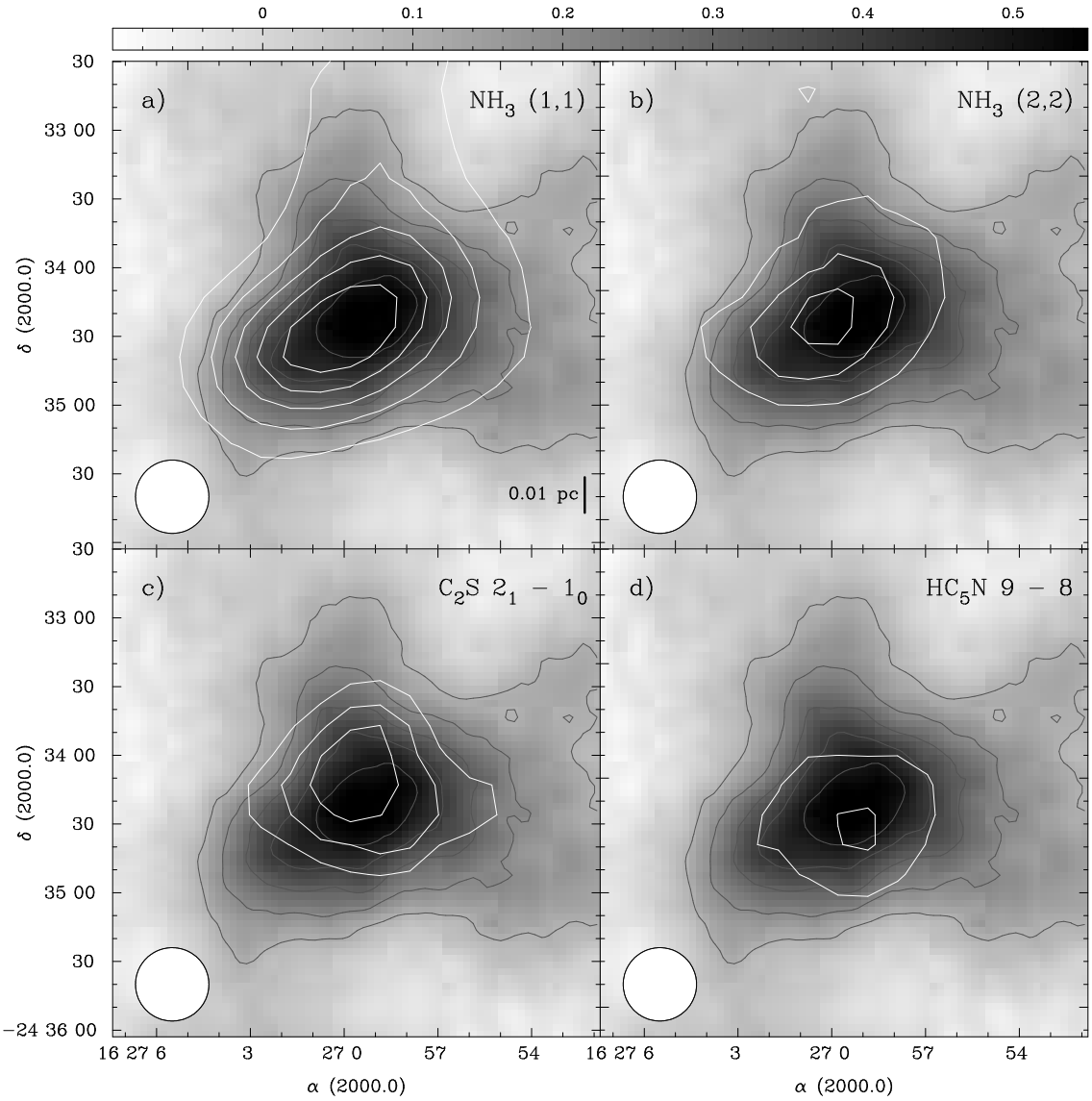


Figure 2.6 GBT observations of Oph C. The circle in each panel gives the relative FWHM of the GBT data. a) The Ophiuchus C core in 850 $\mu$m continuum emission at 15″ resolution (greyscale, Jy beam$^{-1}$ units) overlaid with continuum contours (grey). Black contours show the integrated $NH_3$ (1,1) intensity at $\sim 32''$ resolution, beginning at 3 K km s$^{-1}$ and increasing by 1.5 K km s$^{-1}$. For all plots, emission was integrated over spectral channels with intensities $\geq \pm 2\,\sigma$ rms. b) 850 $\mu$m continuum emission in Oph C overlaid with black $NH_3$ (2,2) integrated emission contours. Contours begin at 0.3 K km s$^{-1}$ and increase by 0.1 K km s$^{-1}$. c) 850 $\mu$m continuum emission in Oph C overlaid with black $C_2S$ $2_1 - 1_0$ integrated emission contours. Contours are 0.2, 0.25, 0.3 K km s$^{-1}$. d) 850 $\mu$m continuum emission in Oph C overlaid with black $HC_5N$ $9 - 8$ integrated emission. Contours are 0.1, 0.2 K km s$^{-1}$.

5100 AU. The results of the Gaussian fitting are listed in Table 2.5. See §4.4.3 for further analysis of $C_2S$ and $HC_5N$.

## 2.4 $NH_3$ Line Analysis

### 2.4.1 $NH_3$ Hyperfine Structure Fitting

The metastable $J = K$ rotational states of the symmetric-top $NH_3$ molecule are split into inversion doublets due to the ability of the N-atom to quantum tunnel through the hydrogen atom plane. Quadrupole and nuclear hyperfine effects further split these inversion transitions, resulting in hyperfine structure of the $(J, K) = (1,1)$ transition, for example, containing 18 separate components. This hyperfine structure allows the direct determination of the optical depth of the line through the relative peaks of the components. Additionally, since transitions between $K$-ladders are forbidden radiatively, the rotational temperature describing the relative populations of two rotational states, such as the (1,1) and (2,2) transitions, can be used to determine directly the kinetic gas temperature (Ho & Townes 1983).

For a given (J,K) inversion transition of $NH_3$ in local thermodynamic equilibrium (LTE), the observed brightness temperature $T_A^*$ as a function of frequency $\nu$ can be written as

$$T_{A,\nu}^*(J,K) = \eta_{MB}\,\Phi\,(J(T_{ex}(J,K)) - J(T_{bg}))(1 - \exp(-\tau_\nu(J,K))) \qquad (2.1)$$

assuming the excitation conditions of all hyperfine components are equal and constant (i.e., $T_{ex,\nu} = T_{ex}$). Here, $\eta_{MB}$ is the main beam efficiency, $\Phi$ is the beam filling factor of the emitting source, $T_{ex}$ is the line excitation temperature, $T_{bg} = 2.73\,\mathrm{K}$ is the temperature of the cosmic microwave background, and $J(T) = (h\nu/k)[\exp(h\nu/kT) - 1]^{-1}$. The line opacity as a function of frequency, $\tau_\nu$, is given by

$$\tau_\nu = \tau_0 \sum_{j=1}^{N} a_j \exp\left(-4\ln 2\left(\frac{\nu - \nu_0 - \nu_j}{\Delta\nu}\right)^2\right) \qquad (2.2)$$

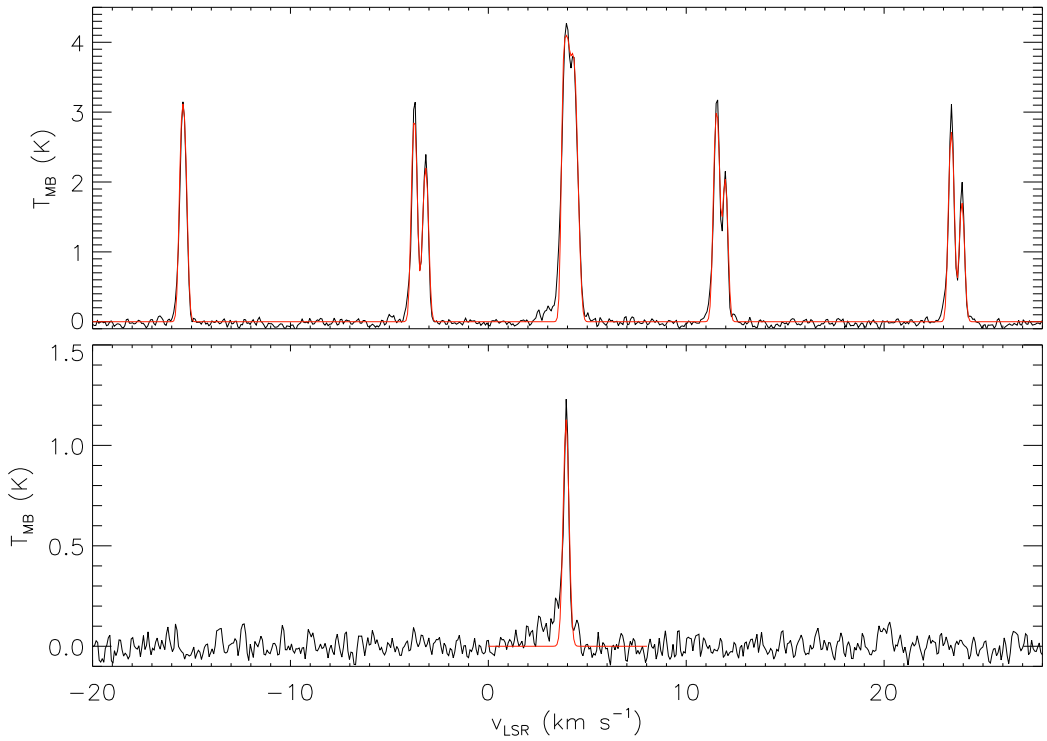


Figure 2.7 Top: $NH_3$ (1,1) emission observed with the GBT towards the Ophiuchus C Core fit using the method described in §2.4.1. The best fit of the hyperfine line structure is shown in red. Bottom: $NH_3$ (2,2) emission observed towards the AN6 clump. The best fit Gaussian is shown in red.

where $N$ is the total number of hyperfine components of the (J,K) transition ($N = 18$ for the (1,1) transition and $N = 21$ for the (2,2) transition). For a given $j^{th}$ hyperfine component, $a_j$ is the emitted line fraction and $\nu_j$ is the expected emission frequency. The observed frequency of the brightest line component is given by $\nu_0$, with a FWHM $\Delta\nu$. Values of $a_j$ and $\nu_j$ were taken from Kukolich (1967). Here, we assume $\Phi = 1$. If the observed emission does not entirely fill the beam, the determined $T_{ex}$ will be a lower limit. In regions where the emission is very optically thin ($\tau << 1$) there is a degeneracy between $\tau$ and $T_{ex}$ and solving for the parameters independently becomes impossible. We restricted our analysis to regions where the $NH_3$ (1,1) intensity in the central component is greater than 2 K, which corresponds roughly in our data to a signal-to-noise ratio of $8 - 10$ in the main component and $\sim 2 - 3$ in the satellite components. With this restriction, we also find $\tau \gtrsim 0.5$ throughout the regions discussed.

To improve the signal-to-noise ratio of the data and to match the resolution of the 850 $\mu$m continuum data, we first convolved the combined data to a final FWHM of 15″ (from 10.6″ × 8.5″), and then binned the convolved data to 15″ × 15″ pixels. Assuming Gaussian profiles, the 18 components of the $NH_3$ (1,1) emission line were fit simultaneously using a chi-square reduction routine custom written in IDL. The returned fits provide estimates of the line centroid velocity ($v_{lsr}$), the observed line FWHM ($\Delta v_{obs}$), the opacity of the line summed over the 18 components ($\tau$), and $[J(T_{ex}) - J(T_{bg})]$. The satellite components of the (2,2) line are not visible above the rms noise of our data. These data were consequently fit (again in IDL) with a single Gaussian component.

The line widths determined by the hyperfine structure fitting routine are artificially broadened by the velocity resolution (0.3 km s$^{-1}$) of the observations. To remove this effect, we subtract in quadrature the resolution width, $\Delta v_{res}$, from the observed line width, $\Delta v_{obs}$, such that $\Delta v_{line} = \sqrt{\Delta v_{obs}^2 - \Delta v_{res}^2}$. In the following, we simply use $\Delta v = \Delta v_{line}$ for clarity. The limitations of the moderately poor velocity resolution are discussed further in Appendix A.3, but do not significantly impact our analysis. In regions where lines are intrinsically narrow, such as Oph C and parts of Oph F, the derived line widths may be overestimated by up to $\sim 20 - 35\,\%$.

The uncertainties reported in the returned parameters are those determined by the fitting routine, and do not take the calibration uncertainty of $\sim 8\,\%$ into account. The calibration uncertainty affects neither the derived parameters that are dependent on ratios of line intensities, such as the opacity and kinetic temperature $T_K$, nor the uncertainties returned for $v_{LSR}$ or $\Delta v$. The excitation temperature, however, as well as the column densities and fractional $NH_3$ abundances discussed below (see §4.4) are dependent on the amplitude of the line emission, and are thus affected by the absolute calibration uncertainty.

Table 2.6 lists the mean, rms, minimum and maximum values of $v_{lsr}$, $\Delta v$, $\tau$ and $T_{ex}$ found in each of the Cores using the above restrictions for the combined $NH_3$ line emission. In the following sections, we describe in detail the results of the line fitting and examine the resulting line centroid velocities and widths, as well as $T_{ex}$ and $\tau$. In addition, we use the fit parameters to calculate the gas kinetic temperature ($T_K$), non-thermal line widths ($\sigma_{NT}$), $NH_3$ column density ($N(NH_3)$), gas density ($n(H_2)$) and $NH_3$ abundance ($X(NH_3)$) across all the cores, as described further in §4.2, 4.3

Table 2.6. $NH_3$ (1,1) Line Characteristics in Combined Data

| Core | Value | Mean | RMS | Min | Max |
|---|---|---|---|---|---|
| Oph B | $v_{lsr}$ ($\mathrm{km\,s^{-1}}$) | 3.96 | 0.24 | 3.15 | 4.57 |
| | $\Delta v$ ($\mathrm{km\,s^{-1}}$) | 0.83 | 0.21 | 0.08 | 1.37 |
| | $\tau$ | 1.6 | 0.8 | 0.5 | 4.7 |
| | $T_{ex}$ (K) | 9.9 | 2.3 | 5.4 | 19.5 |
| Oph C | $v_{lsr}$ ($\mathrm{km\,s^{-1}}$) | 4.01 | 0.07 | 3.81 | 4.10 |
| | $\Delta v$ ($\mathrm{km\,s^{-1}}$) | 0.37 | 0.13 | 0.11 | 0.70 |
| | $\tau$ | 4.7 | 2.6 | 0.7 | 10.8 |
| | $T_{ex}$ (K) | 6.9 | 1.2 | 5.1 | 11.6 |
| Oph F | $v_{lsr}$ ($\mathrm{km\,s^{-1}}$) | 4.34 | 0.12 | 4.24 | 4.82 |
| | $\Delta v$ ($\mathrm{km\,s^{-1}}$) | 0.53 | 0.30 | 0.10 | 1.13 |
| | $\tau$ | 1.9 | 0.8 | 0.7 | 3.6 |
| | $T_{ex}$ (K) | 9.5 | 2.5 | 5.0 | 14.3 |

and 4.4. Table 2.7 summarizes the mean, rms, minimum and maximum values of $T_K$, $\sigma_{NT}$, $N(NH_3)$, $n(H_2)$ and $X(NH_3)$ for each Core. For each $NH_3$ clump, Table 2.8 summarizes the mean, rms, minimum and maximum values of all determined parameters (means were obtained by uniformly weighting each pixel).

### 2.4.2 Line Centroids and Widths

Figures 2.8a, 2.9a, and 2.10a show maps of $v_{LSR}$ of the fitted $NH_3$ (1,1) line in Oph B, C and F respectively from the combined, smoothed and regridded data. These maps reveal that although variations of $v_{LSR}$ are seen within the Cores, they are not that kinematically distinct from each other. For example, only $0.35\,\mathrm{km\,s^{-1}}$ ($\lesssim$ the mean $\Delta v$) separates the average line-of-sight velocity in Oph B from Oph F. This result agrees with the 1D velocity dispersion of $\sim 0.36\,\mathrm{km\,s^{-1}}$ found by André et al. (2007) through $N_2H^+$ observations of the Oph cores.

In Oph B (see Figure 2.8a), the $v_{LSR}$ of $NH_3$ emission has little internal variation, with a mean $v_{LSR} = 3.96\,\mathrm{km\,s^{-1}}$ and an rms of only $0.24\,\mathrm{km\,s^{-1}}$. An overall gradient is seen across Oph B1 and B2, with smaller $v_{LSR}$ values ($3.2\,\mathrm{km\,s^{-1}}$) at the southwest edge of B1 increasing to $4.6\,\mathrm{km\,s^{-1}}$ at the most eastern part of B2. Correspondingly, B1 has a characteristic velocity somewhat less than the average ($3.8\,\mathrm{km\,s^{-1}} \pm 0.1\,\mathrm{km\,s^{-1}}$), while the B2 $v_{LSR}$ is slightly greater ($4.1 \pm 0.2\,\mathrm{km\,s^{-1}}$). The filament connecting B1 and B2 is kinematically more similar to B2, but there is no visible discontinuity in line-of-sight velocity of the lines. B3 has the lowest $v_{LSR}$ in Oph B, with an average velocity of $3.3\,\mathrm{km\,s^{-1}} \pm 0.2\,\mathrm{km\,s^{-1}}$, or $0.7\,\mathrm{km\,s^{-1}}$ less than the average of the group. This large difference, greater than that between the mean $v_{LSR}$ values of Oph B and F, suggests that B3 may not be at the same physical distance as the rest of Oph B. The change in velocity between B2 and B3 occurs over a small projected distance ($\sim 30''$, or $\sim 3600\,\mathrm{AU}$). There is some indication that B2 and B3 may overlap along the line of sight, as the determined $v_{LSR}$ values in B2 immediately south of B3 are less than those to the east and west, as might be expected if lower velocity emission is also contributing to the line at that location. (As discussed further below, the $\Delta v$ line widths in this area are larger than the average, as would be expected if unresolved emission from two different velocities is contributing to the observed line.)

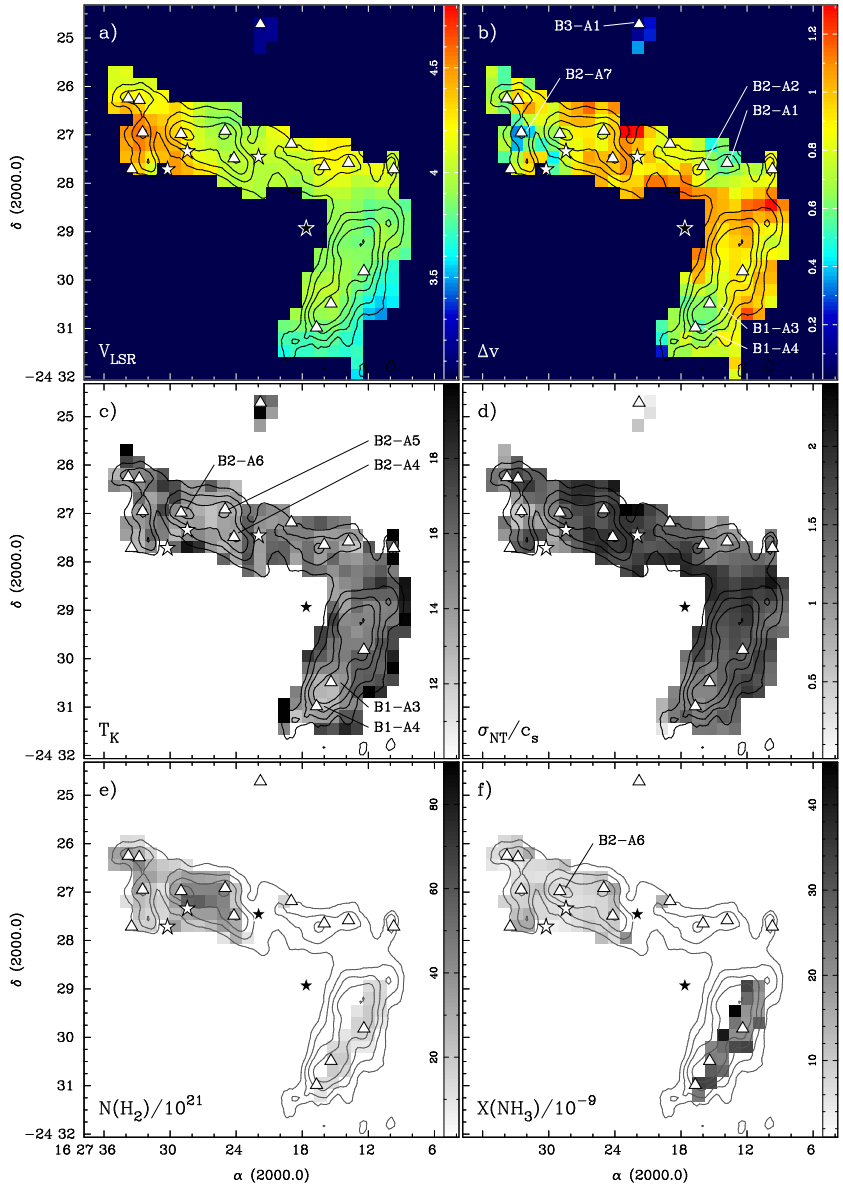


Figure 2.8 a) Line velocity or $v_{LSR}$ in Oph B. Colour scale is in km s$^{-1}$. The values shown are those derived after convolving the data to 15″ resolution and then regridding into 15″ × 15″ pixels. In all plots, contours show integrated $NH_3$ (1,1) intensity convolved to 15″ resolution, beginning at 4.5 K km s$^{-1}$ and increasing by 1.5 K km s$^{-1}$. Stars indicate protostar positions and triangles indicate positions of $NH_3$ clumps. b) Fitted $\Delta v$ in Oph B. Colour scale is in km s$^{-1}$. c) $T_k$ in Oph B. Greyscale from 10 K to 20 K. d) Ratio of the non-thermal to thermal line width components. Greyscale from $\sigma_{NT} / c_s = 0$ to 2.4. e) Total column density of $H_2$ derived from 850 $\mu$m dust continuum observations in Oph B, regridded to match the combined $NH_3$ observations. The dust temperature $T_d$ per pixel was assumed to be equal to the gas temperature $T_k$ derived from HFS line fitting of the $NH_3$ observations. The $N(H_2)$ values shown have been divided by $10^{21}$. f) Fractional abundance of $NH_3$ divided by $10^{-9}$.

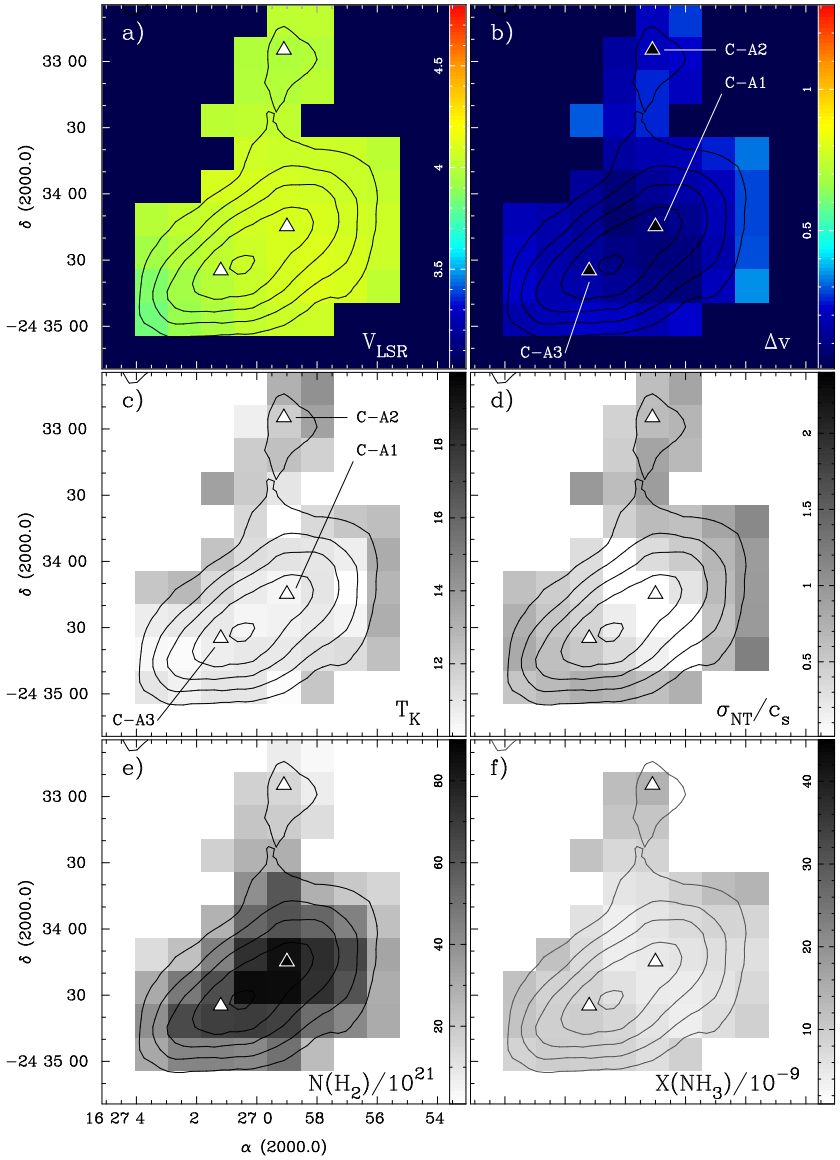


Figure 2.9 a) Line velocity or $v_{LSR}$ in Oph C. Colour scale is in km s$^{-1}$. The values shown are those derived after convolving the data to 15″ resolution and then regridding into 15″ × 15″ pixels. In all plots, contours show integrated $NH_3$ (1,1) intensity convolved to 15″ resolution, beginning at 4.5 K km s$^{-1}$ and increasing by 1.5 K km s$^{-1}$. Stars indicate protostar positions and triangles indicate positions of $NH_3$ clumps. b) Fitted $\Delta v$ in Oph C. Colour scale is in km s$^{-1}$. c) $T_k$ in Oph C. Greyscale from 10 K to 20 K. d) Ratio of the non-thermal to thermal line width components. Greyscale from $\sigma_{NT}\,/\,c_s = 0$ to 2.4. e) Total column density of $H_2$ derived from 850 $\mu$m dust continuum observations in Oph C, convolved to 15″ resolution and regridded to match the combined $NH_3$ observations. The dust temperature $T_d$ per pixel was assumed to be equal to the gas temperature $T_K$ derived from HFS line fitting of the $NH_3$ observations. The $N(H_2)$ values shown have been divided by $10^{21}$. f) Fractional abundance of $NH_3$ divided by $10^{-9}$.

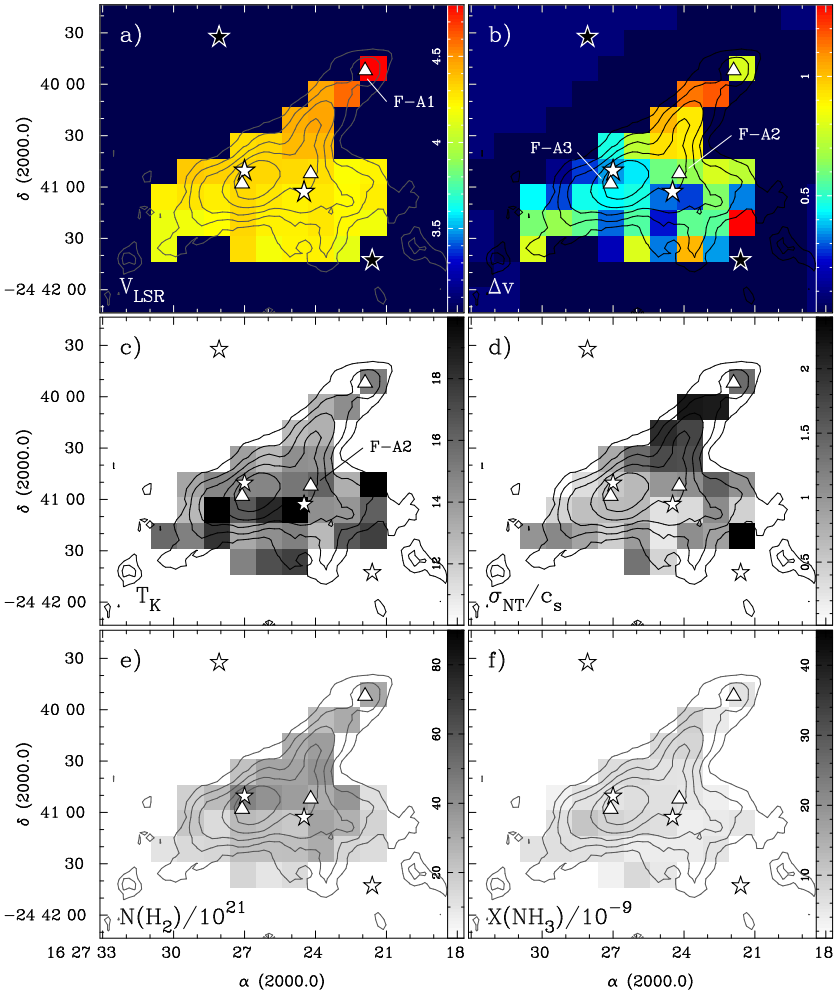


Figure 2.10 a) Line velocity or $v_{LSR}$ in Oph F. Colour scale is in km s$^{-1}$. The values shown are those derived after convolving the data to 15″ resolution and then regridding into 15″ × 15″ pixels. In all plots, contours show integrated $NH_3$ (1,1) intensity convolved to 15″ resolution, beginning at 3 K km s$^{-1}$ and increasing by 1 K km s$^{-1}$. Stars indicate protostar positions and triangles indicate positions of $NH_3$ clumps. b) Fitted $\Delta v$ in Oph F. Colour scale is in km s$^{-1}$. c) $T_k$ in Oph C. Greyscale from 10 K to 20 K. d) Ratio of the non-thermal to thermal line width components. Greyscale from $\sigma_{NT} / c_s = 0$ to 2.4. e) Total column density of $H_2$ derived from 850 $\mu$m dust continuum observations in Oph F, convolved to 15″ resolution and regridded to match the combined $NH_3$ observations. The dust temperature $T_d$ per pixel was assumed to be equal to the gas temperature $T_k$ derived from HFS line fitting of the $NH_3$ observations. The $N(H_2)$ values shown have been divided by $10^{21}$. f) Fractional abundance of $NH_3$ divided by $10^{-9}$.

Oph C (see Figure 2.9a) has a mean $v_{LSR} = 4.01\,\mathrm{km\,s^{-1}}$ with an rms of only $0.07\,\mathrm{km\,s^{-1}}$. A small velocity gradient of $\sim 0.4\,\mathrm{km\,s^{-1}}$ is evident in Oph C, with a minimum line-of-sight velocity of $\sim 3.7\,\mathrm{km\,s^{-1}}$ in the southeast, increasing to a maximum of $\sim 4.1\,\mathrm{km\,s^{-1}}$ in the northwest. A similar gradient was noted in $N_2H^+$(1-0) observations by André et al. (2007), and may be indicative of rotation. The identification of two $NH_3$ clumps in the region, however, could also be indicative of two objects with slightly different $v_{LSR}$. A slight decrease in $v_{LSR}$ values is seen in the $NH_3$ extension to the north, with C-N2 associated with emission at a slightly lower $v_{LSR}$ than the mean.

Oph F (see Figure 2.10a) has a mean $v_{LSR} = 4.34\,\mathrm{km\,s^{-1}}$ and an rms of only $0.26\,\mathrm{km\,s^{-1}}$ over the region containing the bulk of the $NH_3$ (1,1) emission and two of the three identified $NH_3$ peaks, despite the presence of four protostars. The filament extending towards the northwestern $NH_3$ peak gradually increases in $v_{LSR}$, but only by $\sim 0.2\,\mathrm{km\,s^{-1}}$. With higher sensitivity, single-dish data show that outside this area $v_{LSR}$ drops to $\sim 3.7\,\mathrm{km\,s^{-1}}$. There is clear evidence for two velocity components along the line of sight at the peak position of F-A1, with a secondary component at $\sim 3.7\,\mathrm{km\,s^{-1}}$. André et al. (2007) also find two velocity components near F-A1 in $N_2H^+$observations. For the brighter component, their $N_2H^+$ data agree with our $NH_3$ data, but for the secondary component they find a higher $v_{LSR} = 4.1\,\mathrm{km\,s^{-1}}$. Some blue asymmetry is found in the line profiles of F-A2 and F-A3, but this is more likely due to the complicated velocity structure of the core rather than infall motions (comparison with an optically thin tracer at this position is necessary to confirm infall).

In summary, $v_{LSR}$ varies little across any of the Cores (rms $< 0.24\,\mathrm{km\,s^{-1}}$), and additionally varies little between them (maximum mean difference $\sim 0.38\,\mathrm{km\,s^{-1}}$). Some small gradients were found in the larger Cores (i.e., on scales larger than the individual $NH_3$ clumps) which may be indicative of rotation.

Figures 2.8b, 2.9b, and 2.10b show the line $\Delta v$ for Oph B, C and F obtained from the combined, smoothed and regridded data. As stated above, the line widths have been corrected for the resolution of the spectrometer ($0.3\,\mathrm{km\,s^{-1}}$). In the few cases where the returned FWHM from the fits is similar or equal to the resolution, we set the corrected FWHM to the thermal line width (see Appendix A for further discussion).

Line widths range from $\Delta v \lesssim 0.1\,\mathrm{km\,s^{-1}}$ to $\sim 1.2\,\mathrm{km\,s^{-1}}$ in both Oph B and F, with a minimum line width of $0.08\,\mathrm{km\,s^{-1}}$ in B3 and a maximum of $1.37\,\mathrm{km\,s^{-1}}$ in B2. Line widths in Oph C range from $0.11\,\mathrm{km\,s^{-1}}$ to $0.70\,\mathrm{km\,s^{-1}}$. The rms variations $\Delta v$ and $v_{LSR}$ in Oph B and C are similar ($0.2\,\mathrm{km\,s^{-1}}$ and $0.1\,\mathrm{km\,s^{-1}}$, respectively), while in Oph F the rms in $\Delta v$ is much larger than the rms in $v_{LSR}$ (i.e., $0.3\,\mathrm{km\,s^{-1}}$ compared to $0.12\,\mathrm{km\,s^{-1}}$, respectively).

The extended emission in Oph B is dominated by highly non-thermal motions (mean $\Delta v = 0.83\,\mathrm{km\,s^{-1}}$), shown in Figure 2.8b. Several localized pockets of narrow line width are found embedded within the more turbulent gas. The single Oph B3 clump (B3-A1) and B2-A7 are both characterized by extremely narrow $\Delta v$ (i.e., $0.08\,\mathrm{km\,s^{-1}}$ and $0.33\,\mathrm{km\,s^{-1}}$ respectively). As mentioned above, the line emission broadens from B3 to B2 over only $\sim 30''$ (3600 AU) to $\Delta v \sim 1.4\,\mathrm{km\,s^{-1}}$, possibly due to line blending along the line of sight if B2 and B3 overlap in projection at these locations. We find small $\Delta v \sim 0.5\,\mathrm{km\,s^{-1}}$ towards the south-eastern edge of the mapped region in B1 near $NH_3$ clumps B1-A3 and B1-A4, but the line width minimum does not coincide with either core. Another region of low $\Delta v \sim 0.6\,\mathrm{km\,s^{-1}}$ is coincident with the $NH_3$ clumps B2-A1 and B2-A2. A final $\Delta v$ minimum, $\Delta v \sim 0.4\,\mathrm{km\,s^{-1}}$ is found between the two eastern protostars in B2. Note that the protostars in Oph B are all associated with smaller $\Delta v$ than the average value for the core, but none are coincident with a clear local minimum in line width.

The maximum line width in Oph C, $\Delta v = 0.70\,\mathrm{km\,s^{-1}}$, is half that found in Oph B. Figure 2.9b shows that most of the emission in C is narrow, with a minimum $\Delta v = 0.11\,\mathrm{km\,s^{-1}}$, similar to the extremely narrow lines found in B3. These narrowest line widths are found centered on $NH_3$ clump C-A2 in a band perpendicular to the elongated direction of Oph C and are coincident with the highest velocity emission, and are thus not coincident with the $NH_3$ integrated intensity maximum nor the continuum emission peak. Curiously, if C-A2 and C-A3 are indeed physically distinct clumps, we would expect the broadest lines between them due to overlap, but instead find narrow lines at this location. The largest line widths are found at the edges of the integrated intensity contours.

Oph F is characterized by moderately wide line emission more similar to that found in Oph B, with a mean $\Delta v = 0.63\,\mathrm{km\,s^{-1}}$ (see Figure 2.10b). Line widths associated with the central $NH_3$ clumps F-A2 and F-A3 are smaller than the mean

(i.e., $0.6\,\mathrm{km\,s^{-1}}$ and $0.3\,\mathrm{km\,s^{-1}}$ respectively), while clear minima in line width ($\Delta v \sim 0.33\,\mathrm{km\,s^{-1}}$) are found at the locations of the two central protostars. Line widths along the Core extending to the northwest integrated intensity peak broaden to larger values ($\sim 1.2\,\mathrm{km\,s^{-1}}$), but at the tip $NH_3$ clump F-A1 is associated with $\Delta v = 0.4\,\mathrm{km\,s^{-1}}$ in a single $15''$ pixel.

Overall, the observed $NH_3$ $\Delta v$ in the Cores are generally large, excepting Oph C. We also find regions of localized narrow line emission, some of which are associated with $NH_3$ clumps. Line widths near protostars tend to be smaller than the mean values, but only in Oph F are the protostars coincident with clear minima in $\Delta v$.

### 2.4.3 Kinetic Temperatures and Non-Thermal Line widths

Following Mangum et al. (1992), among others, we use the returned $\tau$, $\Delta v$ and line brightnesses of the $NH_3$ (1,1) and (2,2) lines in each pixel to calculate the kinetic temperature of the gas. Details of our calculations can be found in Appendix A. Propagating uncertainties from our hyperfine structure fitting routine gives typical uncertainties in $T_K$ of $\sim 1\,\mathrm{K}$. The mean, rms, minimum and maximum kinetic temperatures are given for Oph B, C and F in Table 2.7. Figures 2.8c, 2.9c and 2.10c show the kinetic temperatures calculated across the Oph Cores.

In Oph B, we find a mean $T_K = 15.1\,\mathrm{K}$ with an rms variation across the entire core of only $1.8\,\mathrm{K}$. Most $NH_3$ emission peaks are associated with lower than average gas temperatures, but only a few are coincident with clear $T_K$ minima. The lowest temperatures in the Core, $T_K = 13.7\,\mathrm{K}$ and $12.4\,\mathrm{K}$, are found in southern B1 towards B1-A3 and B1-A4, respectively. These low temperatures are found at the same location as the detection of single dish $C_2S$ emission. Gas temperatures appear colder ($T_K \sim 13\,\mathrm{K}$) towards the centre of Oph B2, but the minimum temperature, $T_K = 12.4\,\mathrm{K}$, is not coincident with an $NH_3$ clump. Instead, the lowest temperatures are found directly between the $NH_3$ clumps B2-A4, B2-A5 and B2-A6, and closer to the central submillimeter clump.

Oph C is the coldest of the observed cores, with a mean $T_K = 12.8\,\mathrm{K}$ and a similar rms variation ($1.6\,\mathrm{K}$) as in Oph B. The central region is effectively at a single low temperature $T_K = 10.6\,\mathrm{K}$, with the lowest values found near the emission peaks C-A1

and C-A3 in the northwest and southeast, while the gas temperature of the northern core, C-A2, is consistent with the average.

Oph F is characterized by the highest temperatures of the observed Cores, with a mean $T_K = 16.6\,\mathrm{K}$, slightly warmer than Oph B, and with a large rms variation of $3.2\,\mathrm{K}$. No clear minima in gas temperature are observed near any of the $NH_3$ clumps, protostars or continuum peaks identified in the region. The protostar associated with $NH_3$ clump F-A2 is coincident with a temperature maximum in a single $15''$ pixel.

The gas temperatures traced by $NH_3$ emission in the Oph B and F Cores are consistently higher than those found in isolated dense clumps. For example, all five of the starless clumps surveyed by Tafalla et al. (2002) were found to have a constant gas temperature $T_K = 10\,\mathrm{K}$ determined through an analysis similar to that done here. Two recent studies of $NH_3$ emission in dense clumps in the Perseus molecular cloud and the less active Pipe Nebula at $32''$ resolution also found slightly lower temperatures than those found here, with a median $T_K = 11\,\mathrm{K}$ in Perseus (Rosolowsky et al. 2008a) and a mean $T_K = 13\,\mathrm{K} \pm 3\,\mathrm{K}$ for $\lesssim 1\,\mathrm{M}_\odot$ clumps in the Pipe Nebula (Rathborne et al. 2008, we note that one object in the Pipe is warmer than the typical $T_K$ found in Oph B and F). In a sample of $NH_3$ observations towards Galactic high mass star forming regions, Wu et al. (2006) found a mean $T_K = 19\,\mathrm{K}$. The mean kinetic temperatures found in Oph B and F are also slightly greater than the median $T_K = 14.7\,\mathrm{K}$ found in a survey of $NH_3$ observations by Jijina et al. (1999), although their analysis showed that the median temperature of dense gas in clusters was significantly higher, $T_K = 20.5\,\mathrm{K}$, than in non-clustered environments where the median $T_K = 12.4\,\mathrm{K}$. Since L1688 is a clustered star forming environment, it is not unreasonable to expect temperatures higher than those in more isolated regions, given the Jijina et al. results.

Evidence for an extremely cold temperature of $6\,\mathrm{K}$ [obtained through observations of $H_2D^+\,(1_{10} - 1_{11})$, which likely probes denser gas than $NH_3$ (1,1) and (2,2), was recently found for the nearby Oph D Core (Harju et al. 2008). In addition, while the mean gas temperature $T_K = 12\,\mathrm{K}$ in Oph C, temperatures in the highest column density gas drop to $10\,\mathrm{K}$, similar to temperatures found in the studies of isolated clumps described above.

We find little difference in average gas temperatures between $NH_3$ clumps and $NH_3$ emission associated with submillimeter continuum emission peaks, and a mean

$T_K$ increase of only $\sim 1\,\mathrm{K}$, i.e., similar to our uncertainty in $T_K$, in gas temperatures near protostars (but note only five protostars are associated with emission with sufficient S/N to fit the HFS). The Jijina et al. (1999) survey found that $NH_3$ cores not associated with identified IRAS sources (presumably protostellar objects) were slightly colder than those with coincident IRAS detections (12.4 K compared with 15.0 K), but the effect was much smaller than temperature differences seen due to association with a cluster.

Given the determined gas temperature $T_K$, we calculate the expected one-dimensional thermal velocity dispersion $\sigma_T$ of the gas across the cores:

$$\sigma_T = \sqrt{\frac{k_B T_K}{\mu_{\mathrm{NH_3}} m_{\mathrm{H}}}} \tag{2.3}$$

Here, $k_B$ is the Boltzmann constant, $\mu_{\mathrm{NH_3}} = 17.03$ is the molecular weight of $NH_3$ in atomic units, and $m_{\mathrm{H}}$ is the mass of the hydrogen atom. Similarly, the thermal sound speed $c_s$ of the gas can be calculated using a mean molecular weight $\mu = 2.33$.

The non-thermal velocity dispersion $\sigma_{NT}$ is given by

$$\sigma_{NT} = \sqrt{\sigma_{obs}^2 - \sigma_T^2} \tag{2.4}$$

where $\sigma_{obs} = \Delta v/(2\sqrt{2\ln 2})$. The mean, rms, minimum and maximum values for both $\sigma_{NT}$ and the non-thermal to thermal velocity dispersion ratio of the gas, given by $\sigma_{NT}\,/\,c_s$, are given for each of Oph B, C and F in Table 2.7.

Figures 2.8d, 2.9d and 2.10d show the resulting non-thermal to thermal velocity dispersion ratio over the cores. The mean $\sigma_{NT}\,/\,c_s$ values show supersonic velocities are present. At the limits of the velocity resolution of our data, the smallest observed line widths are consistent with motions being purely thermal in nature.

We find that the mean $\sigma_{NT} = 0.35\,\mathrm{km\,s^{-1}}$ and $\sigma_{NT}\,/\,c_s = 1.5$ in Oph B. Across the Core, we find a moderate $\sigma_{NT}\,/\,c_s$ rms of 0.4. The majority of the gas traced by $NH_3$ in Oph B is thus dominated by non-thermal, mildly supersonic motions. Several $NH_3$ clumps are associated with smaller, but still transsonic, non-thermal motions. Thermal motions dominate the observed line widths in only two well-defined locations

in Oph B which additionally coincide with $NH_3$ clumps: B2-A7, with $\sigma_{NT}/c_s = 0.5$, and B3-A1, where the observed line width is consistent with purely thermal motions. Otherwise, little difference is seen between the non-thermal line widths of individual cores and the surrounding gas, with a mean $\sigma_{NT} \,/\, c_s = 1.4\,\mathrm{km\,s^{-1}}$ for the $NH_3$ clumps.

In contrast, Oph C has a mean $\sigma_{NT} = 0.14\,\mathrm{km\,s^{-1}}$. Consequently, the mean $\sigma_{NT} \,/\, c_s = 0.6$ with an rms of only 0.2, showing that thermal motions dominate the observed line widths over much of the Core. The minimum non-thermal line width is found associated with C-A1, which is consistent with purely thermal motions within our velocity resolution limits. On average, non-thermal motions in Oph F are also similar to the expected thermal values, with a mean $\sigma_{NT} \,/\, c_s = 0.9$, but with a larger spread around the mean (0.6 rms) and a maximum value ($\sigma_{NT} \,/\, c_s = 2.2$) similar to that found in Oph B ($\sigma_{NT} \,/\, c_s = 2.5$). The lowest values are found towards F-A2 and F-A3 and the nearby protostars.

The non-thermal $NH_3$ line widths we measure are similar to those recently found for $N_2H^+$(1-0) emission in the Cores at larger angular resolution ($\sim 26''$), where the mean $\sigma_{NT}/c_s = 1.6 \pm 0.3$ in Oph B, $0.9 \pm 0.2$ in Oph C, $1.5 \pm 0.8$ in Oph F (André et al. 2007), and are less than those found in $DCO^+$ emission ($\sigma_{NT}/c_s \sim 2$ in B2, $\sim 1 - 1.5$ in B1, B3, C and F (Loren et al. 1990).

### 2.4.4 Column Density and Fractional Abundance

#### $NH_3$

Given $\Delta v$, $\tau$ and $T_{ex}$ from the $NH_3$ (1,1) line fitting results, we calculate the column density of the upper level of the $NH_3$ (1,1) inversion transition. We then calculate the $NH_3$ partition function (given $T_K$) to determine the total column density of $NH_3$ following Rosolowsky et al. (2008a). Relevant equations are given in Appendix A.

We also calculate the $H_2$ column density, $N(H_2)$, per pixel in the Cores from $850\,\mu$m continuum data using

$$N(\mathrm{H_2}) = S_\nu / [\Omega_m \mu m_{\mathrm{H}} \kappa_\nu B_\nu(T_d)], \tag{2.5}$$

Table 2.7. Physical Properties of Filaments Derived From Fitted Parameters

| Core | Value | Mean | RMS | Min | Max |
|---|---|---|---|---|---|
| Oph B | $T_k$ (K) | 15.1 | 1.8 | 12.3 | 22.9 |
| | $\sigma_{NT}$ ($\mathrm{km\,s^{-1}}$) | 0.35 | 0.09 | 0.04 | 0.57 |
| | $\sigma_{NT}$ / $c_s$ | 1.5 | 0.4 | 0.5 | 2.5 |
| | $N(\mathrm{NH_3})$ ($\times 10^{13}\,\mathrm{cm^{-2}}$) | 22 | 8.8 | 1.3 | 48 |
| | $n(\mathrm{H_2})$ ($\times 10^{4}\,\mathrm{cm^{-3}}$) | 5.9 | 10 | 0.8 | 77 |
| | $X(\mathrm{NH_3})$ ($\times 10^{-9}$) | 14 | 9.1 | 2.4 | 41 |
| Oph C | $T_k$ (K) | 12.0 | 1.6 | 9.4 | 19.8 |
| | $\sigma_{NT}$ ($\mathrm{km\,s^{-1}}$) | 0.14 | 0.06 | 0.0 | 0.29 |
| | $\sigma_{NT}$ / $c_s$ | 0.6 | 0.2 | 0.0 | 1.2 |
| | $N(\mathrm{NH_3})$ ($\times 10^{13}\,\mathrm{cm^{-2}}$) | 24 | 11 | 7.1 | 55 |
| | $n(\mathrm{H_2})$ ($\times 10^{4}\,\mathrm{cm^{-3}}$) | 2.0 | 1.0 | 0.8 | 4.2 |
| | $X(\mathrm{NH_3})$ ($\times 10^{-9}$) | 8.2 | 4.4 | 2.8 | 28 |
| Oph F | $T_k$ (K) | 15.5 | 2.5 | 12.8 | 22.9 |
| | $\sigma_{NT}$ ($\mathrm{km\,s^{-1}}$) | 0.21 | 0.13 | 0.05 | 0.47 |
| | $\sigma_{NT}$ / $c_s$ | 0.9 | 0.6 | 0.2 | 2.2 |
| | $N(\mathrm{NH_3})$ ($\times 10^{13}\,\mathrm{cm^{-2}}$) | 14 | 5.9 | 3.5 | 25 |
| | $n(\mathrm{H_2})$ ($\times 10^{4}\,\mathrm{cm^{-3}}$) | 3.6 | 2.4 | 0.9 | 10.6 |
| | $X(\mathrm{NH_3})$ ($\times 10^{-9}$) | 5.4 | 1.8 | 2.2 | 10 |

where $S_\nu$ is the 850 $\mu$m flux density, $\Omega_m$ is the main-beam solid angle, $\mu = 2.33$ is the mean molecular weight, $m_{\rm H}$ is the mass of hydrogen, $\kappa_\nu$ is the dust opacity per unit mass at 850 $\mu$m, and $B_\nu(T_d)$ is the Planck function at the dust temperature, $T_d$. We take $\kappa_\nu = 0.018\,{\rm cm^2\,g^{-1}}$, following Shirley et al. (2000), using the dust model from Ossenkopf & Henning (1994) which describes grains that have coagulated for $10^5$ years at a density of $10^6\,{\rm cm^{-3}}$ with accreted ice mantles and incorporating a gas-to-dust mass ratio of 100. The 15″ resolution continuum data were regridded to 15″ pixels to match the combined $NH_3$ observations. The dust temperature $T_d$ per pixel was assumed to be equal to the gas temperature $T_k$ derived from HFS line fitting of the combined $NH_3$ observations. This assumption is expected to be good at the densities probed by our $NH_3$ data ($n \gtrsim 10^4{\rm cm^{-3}}$), when thermal coupling between the gas and dust by collisions is expected to begin (Goldsmith & Langer 1978). If these temperatures are systematically high, however, then the derived $N(H_2)$ values are systematically low. There is a $\sim 20\%$ uncertainty in the continuum flux values, and estimates of $\kappa_\nu$ can additionally vary by $\sim 3$ (Shirley et al. 2000). Our derived $H_2$ column densities consequently have uncertainties of factors of a few.

Due to the chopping technique used in the submillimeter observations to remove the bright submillimeter sky, any large scale cloud emission is necessarily removed. As a result, the image reconstruction technique produces negative features around strong emission sources, such as Oph B (Johnstone et al. 2000a). While the flux density measurements of bright sources are likely accurate, emission at the core edges underestimates the true column. We thus limit our analysis to pixels where $S_\nu \geq 0.1\,{\rm Jy\,beam^{-1}}$, though the rms noise level of the continuum map is $\sim 0.03\,{\rm Jy\,beam^{-1}}$. For a dust temperature $T_d = 15\,{\rm K}$, this flux level corresponds to $N(H_2) \sim 6 \times 10^{21}\,{\rm cm^{-2}}$.

Using the calculated $H_2$ and $NH_3$ column densities, we have calculated per pixel the fractional abundance of $NH_3$ relative to $H_2$, $X(NH_3) = N(NH_3)\,/\,N(H_2)$ for each Core. The results of these calculations are shown in Figures 2.8, 2.9 and 2.10, which show the $H_2$ column density derived from submillimeter continuum data, $N(H_2)$ and the fractional $NH_3$ abundance, $X(NH_3)$. The mean, rms, minimum and maximum of the derived column density and fractional abundance in each Core are given in Table 2.7, while specific values for identified $NH_3$ clumps are listed in Table 2.8. The $N(H_2)$ and consequently the $X(NH_3)$ uncertainties given in Table 2.8 include the $\sim 20\%$ uncertainty in the submillimeter continuum flux values only; uncertainty in

$\kappa_\nu$ is not taken into account.

Oph B has a mean $NH_3$ column density of $2.2 \times 10^{14}\,\mathrm{cm}^{-2}$, with the highest $N(NH_3)$ values (maximum $N(NH_3) = 4.8 \times 10^{14}\,\mathrm{cm}^{-2}$) found in B1. Two peaks in $NH_3$ column density are found in B1 which correspond closely with the integrated intensity maxima, but are offset from the B1 $NH_3$ clumps. In B2, the column density also generally follows the integrated intensity contours, with lower values overall than in B1. The highest $NH_3$ column in B2 of $N(NH_3) = 4 \times 10^{14}\,\mathrm{cm}^{-2}$ is found towards B2-A5. The highest opacity in B2, $\tau = 4.7$, was found associated with B2-A7, but the $NH_3$ column density at this location is similar to the core average. Small column density increases are seen at other $NH_3$ intensity peak locations. The $NH_3$ extension connecting B1 and B2 is characterized by similar $NH_3$ column densities to those at the edges of the Core with no obvious $N(NH_3)$ maxima.

The discrepancy between the bright $NH_3$ and faint submillimeter continuum emission in B1 indicates a high $NH_3$ fractional abundance relative to B2, with fractional abundances a factor of $\gtrsim 2-3$ higher than the typical values of $X(NH_3) \sim 10^{-8}$ within B2. This is shown in Figure 2.8f. Abundance *minima* are seen in B2, most notably towards B2-A6 and nearby protostars. Despite the higher $NH_3$ column densities in B1 and B2, the lack of submillimeter emission in the $NH_3$ extension connecting the two regions suggests this connecting material has a higher fractional $NH_3$ abundance. Prominent negative features in the continuum data in this extension preclude a quantitative $X(NH_3)$ estimate.

The mean and maximum $NH_3$ column densities in Oph C are similar to those found in Oph B ($\langle N(NH_3)\rangle = 2.4 \times 10^{14}\,\mathrm{cm}^{-2}$ and $N(NH_3) = 5.5 \times 10^{14}\,\mathrm{cm}^{-2}$, respectively). Oph C contains two $N(NH_3)$ maxima. One is coincident with C-A3 and the second is offset to the west by $\sim 15''$ from C-A1. C-A3 is correspondingly associated with a maximum in $NH_3$ fractional abundance ($X(NH_3) = 8.8 \times 10^{-9}$), but C-A1 is coincident with an elongated minimum $X(NH_3) \sim 3 \times 10^{-9}$ that extends along the same axis perpendicular to the long axis of the core where the smallest line widths were found. The highest $NH_3$ abundances $X(NH_3) \sim 12 \times 10^{-9}$, are found in the northern extension. The mean abundance in Oph C, $X(NH_3) = 8.2 \times 10^{-9}$, is slightly more than half the Oph B average.

In Oph F, the mean $N(NH_3) = 1.4 \times 10^{14}\,\mathrm{cm}^{-2}$ is less than that found in Oph B and C by a factor of $\sim 2$. The maximum $N(NH_3) = 2.5 \times 10^{14}\,\mathrm{cm}^{-2}$ is also significantly

less than the maxima in either B or C, and is found in the emission extending to the northwest from the two central $NH_3$ clumps and protostars. The fractional $NH_3$ abundances are also low compared with B and C, with a mean $X(NH_3) = 5.4 \times 10^{-9}$ and a maximum $X(NH_3) = 1.0 \times 10^{-8}$ found near but not coincident with F-A3.

Studies of isolated starless clumps have determined a wide range of $NH_3$ abundance values for these objects. While in some cases different methods have been used to determine $H_2$ column density values than that performed here, 'typical' observed fractional abundance values in cold, dense regions tend to be on the order of a few $\times 10^{-9}$ to a few $\times 10^{-8}$ (Tafalla et al. 2006; Crapsi et al. 2007; Ohishi et al. 1992; Larsson et al. 2003; Hotzel et al. 2001). Abundances as low as $X(NH_3) = 7 \times 10^{-10}$ and $8.5 \times 10^{-10}$ have been proposed for B68 (Di Francesco et al. 2002) and Oph A (Liseau et al. 2003), respectively. The values found here agree well with previous studies. The wide variations of $X(NH_3)$ in the same general environment suggests dramatic differences in the chemical states of the Cores in L1688 (see §5).

### $C_2S$ and $HC_5N$

Similarly, we can calculate the abundance of $C_2S$ and $HC_5N$ from respective emission detected in the single-dish data, where

$$N = \frac{8\pi k \nu_0}{hc^2} \frac{g1}{g2} \frac{1}{A_{ul}} \sqrt{2\pi} \sigma_v [J(T_{ex}) - J(T_{bg})] \tau_{ul} \tag{2.6}$$

is the column density of the upper state of the observed transition (Rosolowsky et al. 2008a). The values for $A_{ul}$, $g_1$ and $g_2$ were taken from Pickett et al. (1998) for each transition. Assuming the transitions are optically thin, the observed temperature of the line $T_{MB} = [J(T_{ex}) - J(T_{bg})]\tau_{ul}$. The partition function $Z = \sum_i g_i \exp(\frac{-E_i}{kT_K})$ was then used to calculate the total column density of each species as for $NH_3$, with $g_i$ and $E_i$ values taken from Pickett et al. (1998). The column densities thus derived are given in Table 2.5. The molecular column densities derived for $C_2S$ in B1 and C ($N(C_2S) \sim 10^{12-13}\,\mathrm{cm}^{-2}$) are similar to results in young starless cores (Tafalla et al. 2006; Rosolowsky et al. 2008a; Lai et al. 2003). The $N(HC_5N)$ results agree with previous measurements in the Taurus molecular cloud (Codella et al. 1997; Benson & Myers 1983) and the Pipe Nebula (Rathborne et al. 2008). We calculate

molecular abundances as above and find $X(C_2S) = 3.1 \times 10^{-10}$ and $1.5 \times 10^{-10}$ at the $C_2S$ emission peaks in Oph B1 and C, respectively. We further find an abundance $X(HC_5N) = 4.6 \times 10^{-11}$ at the $HC_5N$ emission peak in Oph C.

### 2.4.5 $H_2$ Density

Given the determined excitation and kinetic temperatures, $T_{ex}$ and $T_K$, and assuming the metastable states can be approximated as a two level system, we have calculated the gas density $n(H_2)$ from the $NH_3$ (1,1) transition following Ho & Townes (1983). We list the mean, rms variation and range of densities found for each core in Table 2.7. Note that this density is effectively a mean density along the line of sight. In general, we find $n(H_2) \sim$ a few $\times 10^4\,cm^{-3}$ in all three Cores, with only moderate variation and no clear spatial correspondence with $NH_3$ or continuum clumps. The largest $n(H_2)$ values ($n(H_2) \sim 8 \times 10^5\,cm^{-3}$) were found in Oph B2 towards the central continuum clump MM8 (labelled in Figure 2.2b). While these values agree with $n(H_2)$ estimates based on $NH_3$ emission in other regions, they are an order of magnitude lower than estimates of Ophiuchus clump densities derived from dust continuum emission studies at similar spatial resolutions (Motte et al. 1998; Johnstone et al. 2000b).

## 2.5 Discussion

### 2.5.1 Discussion of small-scale features

#### Correlation between $NH_3$ clumps, $NH_3$ integrated intensity and dust clumps

In §3, we used CLUMPFIND to identify objects in $NH_3$ emission within the Oph Cores in position and velocity space. The returned $NH_3$ clump locations are generally found at locations of peak integrated $NH_3$ intensity, with the exception of Oph C, in which we found two distinct $NH_3$ clumps offset from the $NH_3$ integrated intensity maximum.

In Oph B, we find poor correlation between maxima of $NH_3$ integrated intensity

and thermal dust continuum emission. Since most $NH_3$ clumps are located at integrated intensity maxima, we hence find $NH_3$ clumps identified through CLUMPFIND do not correlate well with dust clumps. Continuum dust emission is a commonly used surrogate tracer of gas column density. The observed flux is a function of the dust emissivity ($\kappa_\nu$) and temperature ($T_d$). If the dust in B1, for example, was colder than that in B2, the same column of dust would produce less emission. In §4.3, we calculated $H_2$ column densities assuming the dust and gas are thermally coupled. For Oph B, we found the $H_2$ column density closely followed the observed continuum emission under this assumption (see Figure 2.8a vs. Figure 2.2b). The dust and gas, however, may not have the same temperature. If the dust is colder than the gas by a small amount ($T_d = 10\,\mathrm{K}$ compared with $T_K = 15\,\mathrm{K}$, for example), the true column density of $H_2$ could be larger by a factor of $\sim 2$ along that line of sight. If these temperature differences occur on small enough scales, e.g., at the $NH_3$ clump positions, they could explain the discrepancy between the locations of dust clumps and $NH_3$ clumps. Thermal coupling of gas and dust is most likely to occur, however, in the coldest and densest clumps, i.e., exactly where we do not find correspondence between the dust and gas tracers.

A more likely cause of the offset between dust and $NH_3$ emission is fractional abundance variation of $NH_3$ in the Oph Cores. If the column densities determined from the dust emission are accurate, then most dust clumps are associated with $X(NH_3)$ minima. Within B1 and B2, we find variations in $X(NH_3)$ of $\gtrsim 2$ on length scales similar to the $NH_3$ clump sizes. Models of nitrogen chemistry in dense regions suggest that a long timescale, greater than the free-fall time, is required for molecules such as $NH_3$ to achieve steady state values, but that during gravitational collapse $X(NH_3)$ begins to decrease at densities $n \gtrsim 10^6\,\mathrm{cm}^{-3}$ (Aikawa et al. 2005; Flower et al. 2006).

The $C_2S$ molecule is easily depleted in cold, dense environments with an estimated lifetime of a few $\times 10^4$ yr (de Gregorio-Monsalvo et al. 2006). It is thus a good tracer of young, undepleted cores (Suzuki et al. 1992; Lai & Crutcher 2000; Tafalla et al. 2004). The detection of $C_2S$ in southern Oph B1 and Oph C therefore suggests that these specific locations are chemically, and hence dynamically, younger compared with other regions. The $C_2S$ emission detected in both B1 and C is coincident with or only slightly offset from the integrated $NH_3$ intensity peak, suggesting significant depletion has not yet occurred at those particular locations. This conclusion is further bolstered

by the fact that we find higher gas densities (see §4.5) in B2 than in B1 or C, and both B2 and F are associated with embedded protostars and are therefore likely more dynamically evolved, i.e., denser. The higher levels of non-thermal motions found in Oph B are at odds with what is expected for an evolved, star forming core, however, and we discuss this further below.

### Comparison of $NH_3$ clumps, submillimeter clumps and protostars

We next compare the mean properties of the dense gas associated with the locations of $NH_3$ clumps, submillimeter clumps and protostars. We note that given the poor correlation between the $NH_3$ clumps and submillimeter clumps and protostars, the derived physical properties (e.g., $T_K$ and $\sigma_{NT}$) at the submillimeter clump and protostellar locations may be associated with larger-scale gas emission along the line-of-sight rather than the dense clump gas.

In general, we find only small differences between the mean properties of the dense gas at the peak locations of the $NH_3$ clumps, submillimeter clumps and embedded protostars. The mean kinetic temperatures for $NH_3$ clumps and submillimeter clumps are nearly equal ($\sim$ 14 K), and only $\sim$ 1.5 K less than the values associated with embedded protostars. This difference is not significant given that the uncertainties in $T_K$ are on the order of 1 K. Conversely, excitation temperatures associated with embedded protostars are $\sim$ 1.5 K lower than that of $NH_3$ clumps and submillimeter clumps where $T_{ex} \sim 10$ K, with uncertainties in $T_{ex}$ also $\sim$ 1 K. The line widths of submillimeter clumps tend to be larger than those associated with $NH_3$ clumps by only $\sim 25\%$.

Some differences in mean properties between objects are notable. For example, protostars have associated $\Delta v$ and $\sigma_{NT} \,/\, c_s$ a factor of 2 *narrower* than both submillimeter and $NH_3$ clumps. Also, submillimeter clumps and protostars have lower fractional abundances than seen for $NH_3$ clumps by a factor of $\sim 2$. Note, however, that only five protostars are found with $NH_3$ emission strong enough to analyze, as we described in §3. For this reason, our comparison sample is limited to protostars that are still associated with significant amounts of gas, where conditions are likely more similar to those found in submillimeter clumps than for more evolved protostars.

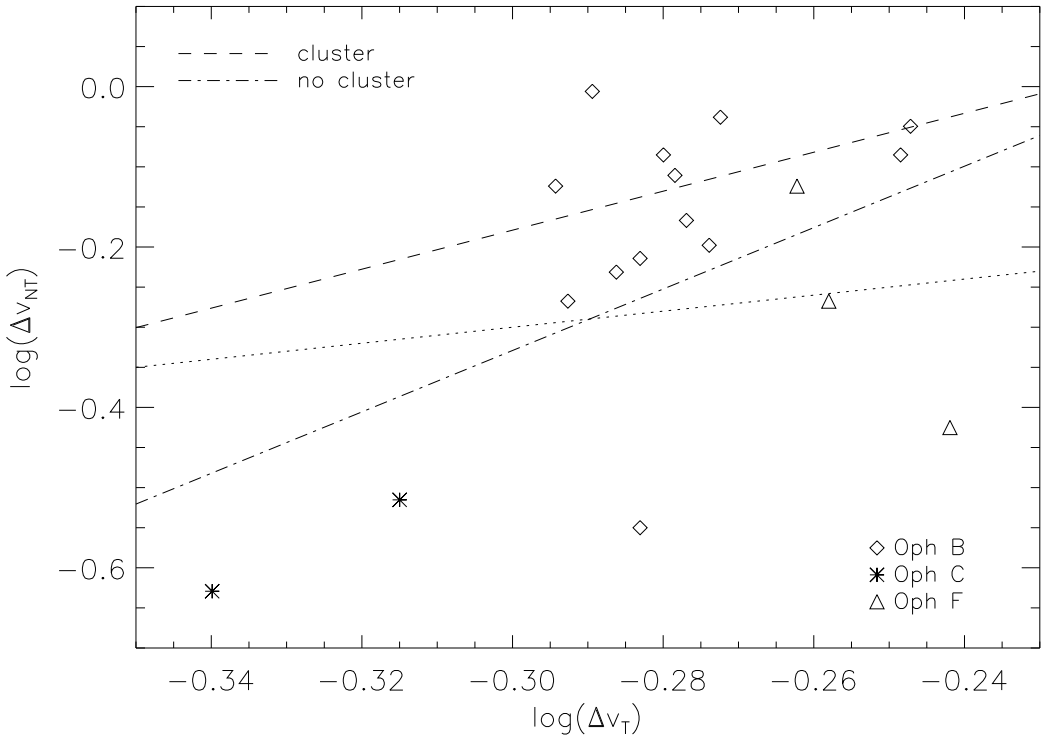


Figure 2.11 Non-thermal versus thermal line widths (FWHM) for individual $NH_3$ clumps in the Oph B, C and F Cores. The two dashed lines show relationships found by Jijina et al. (1999) for $NH_3$ clumps both with and without an associated cluster. Clumps in Oph B follow the clustered trend, but clumps in Oph C are nearer the relationship for more isolated clumps. Clumps in Oph F scatter across the plot. The dotted line represents $\Delta v_{NT} = \Delta v_T$.

### $\sigma_{NT} \,/\, c_s$ in Individual $NH_3$ Clumps

We next look at the non-thermal line widths in the individual $NH_3$ clumps in all three cores. In general, Jijina et al. (1999) found that non-thermal $NH_3$ line widths in clustered environments are larger than those found in isolated regions. In Figure 2.11, we plot $\Delta v_{NT}$ versus $\Delta v_T$ for the $NH_3$ clumps in each core. We omit $NH_3$ clumps B3-A1 and C-A1 where the corrected non-thermal line width is effectively zero. We also show the best fit lines found by Jijina et al. to the relationship between thermal and non-thermal line widths in clustered and in isolated regions. Most of the Oph B clumps lie above the $\Delta v_{NT} - \Delta v_T$ trend for isolated clumps and near the trend for the clumps in clustered regions. The good agreement is somewhat surprising

given that the majority of the objects in the Jijina et al. sample were observed with $\sim 4-8$ times poorer angular resolution, while those observed with high angular resolution are high mass star forming regions $\sim 3-7.5\,\mathrm{kpc}$ distant and thus have very low linear resolution (excepting Orion B, at a distance of 420 pc). Even at the small spatial scales probed by our observations, Oph B is characterized by wide line widths that follow the relationship found for larger objects in clustered environments. In comparison, the $NH_3$ clumps in Oph C lie well below the clustered $\Delta v_{NT} - \Delta v_T$ trend, with $\Delta v_{NT} < \Delta v_T$, and also below the $\Delta v_{NT} - \Delta v_T$ trend seen for objects not associated with a cluster. Two of the three Oph F clumps also fall significantly below the isolated object trend, while the third is more turbulent.

### 2.5.2 Discussion of the Cores

**Trends with $N(\mathbf{H_2})$**

In Figure 2.12, we plot the distribution of $T_K$, $\sigma_{NT} \,/\, c_s$, $N(NH_3)$ and $X(NH_3)$ with $N(H_2)$ (calculated in §4.4 assuming $T_d = T_K$) in Oph B, C and F. We additionally analyse Oph B1 and B2 separately to examine any potential differences between the two. In Figure 2.12a, we find that $T_K$ values in Oph C are nearly universally lower than those in the other filaments, and show a tendency to decrease with increasing $H_2$ column density. As described previously, the other Cores are warmer but also do not show a significant trend with $N(H_2)$. We show in Figure 2.12b that Oph B1 and B2 are both consistent with having a constant, mildly supersonic ratio of non-thermal to thermal line widths over all $N(H_2)$. Oph C line widths are generally dominated by thermal motions, and $\sigma_{NT} \,/\, c_s$ decreases significantly at $N(H_2) \gtrsim 4 \times 10^{22}\,\mathrm{cm}^{-2}$. It is interesting to note that there are few data points at these column densities in the other Cores, and no observed decrease in $\sigma_{NT} \,/\, c_s$. Figure 2.12c and d show that in all Cores $N(NH_3)$ tends to increase with $N(H_2)$, following the general trend that the $NH_3$ emission follows the continuum emission in the Cores. The differences between $NH_3$ and continuum clumps are due to small scale differences in maxima. In addition, the fractional $NH_3$ abundance, $X(NH_3)$, tends to *decrease* with increasing $N(H_2)$, although we note that Oph B1 and F have relatively few data points. Figure 2.12c also illustrates the high $N(NH_3)$ values in Oph B1 relative to $N(H_2)$ compared with values in Oph B2, C and F.

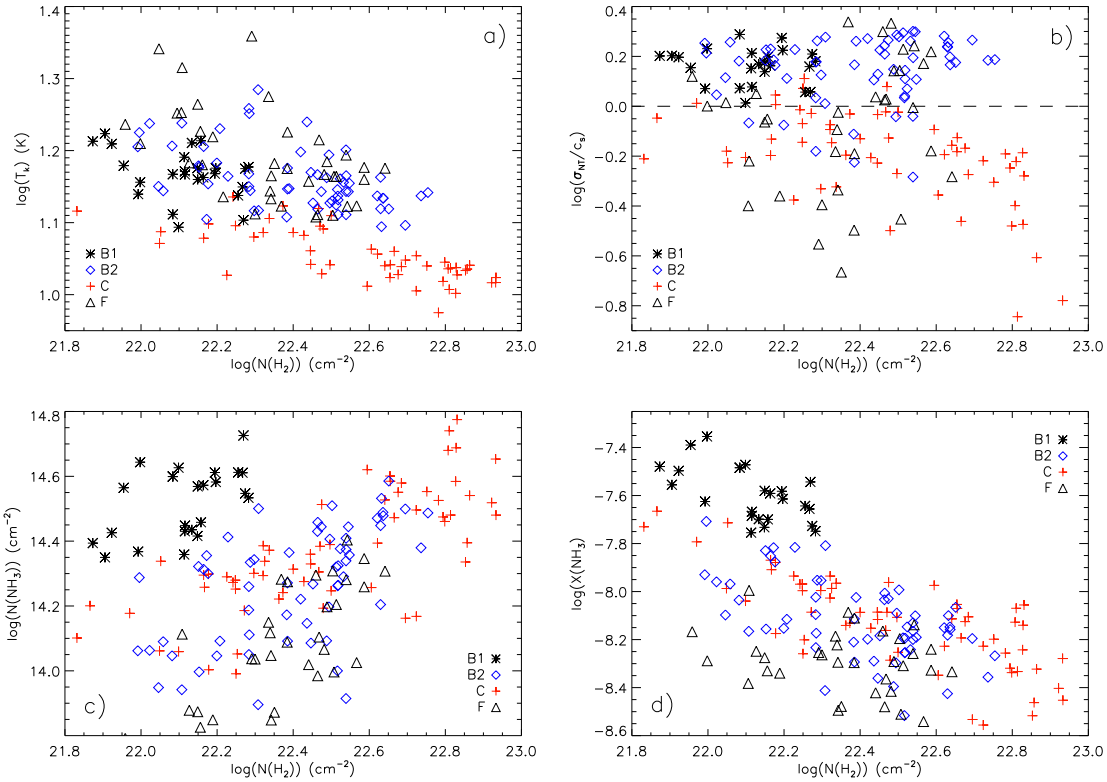


Figure 2.12 a) Kinetic temperature ($T_K$) in K versus $N(\mathrm{H_2})$ (derived from the 850 $\mu$m submillimeter continuum data) in cm$^{-2}$ units for Oph B1, B2, C and F. In all plots, points shown are values in 15″ pixels. Temperatures in Oph C are nearly universally lower than those in B1, B2 and F, and show a tendency to decrease with increasing $\mathrm{H_2}$ column density. A significant trend in temperature with $N(\mathrm{H_2})$ is not obvious in the other Cores. b) $\sigma_{NT} \,/\, c_s$ versus $N(\mathrm{H_2})$ in Oph B1, B2, C and F. The dashed line indicates $\sigma_{NT} \,/\, c_s = 1$. Oph B1 and B2 are consistent with a constant ratio of non-thermal to thermal line widths, where $\sigma_{NT} \,/\, c_s > 1$, over all $\mathrm{H_2}$ column densities. Oph C line widths are generally dominated by thermal motions, and $\sigma_{NT} \,/\, c_s$ decreases significantly at $\mathrm{H_2}$ column densities above $\log(N(\mathrm{H_2})) \sim 22.6$. c) $N(\mathrm{NH_3})$ (derived from the $\mathrm{NH_3}$ HFS line fitting results) versus $N(\mathrm{H_2})$ for Oph B1, B2, C and F. $\mathrm{NH_3}$ column densities tend to increase with $\mathrm{H_2}$ column densities in all Cores. Oph B1 has significantly higher $N(\mathrm{NH_3})$ for its relatively low $N(\mathrm{H_2})$ values compared with the other Cores. d) $X(\mathrm{NH_3})$ versus $N(\mathrm{H_2})$ for Oph B1, B2, C and F. While c) shows the $\mathrm{NH_3}$ column densities tend to increase with increasing $N(\mathrm{H_2})$, the fractional $\mathrm{NH_3}$ abundances appear to decrease with higher $\mathrm{H_2}$ column densities.

If $NH_3$ is depleting at high densities, as the variation of $X(NH_3)$ with $N(H_2)$ suggests, $NH_3$ may not trace well the $T_K$ in the densest and likely coldest regions. Hence, our assumption of $T_d = T_K$ may not be valid towards the highest columns and we may be underestimating $T_d$ and $N(H_2)$ by factors of $\sim 2$. For example, Stamatellos et al. (2007) predicted that $T_d$ in the centers of the Oph Cores could be as low as $\sim 7\,\mathrm{K}$. Furthermore, $X(NH_3)$ ($\propto N(H_2)$, see Figure 2.12) may be overestimated by similar factors. High resolution multiwavelength continuum observations and models are needed to obtain independent assessments of $T_d$ throughout the Oph Cores.

### $\sigma_{NT} \,/\, c_s$ in Oph B

Jijina et al. (1999) compiled numerous observations of $NH_3$ in dense gas and found that while most starless clumps are characterized by largely thermal motions, a large fraction of clumps in clusters have $\sigma_{NT} > \sigma_T$, and that the identification of an $NH_3$ clump as part of a cluster has a larger impact on the observed line widths than association with a protostar. These findings are in agreement with our results in Oph B. The line widths in Oph B, with a mean $\Delta v = 0.89\,\mathrm{km\,s^{-1}}$ and $\sigma_{NT} \,/\, c_s = 1.5$, are significantly wider and more dominated by non-thermal motions than those found in isolated cores. While B2 is associated with at least two embedded protostars and B1 appears starless, when studied separately (shown in Figure 2.13), both Cores have similar $\sigma_{NT} \,/\, c_s$ distributions.

If the non-thermal component is caused by turbulent motions in the gas, then it is interesting to consider the turbulence source. In the following, we consider the source of wide lines in this region as being due to "primordial" (i.e., undamped) turbulence, protostar-driven turbulence, bulk motions or biased sampling.

Firstly, Oph B may have non-thermal motions throughout all the Core that are inherited from the surrounding cloud and that have not yet been damped. Since Oph B is associated with a few embedded protostars, however, it is likely that parts of the Core, at the very least, have been at high density for over a free-fall time $t_{ff}$ ($\sim 3 \times 10^5$ years for $n(H_2) \approx 10^4\,\mathrm{cm^{-3}}$, $\sim n_{cr}$ for the $NH_3$ (1,1) and (2,2) transitions). Since the dissipation timescale for turbulence is $\sim t_{ff}$ (Mac Low & Klessen 2004), it is unlikely that the non-thermal motions from the parent cloud have been retained, if the embedded protostars are indeed physically connected to the Core. Determining

the relative velocities of the YSOs compared with the Core $v_{LSR}$ would help to address this question.

Secondly, the embedded protostars in Oph B may be adding turbulence to the core through energy input associated with mass loss. One outflow has been found in CO emission in the region associated with one of the two protostars near the peak $NH_3$ integrated intensity in B2 (IRS45/GY273 and IRS47/GY279, labelled in Figure 2.2), with a blue lobe towards the west and a red lobe towards the south-east (Kamazaki et al. 2003). We do not, however, see localized regions of wide line widths associated with these or any protostars in Oph B. In fact, protostars are associated with $\Delta v$ *minima*. Additionally, wide line widths are found in B1, where there are no embedded protostars and no known outflows. This suggests that the large non-thermal motions across the core are not driven by embedded YSOs.

Thirdly, the wide line widths seen in the $NH_3$ emission may be indicative of global infall in the Oph B Core. Given the mean $NH_3$ line width in Oph B2, we calculate a virial mass $M_{vir} \sim 8\,M_\odot$, assuming a density distribution which varies as $\rho \propto r^{-2}$. Given mass estimates of the Cores by Motte et al. (1998) (which are uncertain to factors $\sim 2$) and accounting for the different Ophiuchus distance used by the authors (160 pc compared with our preferred value of 120 pc), we find $M/M_{vir} \sim 5$ in Oph B2. Since the mean $NH_3$ (1,1) opacity $\tau = 1.6$ over Oph B, the average individual hyperfine component is optically thin, and we would not expect to see the asymmetrically blue line profiles found in collapsing cores in optically thick line tracers. André et al. (2007) find these spectroscopic signatures of infall motions in B2, with a clear blue infall profile towards our B2-A10 $NH_3$ clump, and profiles suggestive of infall towards B2-A7 and other continuum objects in its eastern half. No evidence of infall motions in the tracers used were found towards central B2, but the lines they used (CS, $H_2CO$ and $HCO^+$) may suffer from depletion at the high densities and low temperatures found at this location, masking any infall signature. Oph B1, however, is also characterized by wide $NH_3$ line widths and has $M/M_{vir} \sim 1$. Additionally, spectroscopic infall signatures were found in Oph C towards our C-A3 $NH_3$ clump by André et al., where we find extremely narrow $NH_3$ line widths (similarly, B2-A7 contains the narrowest lines observed in B2). It does not appear, then, that infall motions are the sole contribution to the wide lines we find in Oph B.

Lastly, rather than acting as a tracer of the densest gas in Oph B, the $NH_3$

emission may be dominated in this high density environment by emission from the more turbulent outer envelope of the Core. Modelling of the expected emission given a constant abundance of $NH_3$ would be necessary to determine accurately whether depletion is a factor in Oph B (note that we see evidence for decreasing abundance of $NH_3$ with $N(H_2)$; see Figure 2.12d). Alternatively, observations of species which are excited at higher densities than $10^4\,\mathrm{cm}^{-3}$, such as $N_2H^+$ and deuterated species such as $N_2D^+$ and $H_2D^+$, may better probe the dense clump gas. Moderate resolution ($\sim 26''$) resolution observations of $N_2H^+$ (1-0) (André et al. 2007) find narrower line emission in small scale $N_2H^+$ condensations (which we call 'clumps') in Oph B1 and the filament connecting B1 and B2 ($\sigma_{NT} = 0.15 \pm 0.04\,\mathrm{km\,s}^{-1}$, or $\sigma_{NT} \,/\, c_s \sim 0.65$ for $T_K = 15\,\mathrm{K}$), but non-thermal line widths in Oph B2 condensations remain transsonic ($\sigma_{NT} \,/\, c_s \sim 1.1 < 2$ on average). In an upcoming paper, we present $H_2D^+$ $1_{10} - 1_{11}$ observations in B2, showing that non-thermal line widths of gas at densities of $\sim 10^6\,\mathrm{cm}^{-3}$ (approximately the critical density of $H_2D^+$, depending on the collisional cross section used) in the core are also transsonic, $\sigma_{NT} \sim 0.25\,\mathrm{km\,s}^{-1}$, or $\sigma_{NT} \,/\, c_s \sim 1.4$ at 10 K (or $\sim 1.1$ at 15 K; Friesen *et al.* 2009, in preparation). Regardless of whether or not the line widths seen in $NH_3$ emission are tracing the highest density gas, the mean non-thermal motions of gas in B2 are greater than typically found in isolated cores.

### $\sigma_{NT} \,/\, c_s$ in Oph C

Motions in the Oph C Core differ substantially from those found in Oph B. Oph C is likely starless, like Oph B1. In contrast to B1 (and also Oph B2 and F), Oph C is dominated by nearly thermal motions ($\langle \sigma_{NT} \,/\, c_s \rangle = 0.6$), shown in Figure 2.13. Oph C thus appears less affected by the clustered environment, and is kinematically more alike isolated clumps. $NH_3$ clumps in the Pipe nebula and Perseus molecular cloud have similarly narrow line emission, for example, with the $\sigma_{NT} \,/\, c_s \sim 1-2$ in the Pipe (Rathborne et al. 2008) and intrinsic line widths $\sigma_v$ typically less than $0.2\,\mathrm{km\,s}^{-1}$ in Perseus (Rosolowsky et al. 2008a).

In addition, we see in Oph C a progressive decrease in the magnitude of non-thermal motions as we look at molecular lines that trace increasingly high densities. Non-thermal line widths $\sigma_{NT} = 0.20 - 0.28\,\mathrm{km\,s}^{-1}$ were determined from $DCO^+$ (1-0) observations (albeit with a large $1'.5$ beam) of Oph C (Loren et al. 1990). At their

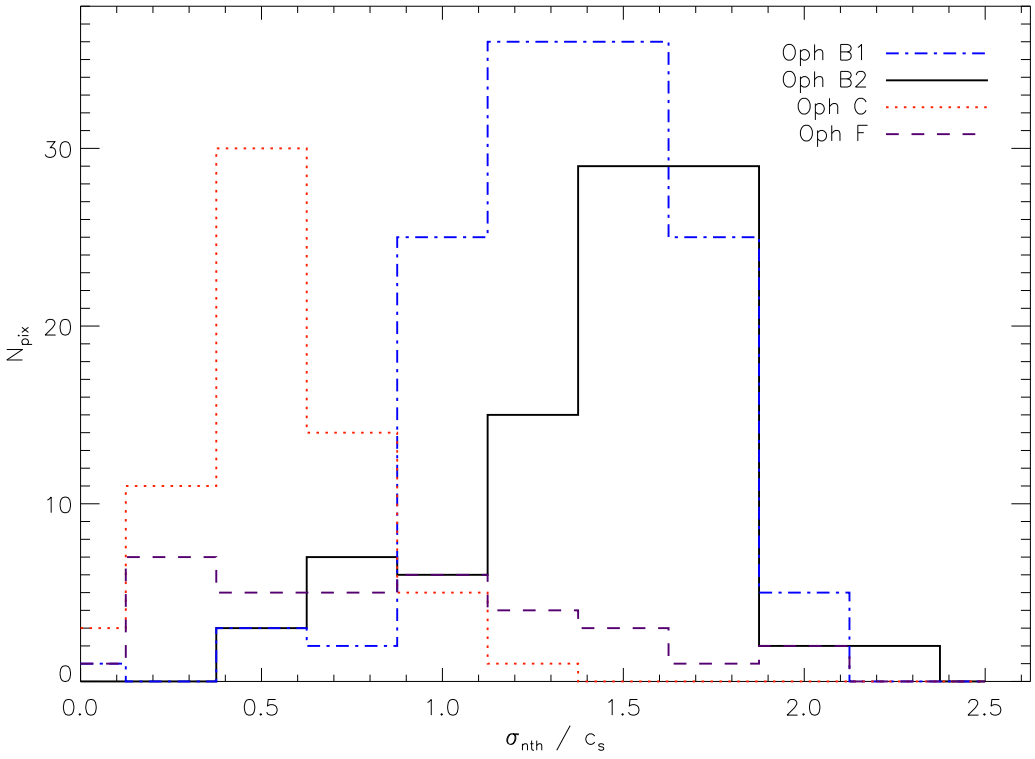


Figure 2.13 Histogram $\sigma_{NT} / c_s$ in Oph B1, B2, C and F. Values plotted are those in 15″ pixels. Oph C is characterized by significantly lower non-thermal to thermal line width ratios than the other Cores. When analysed separately, Oph B1 and B2 are very similar in $\sigma_{NT} / c_s$.

peak emission locations in C, we find $\sigma_{NT} = 0.16\,\mathrm{km\,s^{-1}}$ and $0.17\,\mathrm{km\,s^{-1}}$ for $C_2S$ and $HC_5N$, respectively, from our GBT-only data. These locations coincide with the bulk of the $NH_3$ emission in C, where we find the smallest $\sigma_{NT}$ values (consistent at our velocity resolution with nearly or purely thermal motions), and where recent $N_2H^+$(1-0) observations by André et al. (2007) also find $\sigma_{NT} \sim 0.13\,\mathrm{km\,s^{-1}}$ (their C-MM3 - C-MM6). This trend indicates that turbulent motions have decreased at higher densities.

### Oph B3

Oph B3 is an unusual object within Oph B. It was originally detected in $DCO^+$ emission (Loren et al. 1990). It is not readily apparent in dust continuum maps of Oph

B, and consequently is only identified as a separate clump by Stanke et al. (2006). This lack of prominence suggests that interesting potential sites of star formation may be overlooked by purely continuum surveys. (In a similar result, Di Francesco et al. (2004) found a region of extremely narrow $N_2H^+$(1-0) line width in Oph A associated with extended thermal continuum emission but not correlated with a continuum clump.) The relatively large difference in line of sight velocity between B3 and the Oph B mean (e.g., greater than that between Oph B and F) suggests that B3 may not be physically associated with the rest of Oph B.

B3 is characterized in $NH_3$ emission by moderately bright, extremely narrow lines which are nearly thermal in width. The lack of continuum emission implies a low $H_2$ column density, leading to an $NH_3$ fractional abundance lower limit similar to the $X(NH_3)$ values found for clumps in B1 and C. Interestingly, no $C_2S$ or $HC_5N$ emission was detected in B3, suggesting that B3 may be in a later evolutionary state than B1 and C. Alternatively, if B3 is physically distinct from the rest of Oph B, its initial chemistry may have differed.

The kinetic temperature associated with the B3-A1 $NH_3$ clump is 13.9 K. This is lower than the average $T_K$ in Oph B but not particularly cold compared with other $NH_3$ clumps in Oph B. The uncertainty in this value is large due to the low signal-to-noise ratio of the $NH_3$ (2,2) line in the combined data, but we find a slightly lower value, $T_K = 12.0 \pm 0.3$ K, from the single-dish data alone. This temperature difference is not large enough to account for the lack of submillimeter emission at the B3 peak if the column density of material was similar to that found in B1 or B2.

Based on the flux observed by Stanke et al. (2006) at the location of B3 (their MMS-108) and the gas temperature derived from our observations, we find a total clump mass for Oph B3 of $M \sim 0.4\,M_\odot$, which is within a factor of $\sim 2$ (i.e., within uncertainties) of the virial mass calculated using the observed $NH_3$ line width and core radius from Table 2.4 ($M \sim 0.2\,M_\odot$). Accordingly, if it collapses, Oph B3 may form a very low mass star or brown dwarf, depending on how much material passes into a compact protostar. Future sensitive large format millimetre array detectors, such as SCUBA-2, should easily detect objects like B3 at greater than 3-$\sigma$ levels of confidence with relatively short integration times.

### 2.5.3 Implications for Clustered Star Formation

Comparisons of the mean values of many parameters found in each of the Cores (Tables 2.6 and 2.7) show significant differences between Oph B and C. In particular, Oph C is characterized by significantly narrower line widths and lower kinetic temperatures. This distinction is further illustrated in Figures 2.12 and 2.13. An object like Oph C (and perhaps Oph B3) resembles isolated clumps in the close correspondence between the $NH_3$ line map and the dust continuum map, and in the evidence that the peak of the intensity map coincides with local minima in both $T_K$ and $\Delta v$. Such a core would fit well the idea that clustered star formation is just a spatially concentrated version of isolated star formation, with smaller, denser star forming clumps packed closer together than in isolated regions. The Oph B Core shows a remarkably different behavior. Oph B contains a larger number of $NH_3$ clumps than Oph C or F, and there is much less correspondence between the locations of the $NH_3$ and continuum clumps. The $NH_3$ clumps show modest contrast with interclump gas in their intensity, and little contrast in their velocity or their line width. The greater amount of fragmentation of Oph B than found in C or F may be related to the relatively higher levels of turbulence in the Core, which are significantly greater than typically found in isolated regions. Thus, dense $NH_3$ gas in Oph B does not resemble the dense gas in regions of isolated star formation, and this raises the issue whether this presents a different 'initial condition' for clustered star formation.

## 2.6 Summary

We have presented combined single-dish and interferometer $NH_3$ (1,1) and (2,2) observations of the B, C and F Cores in the clustered star-forming Ophiuchus molecular cloud. We additionally present single-dish $C_2S$ ($2_1 - 1_0$) and $HC_5N$ (9-8) observations of the Cores. Our main results can be summarized thus:

1. While the large-scale features of submillimeter continuum emission and $NH_3$ (1,1) integrated intensity appear similar, on $15''$ scales we find significant discrepancies between the dense gas tracers in Oph B, but good correspondence in Oph C and F. We find poor correspondence in Oph B between continuum clumps and $NH_3$ clumps identified with 3D CLUMPFIND, with only five of fifteen $NH_3$ clumps located

within 30″ (3600 AU) of a dust clump. This is in contrast with previous findings of extremely high spatial correlation between the two gas tracers in isolated, low-mass starless clumps.

2. We find $v_{LSR}$ varies little across any of the Oph Cores, and additionally varies by only $\sim 1.5\,\mathrm{km\,s^{-1}}$ between them.

3. Overall, the observed $NH_3$ line widths in the Cores are generally large, and often slightly supersonic. We also find regions of localized narrow line emission ($\Delta v \lesssim 0.4\,\mathrm{km\,s^{-1}}$), some of which are associated with $NH_3$ clumps. The larger line widths in Oph B ($\langle \Delta v \rangle = 0.8\,\mathrm{km\,s^{-1}}$) agree with previous findings for clumps in clustered regions. Line widths in Oph C, however, decrease to nearly thermal values which are more representative of typical isolated clumps.

4. The derived kinetic temperatures of the gas are remarkably constant across Oph B. Kinetic gas temperatures in both B and F are warmer ($\langle T_K \rangle = 15\,\mathrm{K}$) than generally found in isolated star forming clumps, but are consistent with temperatures determined for cores in clustered environments. The center of Oph C shows a minimum $T_K \sim 9\,\mathrm{K}$, similar to previous results in isolated clumps.

5. We find no significant difference in $T_K$ between $NH_3$ clumps, submillimeter clumps ($\langle T_K \rangle = 14\,\mathrm{K}$) and protostars ($\langle T_K \rangle = 15.5\,\mathrm{K}$). Most other physical parameters have similarly insignificant variations between the objects. We do find that protostars are associated with significantly *smaller* line widths ($\langle \Delta v \rangle = 0.4\,\mathrm{km\,s^{-1}}$) with approximately equal contribution from thermal and non-thermal motions.

6. We have determined $NH_3$ abundance values towards the Cores, and find they agree with previous estimates of $X(NH_3)$ in cold, dense environments. Single-dish observations of $C_2S$ and $HC_5N$ resulted in only a few detections, and derived column densities ($\sim 10^{12} - 10^{13}\,\mathrm{cm^{-2}}$) similar to those found in other molecular clouds.

7. It is unlikely that the wide line widths observed in Oph B are due to pervasive turbulent motions inherited from the parent cloud if the already formed embedded protostars are physically connected with the core. We find no evidence of influence by the protostars on the gas motions, i.e., through local increases in line widths or gas temperatures. The $NH_3$ abundance in Oph B2 appears to decrease with increasing gas density. We therefore suggest that the $NH_3$ emission is biased, i.e., due to depletion

at high inner densities, and is therefore not tracing the densest gas in the Core. This may explain the differences between the locations of $NH_3$ and continuum clumps. Consequently, the gas temperatures may be lower in the center of Oph B than given by the $NH_3$ line ratios.

Table 2.8. Derived Parameters at $NH_3$ (1,1) Peak Locations

| ID | $v_{lsr}$ $\mathrm{km\,s^{-1}}$ | $\Delta v$ $\mathrm{km\,s^{-1}}$ | $\tau$ | $T_k$ K | $T_{ex}$ K | $\sigma_{NT}$ $\mathrm{km\,s^{-1}}$ | $N(H_2)$ $10^{21}\,\mathrm{cm^{-2}}$ | $N(NH_3)_{tot}$ $10^{13}\,\mathrm{cm^{-2}}$ | $X(NH_3)$ $10^{-9}$ | $n(H_2)$ $10^{4}\,\mathrm{cm^{-3}}$ |
|---|---|---|---|---|---|---|---|---|---|---|
| B1-A1 | 4.01(3) | 0.85(7) | 1.6(3) | 16.3(1.9) | 9.4(1) | 0.35(3) | ··· | 22(4) | ··· | 2.8(1) |
| B1-A2 | 3.84(2) | 0.92(5) | 1.5(1) | 16.4(1.3) | 12.1(1) | 0.38(2) | 14(3) | 29(4) | 17(8) | 6.5(2) |
| B1-A3 | 3.98(1) | 0.62(3) | 3.4(2) | 13.7(1.0) | 9.7(1) | 0.25(2) | 18(4) | 41(3) | 23(9) | 4.2(1) |
| B1-A4 | 3.83(2) | 0.54(3) | 4.2(3) | 12.4(0.9) | 8.4(1) | 0.22(2) | 12(2) | 42(3) | 35(12) | 3.2(1) |
| B2-A1 | 4.18(2) | 0.57(5) | 1.6(3) | 13.3(1.2) | 11.6(1) | 0.23(2) | ··· | 22(4) | ··· | 13(1) |
| B2-A2 | 4.13(2) | 0.86(5) | 0.3(*) | 14.1(*) | 19.5(1) | 0.35(*) | ··· | 18(*) | ··· | 0.0(*) |
| B2-A3 | 4.10(3) | 0.80(7) | 1.3(3) | 14.2(1.2) | 10.2(1) | 0.33(3) | 15(2) | 20(4) | 14(6) | 4.7(1) |
| B2-A4 | 4.00(2) | 1.00(6) | 1.4(2) | 13.5(1.0) | 11.6(1) | 0.42(3) | 32(6) | 32(5) | 9.7(4) | 11.7(8) |
| B2-A5 | 3.91(2) | 0.79(5) | 2.4(2) | 13.2(1.0) | 9.7(1) | 0.32(2) | 45(9) | 38(4) | 8.6(3) | 4.8(2) |
| B2-A6 | 4.32(2) | 0.66(4) | 1.3(2) | 14.5(1.1) | 14.1(1) | 0.27(2) | 33(7) | 24(4) | 6.6(3) | 72(26) |
| B2-A7 | 4.57(1) | 0.33(2) | 2.8(2) | 13.9(1.1) | 11.9(1) | 0.12(2) | 35(7) | 22(2) | 6.5(2) | 11.5(8) |
| B2-A8 | 4.35(3) | 0.95(8) | 0.5(*) | 14.6(*) | 16.9(1) | 0.39(*) | 43(7) | 16(*) | 3.7(*) | 0.0(*) |
| B2-A9 | ··· | ··· | ··· | ··· | ··· | ··· | ··· | ··· | ··· | ··· |
| B2-A10 | 4.22(2) | 0.71(6) | 1.6(3) | 14.3(1.2) | 10.3(1) | 0.29(3) | 35(7) | 23(4) | 6.1(3) | 4.8(2) |
| B3-A1 | 3.15(2) | 0.08(8) | 0.7(*) | 13.9(*) | 13.9(1) | 0.0(*) | ··· | 1.3(*) | ··· | 12.4(*) |
| C-A1 | 4.08(1) | 0.16(1) | 9.3(6) | 10.4(0.7) | 8.0(2) | 0.0(*) | 84(14) | 33(2) | 4.0(2) | 4.2(2) |
| C-A2 | 3.97(1) | 0.36(4) | 2.7(6) | 12.0(1.2) | 8.8(2) | 0.13(1) | 14(3) | 20(4) | 14(9) | 4.1(2) |

Table 2.8 (cont'd)

| ID | $v_{lsr}$ $\mathrm{km\,s^{-1}}$ | $\Delta v$ $\mathrm{km\,s^{-1}}$ | $\tau$ | $T_k$ K | $T_{ex}$ K | $\sigma_{NT}$ $\mathrm{km\,s^{-1}}$ | $N(\mathrm{H_2})$ $10^{21}\,\mathrm{cm^{-2}}$ | $N(\mathrm{NH_3})_{tot}$ $10^{13}\,\mathrm{cm^{-2}}$ | $\mathrm{X(NH_3)}$ $10^{-9}$ | $n(\mathrm{H_2})$ $10^{4}\,\mathrm{cm^{-3}}$ |
|---|---|---|---|---|---|---|---|---|---|---|
| C-A3 | 3.98(2) | 0.29(2) | 9.3(5) | 10.7(0.8) | 8.0(2) | 0.10(3) | 68(4) | 60(5) | 8.8(2) | 3.9(2) |
| F-A1 | 4.82(4) | 0.8(1) | 1.5(7) | 15.3(2.0) | 7.4(2) | 0.32(5) | 31(6) | 16(7) | 5.1(4) | 1.6(1) |
| F-A2 | 4.31(2) | 0.58(5) | 1.8(4) | 15.6(1.6) | 9.9(2) | 0.23(2) | 35(7) | 19(5) | 5.5(3) | 3.4(1) |
| F-A3 | 4.31(2) | 0.43(3) | 2.6(4) | 16.8(1.8) | 9.8(2) | 0.16(2) | 24(5) | 19(3) | 7.8(3) | 3.0(1) |

Note. — Uncertainties are given in brackets beside values and show the uncertainty in the last digit of the value, with the exception of the $T_K$ uncertainties which are given in K units. A (*) indicates that the uncertainty in the value at this position were large, even though in most cases the values themselves are reasonable. A good HFS fit was not found at the peak position of $NH_3$ clump B2-A9.

# Chapter 3

# $N_2H^+$ Observations of the Cluster-Forming Ophiuchus B Core

## 3.1 Introduction

Stars form out of the gravitational collapse of centrally condensed cores of dense molecular gas. Recent years have seen leaps forward in our understanding of the structure and evolution of isolated, star forming cores. Most star formation, however, occurs in clustered environments (Lada & Lada 2003). These regions are more complex, with complicated observed geometries, and contain cores which tend to have higher densities and more compact sizes than those found in isolation (Ward-Thompson et al. 2007a). It is likely that due to these differences the evolution of filaments and cores in clustered regions proceeds differently than in the isolated cases. Characterizing the physical and chemical structures of these more complicated regions are thus the first steps towards a better understanding of the process of clustered star formation.

It is now clear that molecular cores become extremely chemically differentiated, as many molecules commonly used for tracing molecular gas, such as CO, become severely depleted in the innermost core regions through adsorption onto dust grains (see, e.g., Di Francesco et al. 2007, for a review). In Chapter 2, we studied the dense gas in several cluster forming Cores in the Ophiuchus molecular cloud (Oph

B, C and F) through high resolution observations of $NH_3$ (1,1) and (2,2) emission made at the Green Bank Telescope (GBT), the Australia Telescope Compact Array (ATCA) and the Very Large Array (VLA). The Ophiuchus molecular cloud ($\sim 120\,\mathrm{pc}$ distant; Loinard et al. 2008; Lombardi et al. 2008; Knude & Hog 1998) is our closest example of ongoing, clustered star formation. We found that the Ophiuchus Cores presented physical characteristics similar to those found in studies of both isolated and clustered environments. In Oph C, for example, gas motions are subsonic (mean $\sigma_v = 0.16\,\mathrm{km\,s^{-1}}$), and decrease in magnitude along with the kinetic gas temperature ($T_K$) towards the thermal dust continuum emission peak in a manner reminiscent of findings in the isolated cores L1544 (Crapsi et al. 2007); etc. In contrast to Oph C, $NH_3$ line widths in Oph B are dominated by transonic non-thermal motions and the gas temperatures are warmer than typically found in isolated regions ($\langle T_K \rangle = 15\,\mathrm{K}$) and nearly constant across the Core. No contrast in any parameters [such as $T_K$, ratio of non-thermal to thermal line width $\sigma_{\mathrm{NT}} \,/\, c_s$, or $NH_3$ column density $N(NH_3)$] was found between the two main components of Oph B, labelled B1 and B2, despite the presence of several embedded Class I protostars in B2 while B1 appears starless. Additionally, on small scales ($\sim 15''$, or 1800 AU at 120 pc), significant offsets were found between the peaks of integrated $NH_3$ (1,1) intensity and those of submillimeter continuum emission, as well as between individual 'clumps' identified through 3D CLUMPFIND (Williams et al. 1994) in the $NH_3$ data cube and those found through 2D CLUMPFIND in $850\,\mu\mathrm{m}$ continuum emission. Finally, evidence was found for a decreasing fractional $NH_3$ abundance with increasing $H_2$ column density (as traced by $850\,\mu\mathrm{m}$ continuum emission), suggesting that $NH_3$ (1,1) may not be tracing the densest gas in the Oph Cores.

The diazenylium ion, $N_2H^+$, has been shown to be a preferential tracer of quiescent dense gas in molecular clouds (Womack et al. 1992; Caselli et al. 2002a; Tafalla et al. 2002, 2004). The 1-0 rotational transition has a critical density $n_{cr} \sim 2 \times 10^5\,\mathrm{cm^{-3}}$, $\sim 10\times$ greater than that of $NH_3$ (1,1), and therefore possibly better suited to probing gas properties at the high densities expected in clustered star forming Cores. Based on both observations and chemical models of starless cores, $N_2H^+$ also appears resilient to depletion at the high densities ($n \gtrsim 10^5\,\mathrm{cm^{-3}}$) and cold temperatures ($T \sim 10\,\mathrm{K}$) characteristic of the later stages of prestellar core evolution (see, e.g., Tafalla et al. 2004; Bergin et al. 2002), and is thus expected to be an excellent tracer of the physical conditions of dense cores and clumps.

Recently, André et al. (2007) observed the Oph A, B, C, E and F Cores in $N_2H^+$ 1-0 emission at 26″ angular resolution using the IRAM 30 m telescope. They found that the gas traced by $N_2H^+$ emission near clumps identified in millimeter continuum emission (Motte et al. 1998) is characterized, on average, with relatively narrow line widths showing small non-thermal velocity dispersions, in contrast to the large non-thermal motions traced by $NH_3$ emission in Chapter 2. The authors derived virial masses from the $N_2H^+$ emission, and found they generally agreed within a factor $\sim 2$ with the masses derived from dust emission, suggesting that the clumps are gravitationally bound and prestellar. The relative motions of the clumps are also small and subvirial, with a crossing time larger than the expected lifetime of the objects, such that clump-clump interactions are not expected to impact their evolution. These results suggest that a dynamic picture of clump evolution involving competitive accretion at the prestellar stage does not accurately describe the star formation process in central Ophiuchus.

In this work, we discuss the results of higher resolution (18″, or $\sim$ 2200 AU at 120 pc) observations of $N_2H^+$ 1-0 in the Ophiuchus B Core that reveal the distribution, kinematics and abundance pattern of the Core and associated embedded clumps on smaller physical scales. We additionally examine $N_2H^+$ 1-0 structure at even higher resolution ($8'' \times 5''$), through observations made with the Australia Telescope Compact Array (ATCA), towards five locations in Oph B2 where small-scale structure was found in $NH_3$ (Chapter 2) and in previously unpublished BIMA $N_2H^+$ 1-0 observations. We compare these data with our recently published analysis of $NH_3$ emission in Oph B, in particular focusing on the kinematics and relative abundances of the two species to compare with physical and chemical models of dense core formation and collapse.

We discuss the observations and calibration and §2. In §3, we present the data, and discuss the results of the hyperfine line structure fitting procedure and derivations of the column density, $N(N_2H^+)$, and fractional $N_2H^+$ abundance, $X(N_2H^+)$, in §4. In §5, we discuss general trends in the data, and compare these results with those found in Chapter 2 and with studies of dense cores in isolated environments. We summarize our findings in §6.

## 3.2 Observations and Data Reduction

### 3.2.1 Nobeyama 45 m Radio Telescope

Single dish mapping observations of Oph B in $N_2H^+$ 1-0 (rest frequency 93.174 GHz) were performed May 10 - 15, 2007 using the 25-BEam Array Receiver System (BEARS) at the Nobeyama 45 m Radio Telescope. BEARS is a $5 \times 5$ SIS heterodyne receiver array. An autocorrelator spectrometer with 8 MHz bandwidth and 1024 channels was used as the backend, giving a spectral resolution of 7.8 kHz or $0.025 \mathrm{km\,s^{-1}}$ at 93 GHz. The final spectral resolution was binned to $0.05 \mathrm{km\,s^{-1}}$. The half-power beamwidth was $\sim 18''$ and the main-beam efficiency at 93 GHz is estimated to be $\eta_{MB} = 0.505$, interpolated from observatory measurements at 86 GHz and 100 GHz, with an uncertainty of $\sim 8 - 10\,\%$. The beams are separated by $41.1''$ on the sky.

Observations were performed in position-switching OTF mode, alternating scanning in Right Ascension (R.A.) and Declination (decl.) to ensure minimal striping artifacts. The array was rotated by an angle of $7^\circ$ such that the spacing of individual detectors was $5''$ in R.A. or decl., and scans of the array were spaced by $25''$. A ten minute integration on the off-source position ($+5^\circ$ in R.A.) was performed to ensure no emission was present. The weather was only moderately variable over the observations, and most data were taken with $T_{sys} \sim 300 - 450$ K (DSB). Telescope pointing was checked every 90 minutes on nearby SiO maser sources AF Sco and RS Lib. Typical pointing offsets were $1 - 3''$.

Calibration of BEARS was done by observing a bright $N_2H^+$ target first with the S100 single sideband receiver, and second with each individual BEARS beam. These data provided a flux scaling factor for each beam to correct for the telescope gain and DSB ratio. The starless core L183 was observed with S100 and the central BEARS beam, but the line emission was not strong enough to use as a calibrator for each BEARS beam. The Oph A core SM1 was then observed with each BEARS beam and the scaling factors for each beam were determined using both sources. The average scaling factor was 1.35, with a range from 1.07 to 1.66.

The scaling factors were applied to the data and a linear baseline was fit to and subtracted from the spectra. The R.A. and Dec. scans were gridded separately and then combined using a basket-weave method to minimize baseline drift effects

(Emerson & Graeve 1988).

### 3.2.2 BIMA

Observations of $N_2H^+$ 1-0 across the Oph B2 Core were made with the Berkeley-Illinois-Maryland Association (BIMA) array located at Hat Creek, CA, U.S.A. Four tracks were observed on 2001 March 18, 21, and 26 and 2001 May 23, when the array was in its C-configuration. Observations of Oph B2 consisted of a serial sequence of 12 overlapping positions with centers spaced by 1.06′, to obtain a Nyquist-sampled mosaic across Oph B2 at 93.2 GHz. The correlator was configured to provide 12.5 MHz of band width in one correlator window at 93.2 GHz, providing 512 channels of $0.04 \mathrm{km\,s^{-1}}$ width. The radio source 3C279 was observed at the start of each track to provide passband and flux calibration. Neptune was observed at the end of each track to provide flux calibration. The radio source 1733-130 was observed between every set of Oph B2 observations to provide phase calibration. Values of $T_{sys}$ during the tracks were typically 250-500 K for all antennas, except antenna 2 where $T_{sys}$ values were a factor of $\sim 1.5$ higher.

The Oph B2 BIMA data were reduced using standard tasks in the MIRIAD package (Sault et al. 1995). To improve sensitivity to diffuse emission and produce a rounder beam, the visibilities were tapered with a Gaussian 10″ FWHM in R.A. and 0.1″ FWHM in decl. For the $N_2H^+$ data, the final beam size achieved was 19.3″ × 10.6″ FHWM (P.A. -12.4°) and the resulting sensitivity (1 $\sigma$ rms) per channel was $0.72 \mathrm{\,Jy\,beam^{-1}}$, or equivalently 0.49 K. Only faint, diffuse $N_2H^+$ emission was detected towards locations in eastern Oph B2, with even weaker emission spots towards central Oph B2. The faint $N_2H^+$ emission was not detected significantly enough to fit the hyperfine line components, but the locations of significant integrated intensity provided targets for later, more sensitive data of Oph B2 with the Australia Telescope Compact Array (ATCA, see below).

### 3.2.3 ATCA

A total of 11 pointings were observed in $N_2H^+$ 1-0 emission at the ATCA towards five targets in July 2006 in the interferometer's most compact (H75) configuration. The

Table 3.1. ATCA Targets in Oph B2

| R.A. J2000 | Dec. J2000 | rms Jy beam$^{-1}$ | Mosaic | Associated Objects |
|---|---|---|---|---|
| 16:27:24.6 | -24:26:55 | 0.13 | N | B2-A5[a] |
| 16:27:29.3 | -24:27:25 | 0.04 | Y | B2-A6[a], B2-MM8[b], 162729-24274[c], Elias 32/VSSG18[d] |
| 16:27:31.3 | -24:27:46 | 0.05 | Y | B2-A9[a] |
| 16:27:32.6 | -24:26:56 | 0.12 | N | B2-A7[a], B2-MM15[b] |
| 16:27:34.7 | -24:26:13 | 0.10 | Y | B2-A8, B2-A10[a], B2-MM16[b], 162733-24262[c] |

[a]Friesen et al. (Chapter 2, 2009b)

[b]Motte et al. (1998)

[c]Jørgensen et al. (2008)

[d]Elias (1978); Vrba et al. (1975)

BIMA data were used as a guide for the pointings. Figure 3.1a shows the positions of all 11 pointings over an 850 $\mu$m continuum map of Oph B. Table 3.1 lists the positions of the targets, the rms noise achieved in Jy beam$^{-1}$, and any associated $NH_3$ clumps identified in Chapter 2, continuum objects, or embedded YSOs. Two of the targets were imaged using mosaics of three Nyquist-spaced pointings each. Three pointings towards the Oph B2 continuum emission peak overlapped, but were not Nyquist-spaced, while the remaining two targets were observed with a single pointing each. An 8 MHz band width with 512 channels was used for the observations, providing a spectral resolution of 15.6 kHz or 0.05 km s$^{-1}$ at 93.2 GHz while allowing all hyperfine components of the transition to fit within the band. Baselines ranged from 31 m to 89 m for five antennas (the sixth antenna is located 6 km from the main group and was not used for these observations due to poor phase stability), corresponding to 10.3 k$\lambda$ - 29.7 k$\lambda$. The primary beam (field-of-view) was 34″ in diameter.

Observations were made in frequency-switching mode. Observations cycled through each individual pointing between phase calibrator observations to maximize $u, v$ coverage and minimize phase errors. The phase calibrator, 1622-297, was observed every 20 minutes, and was also used to check pointing every hour. Flux and bandpass calibration observations were performed each shift on Mars or Uranus.

The ATCA data were reduced using the Miriad data reduction package (Sault et al. 1995). The data were first flagged to remove target observations unbracketed by phase calibrator measurements, data with poor phase stability or anomalous amplitude measurements. The bandpass, gains and phase calibrations were applied, and the data were then deconvolved (or jointly deconvolved, in the case of the mosaiced pointings). First, the data were transformed from the $u, v$ plane into the image plane using the task INVERT and natural weighting to maximize sensitivity. The data were then deconvolved and restored using the tasks MOSSDI and RESTOR to remove the beam response from the image. MOSSDI uses a Steer-Dewdney-Ito CLEAN algorithm (Steer et al. 1984). The cleaning limit was set at twice the rms noise level in the beam overlap region for each object. Clean boxes were used to avoid cleaning noise in the outer regions with less beam overlap. The final synthesized beam had a FWHM of $8'' \times 5''$.

We next convolved the ATCA data only to a final beam FWHM of $18''$ to match the Nobeyama data and estimate the amount of flux recovered by the interferometer. With the exception of the single pointing towards the $NH_3$ clump B2-A7, we found the maximum peak intensities in the convolved maps are only $\sim 15-20\,\%$ of that in the single dish map, suggesting that the interferometer data alone are only sensitive to $\sim 15-20\,\%$ of the total $N_2H^+$ emission. At the B2-A7 location, the single detected interferometer emission peak is $\gtrsim 50\,\%$ of that seen by the single dish telescope.

## 3.3 Results

### 3.3.1 Single Dish Data

In Figure 3.1a, we show $850\,\mu$m continuum emission in the Core at $15''$ FWHM resolution, first mapped with the Submillimetre Common User Bolometer Array (SCUBA) at the James Clerk Maxwell Telescope (JCMT) by Johnstone et al. (2000b) and recently re-reduced and combined with all other SCUBA archive data in the region by Jørgensen et al. (2008), following the description in Kirk et al. (2006). The Oph B Core can be separated into three distinct sub-Cores, B1, B2, and B3, which are labelled on the Figure. We also show the locations of four Class I protostars detected and classified through Spitzer infrared observations (Enoch et al. 2008). Figure 3.1b

shows the $N_2H^+$ 1-0 intensity in the Oph B Core at 18″ FWHM resolution, integrated over only those velocity channels containing emission from the hyperfine components.

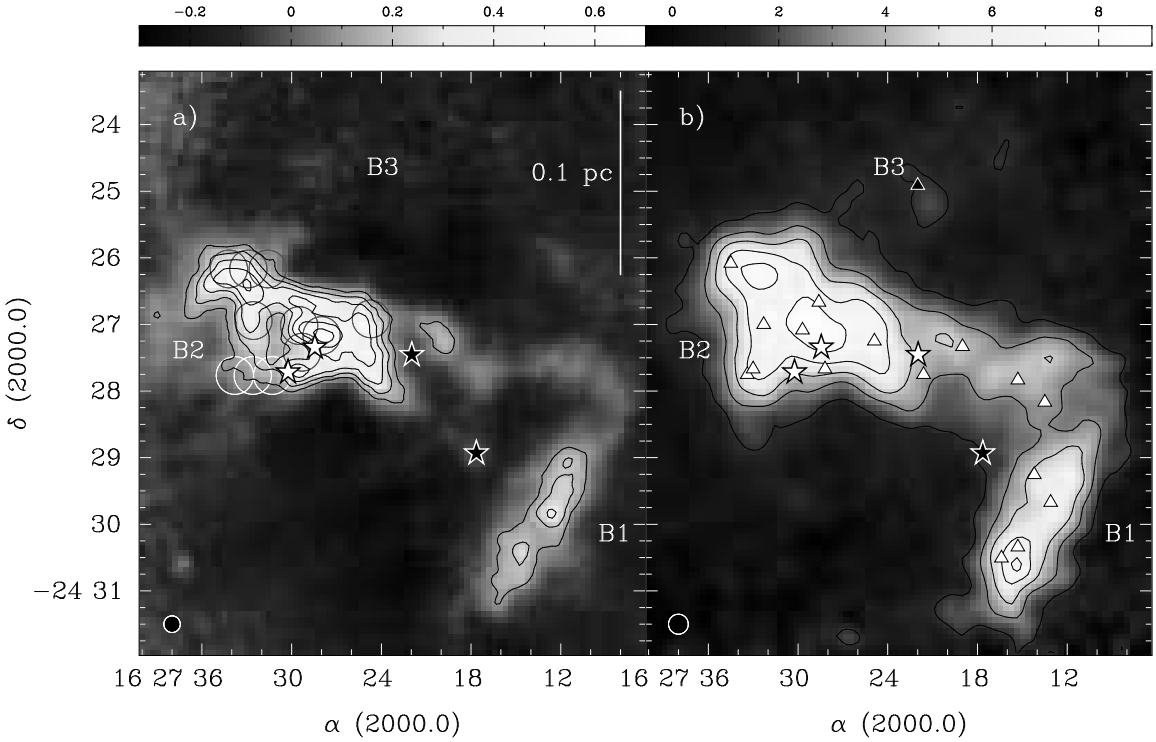


Figure 3.1 a) 850 $\mu$m continuum emission in the Ophiuchus B2 core in Jy beam$^{-1}$, first mapped by Johnstone et al. (2000b) at the JCMT. Black contours begin at 0.1 Jy beam$^{-1}$ and increase by 0.1 Jy beam$^{-1}$. The 15″ beam is shown at lower left. Grey and white circles show locations of ATCA observations with a primary beam diameter of 34″. In both plots, stars indicate the positions of Class I objects (Enoch et al. 2008). b) The Ophiuchus B core in $N_2H^+$ 1-0 integrated intensity in K km s$^{-1}$ ($T_A^*$) observed at Nobeyama. Oph B1, B2 and B3 are labelled. (Oph B3 is not prominent in integrated intensity due to the extremely narrow lines found at this location) Contours begin at 1.5 K km s$^{-1}$ and increase by 1.5 K km s$^{-1}$. The 18″ beam is shown at lower left. Triangles indicate positions of $N_2H^+$ 1-0 clumps discussed in §3.1 and listed in Table 3.2.

On 18″ scales, the integrated $N_2H^+$ intensity within Oph B1 and B2 is remarkably smooth and shows several maxima on scales significantly larger than the beam. On average, the integrated $N_2H^+$ intensity closely follows the continuum emission in the Core, with a few exceptions. First, we find significant $N_2H^+$ emission in southeast Oph B2, where little continuum emission is seen. In fact, the entire eastern half of B2 contains strong $N_2H^+$ emission, while the continuum emission becomes significantly fainter to the east of the central B2 850 $\mu$m emission peak. Second, the integrated

$N_2H^+$ intensity maximum in B2 is offset from the continuum maximum by $\sim 22''$, although strong $N_2H^+$ emission is also found at the continuum peak. Third, the continuum and $N_2H^+$ integrated intensity peaks in Oph B1 are also offset. Fourth, the filament connecting Oph B1 and B2 is more prominent in $N_2H^+$ than in continuum emission. The Oph B3 Core is undetected in 850 $\mu$m continuum. Although it is a clear feature in the $N_2H^+$ data, it is faint in $N_2H^+$ integrated intensity due to the extremely narrow line widths associated with the Core (discussed further in §3.4).

### Identifying discrete $N_2H^+$ 'clumps'

We next identify discrete emission 'clumps' in the Nobeyama $N_2H^+$ 1-0 emission data cube using the 3D version of the automated structure-finding routine CLUMPFIND (Williams et al. 1994). CLUMPFIND uses specified brightness contour intervals to search through the data cube for distinct objects identified by closed contours in position and velocity. The size of the structures found are determined by including adjacent pixels down to an intensity threshold, or until the outer edges of two separate structures meet. The core location is defined as the emission peak within the core.

The rms noise level in the data cube is essentially constant (rms $\sim 0.08$ K in $T_A^*$ units) over most of the region observed, but emission in Oph B1 extends near the edge of the area of best OTF mapping overlap and consequently has slightly lower sensitivity. We therefore created a signal-to-noise data cube by dividing the spectrum at each pixel by the rms noise in the off-line spectral channels. We then ran CLUMPFIND specifying brightness contours of 4× the S/N ratio with an intensity threshold of 3× the data rms. The strongest hyperfine components of the $N_2H^+$ 1-0 line overlap significantly over much of the region observed, so we ran the algorithm on the isolated $F_1F \rightarrow F_1'F' = 01 \rightarrow 12$ component only. This strategy allowed the clear separation of multiple velocity components along the line of sight, but reduced the signal-to-noise ratio of the detections since the isolated component can be substantially fainter (up to a factor of $\sim 2.3$) than the central hyperfine emission. We therefore performed several checks to ensure identified $N_2H^+$ objects were legitimate. We removed any identified clumps with areas less than the Nobeyama beam, clumps with a peak location at the edge of the mapped region, and clumps with reported line widths less than twice the velocity resolution of the observations (0.05 km s$^{-1}$). These limits culled most of the spurious objects, and we finally removed several additional

Table 3.2. $N_2H^+$ 1-0 CLUMPFIND peaks and parameters in Oph B

| ID | RA J2000 | decl. J2000 | FWHM ($x \times y$) (AU) | $T^*_{A,iso}$ (K) | $T^*_{A,main}$ (K) | $S/N_{iso}$ |
|---|---|---|---|---|---|---|
| B1-N1 | 16 27 13.1 | -24 29 40.3 | 4500 × 4300 | 1.45 | 2.58 | 7.3 |
| B1-N2 | 16 27 14.2 | -24 29 15.3 | 5600 × 4400 | 1.53 | 2.72 | 9.4 |
| B1-N3 | 16 27 15.3 | -24 30 20.5 | 4400 × 4800 | 2.28 | 3.01 | 10.9 |
| B1-N4 | 16 27 16.4 | -24 30 30.5 | 5900 × 6600 | 1.53 | 2.63 | 7.2 |
| B12-N1 | 16 27 13.5 | -24 28 10.1 | 6400 × 6000 | 1.17 | 2.00 | 7.3 |
| B12-N2 | 16 27 15.3 | -24 27 50.1 | 6000 × 6000 | 1.36 | 2.23 | 9.4 |
| B12-N3 | 16 27 19.0 | -24 27 20.0 | 5600 × 4900 | 1.05 | 1.85 | 7.0 |
| B2-N1 | 16 27 21.6 | -24 27 45.1 | 4800 × 5300 | 0.99 | 1.86 | 7.3 |
| B2-N2 | 16 27 24.9 | -24 27 15.0 | 4700 × 6000 | 1.75 | 2.61 | 12.6 |
| B2-N3 | 16 27 28.2 | -24 27 40.1 | 5900 × 3800 | 1.33 | 2.60 | 11.6 |
| B2-N4 | 16 27 28.6 | -24 26 40.0 | 6500 × 6200 | 0.95 | 3.07 | 7.1 |
| B2-N5 | 16 27 29.7 | -24 27 05.0 | 4800 × 6000 | 1.84 | 3.46 | 14.5 |
| B2-N6 | 16 27 32.3 | -24 27 00.0 | 4500 × 6900 | 2.42 | 3.43 | 18.5 |
| B2-N7 | 16 27 33.0 | -24 27 40.1 | 4600 × 3500 | 1.22 | 2.45 | 7.6 |
| B2-N8 | 16 27 33.4 | -24 27 45.1 | 4800 × 3500 | 1.53 | 2.36 | 9.6 |
| B2-N9 | 16 27 34.5 | -24 26 04.9 | 7400 × 5100 | 1.11 | 2.48 | 7.6 |
| B3-N1 | 16 27 22.0 | -24 24 54.7 | 10000 × 7900 | 1.26 | 2.27 | 8.8 |

objects through visual inspection.

We found a total of 17 separate $N_2H^+$ clumps in Oph B from the Nobeyama data. Table 3.2 lists the locations and FWHM in AU of the clumps, as well as the peak temperatures ($T^*_A$) of the isolated and main hyperfine $N_2H^+$ components, and the signal-to-noise ratio of the isolated hyperfine component. We plot the positions of the clumps, i.e., the positions of peak brightness temperature of the isolated component, in Figure 3.1a. The centroid velocities and line widths of the $N_2H^+$ clumps are also returned by CLUMPFIND, but we determined these values instead through spectral line fitting (described in further detail in §3, with values listed in Table 3.4). The line fitting algorithm provided more accurate results given the hyperfine structure of the $N_2H^+$ 1-0 line.

We first compared the locations of the $N_2H^+$ clumps with the peak locations of 850 $\mu$m continuum clumps identified by Jørgensen et al. (2008) in the SCUBA

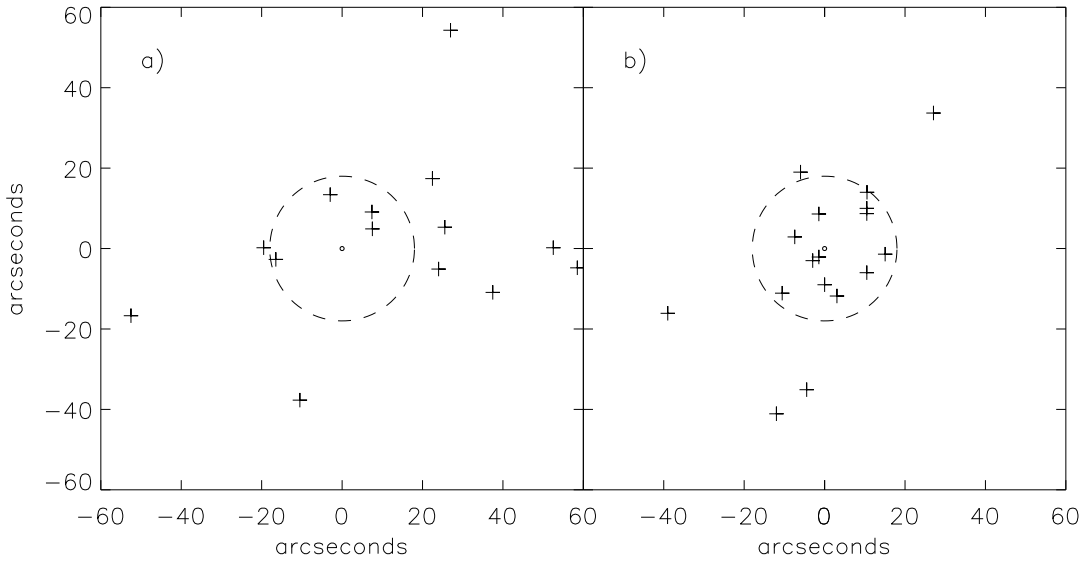


Figure 3.2 a) Minimum angular separation in R.A. and decl. between individual $N_2H^+$ 1-0 clumps identified through CLUMPFIND and 850 $\mu$m continuum clumps identified by Jørgensen et al. (2008). In both plots, the dashed circle has a radius matching the 18″ FWHM of the $N_2H^+$ 1-0 observations. On average, $N_2H^+$ clumps in Oph B show a positional offset from continuum clumps similar to that found for clumps identified in $NH_3$ (1,1) emission in Chapter 2. b) Minimum angular separation in R.A. and decl. between individual $N_2H^+$ 1-0 clumps and $NH_3$ (1,1) clumps identified in Chapter 2. Good correlation is found between $N_2H^+$ and $NH_3$ objects in Oph B.

data. Figure 3.2a shows the angular separation between $N_2H^+$ clumps and the peak location of the nearest 850 $\mu$m continuum clump. Few continuum clumps lie within a radius of 18″ in angular distance from an $N_2H^+$ clump, suggesting that many of the $N_2H^+$ clumps thus identified are not correlated with continuum objects. This result is similar to our findings in Chapter 2, where a similar analysis of $NH_3$ emission in Oph B revealed significant offsets between locations of $NH_3$ clumps and continuum clumps. Interestingly, the mean minimum separation between $N_2H^+$ and continuum clumps in Oph B1 ($\sim 20''$) is half that in Oph B2 ($\sim 40''$), suggesting there is a better correlation between $N_2H^+$ and continuum emission in Oph B1. Furthermore, Figure

3.2b shows the angular separation between $N_2H^+$ clumps and nearest $NH_3$ clumps from Chapter 2, and shows a clear correlation between the two sets of objects. In the majority of cases, $N_2H^+$ and $NH_3$ clumps are coincident within the resolution of the $N_2H^+$ data.

We further compared the locations of the $N_2H^+$ clumps thus determined with $N_2H^+$ clumps identified by André et al. (2007) in $N_2H^+$ 1-0 emission observed with the IRAM 30 m telescope ($\sim 26''$ half power beam width). We find good agreement with the André et al. for most of the clumps despite their use of a spatial filtering scheme rather than the CLUMPFIND algorithm to identify clumps.

### 3.3.2 ATCA Data

In Figures 3.3, 3.4, 3.5 and 3.6 (part a) we show the integrated $N_2H^+$ 1-0 intensity towards four of the five regions observed in Oph B2 with the ATCA. In the fifth, most western region observed (see Figure 3.1a), we found no significant interferometer emission above the rms noise. In all plots, the data were integrated over only those velocity channels containing emission from the hyperfine components. $N_2H^+$, $NH_3$ and continuum clumps mentioned in the text are labelled on the Figures.

Figure 3.3a shows the combined results of three ATCA pointings towards the 850 $\mu$m continuum peak in Oph B2, with the locations of the associated continuum clump B2-MM8 (Motte et al. 1998, also 16273-24271 in Jørgensen et al. 2008), the nearby $N_2H^+$ clump B2-N5 identified in §3.1, and the Class I protostars Elias 32 (Elias 1978, also VSSG17; Vrba et al. 1975) and Elias 33 (also VSSG18) identified (but note Elias 33 is outside the ATCA primary beam). The single dish integrated intensity peak, coincident with B2-N5, is offset to the continuum data (grey contours) and B2-MM8 by $\sim 23''$ (see Figure 3.1b). Two significant integrated intensity peaks are seen in the ATCA data. The first is coincident with B2-N5 (and consequently offset from B2-MM8), while the second is located between the two protostars where little continuum emission is seen. Some emission is also found to the east and west of B2-MM8. Negative emission features are coincident with the continuum clump peak, and additionally between the two strong $N_2H^+$ integrated intensity features. The integrated intensity of the data forms a broken ring-like structure around B2-MM8. The distribution is reminiscent of $N_2H^+$ 1-0 emission in B68, where Bergin

et al. (2002) found strong evidence of $N_2H^+$ depletion through radiative transfer modelling. Evidence for $N_2H^+$ depletion on small scales has also been found in IRAM 04191 (Belloche & André 2004).

In Figure 3.4a, we plot the integrated intensity towards the single pointing in eastern B2, which includes the $N_2H^+$ clump B2-N6 and the $NH_3$ clump B2-A7. Motte et al. (1998) identify a continuum clump here (B2-MM15, unresolved at 11″), but no object was identified by Johnstone et al. (2000b) or Jørgensen et al. (2008) in 850 $\mu$m continuum emission. In the interferometer data, a single integrated intensity peak is seen slightly offset ($\sim 6''$) NNW from B2-N6. The emission is extended along the beam's long axis, but fitting a 2D Gaussian to the data indicate the emission is also unresolved by the $8''\times\ 5''$ FWHM beam ($\sim$ 960 AU $\times$600 AU at 120 pc). The peak integrated intensity brightness of the interferometer data is greater relative to the single dish data in this location by a factor $\sim 2$ compared with the other interferometer observation locations, suggesting that a larger fraction of $N_2H^+$ emission is associated with the small-scale peak rather than the extended $N_2H^+$ emission.

Figure 3.5a shows the results of the south-eastern three pointing mosaic. Strong $NH_3$ emission, including the $NH_3$ clump B2-A9, was found in this region in Chapter 2. The only continuum emission in the mosaiced area is coincident with the Class I protostar Elias 33. Two overlapping $N_2H^+$ clumps identified in §3.1.1 are shown, with clump peaks separated by $\sim 8''$. We find two $N_2H^+$ integrated intensity peaks in the region, separated by $\sim 30''$, of which one is coincident with B2-N8. Two regions of negative integrated intensity are found within the primary beam contours. The most negative feature is coincident with Elias 33, while the second is near B2-N7.

Figure 3.6 shows the combined results of the three-pointing mosaic in north-eastern Oph B2. One $N_2H^+$ clump, B2-N9, is identified in the mosaiced area, which is offset from the continuum clump B2-MM16/16273-24262 by $\sim 30''$. In the interferometer data, no significant emission is associated with either the $N_2H^+$ or continuum clumps. One significant feature is visible in the Figure which is coincident with the western elongation (away from the continuum contours) of the single dish $N_2H^+$ integrated intensity. Multiple negative features are present.

In general, the small scale structure visible in the integrated intensity maps does not correlate well with objects identified in continuum emission, and is also frequently offset from clumps identified on larger scales from the single dish $N_2H^+$ emission. No

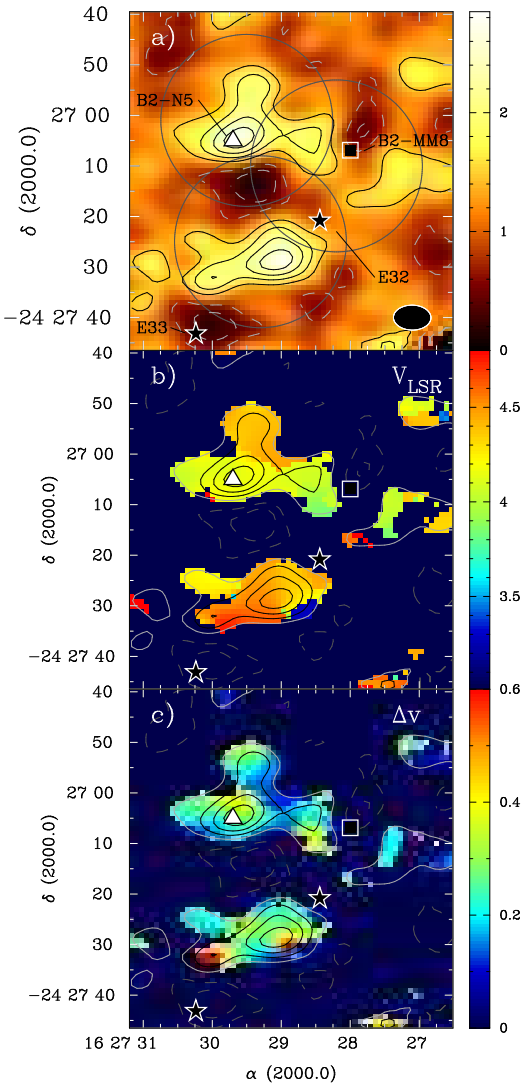


Figure 3.3 a) $N_2H^+$ 1-0 integrated intensity in $\mathrm{K\,km\,s^{-1}}$ ($T_B$) observed at the ATCA. White circles show the primary field of view (34″) of the ATCA at 93 GHz for each of the three pointings included in this mosaic. The $\sim 8'' \times 5''$ FWHM synthesized beam is shown at lower right. In all plots, black contours begin at $0.6\,\mathrm{K\,km\,s^{-1}}$ and increase by $0.6\,\mathrm{K\,km\,s^{-1}}$. Light grey contours show negative integrated intensity at $-0.6\,\mathrm{K\,km\,s^{-1}}$, $-1.2\,\mathrm{K\,km\,s^{-1}}$ and $-1.8\,\mathrm{K\,km\,s^{-1}}$. The $N_2H^+$ clump B2-N5, the continuum clump B2-MM8 (Motte et al. 1998), and two Class I protostars Elias 32 and 33 (Elias 1978) are labelled. b) High resolution $v_{\mathrm{LSR}}$ near B2-MM8. Colour scale is in $\mathrm{km\,s^{-1}}$. c) Fitted $\Delta v$ near MM8. Colour scale is in $\mathrm{km\,s^{-1}}$.

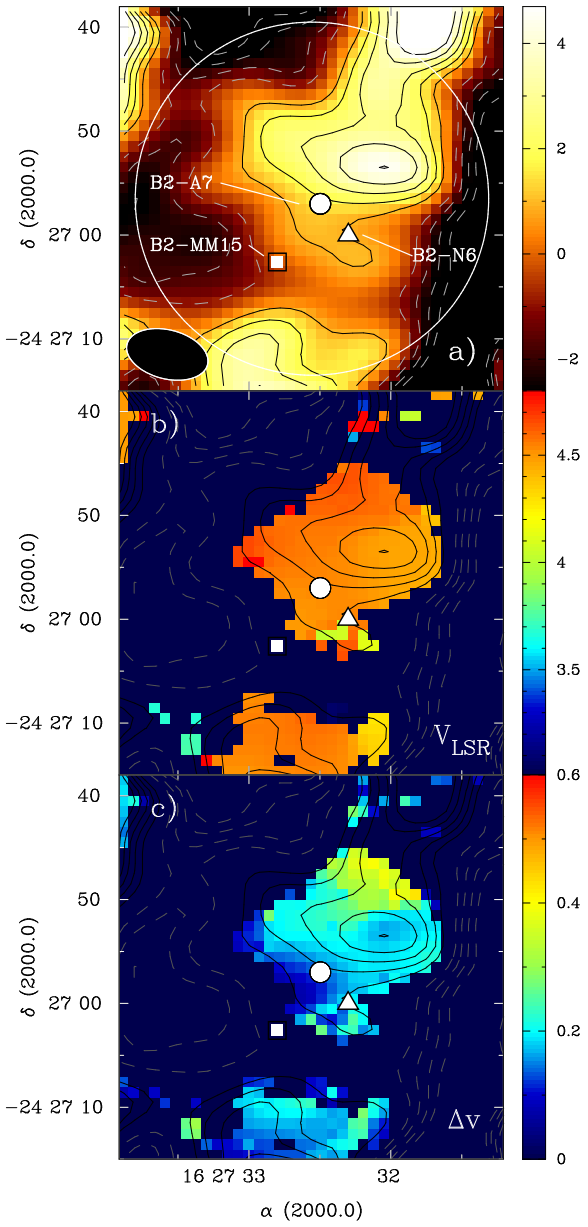


Figure 3.4 a) Single pointing $N_2H^+$ 1-0 integrated intensity in the east Ophiuchus B2 core towards the $NH_3$ (1,1) object B2-A7 identified in Chapter 2. Colour scale in $\mathrm{K\,km\,s^{-1}}$ ($T_B$) observed at the ATCA. In all plots, black contours begin at $0.9\,\mathrm{K\,km\,s^{-1}}$ and increase by $0.9\,\mathrm{K\,km\,s^{-1}}$. Light grey contours show negative integrated intensity at $-0.9\,\mathrm{K\,km\,s^{-1}}$ and $-1.8\,\mathrm{K\,km\,s^{-1}}$. The 34″ diameter white circle shows the primary beam of the ATCA at 93 GHz. The $\sim 8'' \times 5''$ FWHM synthesized beam is shown at lower right. The $N_2H^+$ clump B2-N6, $NH_3$ clump B2-A7 (Chapter 2) and continuum clump B2-MM15 (Motte et al. 1998) are labelled. b) Line velocity or $v_{\rm LSR}$. Colour scale is in $\mathrm{km\,s^{-1}}$. c) Fitted $\Delta v$ at B2-N6. Colour scale is in $\mathrm{km\,s^{-1}}$.

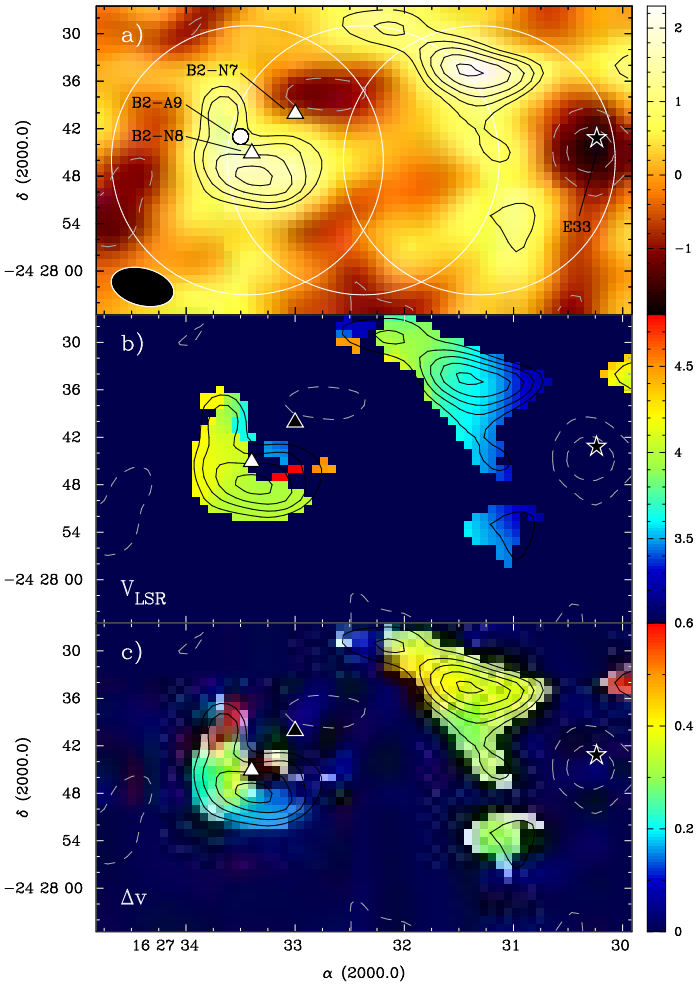


Figure 3.5 a) $N_2H^+$ 1-0 integrated intensity in $\mathrm{K\,km\,s^{-1}}$ ($T_B$) observed at the ATCA in the southeast edge of the Ophiuchus B2 core. White circles show the primary field of view (34″) of the ATCA at 93 GHz for each of the three pointings included in this mosaic. The $\sim 8'' \times 5''$ FWHM synthesized beam is shown at lower right. In all plots, black contours begin at $0.9\,\mathrm{K\,km\,s^{-1}}$ and increase by $0.3\,\mathrm{K\,km\,s^{-1}}$. Light grey contours show negative integrated intensity at $-0.9\,\mathrm{K\,km\,s^{-1}}$ and $-1.5\,\mathrm{K\,km\,s^{-1}}$. The $N_2H^+$ clumps B2-N7 and B2-N8, $NH_3$ clump B2-A9 (Chapter 2) and Class I protostar Elias 33 (Elias 1978) are labelled. b) High resolution $v_{\mathrm{LSR}}$ in south-eastern Oph B2. Colour scale is in $\mathrm{km\,s^{-1}}$. c) Fitted $\Delta v$ in $\mathrm{km\,s^{-1}}$.

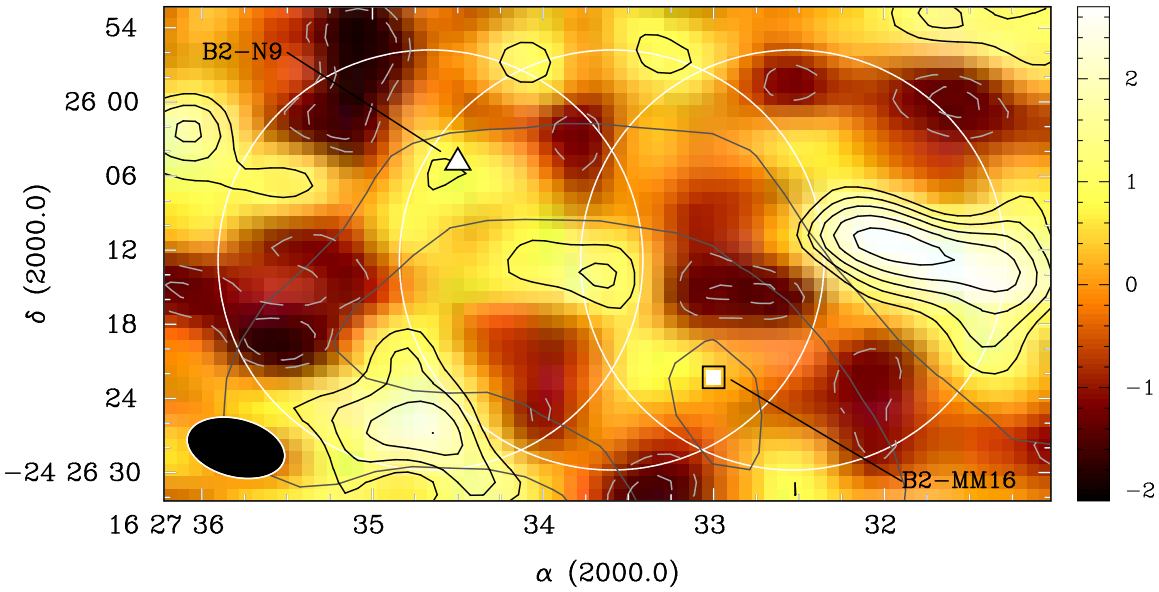


Figure 3.6 $N_2H^+$ 1-0 integrated intensity in $\mathrm{K\,km\,s^{-1}}$ ($T_B$) observed at the ATCA. Black contours begin at $1\,\mathrm{K\,km\,s^{-1}}$ and increase by $0.5\,\mathrm{K\,km\,s^{-1}}$. Light grey contours show negative integrated intensity at $-1\,\mathrm{K\,km\,s^{-1}}$ and $-1.5\,\mathrm{K\,km\,s^{-1}}$. White circles show the primary field of view (34″) of the ATCA at 93 GHz for each of the three pointings included in this mosaic. Dark grey contours show 850 $\mu$m continuum emission, beginning at $0.3\,\mathrm{Jy\,beam^{-1}}$ and increasing by $0.1\,\mathrm{Jy\,beam^{-1}\,km\,s^{-1}}$. The $N_2H^+$ clump B2-N9 and continuum clump B2-MM16/162733-24262 (Motte et al. 1998; Jørgensen et al. 2008) are labelled. The $\sim 8'' \times 5''$ FWHM synthesized beam is shown at lower right.

small-scale emission was found associated with embedded protostars.

## 3.4 $N_2H^+$ Line Analysis

The $N_2H^+$ 1-0 rotational transition has seven hyperfine components (Caselli et al. 1995). We fit each observed $N_2H^+$ 1-0 spectrum with a custom Gaussian hyperfine structure fitting routine written in IDL, described in detail in Chapter 2, assuming local thermodynamic equilibrium (LTE) and equal excitation temperatures $T_{ex}$ for each hyperfine component. The expected emission frequencies and emitted line fractions for the hyperfine components were taken from Pagani et al. (2009). We fit the spectrum at each pixel and obtain maps of the line-of-sight local standard of rest (LSR) velocity ($v_{\mathrm{LSR}}$) of the emission, the line width FWHM ($\Delta v$), the total line opacity ($\tau$),

and the line brightness ($T_{MB}$). We additionally calculate $T_{ex}$ assuming the line emission fills the beam (the determined $T_{ex}$ will be a lower limit if the observed emission does not entirely fill the beam).

The line widths determined by the hyperfine structure fitting routine are artificially broadened by the velocity resolution of the observations ($0.05\,\mathrm{km\,s^{-1}}$). We therefore subtracted in quadrature the resolution width, $\Delta v_{res}$, from the observed line width, $\Delta v_{obs}$, such that $\Delta v_{line} = \sqrt{\Delta v_{obs}^2 - \Delta v_{res}^2}$. In the following, we simply use $\Delta v = \Delta v_{line}$ for clarity.

The uncertainties reported in the returned parameters are those determined by the fitting routine, and do not take the calibration uncertainty ($\sim 8 - 10\,\%$ for the Nobeyama data) into account. The calibration uncertainty does not affect the uncertainties returned for $v_{\rm LSR}$ or $\Delta v$. The excitation temperature, $N_2H^+$ column densities, fractional $N_2H^+$ abundances and volume densities discussed further below, however, are dependent on the amplitude of the line emission, and are thus affected by the absolute calibration uncertainty.

Over most of the map, the spectra could be fit with a single set of hyperfine components, but several small regions showed clear double-peaked line profiles in the isolated $N_2H^+$ 1-0 hyperfine component, including the $N_2H^+$ clumps B1-N1, B1-N3 and B1-N4. To understand better this emission, we fit the spectra with the above Gaussian hyperfine structure fitting routine using two separate velocity components. We show the spectra at the three $N_2H^+$ clump peak locations in Figure 3.7, overlaid with both single and double velocity component fits. In all cases, we are able to determine well the $v_{\rm LSR}$ and $\Delta v$ of both components, but the fainter component is typically very optically thin and we are unable to constrain simultaneously both $\tau$ and $T_{ex}$. Although the angular separation of B2-N7 and B2-N8 clumps is small, visual inspection of the spectra at the clump peaks did not show a separate velocity component above the rms noise. We discuss the nature of the double-peaked objects further in §3.5.3. In the following sections, we discuss the results of the single velocity component fits only, unless otherwise stated.

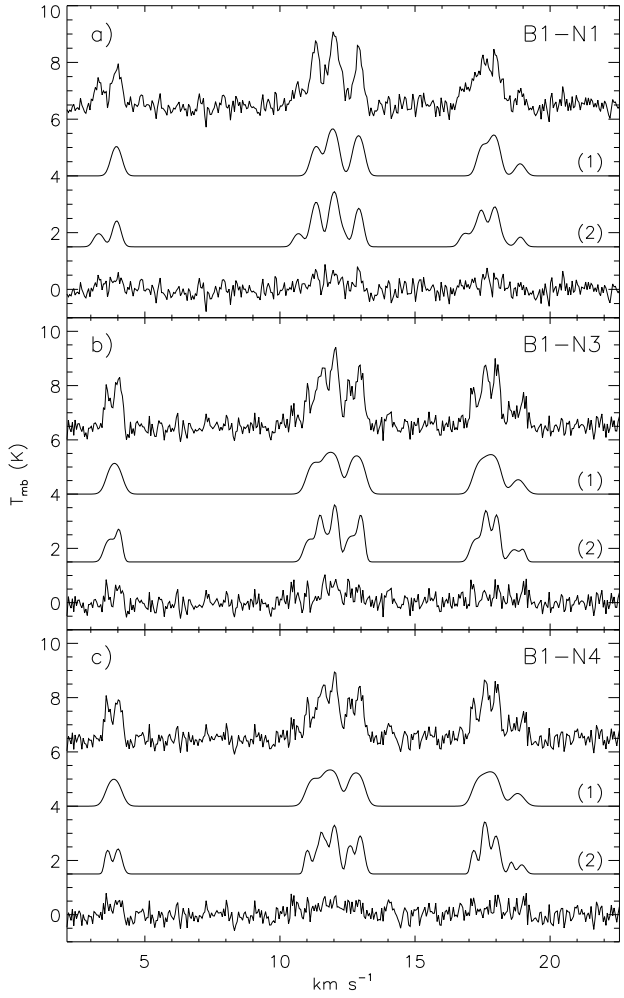


Figure 3.7 Nobeyama $N_2H^+$ 1-0 spectra in $T_{MB}$ (K) towards the B1-N1 (a), B1-N3 (b) and B1-N4 (c) $N_2H^+$ clump locations, showing results of single and double velocity component HFS fits. For each clump, the best single velocity component (1) and double velocity component (2) fits are shown below the $N_2H^+$ 1-0 spectrum, as well as the residual from subtracting the double component fit from the spectrum. For each clump, the spectra and both fits are offset from zero for clarity.

### 3.4.1 Single Dish Results

Table 3.3 lists the mean, rms, minimum and maximum values of $v_{\rm LSR}$, $\Delta v$, $\tau$ and $T_{ex}$ found in Oph B. The results across Oph B are shown in Figure 3.8, where we plot only data points with $S/N \geqq 2.5$ in the isolated $F_1F \rightarrow F_1'F' = 01 \rightarrow 12$ component of the $N_2H^+$ 1-0 line. In the following sections, we describe in detail the results of the line fitting and examine the resulting line centres and widths, as well as $T_{ex}$ and $\tau$. Table 3.4 lists the determined parameters at the peak location of each $N_2H^+$ clump, and Table 3.5 lists the determined parameters at the peak location of 850 $\mu$m continuum clumps in Oph B (Jørgensen et al. 2008) and Class I protostars (Enoch et al. 2009).

#### Line Centroids and Widths

We show in Figures 3.8a and 3.8b, respectively, the fitted values of $v_{\rm LSR}$ and $\Delta v$ of $N_2H^+$ 1-0 across Oph B. Relatively little variation in line-of-sight velocity is seen across Oph B1 and B2, with no evidence of a discontinuity in velocity separating the two sub-Cores. A gradient of increasing $v_{\rm LSR}$ from west to east is seen across Oph B, with the largest $v_{\rm LSR}$ values are found in the eastern half of B2, to a maximum $v_{\rm LSR} = 4.44\,{\rm km\,s^{-1}}$. In Oph B3, the mean $v_{\rm LSR} = 3.06\,{\rm km\,s^{-1}}$, significantly lower than in B1 ($\langle v_{\rm LSR} \rangle = 3.97\,{\rm km\,s^{-1}}$) or B2 ($\langle v_{\rm LSR} \rangle = 4.05\,{\rm km\,s^{-1}}$). The rms variation in $v_{\rm LSR}$ across all Oph B is only $0.23\,{\rm km\,s^{-1}}$, which is dominated by the spread in $v_{\rm LSR}$ in B2 (rms = $0.20\,{\rm km\,s^{-1}}$, compared with $0.12\,{\rm km\,s^{-1}}$ and $0.14\,{\rm km\,s^{-1}}$ in B1 and B3, respectively).

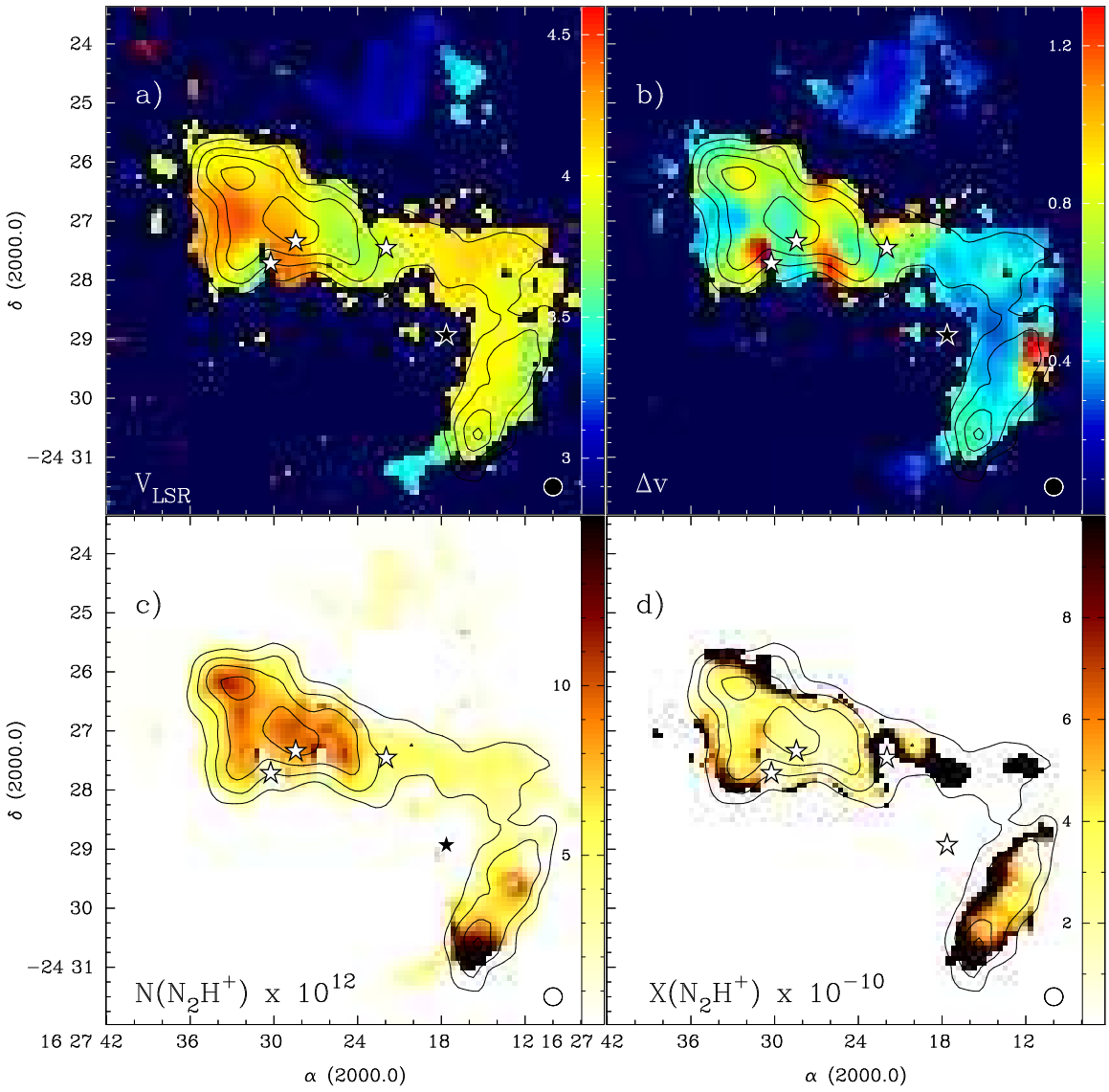


Figure 3.8 a) Line velocity or $v_{\rm LSR}$ in Oph B. Colour scale is in $\mathrm{km\,s^{-1}}$. In all plots, contours show integrated $N_2H^+$ 1-0 intensity, beginning at $3.0\,\mathrm{K\,km\,s^{-1}}$ and increasing by $1.5\,\mathrm{K\,km\,s^{-1}}$. Only pixels where the isolated $N_2H^+$ component was detected with $S/N \geqq 2.5$ are shown. Stars indicate protostar positions. The 18″ FWHM beam is shown at lower right. b) Fitted $\Delta v$ in Oph B. Colour scale is in $\mathrm{km\,s^{-1}}$. c) $N_2H^+$ column density $N(N_2H^+)$ ($\mathrm{cm^{-2}}$) determined using Equation 3.3. Values shown have been divided by $10^{12}$. The maximum column in Oph B1 is $N(N_2H^+) = 3.3 \times 10^{12}\,\mathrm{cm^{-2}}$, but the scale has been truncated to show variations in Oph B2. d) Fractional abundance $X(N_2H^+) = N(N_2H^+)\,/\,N(H_2)$, where $N(H_2)$ was calculated following the discussion in §4.2. Only pixels where the 850 $\mu$m continuum flux density $S_\nu \geqq 0.1\,\mathrm{Jy\,beam^{-1}}$ are shown. The maximum fractional abundance, $X(N_2H^+) = N(N_2H^+)\,/\,N(H_2) = 4.9 \times 10^{-9}$, and is found towards the B1 edge, but the scale has been truncated to show variations in B1 and B2.

Table 3.3. $N_2H^+$ 1-0 Line Characteristics in Oph B1, B2 and B3

| Core | Value | Mean | rms | Min | Max |
|---|---|---|---|---|---|
| Oph B1 | $v_{\rm LSR}$ ($\rm km\,s^{-1}$) | 3.96 | 0.15 | 3.43 | 4.13 |
| | $\Delta v$ ($\rm km\,s^{-1}$) | 0.42 | 0.08 | 0.21 | 0.66 |
| | $\tau$ | 3.1 | 2.6 | 0.2 | 13 |
| | $T_{ex}$ (K) | 6.2 | 2.0 | 2.1 | 12.1 |
| Oph B2 | $v_{\rm LSR}$ ($\rm km\,s^{-1}$) | 4.05 | 0.20 | 3.60 | 4.44 |
| | $\Delta v$ ($\rm km\,s^{-1}$) | 0.68 | 0.21 | 0.30 | 1.30 |
| | $\tau$ | 2.0 | 1.1 | 0.2 | 5.3 |
| | $T_{ex}$ (K) | 7.2 | 2.8 | 1.9 | 17.8 |
| Oph B3 | $v_{\rm LSR}$ ($\rm km\,s^{-1}$) | 3.06 | 0.14 | 2.93 | 3.44 |
| | $\Delta v$ ($\rm km\,s^{-1}$) | 0.27 | 0.04 | 0.20 | 0.35 |
| | $\tau$ | 2.3 | 2.2 | 0.2 | 7.6 |
| | $T_{ex}$ (K) | 4.5 | 2.8 | 1.2 | 11.7 |

Table 3.4. Derived Parameters at $N_2H^+$ 1-0 Peak Locations

| ID | $v_{\rm LSR}$ $\rm km\,s^{-1}$ | $\Delta v$ $\rm km\,s^{-1}$ | $\tau$ | $T_{ex}$ K | $\sigma_{\rm NT}$ / $c_s$ | $N(N_2H^+)$ $10^{12}\,\rm cm^{-2}$ | $N(H_2)$ $10^{22}\,\rm cm^{-2}$ | $X(N_2H^+)$ $10^{-10}$ | $n_{ex}$ $10^5\,\rm cm^{-3}$ |
|---|---|---|---|---|---|---|---|---|---|
| B1-N1 | 3.95 (1) | 0.42(2) | 6(2) | 5.1(1) | 0.71(4) | 8(2) | 1.6(3) | 5(1) | 0.8(1) |
| (1) | 3.96(1) | 0.35(2) | 0.1(1) | 6.8(1) | 0.60 | ··· | ··· | ··· | ··· |
| (2) | 3.29(5) | 0.4(1) | 1(1) | 3.9(1) | 0.65 | ··· | ··· | ··· | ··· |
| B1-N2 | 3.99(1) | 0.35(1) | 3(1) | 6.4(1) | 0.58(2) | 5(2) | ··· | ··· | 1.7(2) |
| B1-N3 | 3.97(1) | 0.50(2) | 5(1) | 5.7(1) | 0.90(3) | 10(2) | 1.6(3) | 6(1) | 1.2(1) |
| (1) | 4.01(1) | 0.35(1) | 5.4(3) | 6.9(1) | 0.58(1) | 8.4(5) | 1.6(3) | 5(1) | 2.1(1) |
| (2) | 3.58(1) | 0.2(2) | ··· | ··· | ··· | ··· | ··· | ··· | ··· |
| B1-N4 | 3.88(1) | 0.53(3) | 9(2) | 4.5(1) | 1.00(5) | 12(3) | 0.8(2) | 17(3) | 0.6(1) |
| (1) | 4.01(1) | 0.32(1) | 3.5(2) | 6.9(1) | 0.53(1) | 5.0(3) | 0.8(2) | 7(1) | 2.1(1) |
| (2) | 3.62(1) | 0.19(8) | ··· | ··· | ··· | ··· | ··· | ··· | ··· |
| B12-N1 | 3.92(1) | 0.40(2) | 2(1) | 7.1(1) | 0.67(4) | 3(3) | ··· | ··· | 2.4(2) |
| B12-N2 | 4.10(1) | 0.40(2) | 2(1) | 7.0(1) | 0.67(3) | 4(3) | ··· | ··· | 2.2(2) |
| B12-N3 | 4.03(1) | 0.55(2) | 3(1) | 5.5(1) | 0.96(4) | 5(2) | 0.6(1) | 9(2) | 1.2(1) |
| B2-N1 | 3.83(1) | 0.55(3) | 0.4(6) | 14.1(1) | 1.02(5) | 4(11) | ··· | ··· | ··· |
| B2-N2 | 3.73(1) | 0.54(1) | 4.8(7) | 5.6(1) | 1.00(3) | 10(2) | 4.0(8) | 2.5(5) | 1.2(1) |
| B2-N3 | 4.32(1) | 0.47(1) | 1.4(8) | 9.0(1) | 0.74(*) | 5(3) | 2.1(4) | 2.6(5) | 3.7(*) |
| B2-N4 | 4.11(1) | 0.58(2) | 2.7(6) | 7.0(1) | 1.05(3) | 8(2) | 3.1(6) | 2.6(5) | 2.2(2) |

Table 3.4 (cont'd)

| ID | $v_{\rm LSR}$ $\rm km\,s^{-1}$ | $\Delta v$ $\rm km\,s^{-1}$ | $\tau$ | $T_{ex}$ K | $\sigma_{\rm NT}$ / $c_s$ | $N(\rm N_2H^+)$ $10^{12}\,\rm cm^{-2}$ | $N(\rm H_2)$ $10^{22}\,\rm cm^{-2}$ | $X(\rm N_2H^+)$ $10^{-10}$ | $n_{ex}$ $10^5\,\rm cm^{-3}$ |
|---|---|---|---|---|---|---|---|---|---|
| B2-N5 | 4.25(1) | 0.50(1) | 3.1(6) | 7.5(1) | 0.89(2) | 9(2) | 3.7(7) | 2.5(5) | 2.7(2) |
| B2-N6 | 4.44(1) | 0.39(1) | 5.2(6) | 6.4(1) | 0.68(1) | 9(1) | 2.7(5) | 3.4(7) | 1.6(1) |
| B2-N7 | 4.10(1) | 0.70(2) | 1.6(7) | 7.7(1) | 1.34(5) | 7(3) | 1.3(3) | 6(1) | 3.4(4) |
| B2-N8 | 4.09(1) | 0.65(2) | 1.6(7) | 7.7(1) | 1.16(4) | 6(3) | 0.8(2) | 9(2) | 2.8(3) |
| B2-N9 | 4.03(1) | 0.61(2) | 2.9(8) | 6.3(1) | 1.13(4) | 8(2) | 2.9(6) | 2.9(6) | 1.7(1) |
| B3-N1 | 2.99(1) | 0.21(1) | 3(1) | 6.3(1) | 0.20(2) | 2(1) | ··· | ··· | 1(2) |

Note. — Uncertainties are given in brackets beside values and show the uncertainty in the last digit of the value. The $N(\rm H_2)$ and $X(\rm N_2H^+)$ uncertainties include the $\sim 20\%$ uncertainty in the submillimeter continuum flux values only; uncertainties in $T_d$ and $\kappa_\nu$ are not taken into account.

Table 3.5. Derived Parameters for 850 $\mu$m clumps and Class I protostars

| ID | $v_{\rm LSR}$ $\rm km\,s^{-1}$ | $\Delta v$ $\rm km\,s^{-1}$ | $\tau$ | $T_{ex}$ K | $\sigma_{\rm NT}$ / $c_s$ | $N(\rm N_2H^+)$ $10^{12}\,\rm cm^{-2}$ | $N(\rm H_2)$ $10^{22}\,\rm cm^{-2}$ | $X(\rm N_2H^+)$ $10^{-10}$ | $n_{ex}$ $10^5\,\rm cm^{-3}$ |
|---|---|---|---|---|---|---|---|---|---|
| 850 $\mu$m | | | | | | | | | |
| 162712-24290 | 3.66(1) | 1.36(1) | ··· | ··· | 2.52(1) | ··· | ··· | ··· | ··· |
| 162713-24295 | 3.86(1) | 0.52(2) | 4(1) | 5.6(1) | 0.90(5) | 8(3) | 2.1(4) | 3.7(7) | 1.1(1) |
| 162715-24303 | 3.93(1) | 0.50(2) | 6(1) | 5.5(1) | 0.92(4) | 10(2) | 2.0(4) | 5(1) | 1.1(1) |
| 162725-24273 | 3.72(1) | 0.61(2) | 4.7(8) | 5.3(1) | 1.16(4) | 10(2) | 4.1(8) | 2.4(5) | 1.0(1) |
| 162728-24271 | 4.18(1) | 0.61(2) | 2.4(6) | 7.9(1) | 1.15(3) | 9(2) | 6(1) | 1.6(3) | 3.4(4) |
| 162729-24274 | 4.36(1) | 0.55(1) | ··· | ··· | 0.94(*) | ··· | ··· | ··· | ··· |
| 162730-24264 | 4.16(1) | 0.57(2) | 1.6(7) | 9.6(1) | 0.94(*) | 8(3) | 2.6(5) | 3.2(6) | ··· |
| 162733-24262 | 4.23(1) | 0.73(2) | 2.8(7) | 6.3(1) | 1.35(4) | 10(2) | 4.2(8) | 2.3(5) | 1.7(1) |
| Class I | | | | | | | | | |
| Oph-emb 5 | 3.82(1) | 0.58(3) | 1(1) | 8.3(1) | 1.07(5) | 4(5) | ··· | ··· | 3.9(5) |
| Oph-emb 11 | ··· | ··· | ··· | ··· | ··· | ··· | ··· | ··· | ··· |
| Oph-emb 19 | 4.31(1) | 0.52(1) | 1.9(7) | 8.4(1) | 0.87(*) | 7(3) | 2.3(5) | 3.1(6) | 3.3(*) |
| Oph-em 26 | 3.87(1) | 1.56(1) | ··· | ··· | 2.96(1) | ··· | 2.3(5) | ··· | ··· |

Note. — 850 $\mu$m continuum clump locations taken from Jørgensen et al. (2008). Class I protostar locations taken from Enoch et al. (2009). Uncertainties are given in brackets beside values and show the uncertainty in the last digit of the value. The $N(\rm H_2)$ and $X(\rm N_2H^+)$ uncertainties include the $\sim$ 20% uncertainty in the submillimeter continuum flux values only; uncertainties in $T_d$ and $\kappa_\nu$ are not taken into account. A (*) indicates that the uncertainty in the value at this position were large, even though in most cases the values themselves are reasonable.

We find greater variation between Oph B1 and B2 in $N_2H^+$ 1-0 line width than in $v_{\rm LSR}$. Oph B1 is generally characterized by narrow lines, with a mean $\Delta v = 0.42\,{\rm km\,s^{-1}}$ and an rms variation $\sigma_{\Delta v}$ of only $0.08\,{\rm km\,s^{-1}}$. Oph B2 contains regions of both small and large line widths, with a larger mean $\Delta v = 0.68\,{\rm km\,s^{-1}}$ and $\sigma_{\Delta v} = 0.21\,{\rm km\,s^{-1}}$ than found in B1. Both B1 and B2 have similar minimum line widths ($\Delta v = 0.21\,{\rm km\,s^{-1}}$ in B1 and $\Delta v = 0.30\,{\rm km\,s^{-1}}$ in B2). Line widths in Oph B3 are extremely narrow, with a mean $\Delta v = 0.27\,{\rm km\,s^{-1}}$, a minimum $\Delta v = 0.21\,{\rm km\,s^{-1}}$ and an rms variation of only $0.04\,{\rm km\,s^{-1}}$.

Two locations in B2, both near Class I protostars, show intriguing gradients in line-of-sight velocity and line width, which we show more closely in Figure 3.9. Figure 3.9a shows teh first, at a location coincident with the millimeter continuum object B2-MM8, which is found at the thermal dust emission peak in B2 and is the most massive clump identified in Oph B ($M \sim 1\,M_\odot$, Motte et al.; Johnstone et al. 2000b). Interestingly, MM8 is associated with neither an $N_2H^+$ clump nor a maximum of integrated $N_2H^+$ 1-0 intensity. The nearest $N_2H^+$ clump to MM8, B2-N5, is offset $\sim 30''$ to the east. The nearby Class I protostar, Elias 32, may be associated with MM8, but is also offset from the clump peak by $\sim 15''$ to the southeast. Across the $\sim 30''$ width of the clump ($\sim 3600\,{\rm AU}$ at 120 pc), $v_{\rm LSR}$ varies from $\sim 3.8\,{\rm km\,s^{-1}}$ in the west to $\sim 4.2\,{\rm km\,s^{-1}}$ in the east. We find no local decrease in line width as might be expected for a starless clump (Di Francesco et al. 2004). Instead, Figure 3.9b shows how at this location $\Delta v$ increases from east to west, from $\Delta v \sim 0.5\,{\rm km\,s^{-1}}$ to $\Delta v \sim 0.9\,{\rm km\,s^{-1}}$. The resulting velocity gradient, given the $\sim 3600\,{\rm AU}$ diameter of the clump, is $\sim 23\,{\rm km\,s^{-1}\,pc^{-1}}$. The variation in line width in particular appears centered on the nearby protostar. Alternatively, we noted in Chapter 2 a region of wide $NH_3$ line width located between Oph B2 and B3, which we suggested was due to the overlap of the two Cores with different $v_{\rm LSR}$ along the line of sight. In this case, the wide line widths seen near MM8 also may be due to this overlap.

Figures 3.9c and 3.9d plot $v_{\rm LSR}$ and $\Delta v$ at the second intriguing gradient, near the Class I protostar Elias 33 in Oph B2. Elias 33 is associated with the millimeter object B2-MM10 (Motte et al. 1998, also 162729-24274 in Jørgensen et al. 2008). Again, no $N_2H^+$ clump was found coincident with the protostar. Both $v_{\rm LSR}$ and $\Delta v$ show strong variations at the protostellar location. An abrupt change in $v_{\rm LSR}$ from $\sim 4.1\,{\rm km\,s^{-1}}$ to $\sim 3.7\,{\rm km\,s^{-1}}$ is seen in over a single $18''$ beam width ($\sim 2200\,{\rm AU}$) from west to east. The resulting velocity gradient is $\sim 38\,{\rm km\,s^{-1}\,pc^{-1}}$. A narrow ridge of large

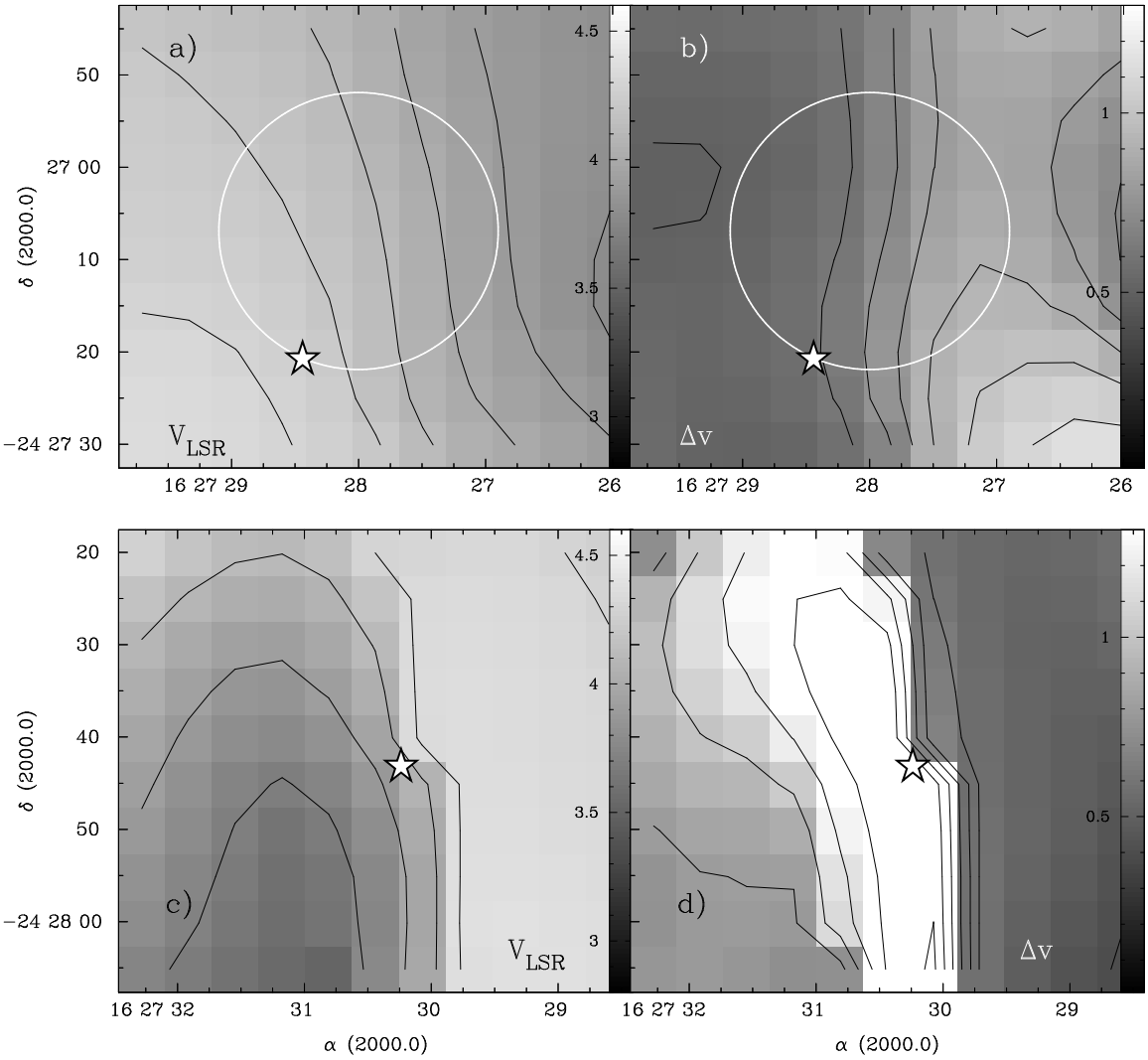


Figure 3.9 a) Line velocity $v_{\rm LSR}$ (km s$^{-1}$) across the continuum object B2-MM8. Contours begin at 3.8 km s$^{-1}$ and increase by 0.1 km s$^{-1}$. The Class I protostar Elias 32 is shown. The diameter of MM8 is $\sim 30''$, shown by the white circle. b) Line FWHM $\Delta v$ (km s$^{-1}$) across MM8. Contours begin at 0.5 km s$^{-1}$ and increase by 0.1 km s$^{-1}$. c) Line velocity $v_{\rm LSR}$ (km s$^{-1}$) across the south-eastern edge of Oph B2, near the Class I protostar Elias 33(shown). Contours begin at 3.5 km s$^{-1}$ and increase by 0.2 km s$^{-1}$. d) Line FWHM $\Delta v$ (km s$^{-1}$) across the south-eastern edge of B2. Contours begin at 0.4 km s$^{-1}$ and increase by 0.2 km s$^{-1}$.

line width, $\Delta v \gtrsim 1.0\,\mathrm{km\,s^{-1}}$, is found with an elongation perpendicular to the $v_{\rm LSR}$ gradient. On either side, line widths are narrow ($\Delta v \lesssim 0.6\,\mathrm{km\,s^{-1}}$).

### $N_2H^+$ Density, Column Density and Fractional Abundance

Given the $N_2H^+$ 1-0 line characteristics $\Delta v$, $\tau_{tot}$ and $T_{ex}$ determined through HFS fitting, and again assuming LTE, we can calculate the volume density, $n_{ex}$, and the $N_2H^+$ column density, $N(N_2H^+)$, in Oph B.

The volume density is calculated following Caselli et al. (2002a) using two-level statistical equilibrium:

$$\frac{n_{ex}}{n'_{cr}} = \frac{T_{ex} - T_{bg}}{(h\nu/k)(1 - T_{ex}/T_k)} \tag{3.1}$$

where the critical density, corrected for trapping, of the $N_2H^+$ 1-0 line is given by:

$$n'_{cr} = n_{cr}\frac{1 - \exp(-\tau_{hf})}{\tau_{hf}}. \tag{3.2}$$

The opacity $\tau_{hf}$ is the opacity of a typical hyperfine component. For $N_2H^+$ 1-0, we take $\tau_{hf} = \tau/9$. We assume that the $N_2H^+$ kinetic temperature is equal to the $T_K$ derived in Chapter 2 from $NH_3$ observations. This assumption introduces some uncertainty in the resulting $n_{ex}$ on the order of $\sim 10 - 50\,\%$ if a difference in $T_K$ exists of $\sim 2 - 5\,\mathrm{K}$ between gas traced by $NH_3$ and $N_2H^+$ emission (a temperature difference $> 5\,\mathrm{K}$ is unlikely given the mean $T_K = 15\,\mathrm{K}$ for Oph B determined in Chapter 2 and the factor $\sim 10$ difference in the expected gas densities traced by $NH_3$ and $N_2H^+$). Mean, standard deviation, minimum and maximum densities for Oph B1, B2 and B3 are given in Table 3.6. For Oph B as a whole, $\langle n_{ex} \rangle = 2.4 \times 10^5\,\mathrm{cm^{-3}}$, with an rms variation of $2.5 \times 10^5\,\mathrm{cm^{-3}}$. Separately, the mean $n_{ex}$ for Oph B1 and B2 ($2.0 \times 10^5\,\mathrm{cm^{-3}}$ and $3.1 \times 10^5\,\mathrm{cm^{-3}}$, respectively) are lower by factors of $\sim 2$ and $\sim 3.5$ than the mean volume densities calculated by Motte et al. (1998) from 1.3 mm continuum observations. We find only moderate variation in $n_{ex}$ across the Core, and consequently the densities determined for the $N_2H^+$ clumps are similar to the mean Core values. This result is discrepant with the $n(H_2) \sim 10^7\,\mathrm{cm^{-3}}$ densities for

the small-scale continuum objects in Oph B, determined by Motte et al., but agrees within a factor of $\sim 2$ with the average $850\,\mu$m clump densities (which we calculated from reported clump masses and radii) from Jørgensen et al. (2008).

We follow Di Francesco et al. (2004) and derive the total $N_2H^+$ column density $N(N_2H^+)$ using

$$N_{tot} = \frac{3h}{8\pi^3}\frac{1}{\mu^2}\frac{\sqrt{\pi}}{2\sqrt{\ln 2}}\frac{1}{(J+1)\exp(-E_J/kT_{ex})}\left(\frac{kT_{ex}}{hB}+\frac{1}{3}\right)\frac{\Delta v\tau}{1-\exp(-h\nu/kT_{ex})} \quad (3.3)$$

where the lower rotational level number $J = 0$, the dipole moment of the $N_2H^+$ molecular ion $\mu_e = 3.4\,$D (Green et al. 1974), the $N_2H^+$ rotational constant $B = 46.586702\,$GHz (Caselli et al. 1995) and the rotational level energy above ground of the lower level $E_J = J(J+1)hB$. Here, the rotational partition function $Q_{rot}$ has been approximated by its integral form for a linear molecular ion, $Q_{rot} = kT_{ex}/hB + 1/3$. Note that this calculation is equivalent to that presented by Caselli et al. (2002c). Figure 3.8c shows the $N(N_2H^+)$ distribution in Oph B.

We also calculate the $H_2$ column density, $N(H_2)$, per pixel in Oph B from $850\,\mu$m continuum data using

$$N(H_2) = S_\nu/[\Omega_m \mu m_H \kappa_\nu B_\nu(T_d)], \quad (3.4)$$

where $S_\nu$ is the $850\,\mu$m flux density, $\Omega_m$ is the main-beam solid angle, $\mu = 2.33$ is the mean molecular weight, $m_H$ is the mass of hydrogen, $\kappa_\nu$ is the dust opacity per unit mass at $850\,\mu$m, and $B_\nu(T_d)$ is the Planck function at the dust temperature, $T_d$. As in Chapter 2, we take $\kappa_\nu = 0.018\,\mathrm{cm^2\,g^{-1}}$, following Shirley et al. (2000), using the OH5 dust model from Ossenkopf & Henning (1994) which describes grains that have coagulated for $10^5$ years at a density of $10^6\,\mathrm{cm^{-3}}$ with accreted ice mantles, and incorporates a gas-to-dust mass ratio of 100. The $15''$ resolution continuum data were convolved to a final angular resolution of $18''$ and regridded to match the Nobeyama $N_2H^+$ data.

We assume that the dust temperature $T_d$ per pixel is equal to the kinetic temperature $T_K$ determined in Chapter 2 for $NH_3$ in Oph B, where we found $\langle T_K \rangle = 15.1\,$K.

This assumption is expected to be good at the densities probed by the $NH_3$ data ($n \gtrsim 10^4 \mathrm{cm}^{-3}$), when thermal coupling between the gas and dust by collisions is expected to begin (Goldsmith & Langer 1978). Our analysis in Chapter 2, however, suggested that $NH_3$ observations may not trace the densest gas in Oph B. As we expect the denser gas to be colder in the absence of a heating source, this assumption may systematically overestimate $T_d$ in the Core. The derived $N(H_2)$ values would then be systematically low. There is additionally a $\sim 20\%$ uncertainty in the continuum flux values, and estimates of $\kappa_\nu$ can vary by $\sim 3$ (Shirley et al. 2000). Our derived $H_2$ column densities consequently have uncertainties of factors of a few.

Due to the chopping technique used in the submillimeter observations to remove the bright submillimeter sky, any large scale cloud emission is necessarily removed. As a result, the image reconstruction technique produces negative features around strong emission sources, such as Oph B (Johnstone et al. 2000a). Emission on scales greater than $130''$ are suppressed by convolving the original continuum map with a $\sigma = 130''$ continuum beam, and subtracting the convolved map from the original data. While the flux density measurements of bright sources are likely accurate, the column densities measured at core edges may be underestimates. Following Chapter 2, we thus limit our analysis to pixels where $S_\nu \geq 0.1\,\mathrm{Jy\,beam}^{-1}$, though the rms noise level of the continuum map is $\sim 0.03\,\mathrm{Jy\,beam}^{-1}$. For a dust temperature $T_d = 15\,\mathrm{K}$, this flux level corresponds to $N(H_2) \sim 6 \times 10^{21}\,\mathrm{cm}^{-2}$.

Using $N(H_2)$ and $N(N_2H^+)$, we next calculate per pixel the fractional abundance of $N_2H^+$ relative to $H_2$, $X(N_2H^+)$, in Oph B. In Figure 3.8d, we show the distribution of $X(N_2H^+)$ in Oph B. The mean, rms, minimum and maximum values of the derived $N_2H^+$ column density and fractional abundance are given in Table 3.6, while specific values for individual $N_2H^+$ clumps are given in Table 3.4. The $N(H_2)$ and consequently the $X(N_2H^+)$ uncertainties given in Table 3.4 include the $\sim 20\%$ uncertainty in the submillimeter continuum flux values only; uncertainties in $T_d$ and $\kappa_\nu$ are not taken into account.

The mean $N_2H^+$ column density $N(N_2H^+) = 5.5 \times 10^{12}\,\mathrm{cm}^{-2}$ in Oph B. Only small differences are found between Oph B1 and B2, while in B3 the mean $N(N_2H^+)$ is smaller by a factor of 2.5. The largest $N_2H^+$ column density is found in B1, with a maximum $N(N_2H^+) = 1.7 \times 10^{13}\,\mathrm{cm}^{-2}$ found near (but not at the peak position of) the $N_2H^+$ clump B1-N4. The smallest average column density is found towards

Table 3.6. Derived Column Densities, Fractional Abundances and Non-thermal Line Widths in Oph B1, B2 and B3

| Core | Value | Mean | rms | Min | Max |
|---|---|---|---|---|---|
| Oph B1 | $N(N_2H^+)$ ($\times 10^{12}\,cm^{-2}$) | 4.5 | 2.7 | 2.1 | 15 |
| | $X(N_2H^+)$ ($\times 10^{-10}$) | 15 | 14 | 3.7 | 54 |
| | $n_{ex}$ ($\times 10^5\,cm^{-3}$) | 2.0 | 2.0 | 0.4 | 8.9 |
| | $\sigma_{NT}\,/\,c_s$ ($km\,s^{-1}$) | 0.71 | 0.16 | 0.38 | 1.16 |
| Oph B2 | $N(N_2H^+)$ ($\times 10^{12}\,cm^{-2}$) | 5.9 | 1.9 | 1.0 | 9.8 |
| | $X(N_2H^+)$ ($\times 10^{-10}$) | 5.6 | 5.4 | 1.6 | 29 |
| | $n_{ex}$ ($\times 10^5\,cm^{-3}$) | 3.1 | 2.9 | 1.0 | 14 |
| | $\sigma_{NT}\,/\,c_s$ ($km\,s^{-1}$) | 1.26 | 0.40 | 0.64 | 2.3 |
| Oph B3[a] | $N(N_2H^+)$ ($\times 10^{12}\,cm^{-2}$) | 1.9 | 0.4 | 1.2 | 2.9 |
| | $n_{ex}$ ($\times 10^5\,cm^{-3}$) | 2.0 | 1.5 | 0.2 | 5.1 |
| | $\sigma_{NT}\,/\,c_s$ ($km\,s^{-1}$) | 0.39 | 0.13 | 0.14 | 0.65 |

[a]The 850 $\mu$m flux at Oph B3 is less than the required threshold of $S_\nu \geq 0.1\,Jy\,beam^{-1}$ (§4.1.2); therefore we do not comment on the fractional $N_2H^+$ abundance.

B3 (mean $N(N_2H^+) = 2.2 \times 10^{12}\,cm^{-2}$), and the maximum value in B3, $N(N_2H^+) = 3.3 \times 10^{12}\,cm^{-2}$, is $\sim 2-4$ times less than peak values found in both B1 and B2 ($N(N_2H^+) = 1.1 \times 10^{13}\,cm^{-2}$ towards B2-N9; similar high values are also found towards B2-N2). The embedded protostars in B2 are not associated with $N(N_2H^+)$ maxima.

The mean fractional $N_2H^+$ abundance for Oph B, $X(N_2H^+) = 8.0 \times 10^{-10}$, is greater by a factor of $\sim 2-4$ than previous measurements in isolated starless cores (Caselli et al. 2002a; Tafalla et al. 2002, 2006; Keto et al. 2004). The mean $N_2H^+$ abundance in Oph B1 ($\langle X(N_2H^+)\rangle = 1.3 \times 10^{-9}$) is greater by a factor $\sim 2$ than in Oph B2 ($\langle X(N_2H^+)\rangle = 6.3 \times 10^{-10}$), although the maximum values are similar. The greatest $N_2H^+$ abundances are found in both Cores towards the Core edges and connecting filament. Most $N_2H^+$ clumps in Oph B, in particular those in Oph B2, are associated with *minima* in $X(N_2H^+)$. For B2 $N_2H^+$ clumps, the mean $X(N_2H^+) = 3.2 \times 10^{-10}$ is still slightly greater than typical values found in isolated starless cores. We discuss further in §5.2 the trend in $X(N_2H^+)$ with $H_2$ column density.

### 3.4.2 Interferometer Results

We next look at the line fitting results in the ATCA pointings. Complex line structures were frequently found in the interferometer data (see §3.3.2), and in combination with relatively low S/N in many locations a full 7-component Gaussian $N_2H^+$ 1-0 line fit did not converge. Instead, we fit a single Gaussian to the isolated $N_2H^+$ 1-0 component to determine the line $v_{\rm LSR}$ and $\Delta v$. In Figures 3.3, 3.4 and 3.5 (parts b and c) we show $v_{\rm LSR}$ and $\Delta v$ over the B2-MM8 region, the eastern $N_2H^+$ object B2-N5, and the south-eastern edge of Oph B2, respectively. While emission was found in the north-eastern mosaic (see Figure 3.6), the relatively low line strengths compared with the mosaic rms and complex line structures precluded good fits to the data.

In general, we find the structures visible in the interferometer data have similar $v_{\rm LSR}$ within uncertainties, and universally narrower $\Delta v$ by a factor $\sim 2$, compared with the single dish data at the same location. This difference can be seen qualitatively in Figure 3.10, where we plot the Nobeyama and ATCA spectra towards B2-MM8, B2-N5, B2-N6, B2-N7 and B2-N8 (we show the B2-N6, B2-N7 and B2-N8 spectra at the interferometer data peak, as the ATCA data show integrated intensity maxima offset by $\sim 5''$ from the single-dish data towards B2-N6 and B2-N8, while significant interferometer emission was not seen towards B2-N7). The B2-N5 $v_{\rm LSR}$ is blueshifted by $0.1\,{\rm km\,s^{-1}}$ in the ATCA data relative to the Nobeyama data, but Figure 3.10 shows this is likely due to strong negative features in the interferometer spectrum.

We find a velocity gradient of $\sim 0.2\,{\rm km\,s^{-1}}$ over $\sim 10''$ (0.005 pc, or $\sim 33\,{\rm km\,s^{-1}\,pc^{-1}}$) with a position angle of $\sim 15^\circ$ across the small interferometer peak north of B2-N6. If this gradient is associated with rotation of the clump, this value is large compared with typical gradient values observed at low resolution, but is comparable to high resolution $N_2H^+$ 1-0 results for dense starless and protostellar clumps. In Ophiuchus A, Di Francesco et al. (2004) found velocity gradients of $0.5\,{\rm km\,s^{-1}}$ over 0.01 pc, or $50\,{\rm km\,s^{-1}\,pc^{-1}}$, towards several submillimeter clumps. In addition, Lee et al. (2007) found a velocity gradient of $30\,/\,\cos(i)\,{\rm km\,s^{-1}\,pc^{-1}}$) within $30''$ (0.04 pc at 300 pc) towards the L1521B protostellar group, perpendicular to an observed outflow direction and suggestive of fast rotation. The gradient seen in L1521B is both an order of magnitude larger than that seen at lower resolution and in the opposite direction (a neighbouring core was included in the low resolution data). In the protostellar core IRAM 04191, Belloche & André (2004) found a mean velocity gradient of

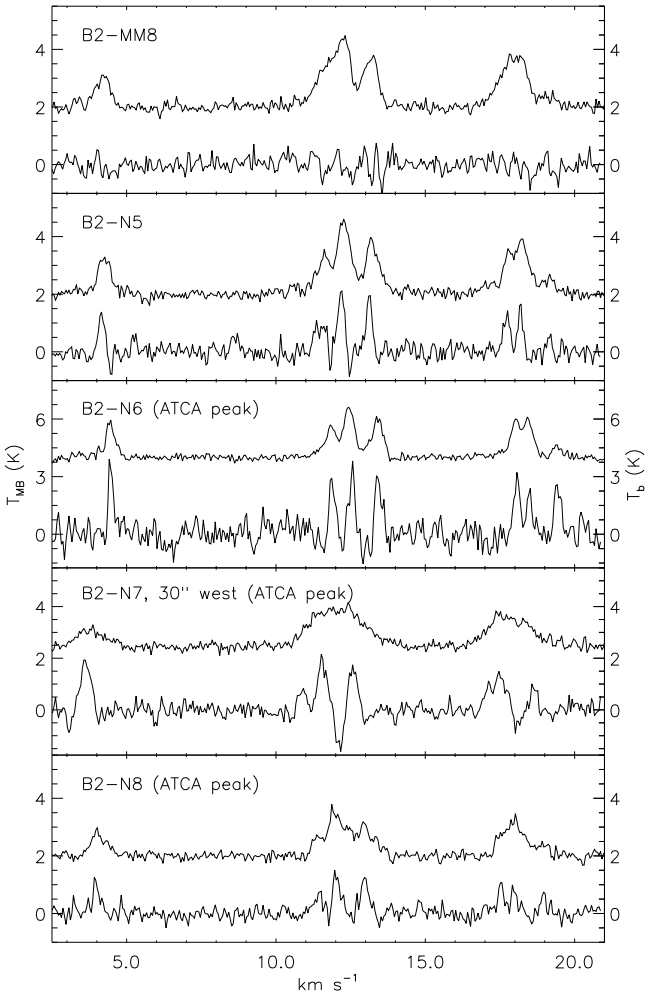


Figure 3.10 $N_2H^+$ 1-0 spectra towards B2-MM8, B2-N5, B2-N6, B2-N7 and B2-N8 observed with Nobeyama and the ATCA. Nobeyama spectra have been offset from 0 by 2 K, 2 K, 4 K, 2.5 K and 2 K for clarity. The temperature scale is in $T_{MB}$ (K; Nobeyama) and $T_B$ (K; ATCA). Spectra towards B2-N6, B2-N7 and B2-N8 are taken from the ATCA integrated intensity maxima nearby, and are offset from the clumps identified in the single-dish data by $\sim 5 - 30''$. Note that little interferometer emission is observed towards the MM8 location. ATCA spectra at B2-N5, B2-N6, B2-N7 and B2-N8 have smaller line widths by a factor $\gtrsim 2$ than are observed with the single dish telescope. The $v_{\rm LSR}$ blueshift of $0.1\,{\rm km\,s^{-1}}$ observed in the ATCA data relative to the Nobeyama data towards B2-N5 may be a result of negative features in the interferometer data. No offset in velocity was found between the ATCA and Nobeyama observations towards B2-N6, B2-N7 or B2-N8.

$\sim 17\,\mathrm{km\,s^{-1}\,pc^{-1}}$ through interferometer $N_2H^+$ observations, which is a factor $\sim 5$ larger than that seen in single-dish data.

B2-N6 is also associated in the interferometer data with extremely narrow $N_2H^+$ 1-0 line widths, with a mean $\Delta v = 0.21 \pm 0.04\,\mathrm{km\,s^{-1}}$ averaged over an $8'' \times 5''$ area matching the beam FWHM. The observed single dish line width at the same location is $0.39 \pm 0.01\,\mathrm{km\,s^{-1}}$, listed in Table 3.4. These are the narrowest lines found in the Oph B2 Core. (Slightly greater line widths are found in Oph B1 towards the B1-N3 and B1-N4 clumps when fitted by a two-velocity component structure in the single dish data, see §3.4.) The velocity gradient, small size and narrow line widths associated with B2-N6 in the interferometer data make it an interesting object in B2, which we discuss further in §3.5.2.

## 3.5 Discussion

### 3.5.1 General trends

We show in Figure 3.11 the distribution of the ratio of the non-thermal dispersion to the sound speed, $\sigma_{\rm NT} \,/\, c_s$, $n_{ex}$, $N(N_2H^+)$ and $X(N_2H^+)$ with $N(H_2)$ in Oph B, omitting pixels where the $850\,\mu$m continuum flux $S_\nu \leq 0.1\,\mathrm{Jy\,beam^{-1}}$. Data points represent values for $18''$ pixels, i.e., approximately the Nobeyama beam FWHM. We show individually pixels in Oph B1 and B2, and also show peak values for $N_2H^+$ clumps, identified in §3.3.1, and $850\,\mu$m continuum clumps (Jørgensen et al. 2008). Note that no Oph B3 values are plotted due to the lack of continuum emission at the B3 location. The Figure shows that the $N_2H^+$ clumps do not reside at the highest $H_2$ column densities, but scatter over the range of $N(H_2)$ calculated above our submillimeter flux threshold. The submillimeter clumps tend to be found at higher $N(H_2)$ values than the $N_2H^+$ clumps, on average, but also show a spread in peak $N(H_2)$.

In Chapter 2, we used the ratio of $NH_3$ (1,1) and (2,2) emission lines in Oph B to determine the kinetic temperature $T_K$ in each pixel, which we can use to calculate $\sigma_{\rm NT}$ and $c_s$ for $N_2H^+$ emission in Oph B. Given $T_K$, $\sigma_{\rm NT} = \sqrt{\sigma^2_{obs} - k_B T_K \,/\, (\mu_{mol} m_{\rm H})}$, where $k_B$ is the Boltzmann constant, $m_{\rm H}$ is the mass of the hydrogen atom, $\mu_{mol}$ is

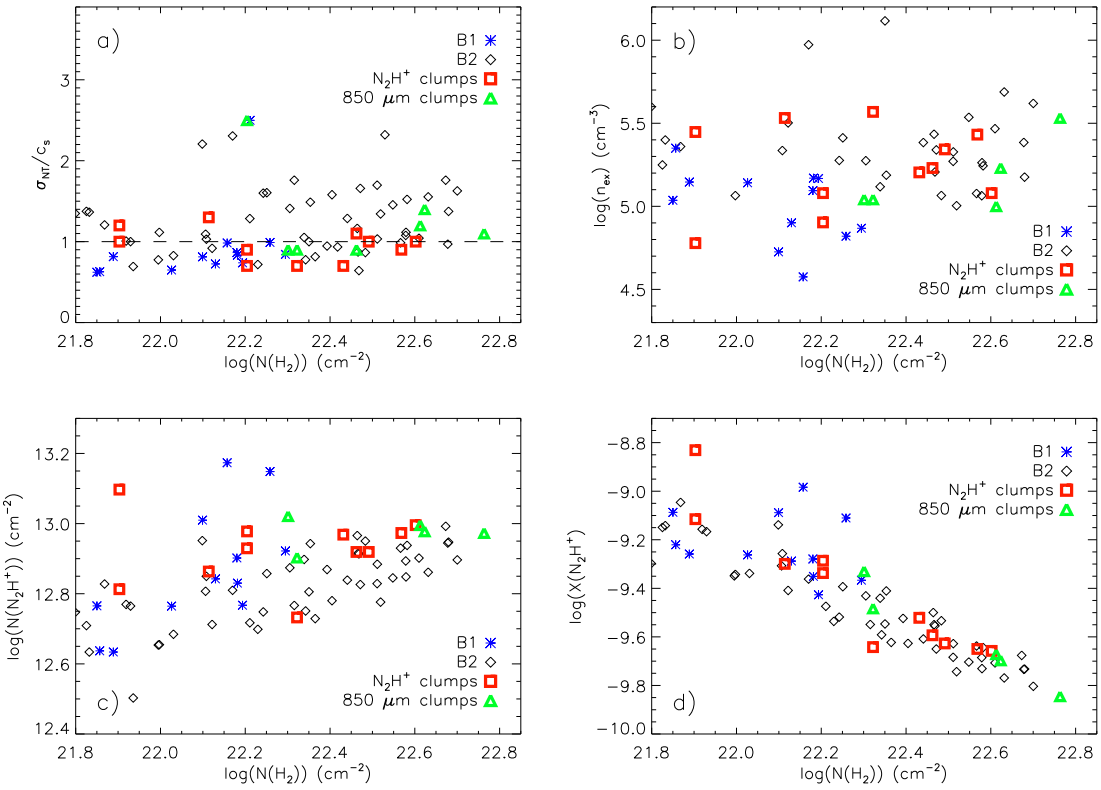


Figure 3.11 a) Ratio of the non-thermal line width to the sound speed, $\sigma_{\rm NT} \,/\, c_s$, versus $N(\rm H_2)$ ($\rm cm^{-2}$, derived from 850 $\mu$m continuum data) in Oph B1 and B2. Each point represents an 18″ pixel (matching the beam FWHM). The dashed line indicates $\sigma_{\rm NT} \,/\, c_s = 1$. Most $\rm N_2H^+$ clumps have subsonic non-thermal motions, as does a large fraction of the $\rm N_2H^+$ emission in both Oph B1 and B2. Note that the velocity resolution of the data, $\Delta v_{res} = 0.05\,\rm km\,s^{-1}$, is significantly smaller than the apparent cutoff in the non-thermal to sound speed ratio at $\sigma_{\rm NT} \,/\, c_s \sim 0.5$. In all plots, also shown are values at the peak positions of $\rm N_2H^+$ clumps identified with CLUMPFIND as described in §3 and 850 $\mu$m clump locations identified by Jørgensen et al. (2008). b) Distribution of $n_{\rm ex}$ ($\rm cm^{-3}$) with $N(\rm H_2)$ in Oph B1 and B2. c) $N(\rm N_2H^+)$ ($\rm cm^{-2}$) versus $N(\rm H_2)$ in Oph B1 and B2. There is no clear trend in $N(\rm N_2H^+)$ seen in Oph B1, but in Oph B2 $N(\rm N_2H^+)$ appears to increase with $N(\rm H_2)$. d) $X(\rm N_2H^+)$ versus $N(\rm H_2)$ in Oph B1 and B2.

the molecular weight in atomic units ($\mu_{\rm N_2H^+} = 29.02$) and $\sigma_{obs} = \Delta v \,/\, (2\sqrt{2\ln 2})$. We list values and propagated uncertainties for individual $N_2H^+$ clumps in Table 3.4, and give the mean, rms, minimum and maximum $\sigma_{\rm NT} \,/\, c_s$ in Table 3.6 for each of Oph B1, B2 and B3.

We find a mean $\sigma_{\rm NT} \,/\, c_s = 1.02$ for $N_2H^+$ 1-0 emission across Oph B with an rms variation of 0.49, indicating that the non-thermal motions are approximately equal, on average, to the sound speed. When looked at separately, we find a difference in the $\sigma_{\rm NT} \,/\, c_s$ ratio between Oph B1 and B2. In Oph B1, the mean $\sigma_{\rm NT} \,/\, c_s = 0.71$, with an rms variation of 0.16. In Oph B2, the mean $\sigma_{\rm NT} \,/\, c_s = 1.26$ with an rms variation of 0.4. Oph B3 is dominated by nearly thermal line widths, with the mean $\sigma_{\rm NT} \,/\, c_s = 0.39$ and an rms variation of only 0.13.

We find little variation in $\sigma_{\rm NT} \,/\, c_s$ with $N(H_2)$ in Oph B, as shown in Figure 3.11a. The difference in the mean $\sigma_{\rm NT} \,/\, c_s$ ratio between B1 and B2 is clear, as is the significantly larger scatter of non-thermal line widths in B2 than in B1. The variation in $\sigma_{\rm NT} \,/\, c_s$ extends to the highest $H_2$ column densities. In B1, all non-thermal line widths $\sigma_{\rm NT} \leqq c_s$, shown by the dashed line. Similar results are found for most $N_2H^+$ clumps, and approximately half the continuum clumps. At $18''$ resolution, the observed non-thermal line widths do not extend to arbitrarily low values, as the data show a cutoff in the $\sigma_{\rm NT} \,/\, c_s$ ratio at $\sigma_{\rm NT} \,/\, c_s \sim 0.5$ for both B1 and B2, below which no data points are found (but note that in §3.4.2, we found narrow line widths at high resolution). For $T_K = 15\,{\rm K}$, the mean temperature found in Oph B, the $\sigma_{\rm NT} \,/\, c_s$ cutoff corresponds to $\sigma_{\rm NT} \sim 0.12\,{\rm km\,s^{-1}}$. Note that the velocity resolution of the $N_2H^+$ data, $\Delta v_{res} = 0.05\,{\rm km\,s^{-1}}$, is significantly less than the observed lower $\sigma_{\rm NT} \,/\, c_s$ limit.

In Chapter 2, we discussed the possible origins of the large non-thermal motions in Oph B, and based on timescale arguments ruled out primordial motions (i.e., motions inherited from the parent cloud). It is interesting that most of the gas traced by $N_2H^+$ 1-0 in Oph B2 remains dominated by transonic non-thermal motions, while the line widths in Oph B1 reveal the Core is significantly more quiescent at the $\sim 10^5\,{\rm cm^{-3}}$ densities traced by $N_2H^+$ 1-0 emission. The most obvious source of this difference is the presence of embedded protostars in Oph B2 while Oph B1 is starless. Kamazaki et al. (2003) found an outflow in CO 3-2 emission in Oph B2 centred near Elias 33 and Elias 32 and oriented approximately east-west, but were unable to pinpoint which

protostar was the driving source. In upcoming results from the JCMT Gould Belt Legacy survey (Ward-Thompson et al. 2007b), which mapped Oph B in CO 3-2, $^{13}$CO 3-2 and C$^{18}$O 3-2 at 14″ resolution, this highly clumped outflow is shown to extend over more than 10′ (i.e., 0.4 pc at 120 pc, White *et al.* 2009, in preparation). The outflow axis is also aligned such that the outflow does not appear to be impacting Oph B1 significantly, potentially explaining the difference in non-thermal line widths between the two sub-Cores.

$N_2H^+$ is not generally thought to be a tracer of protostellar outflows, since it is expected to be destroyed quickly through reactions with CO, which evaporates from dust grains in the higher temperature gas near the driving protostar. On small scales in B2, however, some variations in $v_{\rm LSR}$ and $\Delta v$ appear correlated with the presence of nearby Class I protostars (see §3.4.1 and Figure 3.9). Chen et al. (2008) suggest $N_2H^+$ can be entrained in protostellar jets before a molecular outflow releases CO from grain surfaces which then can destroy $N_2H^+$. In a small $N_2H^+$ 1-0 survey of the Serpens NW cluster, Williams & Myers (2000) found that the largest $\sigma_{\rm NT}$ values ($\sigma_{\rm NT} > 0.6\,{\rm km\,s^{-1}}$, greater than seen here in Oph B2) occurred in cores containing protostellar sources which power strong outflows. If caused by the substantial protostellar outflow, the large line widths on a global scale in Oph B2 suggest that protostellar outflows are able to inject additional turbulence into the *high density* gas in cluster-forming Cores, thereby increasing the mass at which clumps become gravitationally unstable and altering the consequent fragmentation and evolution of existing embedded clumps. Di Francesco et al. (2001) did not see this effect in the $N_2H^+$ 1-0 observations of the circumstellar dense gas associated with the protostellar, outflow-driving source NGC 1333 IRAS4B, suggesting that the ability of the outflow to inject turbulent energy may be determined by additional factors, such as the collimation or strength of the outflow. A comparison of the outflow properties in these regions would be useful to probe further the impact of outflows on cluster forming Cores.

Alternatively, the larger line widths in B2 may be due to global infall motions. In Chapter 2, we determined a virial mass $M_{vir} \sim 8\,{\rm M_\odot}$ for Oph B2 based on $NH_3$ line widths, which is a factor $\sim 5$ less than Core mass estimates based on thermal dust continuum emission (with a factor $\sim 2$ uncertainty). In contrast, $M/M_{vir} \sim 1$ in Oph B1. Some evidence for infall has been observed in self-absorbed molecular line tracers in Oph B2 (André et al. 2007; Gurney et al. 2008), but it is difficult to determine unambiguously given the complex outflow motions also present. Additionally, the

consistent line widths found in $NH_3$ gas for both B1 and B2 (discussed further in §3.5.3 in comparison with the $N_2H^+$ results) suggest a common source for non-thermal motions at gas densities $n \sim 10^4\,\mathrm{cm}^{-3}$, which then impacts differently the gas at higher densities in the two sub-Cores.

Figure 3.11b shows the volume density $n_{\mathrm{ex}}$ as a function of $N(H_2)$. Nearly all pixels have $n_{\mathrm{ex}} \gtrsim 10^5\,\mathrm{cm}^{-3}$, and we find slightly greater $n_{\mathrm{ex}}$ at higher column densities. The $N_2H^+$ and continuum clumps scatter over the full range of density values found in Oph B.

We also find a slight trend of increasing $N_2H^+$ column density, $N(N_2H^+)$, with $N(H_2)$, shown in Figure 3.11c, although the mean $N(N_2H^+)$ changes by less than a factor of $\sim 2$ over the order of magnitude range in $N(H_2)$ found in Oph B. Several pixels in Oph B1, and one $N_2H^+$ clump, have significantly greater $N(N_2H^+)$ for their $N(H_2)$ values compared with the rest of the data. The small gradient in $N(N_2H^+)$ with $N(H_2)$ leads to a trend of *decreasing* fractional $N_2H^+$ abundance with increasing $H_2$ column density, shown in Figure 3.11d. We find $N_2H^+$ abundances decrease by an order of magnitude between the limiting $N(H_2)$ threshold and the peak $N(H_2)$ values. We fit a linear relationship to $\log X(N_2H^+)$ versus $\log N(H_2)$ for Oph B1 and B2 separately. In B1 alone, where we have relatively few data points, we find $\log X(N_2H^+)$ is consistent within the uncertainties with being constant with $N(H_2)$, but in conjunction with the Oph B2 data, we find

$$\log X(N_2H^+) = (7.1 \pm 0.9) - (0.74 \pm 0.04) \times \log N(H_2) \tag{3.5}$$

using the same $H_2$ column density limits as in Figure 3.11.

### 3.5.2 Small-Scale Features

We next discuss at the physical properties of the small-scale structure present in Oph B, including the $N_2H^+$ clumps, continuum clumps, and embedded protostars, and describe in detail the compact, thermal object B2-N6.

**Comparison of $N_2H^+$ clumps, continuum clumps and protostars**

We list in Table 3.5 the physical parameters derived from $N_2H^+$ 1-0 emission towards 850 $\mu$m continuum clump locations (Jørgensen et al. 2008) and embedded Class I protostars (Enoch et al. 2009). Columns are the same as in Table 3.4. In Table 3.7, we list the mean values of each physical parameter towards $N_2H^+$ clumps, continuum clumps and protostars. Note that we were only able to solve for all parameters listed towards a single protostar, and discuss below only those mean parameters where we obtained values from three or more objects.

We find no difference in the mean $v_{LSR}$ between $N_2H^+$ clumps, continuum clumps and protostars. There is a clear reduction in $\Delta v$ towards $N_2H^+$ clumps relative to continuum clumps (mean $\Delta v = 0.49\,\mathrm{km\,s^{-1}}$and $0.68\,\mathrm{km\,s^{-1}}$, respectively), but excluding one continuum clump (162712-24290) reduces the mean $\Delta v$ to $0.58\,\mathrm{km\,s^{-1}}$. Protostars are associated with wider mean $\Delta v$, but the larger mean is driven by large $\Delta v$ towards a single object. The differences between $N_2H^+$ and continuum clumps are marginally significant given the variance of $\Delta v$ across the entire Core is only $0.08\,\mathrm{km\,s^{-1}}$ in Oph B1 and $0.21\,\mathrm{km\,s^{-1}}$ in Oph B2. We find similar $N_2H^+$ line opacities and excitation temperatures towards continuum and $N_2H^+$ clumps. Continuum clumps are associated with larger non-thermal motions, with a mean $\sigma_{NT}/c_s = 1.24$ which is 1.5 times that associated with $N_2H^+$ clumps (mean $\sigma_{NT}/c_s = 0.86$). $N_2H^+$ column densities are similar towards $N_2H^+$ and continuum clumps (within $\sim 25\,\%$), but $N_2H^+$ clumps are associated with smaller $N(H_2)$ and hence greater $X(N_2H^+)$ by a factor $> 2$. In fact, the mean $N_2H^+$ abundance towards continuum clumps is less than $X(N_2H^+)$ averaged over the entire Oph B Core. Derived volume densities are the same for $N_2H^+$ and continuum clumps.

In summary, the $N_2H^+$ clumps are associated with smaller line widths and subsonic non-thermal motions relative to continuum clumps and protostars, but the difference in mean values is similar to the variance in line widths across the Core. The most significant difference between $N_2H^+$ and continuum clumps are found in their $N_2H^+$ abundances, with a mean $X(N_2H^+)$ towards continuum clumps that is lower than $X(N_2H^+)$ in $N_2H^+$ clumps.

Table 3.7. Mean Derived Physical Parameters for $N_2H^+$ clumps, 850 $\mu$m clumps and Class I protostars

| | $v_{\rm LSR}$ $\rm km\,s^{-1}$ | $\Delta v$ $\rm km\,s^{-1}$ | $\tau$ | $T_{ex}$ K | $\sigma_{\rm NT}$ / $c_s$ | $N(N_2H^+)$ $10^{12}\,\rm cm^{-2}$ | $N(H_2)$ $10^{22}\,\rm cm^{-2}$ | $X(N_2H^+)$ $10^{-10}$ | $n_{ex}$ $10^5\,\rm cm^{-3}$ |
|---|---|---|---|---|---|---|---|---|---|
| $N_2H^+$ clumps | 3.98 | 0.49 | 3.2 | 7.0 | 0.86 | 7.0 | 1.9 | 8.0 | 1.9 |
| 850 $\mu$m clumps | 3.99 | 0.70 | 3.9 | 6.7 | 1.27 | 9.4 | 3.2 | 3.1 | 1.7 |
| Class I protostars | 4.00 | 0.89 | 1.5* | 6.5* | 1.67 | 5.8* | 2.3* | 3.1* | 3.6* |

Note. — Only three protostars (two where values labelled with *) were associated with significant $N_2H^+$ 1-0 emission such that physical parameters could be determined from the HFS line fitting routine.

**Oph B2-N6**

The B2-N6 clump is a pocket of narrow $N_2H^+$ 1-0 line emission within the larger, more turbulent B2 Core, with a large fraction ($\gtrsim 50\%$) of the emission at the clump peak coming from the small size scales probed by the ATCA observations. Line widths measured from the interferometer data are a factor $\sim 2$ less than those recorded from the single dish data ($\Delta v = 0.21 \pm 0.04\,\mathrm{km\,s^{-1}}$ compared with $0.39 \pm 0.01\,\mathrm{km\,s^{-1}}$). The millimeter continuum object B2-MM15, identified through a spatial filtering technique (Motte et al. 1998), lies offset by $\sim 12''$ from the peak interferometer integrated intensity (see Figure 3.4). Motte et al. calculate a mass of only $0.17\,\mathrm{M_\odot}$ associated with the B2-MM15 clump, but based on its small size (unresolved, and estimating $r \sim 800\,\mathrm{AU}$) derive an average density of $n \sim 1.2 \times 10^8\,\mathrm{cm^{-3}}$. This is significantly larger than the densities calculated in §3.4.1, but higher sensitivity $N_2H^+$ 1-0 interferometer observations are needed to probe the clump density on small scales.

We calculated in Chapter 2 a gas kinetic temperature $T_K = 13.9 \pm 1.1\,\mathrm{K}$ for the colocated B2-A7 $NH_3$ (1,1) clump. We find $\sigma_{\mathrm{NT}} = 0.06\,\mathrm{km\,s^{-1}}$ for B2-N6, equal to the expected $N_2H^+$ thermal dispersion, and $\sigma_{\mathrm{NT}}/c_s = 0.26$. A similar compact $N_2H^+$ 1-0 clump with nearly thermal line widths was found in Oph A (Oph A-N6, Di Francesco et al. 2004). While both clumps are associated with larger-scale $N_2H^+$ emission, these objects are only distinguishable as compact, nearly purely thermal clumps when observed with interferometric resolution and spatial filtering.

Di Francesco et al. propose Oph A-N6 may be a candidate thermally dominated, critical Bonnor-Ebert sphere embedded within the more turbulent Oph A Core. Such objects have sizes comparable to the cutoff wavelength for MHD waves and are in equilibrium between their self-gravity and internal and external pressures. Myers (1998) called these objects 'kernels', and showed that they could exist in cluster-forming cores with FWHM line widths $\Delta v > 0.9\,\mathrm{km\,s^{-1}}$ and column densities $N(\mathrm{H_2}) > 10^{22}\,\mathrm{cm^{-3}}$, with sizes comparable to the spacing of protostars in embedded clusters, suggesting that a population of kernels within a dense Core could form a stellar cluster. The physical conditions in both Oph A and Oph B2 fit these requirements. The B2-N6 clump, however, is significantly smaller (0.004 pc compared with a predicted $\sim 0.03\,\mathrm{pc}$) and less massive ($0.17\,\mathrm{M_\odot}$ compared with a predicted $\sim 1\,\mathrm{M_\odot}$) than the objects discussed by Myers.

If we calculate the mass of a critical Bonnor-Ebert sphere given the ATCA $N_2H^+$ 1-0 line width and a radius of $\sim 800\,\mathrm{AU}$, where $M/R = 2.4\sigma^2/G$ (Bonnor 1956), we find $M_{\mathrm{BE}} = 0.02\,\mathrm{M}_\odot$, or approximately $10\times$ smaller than the mass determined by Motte et al.. We find a virial mass $M_{vir} = 0.04\,\mathrm{M}_\odot$, assuming B2-N6 is a uniform sphere and $M = 5\sigma^2 R/G$. If the clump mass is accurate, this suggests that while small, B2-N6 may be gravitationally unstable. André et al. (2007) made a tentative detection of infall motions towards the clump through observations of optically thick lines such as CS, $H_2CO$ or $HCO^+$. Thus B2-N6 may be at a very early stage of clump formation, and may eventually form an additional low mass protostar to the three YSOs already associated with dense gas in Oph B2.

### 3.5.3 Comparison of $N_2H^+$ and $NH_3$ emission in Oph B

We next compare the physical properties of the gas in Oph B derived here from $N_2H^+$ observations with those derived from $NH_3$ observations, described in Chapter 2. In the following discussion, all comparisons are made after convolving the $NH_3$ data to a final angular resolution of $18''$ to match the Nobeyama $N_2H^+$ observations.

#### $v_{\mathrm{LSR}}$ and $\sigma_{\mathrm{NT}} / c_s$

We first look at the velocities and non-thermal line widths of the gas traced by $N_2H^+$ gas and those determined from $NH_3$ emission in Chapter 2. Figure 3.13a shows the distribution of $v_{\mathrm{LSR}}$ derived from $N_2H^+$ and $NH_3$ emission in Oph B. There is no significant difference in the measured line-of-sight velocity between the two dense gas tracers, with the mean $v_{\mathrm{LSR}} = 3.98\,\mathrm{km\,s^{-1}}$ for $NH_3$ and $4.01\,\mathrm{km\,s^{-1}}$ for $N_2H^+$.

In Figure 3.13b, we show the distribution of $\sigma_{\mathrm{NT}} / c_s$ as determined with $N_2H^+$ or $NH_3$ using the $NH_3$-derived $T_K$ values. The non-thermal line widths measured in $N_2H^+$ 1-0 are substantially smaller than those measured in $NH_3$ in Chapter 2, and additionally the variation in the relative magnitude of the non-thermal motions between Oph B1 and B2 was not found in $NH_3$ emission. The mean $NH_3$ $\sigma_{\mathrm{NT}} / c_s = 1.64$ in Oph B, and does not vary significantly between B1 ($\langle \sigma_{\mathrm{NT}} / c_s \rangle = 1.62$) and B2 ($\langle \sigma_{\mathrm{NT}} / c_s \rangle = 1.68$).

The assumption that $T_K$ is similar for both $N_2H^+$ and $NH_3$ is reasonable if both

molecules are excited in the same material. The good agreements between the locations of $NH_3$ and $N_2H^+$ clumps, illustrated in Figure 3.2, and the $v_{\rm LSR}$, illustrated in Figure 3.13a, support this assumption. The substantial offset in the $\sigma_{\rm NT} \,/\, c_s$ ratio seen in Figure 3.13b, however, between $NH_3$ and $N_2H^+$ emission indicates significantly different motions are present in the gas traced by $NH_3$ than in the gas traced by $N_2H^+$. The gas densities traced by $N_2H^+$ are an order of magnitude greater than those traced by $NH_3$ ($\sim 10^5\,{\rm cm}^{-3}$ and $\sim 10^4\,{\rm cm}^{-3}$, respectively). In fact, if we attempt to derive the gas kinetic temperature by assuming equal non-thermal motions for the $N_2H^+$ 1-0 and $NH_3$ (1,1) emission (effectively assuming $N_2H^+$ and $NH_3$ trace the same material), the resulting average value is a highly unlikely $T_K = 190\,{\rm K}$ for Oph B2. Given the narrow $N_2H^+$ lines observed in Oph B1, no physical solution for $T_K$ can be found under the assumption of equal $\sigma_{\rm NT}$.

Starless cores are typically found to be well described by gas temperatures that are either constant or decreasing as a function of increasing density (Di Francesco et al. 2007). Given that $N_2H^+$ traces denser gas, we then expect $T_K$ from $NH_3$ measurements to be biased high in starless cores, e.g., gas traced by $N_2H^+$ should be colder than gas traced by $NH_3$. The mean $T_K$ found in Oph B in Chapter 2 was 15 K. With a lower $T_K$, the sound speed would be smaller and the returned $\sigma_{\rm NT}$ would be larger on average. A gas temperature $T_K = 10\,{\rm K}$ rather than 15 K would increase the average $N_2H^+$ $\sigma_{\rm NT} \,/\, c_s$ ratio in Oph B by $\sim 20 - 25\,\%$. This increase, while significant, is not large enough for the mean $N_2H^+$ $\sigma_{\rm NT} \,/\, c_s$ to match the $NH_3$ results in Oph B. With both a constant temperature or decreasing temperature with density, non-thermal motions in Oph B1 and B3 would remain subsonic, while Oph B2 would still be dominated by transonic non-thermal motions. Alternatively, it is possible that the two Class I protostars in Oph B2 could raise the temperature of the dense gas above that traced by $NH_3$ (no $T_K$ difference was found between protostars and starless areas in Chapter 2). In this case, the returned $N_2H^+$ $\sigma_{\rm NT}$ would be smaller, and would further increase the differences in magnitude of non-thermal motions seen between the $NH_3$ and $N_2H^+$ emission in Oph B1. In B2, a temperature of 20 K would decrease the mean $\sigma_{\rm NT} \,/\, c_s$ ratio to 1.1. In a study of dust temperatures in the Ophiuchus Cores, Stamatellos et al. (2007) showed, however, that embedded protostars in the Cores will only heat very nearby gas and will not raise the mean temperature of the Cores by more than $\sim 1 - 2\,{\rm K}$, so an average $T_K = 20\,{\rm K}$ over all Oph B2 is unlikely.

**Double peaked line profiles**

In Figure 3.12, we show the isolated $F_1F \rightarrow F_1'F' = 01 \rightarrow 12$ component of the $N_2H^+$ 1-0 emission line towards the three $N_2H^+$ clumps in Oph B1 (B1-N1, B1-N3, and B1-N4) which show double peaked line profiles, as described in §3.4. Figure 3.12 also shows a single Gaussian line profile overlaid on each $N_2H^+$ spectrum, which represents the $v_{\rm LSR}$ and $\Delta v$ of the 18 component Gaussian fit to the $NH_3$ (1,1) emission at the clump peak, normalized to a peak amplitude of 1 K. We plot the Gaussian fit for clarity since there are no isolated components in the $NH_3$ (1,1) hyperfine structure. Additionally, spectra of $C_2S$ $2_1 - 1_0$ emission line at the peak clump locations are shown. Note that over all Oph B, $C_2S$ emission was only detected towards the southern tip of Oph B1, and thus no significant $C_2S$ emission was found at the peak location of B1-N1. The $C_2S$ emission was observed with the GBT at $\sim 32''$ spatial resolution and $0.08\,{\rm km\,s^{-1}}$ spectral resolution, with the observations and analysis described in Chapter 2. Arrows show the locations of the fitted $v_{\rm LSR}$ for all species, including both $N_2H^+$ velocity components.

The clumps which show the double-peaked line profile structure are the clumps with the highest total $N_2H^+$ 1-0 line opacities based on a single velocity component fit, with $\tau = 5, 6$ and 9, respectively for B1-N1, B1-N3 and B1-N4. The $F_1F \rightarrow F_1'F' = 01 \rightarrow 12$ component is expected to have an opacity $\tau_{iso} = 1/9\,\tau$, so $\tau_{iso} = 0.6, 0.7$, and $\sim 1$ for the three clumps, based on a single component fit. If the line is optically thick, however, this fit is likely to underestimate the true opacity given the missing, self-absorbed flux. This is suggestive that the lines are indeed self-absorbed. Since the $NH_3$ and $C_2S$ emission is optically thin (Chapter 2), however, if the $N_2H^+$ emission was self-absorbed due to high optical depth we would expect the emission peak of both $NH_3$ and $C_2S$ to be found between the two $N_2H^+$ components in $v_{\rm LSR}$, which is not the case. In all three clumps, we find the $v_{\rm LSR}$ of the $NH_3$ emission more closely matches the $v_{\rm LSR}$ of the red $N_2H^+$ component, while the $C_2S$ emission in two clumps ($v_{\rm LSR} = 3.67\,{\rm km\,s^{-1}}$) more closely matches the $v_{\rm LSR}$ of the blue $N_2H^+$ component ($v_{\rm LSR} = 3.85\,{\rm km\,s^{-1}}$ and $3.62\,{\rm km\,s^{-1}}$ for B1-N3 and B1-N4, respectively). This behaviour suggests the $N_2H^+$ 1-0 emission is not self-absorbed towards these positions. A similar offset of $C_2S$ emission relative to $N_2H^+$ was found by Swift et al. (2006) towards the starless Core L1551, however the case of L1551 the $C_2S$ emission is redshifted with respect to the systemic velocity of the Core rather than blueshifted,

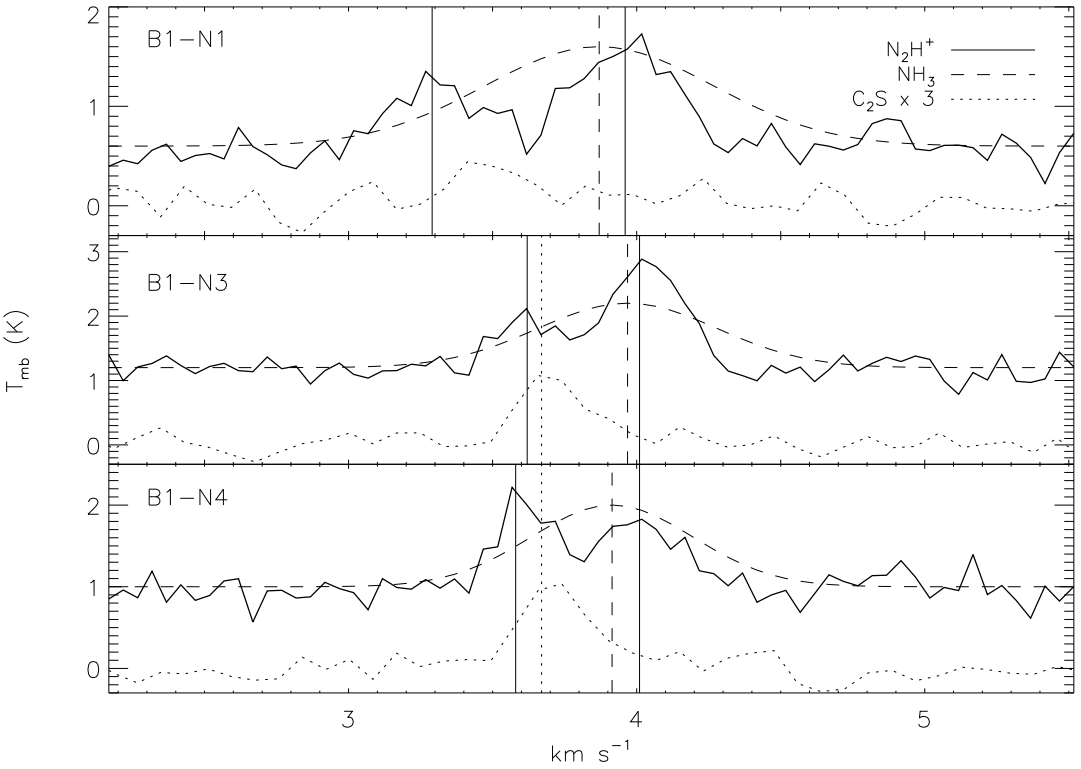


Figure 3.12 Solid black lines show the isolated $F_1F \rightarrow F_1'F' = 01 \rightarrow 12$ component of the $N_2H^+$ 1-0 emission line towards the three $N_2H^+$ clumps in Oph B1 which show a double peaked line profile. The dashed curves show the Gaussian fit to $NH_3$ (1,1) emission, observed wih the GBT, at the $N_2H^+$ clump peak location (observations described in Chapter 2). The dotted lines show the $C_2S$ 2-1 emission at the $N_2H^+$ clump peak, also observed with the GBT. Note no significant $C_2S$ emission was seen towards B1-N1. The $NH_3$ Gaussian fit peaks towards the red $N_2H^+$ component, while the $C_2S$ emission peaks towards the blue $N_2H^+$ component. Vertical lines matching each species spectrum show the locations of the fitted $v_{\rm LSR}$ for all species, including both velocity components from the two-component $N_2H^+$ 1-0 fit.

as we find in B1.

The GBT $NH_3$ (1,1) observations described in Chapter 2 found extensive emission around Oph B, such that it is possible to determine the $v_{\rm LSR}$ and $\Delta v$ of $NH_3$ beyond where continuum emission traced the Oph B Core. We use an intensity threshold of 2 K in the $NH_3$ (1,1) main component to separate Core and off-Core gas. The off-Core gas surrounding Oph B1 has a mean $v_{\rm LSR} = 3.72\,{\rm km\,s^{-1}}$ with an rms variation of $0.13\,{\rm km\,s^{-1}}$, which is significantly different from the mean B1 Core $v_{\rm LSR} = 3.96\,{\rm km\,s^{-1}}$ and rms variation of $0.15\,{\rm km\,s^{-1}}$. Both the $C_2S$ emission and the blue $N_2H^+$ component are thus more kinematically similar to the off-Core $NH_3$ gas. The critical densities of $C_2S$ $2_1 - 1_0$ and $NH_3$ (1,1) are similar (Suzuki et al. 1992; Rosolowsky et al. 2008a). Kinematically, we find $\sigma_{\rm NT} \,/\, c_s = 0.7$ for the $C_2S$ emission if we assume the $T_K$ determined from $NH_3$ emission accurately represents the temperature of the gas traced by $C_2S$. This result closely matches the $N_2H^+$ results in Oph B1, but the non-thermal motions in the gas traced by $NH_3$ are significantly larger (§3.5.1 and Chapter 2). It is impossible to match the non-thermal $C_2S$ and $NH_3$ motions for a given $T_K$, since the $NH_3$ (1,1) line $\sigma_{\rm NT} > \sigma_{obs}$ of the $C_2S$.

At densities $n \gtrsim$ a few $\times 10^3 - 10^4\,{\rm cm^{-3}}$, chemical models predict $C_2S$ is quickly depleted from the gas phase (timescale $t_{dep} \sim 10^5\,{\rm yr}$; Millar & Herbst 1990; Bergin & Langer 1997), and accordingly the molecule is observed to be a sensitive tracer of depletion in isolated cores (Lai & Crutcher 2000; Tafalla et al. 2006). The volume density in Oph B1 is greater than that required for $C_2S$ depletion ($n \gtrsim 10^5 - 10^6\,{\rm cm^{-3}}$ from §3.4.1 and continuum observations), so we would not expect to see any $C_2S$ emission unless the gas has only been at high density for $t < t_{dep}$. $C_2S$ was only detected towards southern B1. An explanation, therefore, for both the presence of $C_2S$ in southern B1 and for its velocity offset relative to the dense gas is that gas from the ambient molecular cloud is accreting onto B1, reaching a density high enough to excite the $C_2S$ emission line. This material would be chemically 'younger' than the rest of the B1 Core gas, such that the $C_2S$ has not had enough time to deplete from the gas phase. A similar result was found in a multi-species study of the starless L1498 and L1517B cores, where Tafalla et al. (2004) conclude that non-spherical contraction of the cores produced asymmetric distributions of CS and CO, where the CS and CO 'hot spots' reveal the distribution of recently accreted, less chemically processed dense gas.

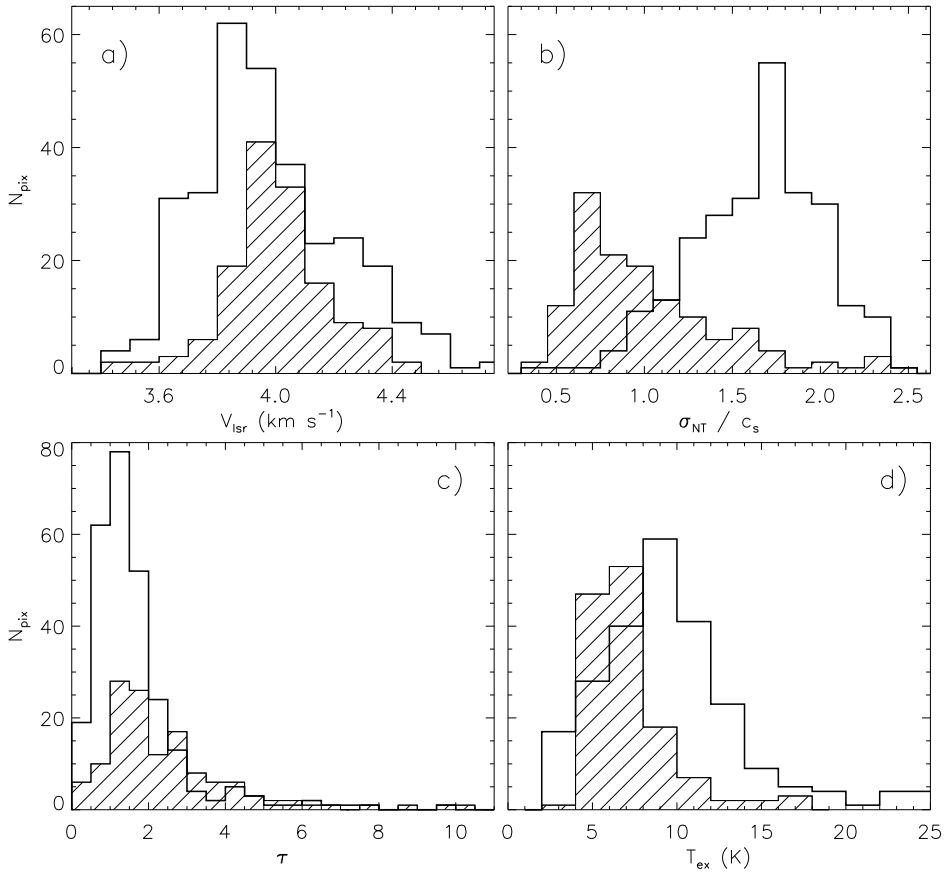


Figure 3.13 a) Comparison of $v_{\rm LSR}$ from $N_2H^+$ 1-0 (hashed) and $NH_3$ (1,1) (non-hashed) determined from hyperfine structure fitting in Oph B. No significant difference is seen in the distribution of line-of-sight velocities between the two dense gas tracers. Only data points in Oph B1 and B2 are included, since B3 was not detected in $NH_3$ emission in Chapter 2 with sufficient significance to perform HFS fitting. b) Comparison of $\sigma_{\rm NT}\,/\,c_s$ from $N_2H^+$ 1-0 (hashed) and $NH_3$ (1,1) (non-hashed) determined from hyperfine structure fitting. The thermal sound speed $c_s$ is calculated using $T_K$ values determined from the ratio of $NH_3$ (1,1) and (2,2) amplitudes in Chapter 2. Non-thermal motions in gas traced by $N_2H^+$ are significantly smaller than in gas traced by $NH_3$. c) Comparison of line opacities $\tau$ from $N_2H^+$ 1-0 (hashed) and $NH_3$ (1,1) (non-hashed) summed over all hyperfine components. d) Comparison of $T_{ex}$ $N_2H^+$ 1-0 (hashed) and $NH_3$ (1,1) (non-hashed) determined from hyperfine structure fitting. The $NH_3$ $T_{ex}$ values have a larger spread and higher mean value ($\langle T_{ex}\rangle = 10\,{\rm K}$) than $N_2H^+$ ($\langle T_{ex}\rangle = 7\,{\rm K}$).

A single 850 $\mu$m continuum clump (162715-24303; Jørgensen et al. 2008) was identified in southern Oph B1 where we find B1-N3 and B1-N4. The authors found a clump mass $M = 0.2\,M_{\odot}$, which is a factor $\sim 2$ less than the virial mass $M_{vir} = 0.4\,M_{\odot}$ we calculate based on the mean line width (of the single velocity component fit) of B1-N3 and B1-N4 ($\Delta v = 0.52\,\mathrm{km\,s^{-1}}$, or $\sigma = 0.22\,\mathrm{km\,s^{-1}}$) and the continuum clump radius. This suggests that the clump is currently stable against collapse. If the clump is gaining mass through ongoing accretion from the ambient gas, however, then eventually the non-thermal support may not be large enough to prevent gravitational collapse, leading to the formation of a low-mass protostar.

### Opacity and Excitation Temperature

We show in Figure 3.13c and 3.13d the distribution of total line opacity $\tau$ and excitation temperature $T_{ex}$ derived from hyperfine line fitting of $NH_3$ (1,1) and $N_2H^+$ 1-0 in Oph B. We find higher total opacities in $N_2H^+$ emission ($\langle\tau\rangle = 2.5$) than in $NH_3$ emission ($\langle\tau\rangle = 1.0$) in Oph B. The $N_2H^+$ emission is characterized by lower excitation temperatures than those found for $NH_3$ emission in Chapter 2, with a mean $T_{ex} = 7.1\,\mathrm{K}$ for $N_2H^+$ 1-0 compared with $T_{ex} = 9.5\,\mathrm{K}$ for $NH_3$ (1,1).

### Fractional Abundances and Chemical Evolution

We next compare the column densities of $NH_3$ and $N_2H^+$ towards the Oph B Core. We only show results for pixels which have well-determined values for both $N(NH_3)$ and $N(N_2H^+)$. In Chapter 2, we found a trend of decreasing fractional $NH_3$ abundance with increasing $N(H_2)$ for *both* B1 and B2. After convolving the $NH_3$ data to match the single dish $N_2H^+$ resolution, we find the following linear relationships between $\log X(NH_3)$ and $\log N(H_2)$:

$$\mathrm{B1} \;:\; \log X(\mathrm{NH_3}) = (5 \pm 4) - (0.6 \pm 0.2)\log N(\mathrm{H_2}) \tag{3.6}$$

$$\mathrm{B2} \;:\; \log X(\mathrm{NH_3}) = (3.5 \pm 2.2) - (0.5 \pm 0.1)\log N(\mathrm{H_2}) \tag{3.7}$$

The slopes found for Oph B1 and B2 are both negative and similar to that found

in Equation 3.5 for the $N_2H^+$ fractional abundance as a function of $N(H_2)$. This result is suggestive of a trend of increasing depletion of both $NH_3$ and $N_2H^+$ with increasing $N(H_2)$ in Oph B.

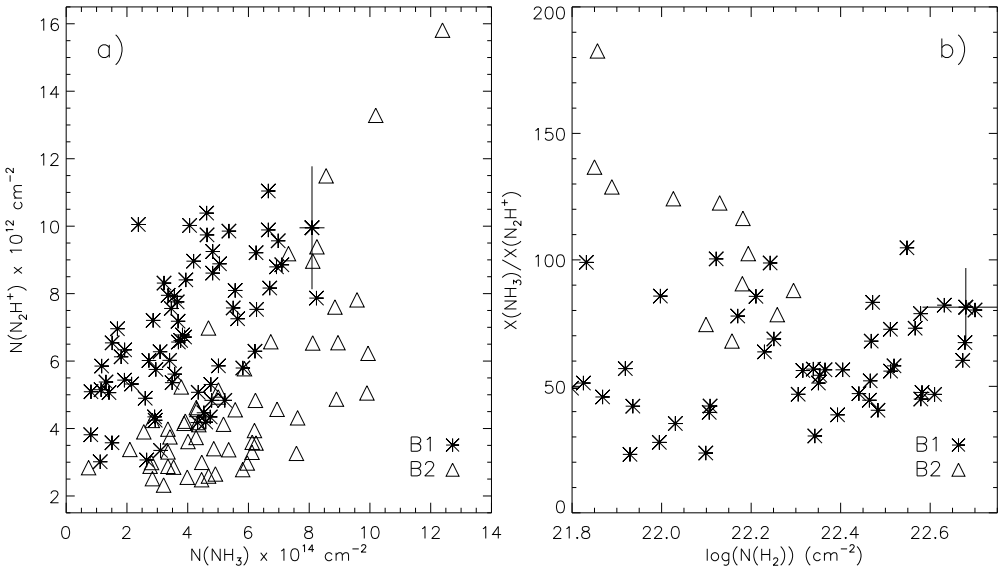


Figure 3.14 a) $N(N_2H^+)$ versus $N(NH_3)$ in Oph B1 and Oph B2. In all plots, the $NH_3$ data have been convolved to a final 18″ FWHM beam, and both the $NH_3$ and $N_2H^+$ data were regridded to 18″ pixels. Only pixels where both $NH_3$ and $N_2H^+$ column densities were calculated are plotted. While the mean $N(NH_3)$ peak at similar values for both B1 and B2, a distribution to higher column values is seen in B1. On average, larger $N(N_2H^+)$ values are found in B2. The combination of the spread to higher $N(NH_3)$ and the lower $N(N_2H^+)$ in lead to a larger $N(NH_3)\,/\,N(N_2H^+)$ ratio in B1 than in B2. b) The ratio of $NH_3$ and $N_2H^+$ column densities, $N(NH_3)\,/\,N(N_2H^+)$ plotted as a function of $N(H_2)$ in Oph B1 and Oph B2. Note that significantly fewer pixels in B1 also have continuum emission above our threshold flux value and are thus not plotted.

We show in Figure 3.14 the $NH_3$ column density, $N(NH_3)$, versus the $N_2H^+$ column density, $N(N_2H^+)$ in Oph B1 and B2, and also the ratio of $N(NH_3)$ to $N(N_2H^+)$ as a function of $N(H_2)$, calculated in §3.4.1 (we do not show results in B3 due to the small number of pixels with both well-determined $NH_3$ and $N_2H^+$ column densities,

but note mean values below). Note that the column density ratio is equivalent to the ratio of fractional abundances:

$$\frac{N(\mathrm{NH_3})}{N(\mathrm{N_2H^+})} = \frac{X(\mathrm{NH_3})}{X(\mathrm{N_2H^+})}. \tag{3.8}$$

Figure 3.14a shows a significant difference in the $N(\mathrm{NH_3}) \,/\, N(\mathrm{N_2H^+})$ ratio between Oph B1 and B2. We find the mean and the standard deviation of this ratio are each twice as large in B1 ($N(\mathrm{NH_3}) \,/\, N(\mathrm{N_2H^+}) = 135$, $\sigma = 52$) as in B2 ($N(\mathrm{NH_3}) \,/\, N(\mathrm{N_2H^+}) = 65$, $\sigma = 31$) and B3 ($N(\mathrm{NH_3}) \,/\, N(\mathrm{N_2H^+}) = 80$, $\sigma = 56$). In Oph B1 and B2, Figure 3.14a illustrates that this difference is largely driven by lower $N(\mathrm{N_2H^+})$ values towards B1, while the spread in the $N(\mathrm{NH_3}) \,/\, N(\mathrm{N_2H^+})$ appears due to a wider spread of $N(\mathrm{NH_3})$ values in B1. We find no variation in the $N(\mathrm{NH_3}) \,/\, N(\mathrm{N_2H^+})$ ratio as a function of $N(\mathrm{H_2})$.

In the clustered star forming region IRAS 20293+3952, Palau et al. (2007) found strong $\mathrm{NH_3}$ and $\mathrm{N_2H^+}$ differentiation associated with the presence or lack of embedded YSOs. Low $N(\mathrm{NH_3}) \,/\, N(\mathrm{N_2H^+}) \sim 50$ values were found near an embedded YSO cluster, while higher $N(\mathrm{NH_3}) \,/\, N(\mathrm{N_2H^+}) \sim 300$ were found towards cores with no associated YSOs. In a survey of 60 low mass cloud cores, Caselli et al. (2002a) find correlations between $N(\mathrm{NH_3})$ and $N(\mathrm{N_2H^+})$ in starless cores, but the relative column density values do not vary significantly between starless and protostellar objects. Our results lie closer to the Palau et al. values in cores with embedded YSOs, which is reasonable given the presence of embedded Class I protostars in and around Oph B2. The higher $\mathrm{NH_3}$ column density relative to $\mathrm{N_2H^+}$ in starless Oph B1 compared with Oph B2 is also in general agreement with their finding of higher $N(\mathrm{NH_3}) \,/\, N(\mathrm{N_2H^+})$ in starless cores, although we only find a factor $\sim 2$ difference in the relative column densities rather than a factor of $\sim 6$. In a study of two dense Cores, each containing a starless main body and a YSO offset from the core center, Hotzel et al. (2004) also find a factor $\sim 2$ smaller $X(\mathrm{NH_3}) \,/\, X(\mathrm{N_2H^+})$ values towards the YSOs, with abundance ratios ($\sim 140 - 190$, towards the starless gas, and $\sim 60 - 90$ towards the YSOs) similar to those found here. The relative abundance variation found by Hotzel et al. is driven by a varying $\mathrm{NH_3}$ abundance while $X(\mathrm{N_2H^+})$ remains constant over the Cores. Although we find both a decrease in $\mathrm{N_2H^+}$ column density as well as an increase in $\mathrm{NH_3}$ column density drives the greater fractional $\mathrm{NH_3}$ abundance towards

Oph B1 (see Figure 3.14), both $X(N_2H^+)$ and $X(NH_3)$ are greater in B1, by factors of $\sim 2$ and $\sim 4$, respectively, compared with B2 given the lower $H_2$ column densities found in B1 in §3.4.1.

Based on this work and the studies described above, it appears that the relative fractional abundance of $NH_3$ to $N_2H^+$ remains larger towards starless cores than towards protostellar cores by a factor of $\sim 2-6$ in both isolated and clustered star forming regions. In their models of collapsing prestellar cores, Aikawa et al. (2005) found that $NH_3$ can be enhanced relative to $N_2H^+$ in core centers at high densities ($n = 3 \times 10^5 - 3 \times 10^6\,\mathrm{cm^{-3}}$) due to dissociative recombination reactions of $N_2H^+$ and $e^-$ to form NH and N. NH then reacts with $H_3^+$ and $H_2$ to form $NH_3$. The $N_2H^+$ recombination reaction is dominant only where CO is depleted (if CO is abundant, $N_2H^+$ is destroyed mainly through proton transfer to CO), and occurs when the abundance ratio of CO to electrons, $n(\mathrm{CO})\,/\,n_e \lesssim 10^3$. When a collapsing core reaches higher central densities ($n \sim 10^7\,\mathrm{cm^{-3}}$), however, Aikawa et al. predict that the $N(NH_3)$ will begin to decrease towards the core centre due to depletion, while $N(N_2H^+)$ continues to increase, leading to a higher fractional $N_2H^+$ abundance relative to $NH_3$ at later times. This prediction is in agreement with $X(NH_3)/X(N_2H^+)$ results since B2 is more evolved than B1, having already formed protostars, but seems inconsistent with the common slope we find for the decrease in $X(NH_3)$ and $X(N_2H^+)$ with $N(H_2)$ in both Cores. Detailed modelling of the physical and chemical structure of the (non-spherical and clumpy) Cores is beyond the scope of this study, but would help to constrain the central density and abundance structure as a function of Core radius needed for a direct comparison with the Aikawa et al. models.

### 3.5.4 Are $N_2H^+$ and $NH_3$ tracing the Oph B Core interior?

The hyperfine structure of the $NH_3$ (1,1) inversion transition allows the calculation of volume density $n_{ex}$ as in Equation 3.1, with the opacity of a typical hyperfine component $\tau_{hf} = 0.233\tau$. The resulting mean density $n_{ex,\mathrm{NH_3}} = 7.8 \times 10^3\,\mathrm{cm^{-3}}$ and $n_{ex,\mathrm{NH_3}} = 1.7 \times 10^4\,\mathrm{cm^{-3}}$ for Oph B1 and B2, respectively (note that these values are slightly less than reported in Chapter 2 due to using the larger $18''$ beam FWHM). These volume densities are a factor $\gtrsim 20$ less than those calculated in §3.4.1 from $N_2H^+$ 1-0 emission ($\sim 26$ in B1 and $\sim 18$ in B2). There is some question whether the $NH_3$ volume densities are accurate, as recent studies (Chapter 2; Foster et al. 2009)

have found $NH_3$-derived $n_{ex}$ values which are an order of magnitude less ($10^4\,cm^{-3}$ versus $10^5\,cm^{-3}$ and greater) than volume densities determined from continuum emission. One possible source of error is the collisional de-excitation rate coefficient, $\gamma_{ul}$, which Foster et al. note is reported in various publications with factor of $\sim 10$ variation. Since $n_{cr} = A_{ul} \,/\, \gamma_{ul}$, the critical density used in Equation 3.1 is therefore also suspect within $\sim 10$.

It is clear that in Oph B $NH_3$ and $N_2H^+$ are tracing different motions in the gas. The gas traced by $N_2H^+$ emission is significantly more quiescent, as has been observed in high density gas in other star forming cores. The fact that higher densities are calculated from $N_2H^+$ emission relative to those calculated from $NH_3$ emission is thus reasonable, and bolsters the hypothesis that $NH_3$ (1,1) emission is not tracing the highest density gas.

In agreement with results in Chapter 2, we find that the clumps found in $N_2H^+$ emission also do not match well continuum clump locations, and significant offsets between $N_2H^+$ and continuum emission are also apparent in the integrated intensity maps. In particular, both the single dish and interferometer integrated $N_2H^+$ 1-0 intensity towards the continuum clump B2-MM8 peak offset to the clump, and in the interferometer data we see an integrated intensity minimum at the MM8 location. On larger scales, we find a trend of *decreasing* $N_2H^+$ abundance with increasing $H_2$ column density, described above, with a slope in Oph B2 that agrees within uncertainties with that determined for $N(NH_3)$ versus $N(H_2)$ for both Oph B1 and B2 (see §3.5.1 and §3.5.3).

## 3.6 Summary

We have presented Nobeyama Radio Telescope (18″ FWHM) and Australia Telescope Compact Array (8″ × 5″ FWHM) $N_2H^+$ 1-0 observations of the Ophiuchus B Core. Our main results are summarized below.

1. The integrated $N_2H^+$ 1-0 intensity is smooth at 18″ resolution, and follows generally the 850 $\mu$m continuum emission in the Core as expected from studies of isolated regions, but significant offsets are found between continuum emission and $N_2H^+$ integrated intensity peaks. $N_2H^+$ clumps identified through the 3D CLUMPFIND algo-

rithm correlate well with those previously found in $NH_3$ emission, but do not correlate well with continuum objects. Closer correspondence between continuum and $N_2H^+$ clump locations is found in Oph B1 compared with B2, suggesting $N_2H^+$ is better tracing dense gas in this Core.

2. We find small-scale structure in B2 through high resolution ATCA $N_2H^+$ 1-0 data. Towards the continuum object B2-MM8, we find a broken ring of integrated $N_2H^+$ emission suggestive of $N_2H^+$ depletion. The line widths of the $N_2H^+$ emission at high resolution are universally narrower by factors $\gtrsim 2$ than seen in the single-dish data. Some small scale $N_2H^+$ structures show velocity gradients which, if due to rotation, are substantially larger than typically seen in star forming cores at lower spatial resolution, but are similar to other interferometric results.

3. Over all $H_2$ column densities, line widths in Oph B2 are dominated by transonic non-thermal line widths, while non-thermal motions Oph B1 are subsonic. This result shows that $N_2H^+$ and $NH_3$ are not tracing the same material in Oph B, as $NH_3$ line widths were shown in Chapter 2 to be large and supersonic in both Cores. Attempting to determine a kinetic temperature by forcing equal non-thermal contributions to the $NH_3$ and $N_2H^+$ line widths produces unphysical results.

4. We find double-peaked $N_2H^+$ line profiles in Oph B1. The blue line component is found to match the $v_{LSR}$ of the ambient cloud as traced by $NH_3$ off-Core emission, while the $v_{LSR}$ of the red line component matches the $NH_3$ Core gas. The $v_{\rm LSR}$ of optically thin $C_2S$ emission also appears to match better that of the ambient cloud, suggesting that Oph B1 is accreting gas from its surroundings. Accretion may cause the co-located continuum clump (currently stable against gravitational collapse) to become unstable and form a low mass protostar.

5. We find a larger $NH_3$ fractional abundance relative to $N_2H^+$ in starless Oph B1 compared with protostellar Oph B2. This result is in agreement with other studies. Chemical models of collapsing cores produce relatively high $N(NH_3)$ at moderate densities ($n \sim 10^{5-6}\,\mathrm{cm}^{-3}$) and relatively high $N(N_2H^+)$ at high densities ($n \sim 10^{6-7}\,\mathrm{cm}^{-3}$), in agreement with our results.

6. We find a trend of decreasing fractional $N_2H^+$ abundance with increasing $H_2$ column density, as traced by $850\,\mu$m continuum emission. If due to $N_2H^+$ depletion, this could explain the offsets between continuum and $N_2H^+$ clumps we find in Oph

B, and suggests that deuterated species, such as $H_2D^+$, may be the best tracers of the physical conditions of dense, cluster-forming Cores.

# Chapter 4

# The Deuterium Fractionation of the Ophiuchus B2 Core

## 4.1 Introduction

The Ophiuchus molecular cloud is a source of ongoing low-mass clustered star formation relatively close to the Sun ($d \sim 120\,\mathrm{pc}$ Lombardi et al. 2008). Through low resolution $DCO^+$ observations, Loren et al. (1990) discovered a number of dense Cores (labelled A through F) in the central Ophiuchus region with masses of a few to several tens of solar masses, which represented a range in evolutionary status given the presence or absence of embedded protostars. Large-scale submillimetre and millimetre observations of Ophiuchus identified several new Cores, and revealed the Cores were further fragmented into multiple dense clumps, each with masses $M \lesssim 1\,\mathrm{M}_\odot$ (Motte et al. 1998; Johnstone et al. 2000b, 2004). Analysis of the clump kinematics suggest most are in virial equilibrium and hence not transient objects (André et al. 2007). Recent Spitzer Space Telescope studies of infrared emission towards the Cores have characterized in detail the starless and protostellar clump population (Jørgensen et al. 2008; Enoch et al. 2009). The dense Cores in Ophiuchus are thus ideal locations to study the physical characteristics of dense Cores in the process of forming small stellar clusters.

To characterize the physical properties of the dense, cluster forming Ophiuchus

Cores, we have studied the Oph B, C and F Cores through high resolution $NH_3$ (1,1) and (2,2) observations (Friesen et al. 2009b, hereafter Chapter 2), and the Oph B Core in both single-dish and interferometer $N_2H^+$ 1-0 emission (Friesen et al. 2009a, hereafter Chapter 3). The $NH_3$ and $N_2H^+$ observations probe gas at densities $n \sim 10^4\,\mathrm{cm}^{-3}$ and $n \sim 10^5\,\mathrm{cm}^{-3}$, respectively.

In Chapter 2, we identified (through the 3D CLUMPFIND structure-finding algorithm; Williams et al. 1994) a number of individual clumps in $NH_3$ emission in the Cores, which did not correlate well with those identified in continuum emission. We determined that the B and F cores were warmer on average than typically found for isolated cores (mean $T_K \sim 15\,\mathrm{K}$), and we found no trend with temperatures and $H_2$ column density calculated from submillimetre continuum emission. In contrast, Oph C is colder, with temperatures decreasing to a minimum of 9 K at the dust continuum emission peak. Line widths in both the Oph B1 and B2 sub-Cores were found to be wide and transonic, despite the presence of three embedded protostars in B2 and none in B1. Oph F, with four embedded protostars, has regions of narrow and wide line widths and complicated line structures. Again similar to isolated objects, $NH_3$ line widths in Oph C are extremely narrow and consistent with being due to purely thermal motions. In an interesting result, the fractional abundance of $NH_3$ with respect to $H_2$, $X(NH_3)$, appeared to decrease with increasing $H_2$ column density, $N(H_2)$, suggesting $NH_3$ may be depleted towards locations of high column density and thus may not be tracing the densest Core gas. Finally, Chapter 2 revealed that Cores with characteristics of both isolated and clustered environments can coexist in a clustered star forming environment.

In Chapter 3, we again used CLUMPFIND to identify small-scale structure in $N_2H^+$ emission from the Oph B Core and found that the $N_2H^+$ clumps matched well $NH_3$ clumps from Chapter 2, and were consequently again offset from continuum objects. In both studies, little difference was found in the gas properties towards embedded protostars compared with the general Core gas. Line widths in Oph B2 remain large at the densities traced by $N_2H^+$. In B1, however, $N_2H^+$ line widths are significantly narrower than found in $NH_3$ emission. Applying the gas temperatures determined in Chapter 2, we found that motions in Oph B1 were subsonic with a mean ratio of non-thermal line width to sound speed $\sigma_{\mathrm{NT}}/c_s = 0.7$ across the Core, while in B2 $\sigma_{\mathrm{NT}}/c_s = 1.3$. A clear trend of decreasing $X(N_2H^+)$ with increasing $N(H_2)$ was found towards Oph B2, with emission suggestive of a $N_2H^+$ hole towards the continuum

emission peak found in high resolution $N_2H^+$ emission observed with the Australia Telescope Compact Array.

The results of $NH_3$ and $N_2H^+$ observations towards Oph B2 in Chapter 2 and Chapter 3 indicate that the highest density Core gas may best be probed by molecular emission lines excited at higher critical densities, or by deuterated molecules which are expected to be abundant in cold cores where significant depletion has occurred. To this end, we present in this chapter $N_2D^+$ 3-2, $N_2H^+$ 4-3 and $H_2D^+$ $1_{11} - 1_{10}$ emission maps of the Oph B2 Core.

In cold molecular cloud cores, the deuteration process is initiated by the reaction

$$H_3^+ + HD \rightleftharpoons H_2D^+ + H_2 \tag{4.1}$$

making $H_2D^+$ a key molecular ion in the enhancement of deuterated species in a molecular core. The reaction shown in Equation 4.1 is exothermic in the forward direction with $\Delta E = 232\,\mathrm{K}$ (Millar et al. 1989). The additional depletion of CO from the gas phase removes a second $H_2D^+$ destruction mechanism (via proton transfer with CO), with the result that $H_2D^+$ forms faster than it is destroyed at the low temperatures characteristic of starless cores ($T \sim 10 - 15\,\mathrm{K}$) .

In the following sections, we present the observations in §4.2, and discuss the observed distributions of $N_2D^+$ 3-2, $H_2D^+$ $1_{11} - 1_{10}$ and $N_2H^+$ 4-3 in §4.3. We fit the observed spectra with a single Gaussian (for $H_2D^+$) or a multiple-component Gaussian (for $N_2D^+$ and $N_2H^+$ due to their hyperfine line structure) and discuss the line velocity centroids and widths in §4.4, and also present column density and fractional abundance calculations. In §4.5 we look at the non-thermal line widths in Oph B2 as a function of critical density of the observed emission lines, and discuss trends in the deuterium fractionation. Finally, we present a lower limit to the electron abundance in B2, and summarize our results in §4.6.

Table 4.1. Observed Species, Transitions and Frequencies

| Species | Transition | Frequency GHz |
|---|---|---|
| $N_2D^+$ | $3-2$ | 231.321961431[a] |
| $N_2H^+$ | $4-3$ | 372.67251[b] |
| $H_2D^+$ | $1_{11}-1_{10}$ | 372.42134[b] |

[a]Gerin et al. (2001)

[b]Pickett et al. (1998)

## 4.2 Observations

In the following section we discuss the observations presented in this chapter. We list the species, transitions, and rest frequencies observed in Table 4.1.

### 4.2.1 $N_2D^+$ at IRAM

An On-The-Fly (OTF) map of the $N_2D^+$ 3-2 line at 231.321 GHz in Oph B2 was made at the Institut de Radio Astronomie Millimetrique (IRAM) 30 m Telescope during the 2007 and 2008 winter semesters using the HEterodyne Receiver Array (HERA, Schuster et al. 2004). HERA is a multi-beam spectral line receiver with nine dual polarization pixels arranged in a $3 \times 3$ array, with pixels separated by $24''$ [approximately twice the 231 GHz $11''$ half power beam width (FWHP)]. The maps were performed with the array tracking the sky rotation, and rotated by $9.5^\circ$ with respect to the equatorial system, such that the spacing between OTF lines was $4''$. Observations were frequency-switched in-band with a throw of $2 \times 6.9$ MHz. The Versatile Spectrometer Assembly (VESPA) autocorrelator was used as the backend, with a 20 MHz bandwidth and 40 kHz channel spacing, corresponding to 0.05 km s$^{-1}$ per channel at 231 GHz.

The data were calibrated to $T_A^*$ units at the telescope using the Multichannel Imaging and Calibration Software for Receiver Arrays (MIRA). Further calibration,

including baselining and folding of the frequency-switched spectra, was performed using the CLASS software package[1]. The data were smoothed by two spectral channels along the frequency axis to improve sensitivity, for a final spectral resolution of 20 kHz, or 0.1 km s$^{-1}$. A second-order polynomial baseline was fitted to the non-line channels and subtracted from the individual spectra before folding the data. The forward ($F_{eff}$) and beam ($B_{eff}$) efficiencies of the telescope were interpolated from determined values at 210 GHz and 260 GHz, giving $F_{eff} = 0.92$ and $B_{eff} = 0.58$ at 231 GHz. The data were then calibrated to main beam temperature via the relation $T_{MB} = (F_{eff} \,/\, B_{eff})\, T_A^*$. For comparison with the $N_2H^+$ 1-0 results in Chapter 3, we further converted the data to units of Jy / beam$^{-1}$ and convolved the map to a final angular resolution of 18″ to match the $N_2H^+$ data.

As the observations were performed in a pooled mode, the 4′ × 3′ map was observed in three 4′ × 1′ strips to ensure good sensitivity in potentially limited time. Two-thirds of the map was completed in this manner in winter 2007, while the remaining strip was observed in winter 2008. The sensitivity of the map is consequently not entirely uniform, with the rms noise in the most southern 4′ × 1′ strip greater [0.15 K ($T_{MB}$)] than in the rest of the map [0.08 K ($T_{MB}$)]. Most emission was found in the central and northern map sections, however, so this noise increase does not affect our results significantly.

### 4.2.2 $H_2D^+$ and $N_2H^+$ at the JCMT

Simultaneous observations of the $H_2D^+$ $1_{10} - 1_{11}$ and $N_2H^+$ 4-3 emission lines at 372.4 GHz and 372.7 GHz, respectively, were performed at the JCMT over the 07A - 08B semesters using the 16-receptor Heterodyne Array Receiver Program B-band receiver (HARP-B, Smith et al. 2008). HARP-B is a 4 × 4 pixel array, with array spacing of 30″ and a 2′ × 2′ footprint. The JCMT beam at 372 GHz is ∼ 11″ FWHM. We used the ACSIS correlator as the backend, configured to have a 400 MHz effective bandwidth (e.g., wide enough to encompass both lines), tuned halfway in frequency between the two lines, and a frequency resolution of 61 kHz, or 0.05 km s$^{-1}$ at 372.4 GHz. Observations of five separate HARP footprints were performed in position-switching mode to create an undersampled map of $H_2D^+$ and $N_2H^+$ over the

[1] see http://www.iram.fr/IRAMFR/GILDAS.

Oph B2 Core. The footprints were placed such that the final beam spacing on the sky is $21''$ with a coverage of $\sim 4' \times 2'$. The fifth footprint provided additional coverage towards the location of peak continuum emission in B2, but has lower sensitivity compared with the other footprints. The observations were performed in band 1 weather only ($\tau_{225\,GHz} < 0.05$) and generally while Ophiuchus was above $30^\circ$ in elevation. The mean rms across the $H_2D^+$ map is 0.04 K ($T_A^*$) and 0.05 K ($T_A^*$) across the $N_2H^+$ map. The main beam efficiency at 372 GHz is not currently well-known. We therefore estimate $\eta_{MB} \sim 0.6$, slightly less than standard measurements at 345 GHz, with an uncertainty of $\sim 10\%$.

Data reduction was performed using the Starlink software package. Each night's data were first checked for noisy or malfunctioning pixels, and these pixels were flagged individually for each integration. A linear baseline was then removed from each integration, and the data were combined into a final cube with $15''$ pixels. To increase sensitivity, the data were averaged along the velocity axis by 2 channels, giving a final velocity resolution of $0.1\,\mathrm{km\,s^{-1}}$.

## 4.3 Results

We first discuss the integrated intensity of $N_2D^+$ 3-2, $H_2D^+$ $1_{11} - 1_{10}$ and $N_2H^+$ 4-3 over the Oph B2 Core and compare the species distributions with submillimetre continuum emission and the locations of embedded protostars in the Core.

In Figure 4.1a, we show the integrated $N_2D^+$ 3-2 intensity (convolved to $18''$ resolution as described in §4.2.1) in Oph B2 against contours of 850 $\mu$m continuum emission observed at the JCMT at $15''$ FWHM resolution. The locations of 850 $\mu$m continuum clumps (Jørgensen et al. 2008) and embedded Class I protostars (Enoch et al. 2009) are also identified. The $N_2D^+$ emission is confined to the northern edge of the B2 Core, and avoids entirely areas near the embedded protostars. Additionally, little $N_2D^+$ is seen towards the continuum emission peak. The $N_2D^+$ emission generally follows the continuum contours in the north, but a very close correspondence is only seen towards the north-east tip of B2. Three maxima of integrated intensity are present, of which two are co-located with continuum clumps, while the third is seen to the north-west of the continuum peak.

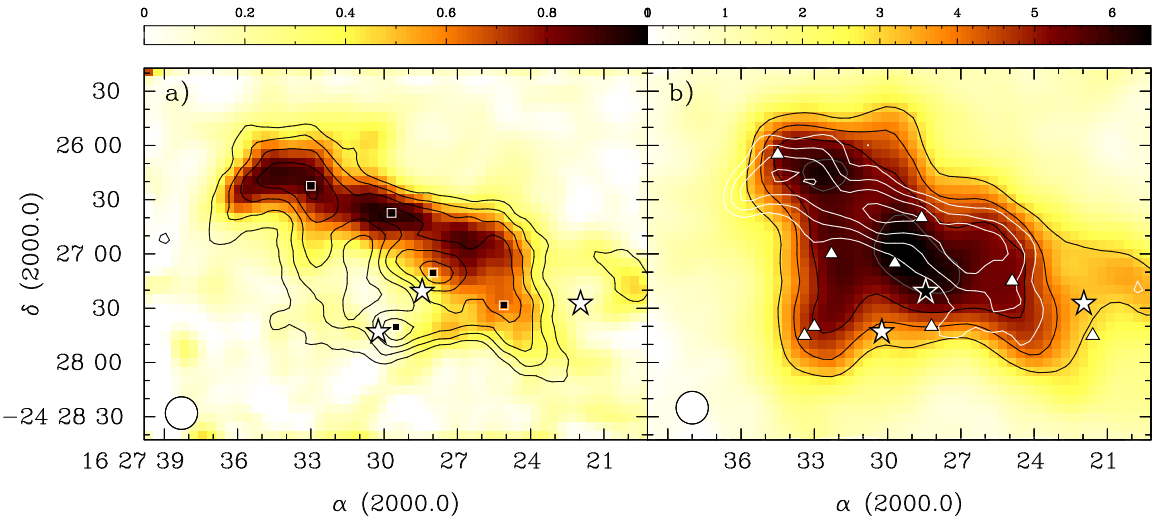


Figure 4.1 a) Integrated $N_2D^+$ 3-2 emission towards Oph B2 (greyscale) in $T_B$ units. Data have been convolved to a final 18″ beam (FWHM). Black contours show 850 $\mu$m continuum emission in increments of 0.1 Jy beam$^{-1}$. Squares show the locations of continuum clumps identified by Jørgensen et al. (2008). In both plots, stars indicate the positions of Class I protostars and the 18″ beam is shown at lower left. b) $N_2H^+$ 1-0 emission towards Oph B2 observed with the Nobeyama 45 m Telescope at 18″ (FWHM) resolution (Chapter 3). Black and grey contours begin at 3 K km s$^{-1}$ ($T_{MB}$) and increase by 1 K km s$^{-1}$. Triangles show the peak locations of $N_2H^+$ clumps identified with CLUMPFIND. White contours trace $N_2D^+$ emission from a), beginning at 0.45 K km s$^{-1}$ ($T_B$) and increasing by 0.15 K km s$^{-1}$.

In Figure 4.1b, we plot the $N_2D^+$ 3-2 integrated intensity contours over a map of $N_2H^+$ 1-0 integrated intensity, observed with the Nobeyama 45 m Telescope at 18″ resolution. The $N_2H^+$ observations and analysis were presented in Chapter 3. We also show the locations of $N_2H^+$ clumps, identified through the structure-finding algorithm CLUMPFIND (Williams et al. 1994) in Chapter 3. Overall, $N_2D^+$ emission is found within the extent of $N_2H^+$ 1-0 emission. In a similar fashion to the continuum emission, however, we find offsets between the locations of peak $N_2D^+$ and $N_2H^+$ integrated intensity. In particular, the $N_2D^+$ integrated intensity maximum is offset from the integrated $N_2H^+$ 1-0 maximum in B2 by $\sim 20''$ to the northeast. The $N_2H^+$ 1-0 integrated intensity maximum is itself offset to the east from the continuum peak by $\sim 22''$ (Chapter 3). The northeastern $N_2D^+$ integrated intensity peak, which corresponds well with continuum contours, is also offset from the integrated $N_2H^+$ intensity peak by $\sim 20''$ to the east. Since $N_2D^+$ forms from $N_2H^+$, this offset is unexpected, and provides the basis for a discussion of Oph B2's dense gas chemistry

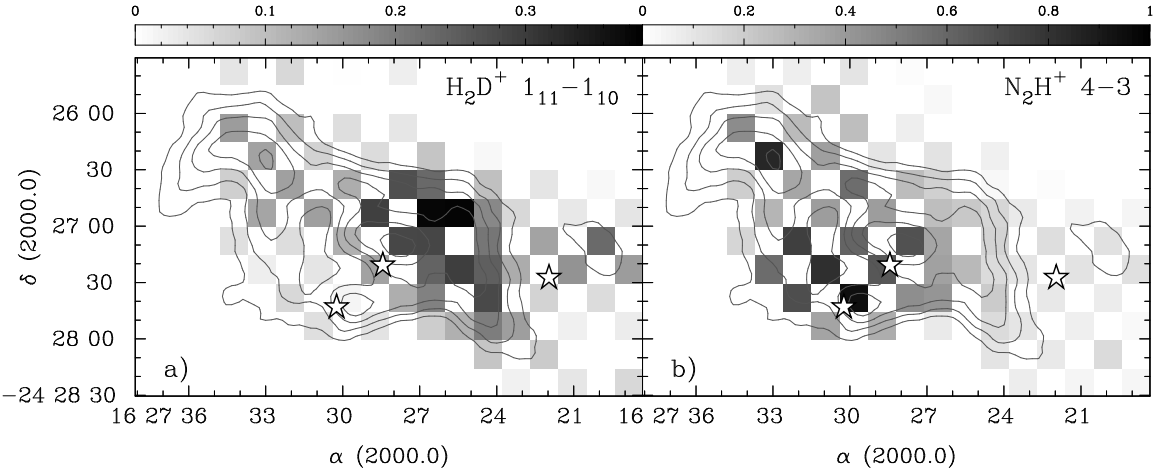


Figure 4.2 a) Integrated $H_2D^+$ $1_{11} - 1_{10}$ intensity towards Oph B2 (greyscale) in $\mathrm{K\,km\,s^{-1}}$ ($T_A^*$) units. The undersampled map is shown with 15″ pixels showing the spacing of beams in five overlapping footprints with the HARP array. The beam FWHM was $\sim 11''$. In both plots, grey contours show 850 $\mu$m continuum emission observed with 15″ FWHM at the JCMT in intervals of 0.1 $\mathrm{Jy\,beam^{-1}}$. Stars show the positions of Class I protostars. b) Integrated $N_2H^+$ 4-3 intensity towards Oph B2 (greyscale) in $\mathrm{K\,km\,s^{-1}}$ ($T_A^*$) units. Pixels and beam as in a).

in §4.5.2.

We show in Figure 4.2a the distribution of $H_2D^+ 1_{11} - 1_{10}$ integrated intensity across Oph B2 with overlaid 850 $\mu$m continuum contours. We find that significant $H_2D^+$ is present over several much of Oph B2, with a larger extent than found in $H_2D^+$ observations towards any other cores so far observed (Caselli et al. 2003; Pagani et al. 2009). Similarly to the $N_2D^+$ emission described above, the $H_2D^+$ emission again follows generally the continuum emission but avoids the embedded protostars in B2. While relatively strong emission is seen towards the continuum peak, the $H_2D^+$ integrated intensity maximum is also offset the continuum peak by an estimated $\sim 20 - 30''$ (due to the map's undersampling we are unable to determine exactly the location of maximum integrated intensity). In contrast to the $N_2D^+$ emission the $H_2D^+$ integrated intensity maximum is found to the northwest rather than the northeast, but $N_2D^+$ emission is also found there. We detect some $H_2D^+$ emission in north-east B2 where was found strong $N_2D^+$ emission, but do not see a significant integrated intensity maximum. (Note, however, that the HARP footprints do not extend past an R.A. of 16:27:35, and are therefore not sensitive to any emission at the tip of the continuum contours in this region.) Overall, where $N_2D^+$ emission appears

strongest in the north and east of Oph B2, $H_2D^+$ emission is strongest towards the west edge Oph B2.

In Figure 4.2b, the distribution of $N_2H^+$ 4-3 integrated intensity across Oph B2 is shown with overlaid 850 $\mu$m continuum emission contours. We find $N_2H^+$ 4-3 emission over most of the Core. The locations of bright $N_2H^+$ 4-3 and $H_2D^+$ $1_{11} - 1_{10}$ emission appear almost anti-correlated, with the greatest integrated $N_2H^+$ 4-3 intensity found towards the embedded protostar Elias 33. Additional strong $N_2H^+$ 4-3 emission is found towards the protostar Elias 32 and continuum emission peak, while a separate integrated intensity peak is found in northeast B2 (where we also find strong $N_2D^+$ 3-2 emission). Overall, while the $N_2H^+$ 4-3 emission is generally confined to areas where there is also continuum emission, the strongest $N_2H^+$ 4-3 emission is found away from the brightest continuum contours.

## 4.4 Analysis

### 4.4.1 $N_2H^+$ and $N_2D^+$ multi-component line fitting

The rotational transitions of the linear molecular ions $N_2H^+$ and $N_2D^+$ contain hyperfine structure, which is dominated by the interactions between the molecular electric field gradient and the electric quadrupole moments of the two nitrogen nuclei (Dore et al. 2004). Rotational transitions at higher $J$ contain greater numbers of hyperfine components at smaller frequency intervals, i.e., the satellite components are found more closely spaced and can overlap significantly. In particular, the $N_2H^+$ 4-3 and the $N_2D^+$ 3-2 transitions contain 37 and 25 hyperfine components respectively (Daniel et al. 2006; Gerin et al. 2001).

For $N_2H^+$ 4-3, we calculate the relative line strengths $s_{J\,F1\,F\rightarrow J'\,F1'\,F'}$ from the Einstein A coefficients $A_{J\,F_1\,F\rightarrow J'\,F_1'\,F'}$ and frequencies $\nu_{J\,F_1\,F\rightarrow J'\,F_1'\,F'}$ given by Pagani et al. (2009), using

$$A_{J\,F_1\,F\rightarrow J'\,F_1'\,F'} = \frac{64\pi^4}{3hc^2}\mu^2\nu^3_{J\,F_1\,F\rightarrow J'\,F_1'\,F'}\frac{J}{[F]}s_{J\,F_1\,F\rightarrow J'\,F_1'\,F'} \tag{4.2}$$

where $\mu = 3.4\,\mathrm{D}$ is the permanent electric dipole moment, $J$ is the upper rotational quantum number and $[F] = 2F+1$ accounts for the degeneracy of the hyperfine states. We show the quantum numbers, velocities and relative line strengths of the hyperfine components in Table 4.2. Of the 37 $N_2H^+$ 4-3 hyperfine components, 24 have LTE line strengths which are $< 5\,\%$ of the strongest component. Fourteen components at 8 distinct velocities between $-0.2\,\mathrm{km\,s^{-1}}$ and $0.2\,\mathrm{km\,s^{-1}}$ make up the main centroid emission, resulting in a line profile that is substantially non-Gaussian. Due to the non-Gaussian nature of the line profile, a single Gaussian fits the line emission poorly, as shown in Figure 4.3 where we plot the $N_2H^+$ 4-3 emission towards two embedded protostars in B2, Elias 32 and 33, and the B2-MM8 continuum object which resides at the Oph B continuum emission peak. Overlaid on the $N_2H^+$ emission are both a single Gaussian and the full hyperfine structure fits. In all cases, the hyperfine fit better matches the emission. Note the additional line substructure, in particular the blue shoulder seen towards Elias 32 and B2-MM8, is not due to hyperfine structure of the $N_2H^+$ line and we discuss the source of the line asymmetries further in §4.4.3.

Table 4.2. $N_2H^+$ 4-3 hyperfine components, velocities and LTE line strengths

| J | $F_1$ | F | J′ | $F'_1$ | F′ | Velocity $km\,s^{-1}$ | Line strength |
|---|---|---|---|---|---|---|---|
| 4 | 4 | 4 | 3 | 4 | 5 | 1.9860 | 0.0031 |
| 4 | 4 | 3 | 3 | 4 | 3 | 1.6592 | 0.0456 |
| 4 | 4 | 5 | 3 | 4 | 5 | 1.6340 | 0.0733 |
| 4 | 4 | 4 | 3 | 4 | 4 | 1.6340 | 0.0564 |
| 4 | 4 | 5 | 3 | 4 | 4 | 1.2821 | 0.0031 |
| 4 | 4 | 3 | 3 | 4 | 4 | 1.2569 | 0.0030 |
| 4 | 3 | 3 | 3 | 2 | 3 | 0.5028 | 0.0794 |
| 4 | 5 | 5 | 3 | 4 | 5 | 0.4022 | 0.0489 |
| 4 | 4 | 4 | 3 | 3 | 4 | 0.4022 | 0.0586 |
| 4 | 3 | 3 | 3 | 2 | 2 | 0.2011 | 0.6350 |
| 4 | 3 | 2 | 3 | 2 | 1 | 0.2011 | 0.4286 |
| 4 | 3 | 4 | 3 | 2 | 3 | 0.1508 | 0.9185 |
| 4 | 3 | 3 | 3 | 4 | 3 | 0.1006 | 0.0001 |
| 4 | 3 | 2 | 3 | 2 | 3 | 0.1006 | 0.0023 |
| 4 | 4 | 4 | 3 | 3 | 3 | 0.0754 | 0.8788 |
| 4 | 4 | 3 | 3 | 3 | 2 | 0.0754 | 0.6697 |
| 4 | 4 | 5 | 3 | 3 | 4 | 0.0503 | 1.1459 |
| 4 | 5 | 4 | 3 | 4 | 3 | 0.0251 | 0.9505 |
| 4 | 5 | 5 | 3 | 4 | 4 | 0.0251 | 1.1732 |
| 4 | 4 | 3 | 3 | 3 | 4 | 0.0251 | 0.0009 |
| 4 | 5 | 6 | 3 | 4 | 5 | 0.0000 | 1.4443 |
| 4 | 5 | 4 | 3 | 4 | 5 | 0.0000 | 0.0005 |
| 4 | 3 | 2 | 3 | 2 | 2 | -0.2011 | 0.0794 |
| 4 | 3 | 4 | 3 | 4 | 3 | -0.2514 | 0.0000 |
| 4 | 4 | 3 | 3 | 3 | 3 | -0.2765 | 0.0586 |
| 4 | 3 | 4 | 3 | 4 | 5 | -0.3017 | 0.0012 |
| 4 | 3 | 2 | 3 | 4 | 3 | -0.3017 | 0.0007 |

Table 4.2 (cont'd)

| J | $F_1$ | F | J′ | $F'_1$ | F′ | Velocity $km\,s^{-1}$ | Line strength |
|---|---|---|---|---|---|---|---|
| 4 | 3 | 3 | 3 | 4 | 4 | -0.3017 | 0.0009 |
| 4 | 5 | 4 | 3 | 4 | 4 | -0.3771 | 0.0489 |
| 4 | 3 | 4 | 3 | 4 | 4 | -0.6536 | 0.0001 |
| 4 | 3 | 3 | 3 | 3 | 2 | -1.4832 | 0.0050 |
| 4 | 3 | 3 | 3 | 3 | 4 | -1.5335 | 0.0050 |
| 4 | 3 | 3 | 3 | 3 | 3 | -1.8351 | 0.0525 |
| 4 | 3 | 4 | 3 | 3 | 4 | -1.8854 | 0.0753 |
| 4 | 3 | 2 | 3 | 3 | 2 | -1.8854 | 0.0397 |
| 4 | 3 | 4 | 3 | 3 | 3 | -2.1871 | 0.0050 |
| 4 | 3 | 2 | 3 | 3 | 3 | -2.2373 | 0.0050 |

For $N_2D^+$ 3-2, we take the hyperfine line component velocities and strengths from Gerin et al. (2001). Similarly to $N_2H^+$ 4-3, the main $N_2D^+$ 3-2 line centroid is comprised of six separate components at four distinct velocities, creating a non-Gaussian line profile. No satellite line structure was visible in the $N_2D^+$ observations.

We fit the hyperfine structure at each pixel with a custom Gaussian hyperfine structure fitting routine written in IDL, described in detail in Chapter 2, assuming local thermodynamic equilibrium (LTE) and equal excitation temperatures $T_{ex}$ for each hyperfine component. The line fitting routine does not take into account the significant overlap between hyperfine components in both the $N_2H^+$ and $N_2D^+$ transitions, but we find the total line opacities are small ($< 1$, see §4.4.4) and we therefore do not expect line overlap to introduce substantial errors. We are able to fit very well the line centroid local standard of rest (LSR) velocity, $v_{LSR}$, and the line width, $\Delta v$, for both lines using the hyperfine structure fitting routine. For $N_2H^+$ 4-3, we are additionally able to fit reasonably well the excitation temperature $T_{ex}$ and total line opacity $\tau$, defined as the sum of the opacities of the individual hyperfine components, despite the lack of satellite line structure visible in our observations. At low opacities, there is a degeneracy between $\tau$ and $T_{ex}$ such that it becomes impossible to solve for both parameters, but we show in §4.4.4 that the values we determine are reasonable.

The line widths are artificially broadened by the velocity resolution of the obser-

vations ($0.05\,\mathrm{km\,s^{-1}}$). We therefore subtracted in quadrature the resolution width, $\Delta v_{res}$, from the observed line width, $\Delta v_{obs}$, such that $\Delta v_{line} = \sqrt{\Delta v_{obs}^2 - \Delta v_{res}^2}$. In the following, we simply use $\Delta v = \Delta v_{line}$ for clarity.

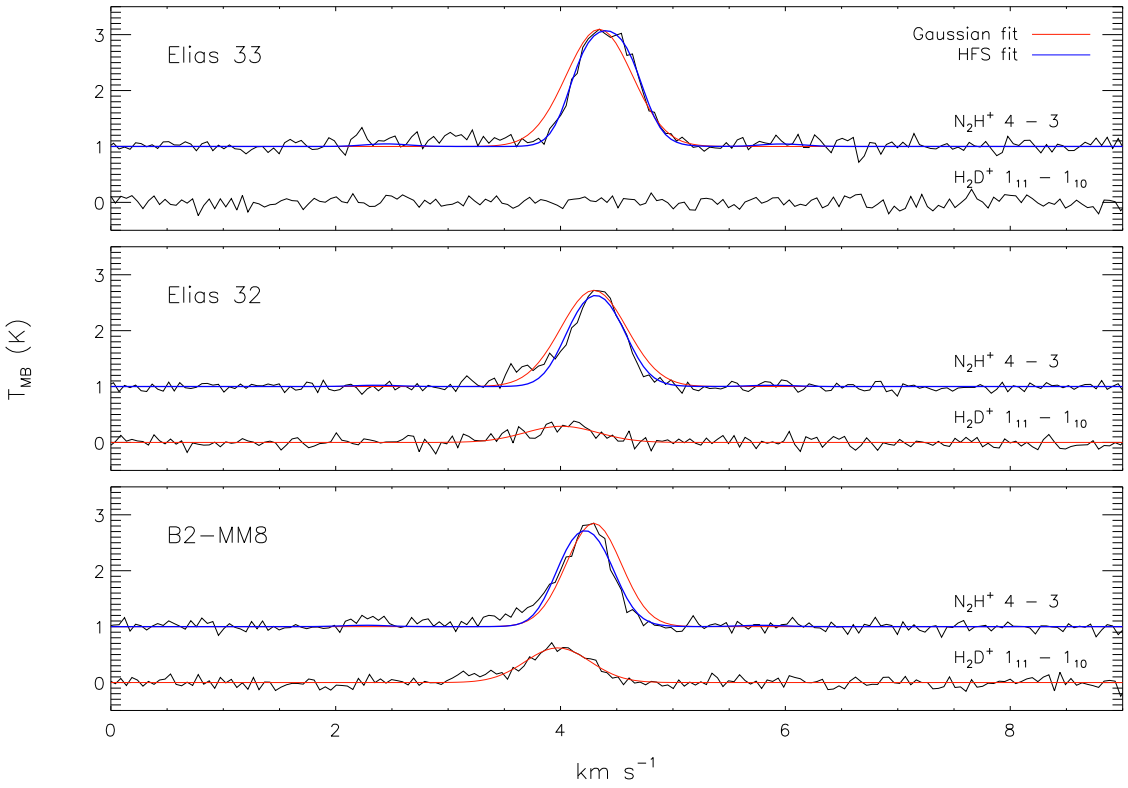


Figure 4.3 $N_2H^+$ 4-3 and $H_2D^+1_{11} - 1_{10}$ spectra and fits towards the two Class I protostars, Elias 33 and Elias 32, and the 1 mm continuum object B2-MM8 (Motte et al. 1998).

The uncertainties reported in the returned parameters are those determined by the fitting routine, and do not take the calibration uncertainty into account. The calibration uncertainty does not affect the uncertainties returned for $v_{\rm LSR}$ or $\Delta v$. The excitation temperature, column densities and fractional abundances discussed further below, however, are dependent on the amplitude of the line emission, and are thus affected by the absolute calibration uncertainty.

We are unable to fit well the $N_2D^+$ 3-2 hyperfine structure solving for both $\tau$ and $T_{ex}$. Instead, we set the excitation temperature at each pixel to $T_{ex}$ values derived in Chapter 3 through hyperfine fitting of $N_2H^+$ 1-0 emission observed in Oph B2 (shown in Figure 4.1b). In LTE, we expect the equal $T_{ex}$ to describe the excitation

of all rotational levels of $N_2H^+$. $N_2D^+$ is formed directly from $N_2H^+$, and we show in Figure 4.1 that the distributions of the two species are similar in B2. We thus expect this approximation to be valid. Accordingly, in a recent study of $N_2H^+$ and $N_2D^+$ emission in L1544, Caselli et al. (2002b) were able to determine separately the excitation temperatures for $N_2H^+$ 1-0, 3-2 and $N_2D^+$ 2-1 and 3-2, and found they were consistent within uncertainties.

### 4.4.2 $H_2D^+$ Gaussian line fitting

The $H_2D^+$ $1_{11} - 1_{10}$ emission line has no hyperfine structure. We consequently fit the emission at each pixel with a single Gaussian (again in IDL) to determine the line $v_{LSR}$ and $\Delta v$ across Oph B2. In addition to $N_2H^+$ 4-3 emission, Figure 4.3 also shows the $H_2D^+$ emission towards Elias 32, 33 and B2-MM8 with overlaid Gaussian fits. Note that no significant $H_2D^+$ emission was detected towards Elias 33.

### 4.4.3 Centroid velocity and line widths

Table 4.4 lists the mean, rms, minimum and maximum values of $v_{LSR}$ and $\Delta v$ for $N_2H^+$ 4-3, $N_2D^+$ 3-2, and $H_2D^+$ $1_{11} - 1_{10}$, along with the same results from $NH_3$ (1,1) and $N_2H^+$ 1-0 presented in Chapter 2 and Chapter 3 for comparison.

We show in Figure 4.4 the $N_2D^+$ $v_{\rm LSR}$ and $\Delta v$ over Oph B2. We only plot values where the S/N ratio of the peak line intensity was $\geq 5$. The mean $v_{\rm LSR}$ across B2 is $4.05\,{\rm km\,s^{-1}}$ with an rms variation of $0.25\,{\rm km\,s^{-1}}$. Lower $v_{\rm LSR}$ values are found towards the western and northeastern regions of the Core, with the maximum $v_{\rm LSR}$ $= 4.44\,{\rm km\,s^{-1}}$ in the east towards the $N_2H^+$ 1-0 clump B2-N6 identified in Chapter 3. The variation in $v_{\rm LSR}$ is therefore not indicative of global rotation of the Core. The $N_2D^+$ line velocities shift between $3.7\,{\rm km\,s^{-1}}$ to $4.4\,{\rm km\,s^{-1}}$ over $\sim 40''$, or $\sim 4800\,{\rm AU}$, to the west of the embedded Class I protostar Elias 32. In this same region, the line $v_{\rm LSR}$ shifts from $3.7\,{\rm km\,s^{-1}}$ to $4.2\,{\rm km\,s^{-1}}$ on either side of the western embedded protostar. In both regions, a good fit to the $N_2D^+$ line was not found between the $v_{\rm LSR}$ minima and maxima.

The mean $N_2D^+$ 3-2 line width $\Delta v = 0.53\,{\rm km\,s^{-1}}$ with an rms variation of

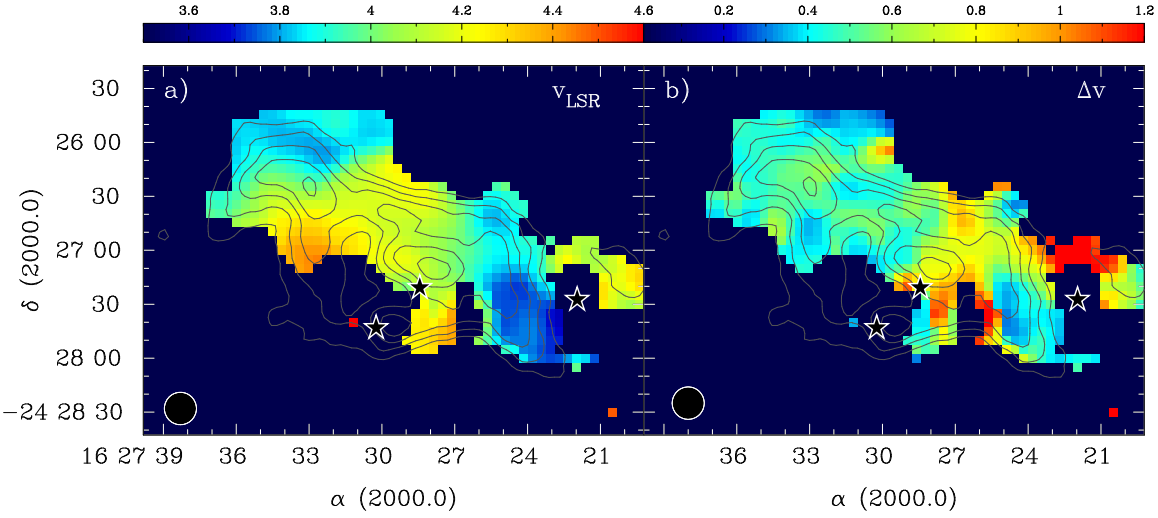


Figure 4.4 a) $N_2D^+$ 3-2 line velocity or $v_{LSR}$ in Oph B2. Colour scale is in $\mathrm{km\,s^{-1}}$. Only results from pixels where the S/N of the peak line intensity is $\geq 5$ are shown. In all plots, contours show 850 $\mu$m continuum emission at 15″ (FWHM) resolution observed with the JCMT (Johnstone et al. 2000b), in increments of $0.1\,\mathrm{Jy\,beam^{-1}}$. The 18″ (FWHM) beam is shown at lower left. Stars indicate the positions of Class I protostars. b) Fitted $\Delta v$ in Oph B2. Colour scale is in $\mathrm{km\,s^{-1}}$.

$0.20\,\mathrm{km\,s^{-1}}$. In general, the widest line widths are found near the embedded protostars, to a maximum $\Delta v = 1.36\,\mathrm{km\,s^{-1}}$ in eastern B2 (but note the largest $\Delta v$ values are found only $\sim 45''$ to the northwest of some of the narrowest $\Delta v$ values). Away from the protostars, only small variations in the relatively narrow line widths are seen, notably towards the northeast and southwest, with $\Delta v \sim 0.3\,\mathrm{km\,s^{-1}}$. Two objects are associated with localized narrow $\Delta v$. An 850 $\mu$m continuum clump (16275-24273, Jørgensen et al. 2008), shown on the image, was identified where the southwestern narrow line widths are found. In the east, the B2-N6 $N_2H^+$ clump (labelled on Figure 4.4, Chapter 2) is also associated with a $\Delta v$ minimum of $0.36\,\mathrm{km\,s^{-1}}$. This is similar to the clump line width in $N_2H^+$ 1-0 emission at 18″ resolution, but nearly a factor of two larger than found in $N_2H^+$ 1-0 interferometer observations of the clump presented in Chapter 3.

In Figure 4.5a and Figure 4.5c we show the $v_{\rm LSR}$ determined through Gaussian fitting of the $H_2D^+$ $1_{11} - 1_{10}$ and hyperfine structure fitting of the $N_2H^+$ 4-3 lines, respectively. Visual inspection of the $v_{\rm LSR}$ values shows that the $H_2D^+$ emission is similar kinematically to the $N_2D^+$ 4-3 values in Figure 4.4a, while a small shift in $v_{\rm LSR}$ of $\sim +0.2\,\mathrm{km\,s^{-1}}$ is seen in $N_2H^+$ 4-3 emission towards Elias 32 and the 850 $\mu$m

continuum emission peak and co-located continuum clump B2-MM8. The offset in $v_{\rm LSR}$ between $H_2D^+$ and $N_2H^+$ is also clearly seen in the spectra plotted in Figure 4.3. The shift is small but significant given the otherwise excellent agreement in $v_{\rm LSR}$ between the different tracers over the Core (see Table 4.4).

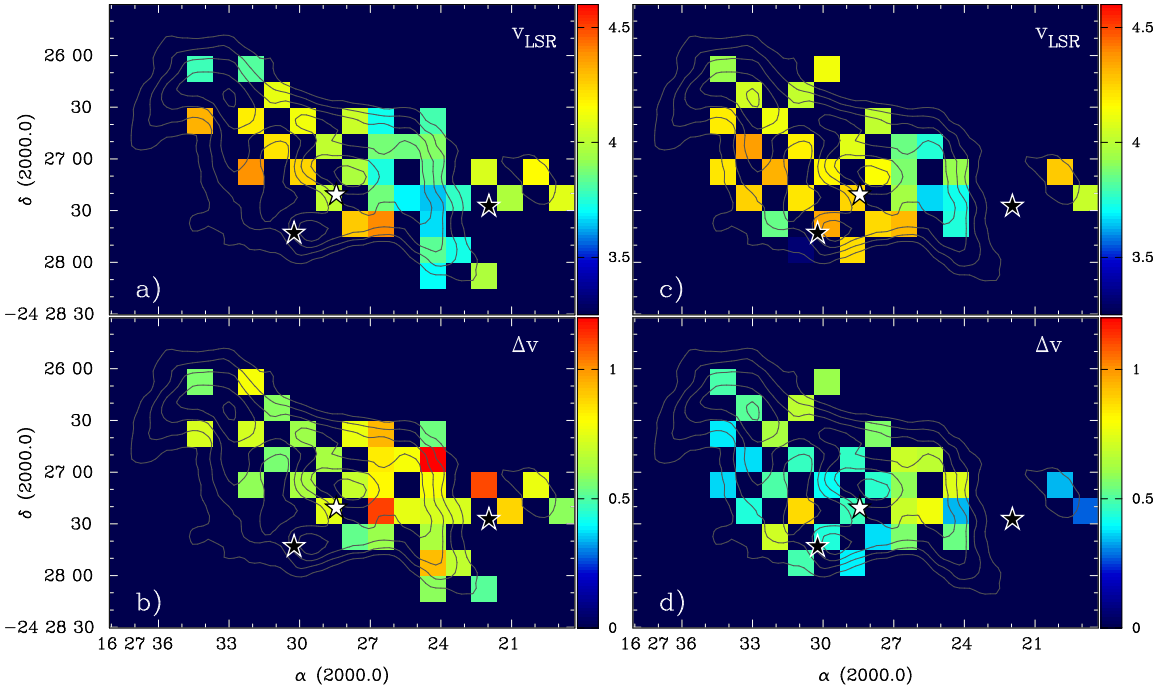


Figure 4.5 a, c) $H_2D^+$ $1_{11} - 1_{10}$ and $N_2H^+$ 4-3 line velocity $v_{\rm LSR}$ in Oph B2, respectively. Colour scale is in $\rm km\,s^{-1}$. We show only results from pixels where the S/N of the peak line intensity is $\geq 5$. In all plots, contours show 850 $\mu$m continuum emission at 15″ (FWHM) resolution observed with the JCMT (Johnstone et al. 2000b), in increments of 0.1 $\rm Jy\,beam^{-1}$. Stars indicate positions of embedded Class I protostars. b, d) $H_2D^+$ and $N_2H^+$ line width $\Delta v$ in Oph B2, respectively. Colour scale is in $\rm km\,s^{-1}$.

We show in Figure 4.5b and Figure 4.5d the $\Delta v$ of the $H_2D^+$ and $N_2H^+$ lines. The $H_2D^+$ line widths are wide, with a mean $\Delta v = 0.69\,\rm km\,s^{-1}$, and do not vary greatly over the Core ($\Delta v$ rms $= 0.19\,\rm km\,s^{-1}$). Slightly wider lines are found in the western half of B2. $N_2H^+$ 4-3 line widths are narrower, with a mean $\Delta v = 0.54\,\rm km\,s^{-1}$. Wider $N_2H^+$ lines are also found towards western B2, while narrower lines are seen towards the submillimetre continuum emission peak and in the eastern half of the Core. Narrow line widths are found towards the embedded protostars, but become wider at pixels directly offset from the infrared sources. In particular, directly to the east of the Elias 32 and 33 protostars, the $N_2H^+$ 4-3 line profiles show a significant

blue shoulder with emission extending to $v_{\rm LSR} \sim 2.5\,{\rm km\,s^{-1}}$.

### 4.4.4 Opacity and excitation temperature

Comparison of the $N_2H^+$ 1-0 and 4-3 line emission (see Figure 4.1b and Figure 4.2b) shows that while in both cases emission is found over much of Oph B2, the integrated intensity distribution of the two transitions is quite different. It is thus unclear whether the excitation conditions for both transitions would be equal as expected for LTE. For the $N_2H^+$ 4-3 emission line, we were able to determine simultaneously $T_{ex}$ and $\tau$ through fitting of the hyperfine line components. Limiting our analysis to pixels where the S/N $\geq 5$, we find a mean $T_{ex} = 7.2\,{\rm K}$ with an rms variation of 1.5 K, and minimum and maximum values of 4.9 K and 10.1 K, respectively. These values are consistent within uncertainties with $T_{ex}$ determined through hyperfine fitting of $N_2H^+$ 1-0 emission in Chapter 3, where was found a mean $T_{ex} = 7.2\,{\rm K}$ and a slightly greater rms variation of 2.8 K. If we regrid the $N_2H^+$ 1-0 map to match the $N_2H^+$ 4-3 map and include only those $T_{ex}$ values where the $N_2H^+$ 4-3 S/N $\geq 5$, we find a slightly lower mean $T_{ex} = 6.8\,{\rm K}$ describes the 1-0 excitation. Slightly greater $N_2H^+$ 4-3 $T_{ex}$ values tend to be found at higher $H_2$ column densities, but we note that the difference (0.4 K) is less than the relative uncertainty in $T_{ex}$ due to the calibration uncertainties, and thus the emission is consistent with being in LTE.

The mean $N_2H^+$ 4-3 opacity $\tau = 1.1$, with an rms of 0.5. The opacities are nearly constant ($\tau \sim 0.9$) across the Core, with a localized maximum of $2 \pm 0.4$ towards the protostar Elias 33. The mean $N_2D^+$ 3-2 line opacity $\tau = 0.5$ with an rms of 0.4 in Oph B2 and a maximum $\tau = 2.5$ towards the eastern integrated intensity peak seen in Figure 4.1a. We find extremely small $N_2D^+$ opacities ($\tau < 0.1$) towards the continuum emission peak.

We calculate and discuss the $H_2D^+$ $1_{11} - 1_{10}$ line opacity in §4.4.5.

### 4.4.5 Column density and fractional abundance

We next discuss the column densities of $N_2D^+$ and $H_2D^+$ derived from the observed line emission. Note that the column density of $N_2H^+$ was calculated in Chapter 3

using the $N_2H^+$ 1-0 rotational line, and we therefore do not recalculate $N(N_2H^+)$ based on the $N_2H^+$ 4-3 emission.

**$N_2D^+$**

We convolve the $N_2D^+$ data to 18″ resolution to match the $N_2H^+$ 1-0 observations in Chapter 3, and calculate the total $N_2D^+$ column density, $N_{tot}(N_2D^+)$, from the integrated intensity of the 3-2 transition assuming the emission is optically thin (Caselli et al. 2002a):

$$N_{tot} = \frac{8\pi W}{\lambda^3 A}\frac{g_u}{g_l}\frac{1}{J_\nu(T_{ex}) - J_\nu(T_{bg})}\frac{1}{1-\exp(-h\nu/kT_{ex})}\frac{Q_{rot}}{g_l \exp(-E_l/kT_{ex})} \tag{4.3}$$

where $W$ is the integrated intensity ($W = \pi^{1/2} / (2\sqrt{\ln 2})\, \Delta v T_{MB}$ for a Gaussian line), $A$ is the Einstein spontaneous emission coefficient, $g_u$ and $g_l$ are the statistical weights of the upper and lower states, respectively, and the equivalent Rayleigh-Jeans excitation and background temperatures are given by $J_\nu(T_{ex})$ and $J_\nu(T_{bg})$. The rotational energy $E_J = J(J+1)hB$ for linear molecules, where the rotation quantum number $J = 2$ for the lower energy state and $B = 38554.717\,\mathrm{MHz}$ is the stimulated emission coefficient (Sastry et al. 1981). The partition function $Q_{rot}$ is defined for linear molecules:

$$Q_{rot} = \sum_{J=0}^{\infty}(2J+1)\exp(-E_J/kT_{ex}) \tag{4.4}$$

where we use the integrated value, $Q_{rot} = kT_{ex} / (hB) + 1/3$. We assume LTE such that the excitation temperature $T_{ex}$ is the same for all rotational levels. Since we were unable to determine robustly both $\tau$ and $T_{ex}$ in §4.4.1 due to the low optical depth of the $N_2D^+$ 3-2 line in most locations, we take the fitted $N_2H^+$ 1-0 $T_{ex}$ from Chapter 3 as an estimate of the excitation temperature of the $N_2D^+$ line at each pixel. $T_{ex}$ was determined with high accuracy for the $N_2H^+$ 1-0 emission, with a mean $N_2H^+$ 1-0 $T_{ex} = 7.2\,\mathrm{K}$ and an rms variation of 2.8 K in Oph B2. All other parameters remaining equal, a decrease in $T_{ex}$ by 2 K would increase the resulting $N_2D^+$ column density

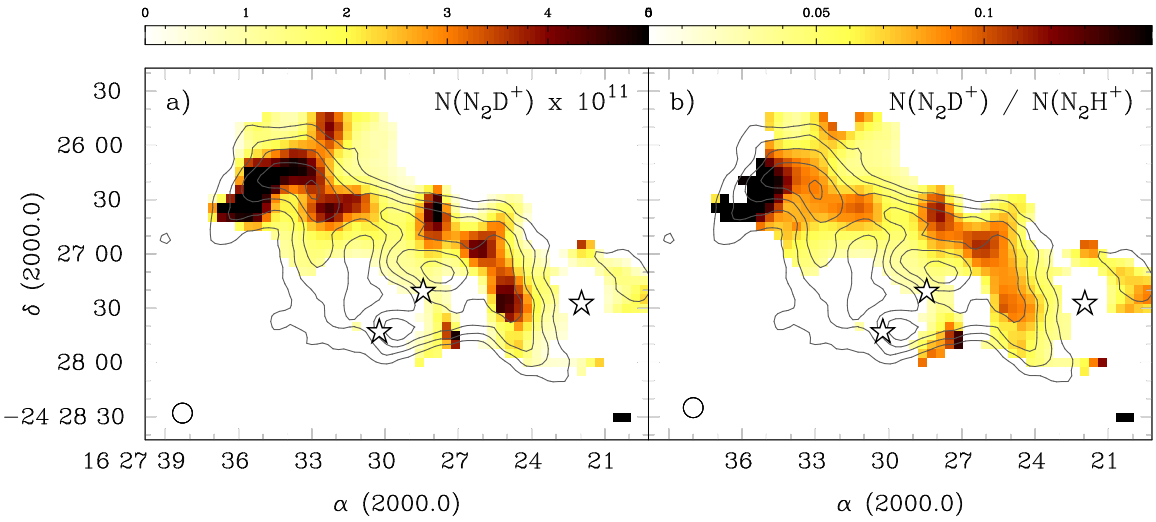


Figure 4.6 a) Total $N_2D^+$ column density $N(N_2D^+)$ ($cm^{-2}$) in Oph B2 determined using Equation 4.3. Values shown have been divided by $10^{11}$. In all plots, contours show 850 $\mu$m continuum emission at 15″ (FWHM) resolution observed with the JCMT (Johnstone et al. 2000b), in increments of 0.1 Jy $beam^{-1}$. The 18″ (FWHM) beam is shown at lower left. Stars indicate the positions of Class I protostars. b) Fractional abundance of $N_2D^+$ relative to $N_2H^+$, $N(N_2D^+)\,/\,N(N_2H^+)$ in Oph B2.

by a factor $\lesssim 2$, while an increase in $T_{ex}$ by 2 K would decrease the resulting $N_2D^+$ column density by $\lesssim 0.5$. We show $N(N_2D^+)$ across Oph B2 in Figure 4.6a.

We then calculate the fractional $N_2D^+$ abundance per pixel,

$$X(N_2D^+) = N(N_2D^+)/N(H_2) \tag{4.5}$$

using the $H_2$ column density, $N(H_2)$, which was determined in Oph B2 in Chapter 3 from 850 $\mu$m continuum emission first mapped with the Submillimetre Common User Bolometer Array (SCUBA) by Johnstone et al. (2000b) at 15″ FWHM resolution at the James Clerk Maxwell Telescope (JCMT). These data were recently re-reduced and combined with all other SCUBA archive data in the region by Jørgensen et al. (2008), following the description in Kirk et al. (2006). The 15″ data were convolved to a final 18″ FWHM resolution to match the $N_2H^+$ 1-0 data presented in Chapter 3, and thus match the convolved $N_2D^+$ data presented here. The $H_2$ column density is then given by $N(H_2) = S_\nu/[\Omega_m \mu m_H \kappa_\nu B_\nu(T_d)]$, where $S_\nu$ is the 850 $\mu$m flux density, $\Omega_m$ is the main-beam solid angle, $\mu = 2.33$ is the mean molecular weight, $m_H$ is the mass of

hydrogen, $\kappa_\nu$ is the dust opacity per unit mass at 850 $\mu$m, and $B_\nu(T_d)$ is the Planck function at the dust temperature, $T_d$. As in Chapter 2 and Chapter 3, we take $\kappa_\nu = 0.018\,\mathrm{cm^2\,g^{-1}}$. We refer the reader to the detailed discussion of the uncertainties in the $N(\mathrm{H_2})$ values presented in Chapter 3, but note that the derived $\mathrm{H_2}$ column densities have uncertainties of factors of a few. Additionally, due to the negative artifacts introduced into the data from the observational chopping technique (again discussed in detail in Chapter 3), we limit the analysis to pixels where $S_\nu \geq 0.1\,\mathrm{Jy\,beam^{-1}}$, though the rms noise level of the continuum map is $\sim 0.03\,\mathrm{Jy\,beam^{-1}}$. For a dust temperature $T_d = 15\,\mathrm{K}$, this flux level corresponds to $N(\mathrm{H_2}) \sim 6 \times 10^{21}\,\mathrm{cm^{-2}}$.

The column density distribution is not similar to the the integrated intensity map shown in Figure 4.1a. Figure 4.6a shows several small peaks of $N(\mathrm{N_2D^+})$ in B2 which largely correspond with local minima ($T_{ex} \sim 5\,\mathrm{K}$ compared with the mean $T_{ex} \sim 7\,\mathrm{K}$) in the excitation temperature. The $N(\mathrm{N_2D^+})$ peaks remain within the continuum contours but avoid maxima of continuum emission. We find a mean $N(\mathrm{N_2D^+}) = 1.8 \times 10^{11}\,\mathrm{cm^{-2}}$ in Oph B2 with an rms variation of $1.3 \times 10^{11}\,\mathrm{cm^{-2}}$. The maximum $N(\mathrm{N_2D^+}) = 7.1 \times 10^{11}\,\mathrm{cm^{-2}}$ is found towards the northeast.

The fractional $\mathrm{N_2D^+}$ abundance (not shown) follows a similar distribution to the $\mathrm{N_2D^+}$ column density. We find a mean $X(\mathrm{N_2D^+}) = 8.2 \times 10^{-12}$ with an rms variation of $5.1 \times 10^{-12}$. The maximum $X(\mathrm{N_2D^+}) = 2.9 \times 10^{-11}$ is again found towards northeast Oph B2. Within the continuum emission contours, the lowest *measured* $\mathrm{N_2D^+}$ abundances ($X(\mathrm{N_2D^+}) \sim 2 \times 10^{-12}$) are found towards the continuum emission peak and B2-MM8 clump (emission towards the Elias 33 protostar was not above our S/N limit for analysis).

### $\mathbf{H_2D^+}$

To calculate the $\mathrm{H_2D^+}$ column density, $N(\mathrm{H_2D^+})$, we first estimate the line opacity $\tau$ from the $\mathrm{H_2D^+}$ $1_{11} - 1_{10}$ line emission using

$$\tau = -\ln\left[1 - \frac{T_{MB}}{J(T_{ex}) - J(T_{bg})}\right] \tag{4.6}$$

where we must assume a priori an excitation temperature $T_{ex}$ for the transition. An upper limit is given by the gas kinetic temperature $T_K$, which was determined across

Oph B2 in Chapter 2 from $NH_3$ (1,1) and (2,2) inversion line ratios. For the pixels where the $H_2D^+$ S/N ratio $> 5$, the mean temperature $T_K = 14.5\,\mathrm{K}$ with an rms variation of 1.1 K (slightly less than the mean $T_K = 15\,\mathrm{K}$ found for the entire Oph B Core in Chapter 2), with a minimum $T_K \lesssim 13\,\mathrm{K}$ towards the highest $N(H_2)$ values. We note, however, that the critical density at which $NH_3$ is excited ($n_{cr} \sim 10^4\,\mathrm{cm}^{-3}$) is lower than that of the $H_2D^+$ transition by an order of magnitude, and the $NH_3$ temperatures, or the variation in $T_K$, may not accurately reflect the conditions where $H_2D^+$ is excited.

In their recent $H_2D^+$ study of several starless and protostellar cores, Caselli et al. (2008) found that the $H_2D^+$ $T_{ex}$ was similar to or slightly less than the core $T_K$ values, which were estimated through a variety of methods (e.g., continuum observations, $NH_3$ inversion observations as for B2, multiple transition observations of molecules such as $HCO^+$). Six of the seven protostellar cores in their sample had excitation temperatures which ranged from 9 K to 14 K and similar densities to those calculated for B2 in Chapter 3. Based on these values, and to better compare our results with Caselli et al., we use a constant excitation temperature $T_{ex} = 12\,\mathrm{K}$ in Equation 4.6. Given $T_{ex} = 12\,\mathrm{K}$, we find a mean $\tau = 0.13$, with a minimum $\tau = 0.05$ and maximum $\tau = 0.28$, which agree well with the Caselli et al. results in protostellar cores.

The total column density of ortho-$H_2D^+$ is then given by (Vastel et al. 2006)

$$N(\text{ortho-}H_2D^+) = \frac{8\pi\nu^3}{c^3}\frac{Q_{rot}(T_{ex})}{g_u A_{ul}}\frac{\exp(E_u/kT_{ex})}{\exp(E_u/kT_{ex})-1}\int \tau \mathrm{d}v \qquad (4.7)$$

where $g_u = 9$, $E_u/k = 17.8\,\mathrm{K}$, and $A_{ul} = 1.08 \times 10^{-4}\,\mathrm{s}^{-1}$ for the $1_{11} - 1_{10}$ transition (Ramanlal & Tennyson 2004). The integral $\int \tau \mathrm{d}v = \frac{1}{2}\sqrt{\pi/(\ln(2)}\tau\Delta v$. We calculate $Q_{rot}$ by reducing the $H_2D^+$ level structure to a 2-level system following Caselli et al. (2008). Since the energy of the first excited state above ground is $E/k = 17.8\,\mathrm{K}$ and that of the second excited state is $E/k = 110\,\mathrm{K}$, we expect this approximation to be valid in Oph B2 given the low temperatures determined for the Core in Chapter 2. The partition function depends on $T_{ex}$, which we have estimated to be 12 K. In Figure 4.7, we plot the variation in $\tau$, $Q_{rot}$ and $N(\text{ortho-}H_2D^+)$ with $T_{ex}$ given a line $T_{MB} = 0.5\,\mathrm{K}$ and $\Delta v = 0.7\,\mathrm{km\,s}^{-1}$ (typical values in B2), and have listed the returned values for $T_{ex}$ between 7 K and 15 K in Table 4.3. While the variation in returned parameters is fairly large with small $T_{ex}$ changes at low $T_{ex}$ values (i.e., factors $\sim 2$ or

Table 4.3. Impact of $T_{ex}$ on $\tau$, $Q_{rot}$ and $N$(ortho-$H_2D^+$)

| $T_{ex}$ K | $\tau$ | $Q_{rot}$ | $N$(ortho-$H_2D^+$) $10^{13}\,\mathrm{cm}^{-2}$ |
|---|---|---|---|
| 7 | 0.41 | 9.7 | 1.60 |
| 8 | 0.27 | 10.0 | 1.11 |
| 9 | 0.20 | 10.2 | 0.86 |
| 10 | 0.15 | 10.5 | 0.71 |
| 11 | 0.12 | 10.8 | 0.61 |
| 12 | 0.10 | 11.0 | 0.54 |
| 13 | 0.09 | 11.3 | 0.48 |
| 14 | 0.08 | 11.5 | 0.45 |
| 15 | 0.07 | 11.7 | 0.42 |

Note. — Values were calculated for a line strength $T_{MB} = 0.5\,\mathrm{K}$ and width $\Delta v = 0.7\,\mathrm{km\,s^{-1}}$.

more around $T_{ex} \sim 7\,\mathrm{K}$), at higher $T_{ex}$ the results vary less. For example, an increased $T_{ex} = 14\,\mathrm{K}$ rather than $T_{ex} = 12\,\mathrm{K}$ would result in a decreased $N$(ortho-$H_2D^+$) by $\sim 20\,\%$, while a decreased $T_{ex} = 10\,\mathrm{K}$ would result in an increased $N$(ortho-$H_2D^+$) by $\sim 30\,\%$.

To estimate the total $H_2D^+$ column density in B2, an estimate the ortho- to para-$H_2D^+$ (o/p-$H_2D^+$) ratio is needed. The ground state para-$H_2D^+$ transition occurs at a frequency of 1.37 THz, and is difficult to observe from the ground and is not likely to be excited at the low temperatures in starless cores. Chemical models show that the o/p-$H_2D^+$ ratio is directly dependent on o/p-$H_2$, where o/p-$H_2 = 10^{-4}$ is predicted in models at gas densities $n \sim 10^5 - 10^6\,\mathrm{cm}^{-3}$ (Walmsley et al. 2004), matching the densities determined for Oph B2 in Chapter 3. With o/p-$H_2 = 10^{-4}$, o/p-$H_2D^+$ $\sim 0.7$ at $T = 10\,\mathrm{K}$ (Miettinen et al. 2009), assuming the ortho- to para-$H_2D^+$ ratio is determined through collisions with ortho- and para-$H_2$. In L183, however, Pagani et al. (2009) calculate larger o/p-$H_2$ ratios through chemical modeling of the starless core L183, finding o/p-$H_2 \sim 4 \times 10^{-3} - 6 \times 10^{-2}$ over core radii of $\sim 10^2 - 10^4\,\mathrm{AU}$ and o/p-$H_2D^+$ $\sim 0.1$. Given the uncertainty in the o/p-$H_2$ ratio and in the gas

temperature where $H_2D^+$ is excited, and consequently in the o/p-$H_2D^+$ ratio, we limit discussion to $N$(ortho-$H_2D^+$) but note that the total $N(H_2D^+)$ is greater than $N$(ortho-$H_2D^+$) by a factor of a few.

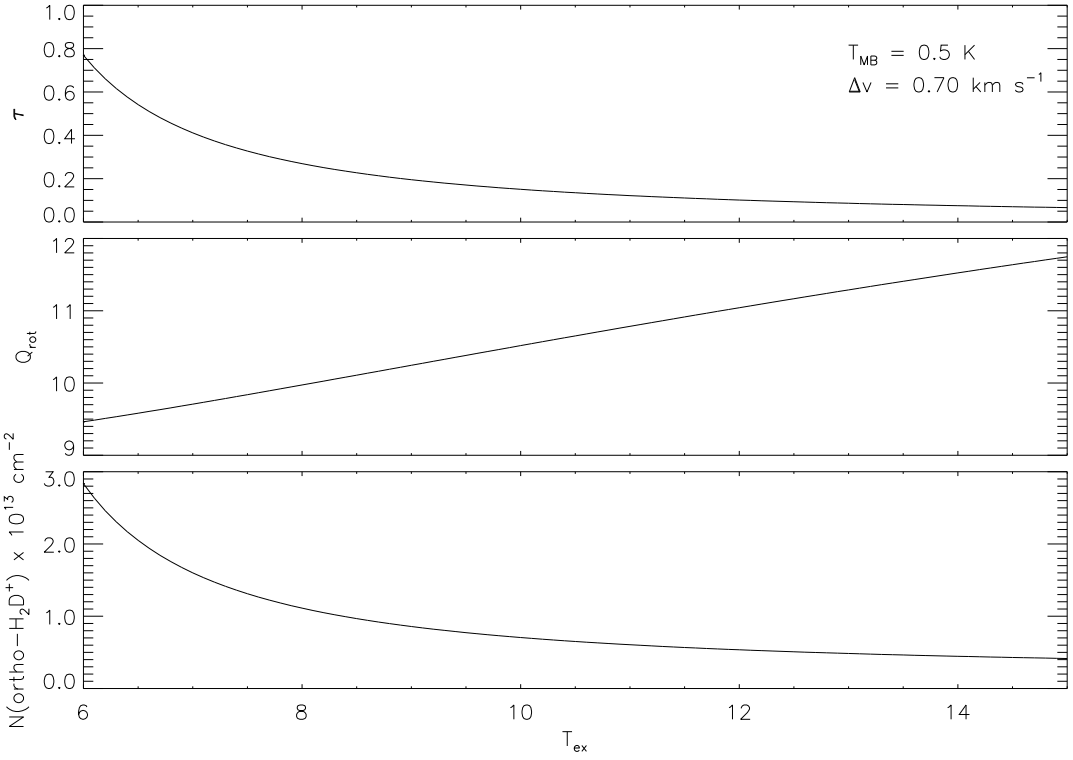


Figure 4.7 Impact of the assumed excitation temperature, $T_{ex}$, on returned $H_2D^+$ $1_{11} - 1_{10}$ line opacity (top), partition function $Q_{rot}$ (middle), and column density, $N$(ortho-$H_2D^+$), given a line brightness temperature $T_{MB}$ and line width $\Delta v$ similar to observed mean values in Oph B2. At low $T_{ex}$, $\tau$ and $N$(ortho-$H_2D^+$) vary strongly with $T_{ex}$, but the effect of changes in $T_{ex}$ at higher temperatures becomes small.

We show in Figure 4.8 the resulting $N$(ortho-$H_2D^+$) distribution across Oph B2. Including only pixels where the S/N $> 5$, we find the mean $N$(ortho-$H_2D^+$) $= 1.4 \times 10^{13}\,\mathrm{cm}^{-2}$ with an rms variation of $0.7 \times 10^{13}\,\mathrm{cm}^{-2}$ over Oph B2. To this sensitivity limit, we find a minimum $N$(ortho-$H_2D^+$) $= 4.1 \times 10^{12}\,\mathrm{cm}^{-2}$. The maximum $N$(ortho-$H_2D^+$) $= 3.3 \times 10^{13}\,\mathrm{cm}^{-2}$ is found $\sim 30''$ to the northwest of the $850\,\mu$m continuum peak. The largest ortho-$H_2D^+$ column densities are found in the western half of the Core, with moderate $N$(ortho-$H_2D^+$ values extending to the Core northeast.

We next calculate $X(\text{ortho-}H_2D^+)$ as described for $N_2D^+$ above, and show in Figure 4.8b the $X(\text{ortho-}H_2D^+)$ distribution across B2. Similarly to the column density distribution, the largest $H_2D^+$ abundances, $X(\text{ortho-}H_2D^+) \sim 4 - 5 \times 10^{-10}$, are found in the west. A local $X(\text{ortho-}H_2D^+)$ minimum of $\sim 2 \times 10^{-10}$ is found towards the central continuum emission peak, with similar abundances towards the Core northeast.

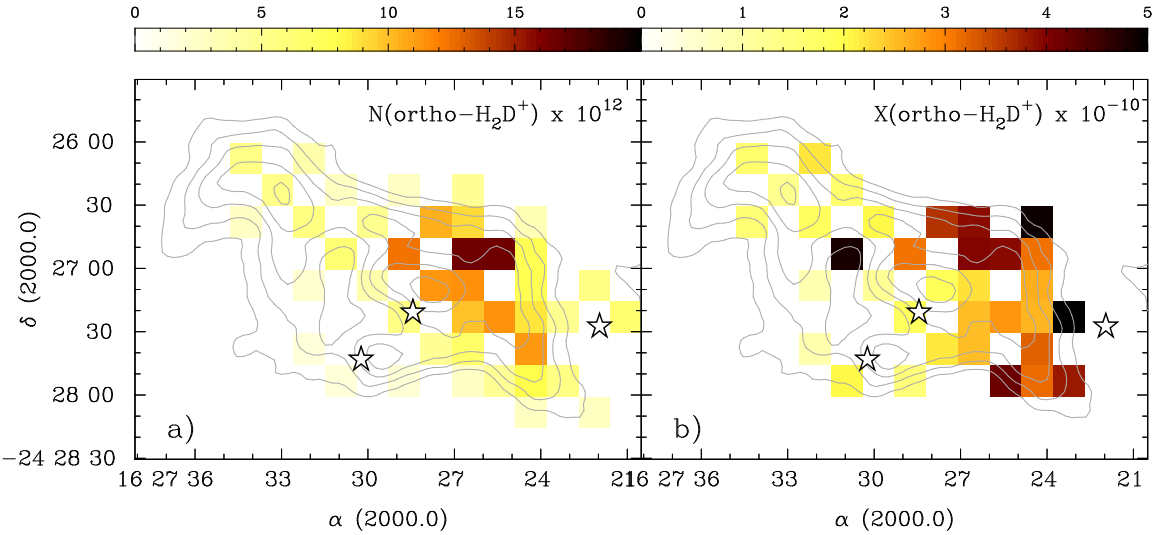


Figure 4.8 a) Ortho-$H_2D^+$ column density in $\text{cm}^{-2}$. $N(\text{ortho-}H_2D^+)$ values have been divided by $10^{12}$. b) Fractional ortho-$H_2D^+$ abundance $X(\text{ortho-}H_2D^+)$. Values have been divided by $10^{-10}$.

### 4.4.6 Using $H_2D^+$, $N_2H^+$ and $N_2D^+$ to determine $T_K$

The molecular weight of $H_2D^+$ ($m_{mol} = 4.01\,\text{m}_H$) is much less than that of $N_2H^+$ or $N_2D^+$ ($29.01\,\text{m}_H$ and $30.02\,\text{m}_H$, respectively). If we assume that the $H_2D^+$ $1_{11} - 1_{10}$, $N_2H^+$ 4-3 or $N_2D^+$ 3-2 transitions are excited in the same environment within the Core, we would expect the two species to trace the same Core motions, and be described by the same kinetic temperature $T_K$. (This assumption is not unreasonable, given the similar critical densities of the transitions, but requires some further examination below given the dissimilar integrated intensity distributions of the $H_2D^+$ and $N_2H^+$ emission.) This co-location would imply that the non-thermal line widths for the two species should be equal, where $\sigma^2_{NT} = \sigma^2_{obs} - \sigma^2_{th}$ . Given equal $T_K$, the $H_2D^+$ thermal line width, $\sigma_{th} = (kT_k/m_{mol})^{1/2}$, will be measurably larger than that of $N_2H^+$

due to its smaller molecular weight. At $T_K = 12\,\mathrm{K}$, for example, $\sigma_{th} = 0.06\,\mathrm{km\,s^{-1}}$ for $N_2H^+$ and $0.16\,\mathrm{km\,s^{-1}}$ for $H_2D^+$. We can use this difference in thermal line widths to determine the kinetic gas temperature by equating the non-thermal line widths and solving for $T_K$ (e.g., in the case of $N_2D^+$):

$$T_K = \frac{1}{k_B}\left(\frac{1}{m_{\mathrm{H_2D^+}}} - \frac{1}{m_{\mathrm{N_2D^+}}}\right)^{-1}[\sigma^2_{obs}(\mathrm{H_2D^+}) - \sigma^2_{obs}(\mathrm{N_2D^+})] \tag{4.8}$$

Mean temperatures of $9.2 \pm 0.2\,\mathrm{K}$, in good agreement with temperatures derived from $NH_3$ alone, were derived in this manner towards a number of dense cores by Fuller & Myers (1993) using the molecular species $HC_3N$ and $NH_3$. Using this method, the largest source of error in the derived $T_K$ likely arises from the assumptions listed above rather than from the propagation of the small uncertainties on the observed line widths. We show in Figure 4.9 the resulting $T_K$ over Oph B2 calculated via a comparison of $H_2D^+$ and $N_2H^+$ or $N_2D^+$ emission, respectively, where $T_K$ has been calculated only for pixels where the signal-to-noise ratio of both lines was $> 5$.

We show in Figure 4.9 the temperatures calculated based on Equation 4.8 for $H_2D^+$ and $N_2D^+$ 3-2 (Figure 4.9a) and $H_2D^+$ and $N_2H^+$ 4-3 (Figure 4.9b). The derived $T_K$ values span a large range in both cases, from unphysical negative values ($\sim -11\,\mathrm{K}$) to unrealistically large values ($\sim 75\,\mathrm{K}$). Using the mean $\Delta v$ values from Table 4.4, We calculate a mean $T_K = 16\,\mathrm{K}$ using $H_2D^+$ - $N_2D^+$, and $T_K = 25\,\mathrm{K}$ using $H_2D^+$ - $N_2H^+$ $4-3$. The same analysis using $H_2D^+$ and $N_2H^+$ 1-0 $\Delta v$ gives a mean $T_K = 3\,\mathrm{K}$ due to the near-equality of average line widths. Both values are *warmer* than temperatures determined in Chapter 2 through $NH_3$ analysis, and if accurate imply that an increasing temperature gradient with increasing density is found in B2 (since $NH_3$ emission traces lower gas densities). Given the presence of embedded protostars in the Core, this may not be unreasonable, but these results are discrepant with modelling which suggests embedded protostars are unable to heat regions in dense cores beyond their immediate surroundings (Stamatellos et al. 2007). In addition, the high temperatures derived from comparison of the $H_2D^+$ and $N_2H^+$ 4-3 line widths are unlikely, as $H_2D^+$ abundances are expected to decrease rapidly at $T > 20\,\mathrm{K}$ (Caselli et al. 2008).

Overall, we expect the comparison of $H_2D^+$ and $N_2D^+$ to be most accurate, given the similar critical densities of the transitions and the fact that $N_2D^+$ must form from

$H_2D^+$. The similar distribution of integrated intensity (see Figures 4.1a and 4.2a) also suggest the two molecules are excited in the same Core regions, in contrast with the poor correlation between $H_2D^+$ and $N_2H^+$ 4-3 emission. The derived $H_2D^+$-$N_2D^+$ temperatures vary less than the $H_2D^+$-$N_2H^+$ temperatures, and multiple pixels with $T_K \sim 12\,\mathrm{K}$ are found surrounding the central continuum emission peak. The negative temperatures, however, are found associated with the continuum peak and associated clump B2-MM8.

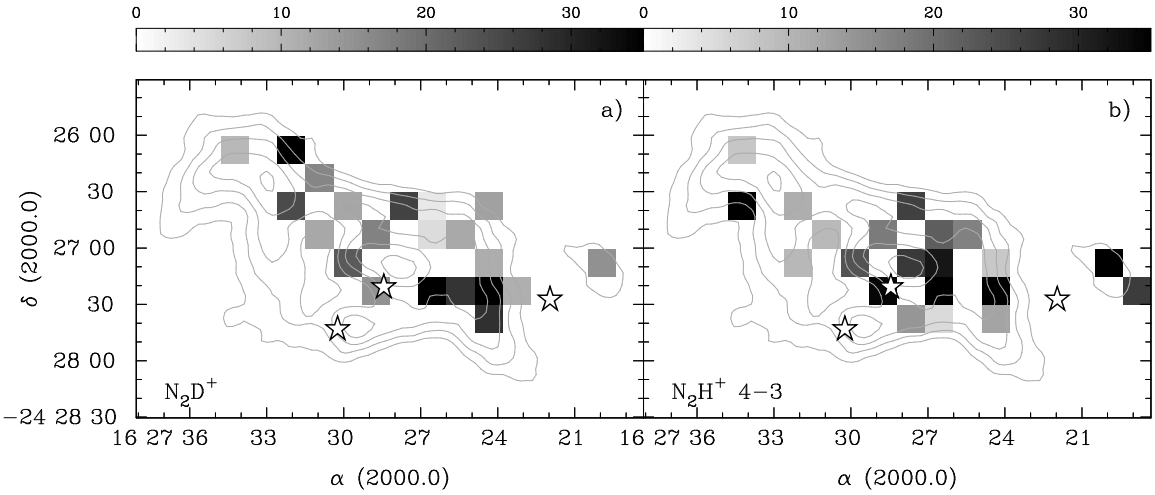


Figure 4.9 a) $T_K$ determined using Equation 4.8 for $H_2D^+$ and $N_2D^+$ emission. Note that a negative $T_K$ was found for the blank pixel towards the submillimetre continuum emission peak because the observed $H_2D^+$ $\Delta v > N_2D^+$ $\Delta v$. b) $T_K$ determined using Equation 4.8 for $H_2D^+$ and $N_2H^+$ 4-3 emission.

From Equation 4.8, we calculate negative $T_K$ values when the observed $H_2D^+$ line widths are less than those of $N_2H^+$ 4-3 or $N_2D^+$ 3-2. We show in Figure 4.10 (bottom) $\Delta v$ derived for $H_2D^+$ and $N_2D^+$ emission (data values in 15″ pixels plotted), along with the spectra and relative fits towards B2-MM8. Over most of the B2 Core, $N_2D^+$ line widths are narrower than $H_2D^+$, and thus $T_K > 0\,\mathrm{K}$. The negative temperatures derive from two adjacent pixels towards B2-MM8 where the $N_2D^+$ $\Delta v > \Delta v$ of $H_2D^+$. Figure 4.10 shows non-Gaussianity in the spectra of both species towards B2-MM8, which complicates the calculation of a single line width to describe the emission.

Why would we find $N_2D^+$ $\Delta v$ wider than $H_2D^+$ $\Delta v$ only towards the central continuum peak? One possibility is suggested by the spectra in Figure 4.10, where additional emission in the $H_2D^+$ spectrum is clearly seen blue-shifted relative to the main Gaussian peak. For the $H_2D^+$ line, the best-fit Gaussian does not include

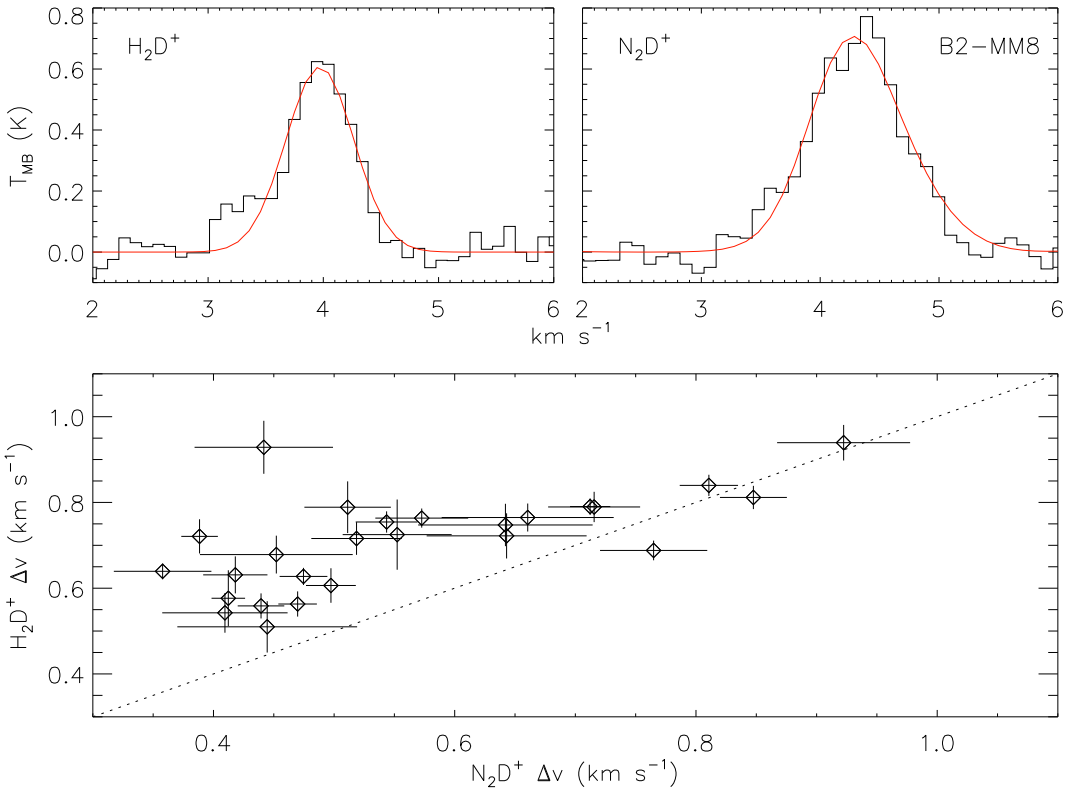


Figure 4.10 Top left: $H_2D^+$ $1_{11}-1_{10}$ spectrum towards B2-MM8 overlaid with a Gaussian fit. Top right: $N_2D^+$ 3-2 spectrum towards B2-MM8 overlaid with a hyperfine structure fit (note no individual hyperfine components are visible due to their small separation in velocity and the relatively wide line width). Bottom: Returned $H_2D^+$ line widths $\Delta v$ versus $N_2D^+$ $\Delta v$. Each point represents a 15″ pixel. An equality relation is shown by the dotted line. Despite appearing wider, in most locations the $N_2D^+$ $\Delta v$ is narrower than that of $H_2D^+$ due to the presence of overlapping hyperfine lines. The two points where $N_2D^+$ $\Delta v > H_2D^+$ $\Delta v$ are located at and immediately adjacent to the 850 $\mu$m continuum peak and B2-MM8. At these locations, temperatures calculated via Equation 4.8 become negative and unphysical. Uncertainties shown are returned from the line fitting routines.

the blue line shoulder. Blue asymmetry is also visible in the $N_2D^+$ line, but the distinction between the main component and the shoulder is less obvious. It is possible that the shoulder emission of $N_2D^+$ 3-2 is spread over a larger range in $v_{\rm LSR}$ due to the contribution of multiple hyperfine components to the observed emission (which would each contain emission at the central line velocity and at the shoulder velocity), broadening the line overall. The best fit to the $N_2D^+$ line thus cannot distinguish well between the main and shoulder emission, resulting in an artificially broad $\Delta v$. We discuss the possible origins of the blue line shoulder further in the next section.

## 4.5 Discussion

### 4.5.1 Line widths and density

The mean line widths listed in Table 4.4 show that on average, the observed $\Delta v$ for a given molecular line decreases with increasing critical line density, suggesting that the gas in B2 becomes more quiescent at higher densities. For an average gas temperature $T_K = 15\,{\rm K}$, the resulting non-thermal line contribution decreases from $\sigma_{\rm NT} = 0.36\,{\rm km\,s^{-1}}$ for $NH_3$ (1,1) emission to $\sigma_{\rm NT} = 0.21\,{\rm km\,s^{-1}}$ for $N_2H^+$ 4-3 emission. Comparing with the thermal sound speed at 15 K, where $c_s = \sqrt{kT_K/(\mu m_{\rm H})}$, we find an average $\sigma_{\rm NT} = 1.6\,{\rm km\,s^{-1}}$ for $NH_3$ and $\sigma_{\rm NT}\,/\,c_s = 1.0$ for $N_2H^+$ 4-3 emission. This comparison shows that despite the decrease in non-thermal motions, the Core non-thermal motions are equal in magnitude with the sound speed, even at high density. A lower gas temperature would result in even larger magnitudes of $\sigma_{\rm NT}$, while significantly higher temperatures are unlikely, as discussed in §4.4.6.

This decrease in non-thermal motions at higher densities has been observed in starless cores (e.g., Pon et al. 2009; Tafalla et al. 2004; Lada et al. 2003). Frequently in starless cores, however, the narrowest observed line widths are consistent with being due to nearly purely thermal motions, in contrast to the results found here. As $\sigma_{\rm NT}$ values decrease, the ability for turbulent pressure to support the core against collapse is reduced, which impacts the stability of the core against its self-gravity. The narrow $\sigma_{\rm NT}$ widths found in starless cores are often explained as the result of the dissipation of turbulent motions in the core centre. If the non-thermal line widths in B2 are due to turbulent motions, the corresponding turbulent pressure ($P_{NT} = mn\sigma_{\rm NT}^2$) is equal

to or greater than the thermal pressure ($P_T = nkT$).

In Chapter 2, we discussed the source of wide $NH_3$ line widths in Oph B, and concluded that if the relatively large $\sigma_{\rm NT}$ values are caused by turbulent motions, they could not be primordial (i.e., inherited from the parent cloud). This is because the damping timescale of such motions (with no external driving force) is approximately the dynamical time (Mac Low & Klessen 2004), and the existence of embedded protostars in B2 implies that B2 has existed, with high density gas, for at least a dynamical time.

The wide lines in Oph B2 may, however, be due to more organized motions such as infall or outflow. None of the observed molecular lines are optically thick, and we therefore do not see the self-absorbed, asymmetric line profiles frequently used to infer the infall of gas within a core. Infall signatures were observed in CS, $H_2CO$ or $HCO^+$ emission towards several locations in eastern B2 by André et al. (2007), but not in central or western B2. Gurney et al. (2008) observed complicated CO (and CO isotopologues) line structures towards the B2 continuum peak, but were unable to distinguish infall conclusively. The analysis of line profiles is complicated by a substantial outflow discovered in CO emission and emanating from one of the two embedded YSOs in B2 (Kamazaki et al. 2003) which extends over $10'$ ($\sim 0.4$ pc) in size[2]. Upcoming results of CO, $^{13}$CO and C$^{18}$0 3-2 observations in Ophiuchus (White et al. 2009, in preparation) from the JCMT Gould Belt Legacy Survey (GBLS, Ward-Thompson et al. 2007b) will be better able to study the infall and outflow motions in Oph B. In conjunction with these data, the process of how the outflow motions affect the dense gas may be studied. There is clear evidence, however, for protostellar influence on the $N_2D^+$ line widths shown in Figure 4.4b, as discussed in §4.4.3.

[2]JCMT Spring 2009 Newsletter, http://jach.hawaii.edu/JCMT/publications/newsletter/

Table 4.4. Mean $NH_3$, $N_2H^+$, $N_2D^+$ and $H_2D^+$ $v_{LSR}$ and $\Delta v$ in Oph B2

| Species | Transition | $v_{LSR}$ km s$^{-1}$ | | | | $\Delta v$ km s$^{-1}$ | | | | $n_{cr}$ cm$^{-3}$ |
|---|---|---|---|---|---|---|---|---|---|---|
| | | Mean | RMS | Min | Max | Mean | RMS | Min | Max | |
| $NH_3$ | $(J,K) = (1,1)$ | 4.14 | 0.19 | 3.85 | 4.58 | 0.87 | 0.16 | 0.42 | 1.11 | $2 \times 10^{4}$ [a] |
| $N_2H^+$ | $J = 1 - 0$ | 4.04 | 0.20 | 3.61 | 4.43 | 0.71 | 0.22 | 0.38 | 1.42 | $1.4 \times 10^{5}$ [b] |
| $H_2D^+$ | $J_{K_{-1}K_1}$ | | | | | | | | | |
| | $= 1_{11} - 1_{10}$ | 4.01 | 0.24 | 3.65 | 4.50 | 0.74 | 0.19 | 0.51 | 1.36 | $\sim 10^{5}$ [c] |
| $N_2D^+$ | $J = 3 - 2$ | 4.05 | 0.25 | 3.37 | 4.65 | 0.62 | 0.25 | 0.28 | 1.24 | $8 \times 10^{5}$ [d] |
| $N_2H^+$ | $J = 4 - 3$ | 4.02 | 0.20 | 3.72 | 4.43 | 0.54 | 0.15 | 0.28 | 0.87 | $7.7 \times 10^{6}$ [b] |

Note. — The velocity resolution of the $NH_3$ observations was 0.3 km s$^{-1}$. All other species were observed with 0.1 km s$^{-1}$ velocity resolution or better.

[a]Caselli et al. (2002a)

[b]Schöier et al. ($n_{cr}$ calculated using Einstein A coefficients and collision rates $\gamma_{ul}$ at 10 K from the Leiden Atomic and Molecular Database; 2005)

[c]Caselli et al. (2008)

[d]Calculated using Einstein A coefficients and collision rates for $N_2H^+$ 3-2 at 10 K (Schöier et al. 2005). Daniel et al. (2007) (see their Figure 17) found that despite small differences in Einstein A coefficients and collision rates, critical densities of $N_2H^+$ and $N_2D^+$ are similar for transitions other than $J = 1 - 0$.

We also noted in §4.4.3 (and shown in Figure 4.3) that there is an offset in $v_{\rm LSR}$ of $\sim 0.2\,{\rm km\,s^{-1}}$ between $N_2H^+$ 4-3 and $H_2D^+$ emission towards B2-MM8 and the nearby embedded protostar Elias 32, with the $N_2H^+$ emission redshifted relative to the $H_2D^+$ emission. Over the rest of the Core, the correlation between the $v_{\rm LSR}$ of the two lines is good, suggesting the offset is real and localized. Comparison with $N_2D^+$ emission at the same location shows that the $v_{\rm LSR}$ of the $H_2D^+$ and $N_2D^+$ agree well, and it is consequently the $N_2H^+$ emission which is offset in velocity from the rest of the core gas. $N_2H^+$ 4-3 has a critical density approximately an order of magnitude greater than the $H_2D^+$ and $N_2D^+$ lines discussed here. The offset in $v_{\rm LSR}$ may thus be probing a shift in the gas motions at extremely high densities in the Core interior.

### 4.5.2 Trends in the deuterium fractionation

#### The $N_2D^+/N_2H^+$ ratio

The deuterium fractionation, $R_D$, can be defined as the ratio between the column densities of a hydrogen-bearing molecule and its deuterated counterpart. Here, we define $R_D = N(N_2D^+)/N(N_2H^+)$, and calculate $R_D$ in Oph B2 from $N(N_2D^+)$ calculated in §4.4.5 and $N(N_2H^+)$ calculated in Chapter 3. Figure 4.6b shows $R_D$ across B2. The distribution is similar to the $N_2D^+$ column density in Figure 4.6a. The largest values of $R_D$, to a maximum $R_D = 0.16$, are found towards northeast B2, while towards the smaller scale $R_D$ maxima in the Core $R_D \sim 0.1$ or less. We find a moderate mean $R_D = 0.03$ with an rms variation of 0.01 towards B2, comparable to results in Ori B9 towards two $N_2H^+$ emission peaks and a protostellar source ($R_D = 0.03 - 0.04$, Miettinen et al. 2009). While Pagani et al. (2009) find substantially greater central $R_D$ values through modelling of the starless core L183 ($R_D \sim 0.7$ at the core centre) which decrease to $\sim 0.06$ at $\sim 5000\,{\rm AU}$, it is not clear how to compare their model of $R_D$ as a function of core radius to our observed column density ratio. Fontani et al. (2006) found an average $R_D \sim 0.01$ towards the high mass star forming region IRAS 05345+3157, which at high resolution resolved into two $N_2D^+$ condensations each with $R_D = 0.11$ (Fontani et al. 2008). In a study of starless cores, Crapsi et al. (2005) find a range in $R_D$ between a lower limit of 0.02 to a maximum of 0.44 (which was found towards the Oph D Core). Crapsi et al. also note that $R_D > 0.1$ are generally only found for cores with $N(N_2H^+) > 10^{13}\,{\rm cm^{-2}}$, which is approximately the maxi-

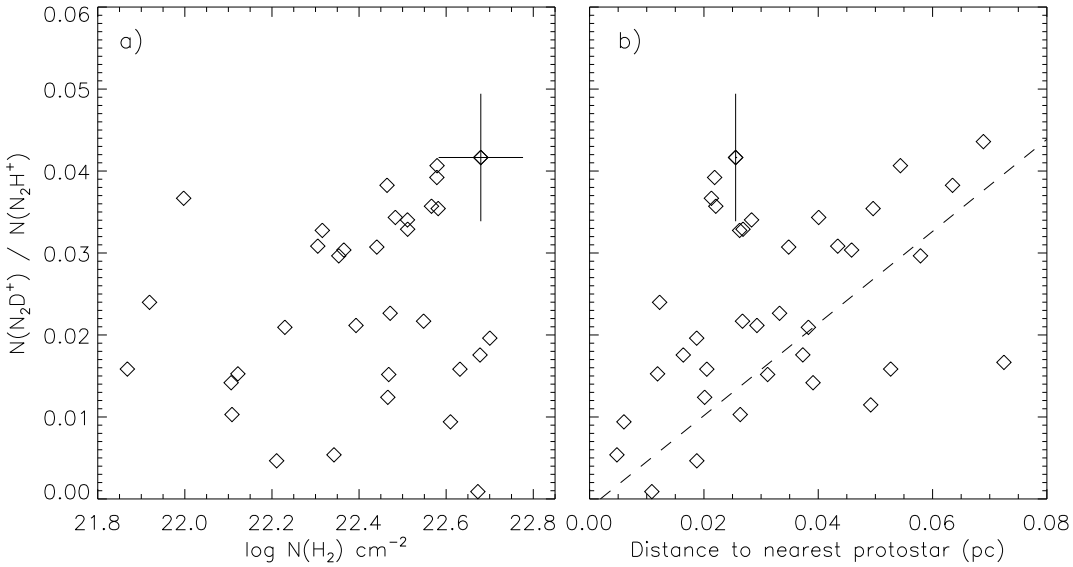


Figure 4.11 a) Variation of $R_D = N(\mathrm{N_2D^+})/N(\mathrm{N_2H^+})$ with $\log N(\mathrm{H_2})$ in Oph B2. Each point shown represents an 18″ pixel (matching the convolved beam FWHM) and only pixels where the S/N $> 5$ of both $N_2H^+$ and $N_2D^+$ peak intensity. A strong correlation is not apparent. b) Variation of $R_D$ with the distance in parsecs to the nearest embedded protostar. The data are consistent with an increasing deuterium fractionation with increasing distance from an embedded source, albeit with significant scatter. A linear fit to the data is shown by the dashed line.

mum $N(\mathrm{N_2H^+})$ in Oph B2. A similar range in $R_D$ was found towards protostellar, Class 0 sources (Emprechtinger et al. 2009). On average, then, our results agree with previous results. Given our map of B2, however, we can also probe the variation of $R_D$ across the Core.

In Figure 4.11a, we show $R_D$ as a function of increasing $N(\mathrm{H_2})$, where each data point represents an 18″ pixel (to match the beam FWHM) and pixels with S/N $< 5$ in either $N_2H^+$ or $N_2D^+$ emission are omitted. Note that the S/N limit removes the large $R_D$ values found towards northeast B2, and the plot maximum $R_D = 0.042$. We find no trend in the deuterium fractionation with $N(\mathrm{H_2})$.

In Figure 4.11b, we show $R_D$ as a function of increasing distance (in projection) from the nearest embedded protostar. We find that $R_D$ increases at greater projected distances from the embedded sources, as might be expected from the $N_2D^+$ integrated intensity distribution. We fit a linear trend to the data, where $R_D = (-0.001 \pm 0.001) + (0.56 \pm 0.05) d\,[\mathrm{pc}]$, but note that there is large scatter in the relation. A similar analysis of the $N_2D^+$ abundance, $X(N_2D^+)$ with $N(H_2)$ shows that the increasing $R_D$ trend with projected protostellar distance is dominated by an increase in $X(N_2D^+)$ with projected protostellar distance, while $X(N_2H^+)$ is approximately constant over the range plotted.

**$H_2D^+$**

We next look at the distribution of the ortho-$H_2D^+$ abundance over the B2 Core. In Figure 4.12a, we show $X(\text{ortho-}H_2D^+)$ as a function of $N(H_2)$. We show data in $15''$ pixels, and omit pixels with S/N $< 5$. We find no trend in the fractional ortho-$H_2D^+$ abundance with $H_2$ column density (an increasing trend is found, but not shown, in the ortho-$H_2D^+$ column density with $N(H_2)$).

In Figure 4.12b, we plot $X(\text{ortho-}H_2D^+)$ as a function of increasing projected protostellar distance. The result is not entirely a scatter plot, as the ortho-$H_2D^+$ abundance tends to increase with projected protostellar distance to a maximum $X(\text{ortho-}H_2D^+) = 4.9 \times 10^{-10}$ at $d = 0.035\,\mathrm{pc}$, with $X(\text{ortho-}H_2D^+) \sim 1.8 \times 10^{-10}$ at larger distances. All data points at $d > 0.035\,\mathrm{pc}$ correspond to the emission found in northeast B2, while the rest show emission closer to the central continuum emission peak. If we fit a linear relationship to the data, omitting the northeast B2 points, we find $X(\text{ortho-}H_2D^+) = (0.9 \pm 0.5) \times 10^{-10} + (89 \pm 21) \times 10^{-10} d\,[\mathrm{pc}]$.

There is also no clear trend in $N(\text{ortho-}H_2D^+)$ with $R_D$ where both $H_2D^+$ and $N_2D^+$ are strongly detected across the Core, although both species are found with relatively large column densities north and west of the continuum peak. Given the small-scale structure found in the $N(N_2D^+)$ distribution in B2, the spatial resolution and sampling of our $H_2D^+$ observations may not be high enough to discern a correlation. We note, however, that (Caselli et al. 2008) also found no clear correlation between $R_D$ and $N(\text{ortho-}H_2D^+)$ in their sample of starless and protostellar cores (with the caveat that some $R_D$ values were derived using column density ra-

tios of deuterated $NH_3$ and deuterated $H_2CO$ with their undeuterated counterparts rather than $N(N_2D^+)/N(N_2H^+)$). In particular, high values of $R_D$ and relatively low $N(\text{ortho-}H_2D^+)$ were found towards two objects in Ophiuchus.

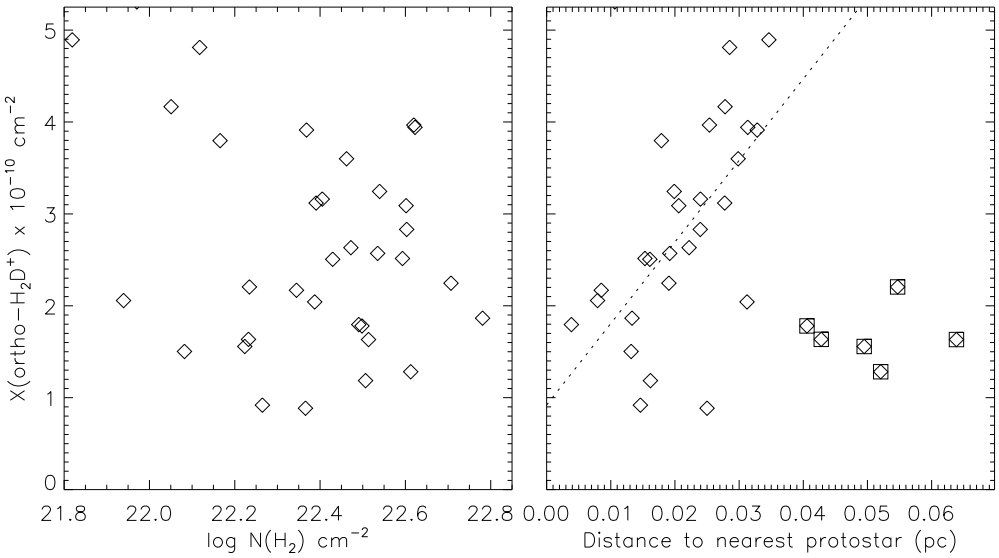


Figure 4.12 Variation of $X(H_2D^+)$ with $\log N(H_2)$ in Oph B2. Each point shown represents a 15″ pixel (matching the beam FWHM). Only pixels where the $H_2D^+$ S/N $> 5$ are plotted. No correlation is seen. b) Variation of $X(\text{ortho-}H_2D^+)$ with the distance in parsecs to the nearest embedded protostar. The data do not scatter about a central point, but instead show a trend of increasing $X(H_2D^+)$ with increased distance from an embedded protostar to $d \sim 0.04$ pc, and a smaller, constant $H_2D^+$ abundance at further distances. The points identified with squares represent pixels in the northeast portion of the B core. A linear fit to the data, minus the highlighted pixels, is shown by the dotted line.

### 4.5.3 What is affecting the deuterium fractionation in Oph B2?

The largest deuterium fractionation values in Oph B2 are not found towards the continuum emission peak, but instead avoid the continuum peak and nearby protostars. The results of the previous section indicate that the distance to the nearest protostar is the dominant parameter impacting the deuterium fractionation in Oph B2. We next discuss what effects on the dense Core gas by the embedded sources are most likely to impact the deuterium fractionation distribution in B2.

#### Temperature and CO depletion

The gas temperature can have a substantial impact on the deuterium fractionation in a dense core in two ways. First, at higher gas temperatures Equation 4.1 can proceed in both the forward and reverse reaction, resulting in no net increase in $H_2D^+$, and consequently other deuterated species formed via reactions with $H_2D^+$. Temperatures in excess of $\sim 20\,\mathrm{K}$ are required for the reverse, endothermic reaction to proceed. Second, the CO which was deposited (adsorbed) as an icy mantle onto dust grains while at low temperatures will evaporate (desorb) back into the gas phase if the dust grains are heated, providing a destruction mechanism for $H_2D^+$ and again interrupting the deuteration chain.

An obvious potential source of heating is the presence of embedded protostars within Oph B2. Very little gas temperature variation across Oph B was found in Chapter 2, with no evidence for increased temperatures above the mean $T_K = 15\,\mathrm{K}$ near the embedded protostars. It is possible that very near the protostars, the higher density gas (i.e., greater than that probed by $NH_3$) may be warmer by $\sim 5\,\mathrm{K}$ within a few thousand AU ($\sim 0.01-0.02\,\mathrm{pc}$; $\sim 30''$ at 120 pc), but most of the core will remain at low temperatures (Stamatellos et al. 2007). A temperature increase of 5 K over the mean $T_K = 15\,\mathrm{K}$ of the Core would then allow the backwards reaction in Equation 4.1 to proceed. This effect would be extremely localized, however, and unlikely to be responsible for reducing the deuterium fractionation apart from in the immediate vicinity of the protostar.

The CO depletion factor, $f_D(\mathrm{CO})$, is defined as the canonical CO abundance,

$X_{can}$(CO), divided by the CO abundance, $X(\mathrm{CO}) = N(\mathrm{CO})/N(\mathrm{H_2})$, in the observed region:

$$f_D(\mathrm{CO}) = \frac{X_{can}(\mathrm{CO})}{X(\mathrm{CO})} \tag{4.9}$$

such that $f_D$ values are low where observed CO abundances are high. Low CO depletion factors can dramatically lower the $H_2D^+$ abundance at temperatures $T <$ 15 K (Caselli et al. 2008). Currently no estimates of $f_D$ exist in B2 due to a lack of data at spatial resolutions matching the available continuum data. The CO observations of the JCMT GBLS should enable the first calculations of $f_D$ and allow further analysis of the relationship between CO and the deuterium distribution in B2. We can look, however, for indirect evidence of variation in the CO abundance in B2 to assess the potential impact on the deuterium fractionation across the Core.

The extended distribution of $H_2D^+$ and $N_2D^+$ across Oph B2 implies extensive depletion of CO has occurred over much of the Core. At densities of $n = 10^6\,\mathrm{cm^{-3}}$, CO adsorption and desorption occur equally frequently at temperatures $T = 18$ K (Visser et al. 2009). At $T > 18$ K, CO will thus again become present in the gas phase. In a 1D dynamic/chemical model of an isolated dense core which collapses to form a protostar, Aikawa et al. (2008, see their Figure 2) find temperatures greater than 18 K can be found at radii $\sim 5000$ AU ($\sim 0.02$ pc) from the protostar at $\sim 10^5$ yr after its formation. Both embedded YSOs in central B2 have been classified as Class I (Enoch et al. 2007; Jørgensen et al. 2008), and consequently likely have ages $\sim 5 \times 10^5$ yr based on lifetime estimates of the different protostellar stages (Evans et al. 2009). This prediction is in conflict, however, with the $\sim 15$ K temperatures calculated in Chapter 2. The B2 protostars may, however, have denser, more compact and clumpier envelopes compared with the isolated case, which would affect their ability to heat nearby regions.

Since CO also destroys $N_2H^+$, significant evaporation of CO from dust grains should also be observable in the $N_2H^+$ distribution. Accordingly, in Figure 4.1b we see a decrease in the integrated $N_2H^+$ 1-0 intensity towards the Elias 33 protostar (no obvious decrease is found towards the Elias 32 protostar, but the maximum $N_2H^+$ emission is offset from the embedded source). In Chapter 3, no good fit to the $N_2H^+$ spectra was found at this location due to complicated line structures. As stated above,

however, where good fits were found the fractional $N_2H^+$ abundance was found to be constant with protostellar distance, implying that any impact of CO evaporation on $N_2H^+$ is limited to very near ($\sim 3500$ AU or 0.02 pc) the protostar.

In summary, heating by an embedded protostar can produce slightly greater gas temperatures and evaporate CO from the surface of dust grains, which would decrease the deuterium fractionation in the gas. The gas temperatures derived in Chapter 2 appear to be not sufficiently high, however, for either $H_2D^+$ destruction mechanism described above to impact significantly the $H_2D^+$ abundance. Either these temperatures are not accurately representative of the true $T_K$ of the locations of $H_2D^+$ across B2 or some other mechanism is depleting $H_2D^+$ with projected protostellar distance.

**Ionization fraction and electron abundance** $x(e)$

Since the deuterium fractionation depends strongly on the electron abundance in regions of high CO depletion, the abundances of deuterated molecules can be used as a probe of the electron abundance, $x(e)$, in dense cores. The electron abundance, $x(e) = n_e/n_{\rm H_2}$, is the ratio of the electron number density ($n_e$) with the number density of molecular hydrogen, $n_{\rm H_2}$, and is equivalent to the ionization fraction. The ionization fraction impacts the core dynamics through interaction of charged species with core magnetic fields, which can provide support to the core, and also affects the core chemistry through reactions between ions and neutral species. At high extinction towards dense starless cores, the creation of ions is expected to be dominated by the cosmic ray flux, with $x(e) \propto n_{\rm H_2}^{-1/2}$ (McKee 1989). Studies investigating $x(e)$ in dense cores using the $DCO^+/HCO^+$ ratio have found average line-of-sight $x(e) \sim 10^{-7}$, suggesting the core gas was only weakly coupled to the magnetic field (Bergin & Tafalla 2007, and references therein).

Both $DCO^+$ and $HCO^+$ can deplete in star forming cores, and thus may not be the best tracers of $x(e)$ at high density. In regions of high depletion, the column density ratio of $N_2D^+$ with $N_2H^+$ is expected to be a better probe of $x(e)$. Since $H_3^+$ is expected to be the major molecular ion in cores strongly depleted in heavy elements, observations of $H_2D^+$ can thus be used to set limits on $x(e)$ assuming the numbers of positive and negative charges are approximately equal (i.e., the core gas is neutral). Given the abundances of $N_2H^+$, $N_2D^+$and $H_2D^+$ in B2, we can thus derive

a lower limit on $x(e)$ following Miettinen et al. (2009):

$$x(e) > X(\mathrm{N_2H^+}) + X(\mathrm{N_2D^+}) + X(\mathrm{H_3^+}) + X(\mathrm{H_2D^+}) \tag{4.10}$$

where we neglect multiply deuterated forms of $\mathrm{H_3^+}$. As discussed in §4.4.5, predictions of the o/p-$\mathrm{H_2D^+}$ ratio vary from $\sim 0.1$ to $\gtrsim 1$, and we use a moderate o/p-$\mathrm{H_2D^+} = 0.5$ to estimate $X(\mathrm{H_2D^+})$ from $X(\mathrm{ortho\text{-}H_2D^+})$. In a simple, steady state analytical model, Crapsi et al. (2004) relate $R_D$ to the relative $\mathrm{H_2D^+}$-$\mathrm{H_3^+}$ abundance, $r = [\mathrm{H_2D^+}]/[\mathrm{H_3^+}]$, and also neglect multiply deuterated forms of $\mathrm{H_3^+}$ such that $R_D \approx r/(3+2r)$. In an updated result, Miettinen et al. (2009) find $R_D \approx (r+2r^2)/(3+2r+r^2)$. Using the Miettinen et al. relation we then find a mean $r = 0.07$ across Oph B2, and a lower limit $x(e) > 1.5 \times 10^{-8}$ through Equation 4.10. We find small variations in the lower limit across B2, with a larger limit $x(e) > 2.7 \times 10^{-8}$ towards Elias 32 and higher values in general near the 850 $\mu$m continuum peak. Detailed modelling, in conjunction with a measurement of the CO depletion factor in B2, is needed to improve our analysis of $x(e)$ beyond a lower limit only.

Low mass protostars emit x-rays, which could potentially increase the local ionization fraction and consequently decrease locally the deuterium fractionation of gas in Oph B. No difference in the ionization fraction has yet been discovered towards either low mass (Williams et al. 1998; Caselli et al. 1998) or high mass (Bergin et al. 1999) dense cores with and without embedded sources, suggesting that the ionization fraction is dominated instead by the cosmic ray ionization. We note, however, that the angular resolution of the data used in these studies ($\sim 1'$) is comparable to the size scales on which we find variation in the deuterium fractionation in Oph B.

## 4.6 Summary

In this chapter we have presented the results of $\mathrm{N_2D^+}$ 3-2, $\mathrm{N_2H^+}$ 4-3 and ortho-$\mathrm{H_2D^+}$ $1_{11}-1_{10}$ mapping of the cluster-forming Ophiuchus B Core. We summarize our results below.

1. Significant emission from the deuterated species $\mathrm{N_2D^+}$ and $\mathrm{H_2D^+}$ extends over

several square arcminutes in B2. In particular, the extent of the $H_2D^+$ emission is the largest yet mapped. Both species' integrated intensity distributions are offset from the continuum emission, and avoid entirely parts of the Core near embedded protostars and the peak of continuum emission from cold dust. In contrast, the $N_2H^+$ 4-3 emission is strongest near embedded protostars, but this is due to higher excitation temperatures of the line rather than an increase in column density.

2. Through fitting of the spectral lines, including multiple component Gaussian fitting of the $N_2H^+$ 4-3 and $N_2D^+$ 3-2 hyperfine line structures, we find wider $N_2D^+$ line widths near protostars embedded in B2, suggestive of protostellar influence on the dense gas. Complicated line structures are found, including red line shoulders in all three tracers. We estimate the non-thermal line widths for the species observed here and compare with $NH_3$ and $N_2H^+$ results from Chapter 2 and Chapter 3. In B2, non-thermal line widths decrease with increasing critical density of the molecular tracer, but remain transonic or only slightly subsonic even at high densities. This result is in contrast with the nearly thermal line widths found in many isolated cores.

3. We test a method to estimate the gas temperature by equating the non-thermal line widths of $N_2D^+$ and $H_2D^+$ and solving for $T_K$. We find both realistic ($T_K \sim 11\,\mathrm{K}$) and unrealistic ($T_K < 0\,\mathrm{K}$ and $T_K \gtrsim 25\,\mathrm{K}$) values in B2. Complicated line structure in B2 likely affects this analysis, but we expect good results can be found in regions with simple velocity structure.

4. The deuterium fraction of $N_2H^+$ $R_D = N(N_2D^+)/N(N_2H^+) \sim 0.03$ on average where $N_2D^+$ is detected. Small scale features with enhanced $R_D$ are seen in B2, but most do not correlate with previously identified continuum clumps or $N_2H^+$ clumps. This $R_D$ is consistent with previous results in protostellar cores, and is less than values found for starless cores.

5. The average ortho-$H_2D^+$ abundance, $X(\text{ortho-}H_2D^+) \sim 3 \times 10^{-10}$, given an assumed excitation temperature of 12 K. An accurate measure of the ortho- to para-$H_2D^+$ ratio is needed to convert to total $H_2D^+$ abundance, and has been found in previous studies to vary between 0.1 and $> 1$. Future observations of para-$H_2D^+$ transitions are needed to constrain this value in dense cores.

6. An anti-correlation is found with $R_D$ and $X(\text{ortho-}H_2D^+)$ and proximity to the nearest embedded protostar in B2. This indicates that the embedded protostars

in B2 are affecting the internal chemistry. Possible mechanisms are through heating, evaporation of CO off dust grains, or by increasing the local ionization fraction. If gas temperatures determined through $NH_3$ analysis in Chapter 2 are applicable to the higher density gas, they do not appear sufficiently high for the first two mechanisms to proceed. Further research on the effect of young stars on the local ionization fraction and the chemistry of deuterated species in protostellar cores is needed.

7. We use the observed $R_D$ and $X(\text{ortho-}H_2D^+)$ to estimate a lower limit on the ionization fraction in B2, and find $x(e) > 1.5 \times 10^{-8}$ given an assumed ortho- to para-$H_2D^+$ ratio.

# Chapter 5

# Conclusions

In this dissertation, I have presented the results of a systematic observational program investigating the dynamical and chemical nature of dense Cores in the Ophiuchus molecular cloud. In the following Chapter, I discuss the surprising results of this study and look briefly at future research initiatives that will improve our understanding of the interplay between dynamics and chemistry in star forming environments.

## 5.1 Surprises and implications for future research

The first surprising result of this study was the poor correlation in both the $NH_3$ and $N_2H^+$ distribution compared with the thermal continuum emission from cold dust in the Oph B Core discussed in Chapters 2 and 3. The initial goals of the $NH_3$ and $N_2H^+$ observations were to probe the dynamics of the dense clumps embedded within the Cores at the high densities where these species are excited. Indeed, such observations of more isolated, simple cores have provided significant insights in to their dynamics. Using publicly-available continuum data to obtain information on clump mass, size and density, the line data were meant to constrain the clump stability and provide a starting point to probe the condensation and fragmentation processes in the Oph Cores.

Due to the lack of correspondence between the continuum emission and dense gas tracers, it was not clear that the motions traced by $NH_3$ and $N_2H^+$ were an

accurate measure of the motions within the clumps identified in continuum emission. This is especially true towards the most massive continuum clump identified in Oph B2, B2-MM8, where interferometer observations (presented in Chapter 3) show a broken ring-like structure in $N_2H^+$ emission that is suggestive of localized depletion. A depleted species is necessarily a poor tracer of kinematics since it is no longer abundant in the gas phase.

A related result was the apparent decline seen in $NH_3$ and $N_2H^+$ abundance with increasing $H_2$ column density, described in Chapters 2 and 3. While depletions of $NH_3$ and $N_2H^+$ have recently been found on small scales towards a few other star forming cores and clumps (e.g., B68; Bergin et al. 2002), global trends, such as those plotted in Figure 2.12 and Figure 3.11, is new. Future *maps* of $NH_3$ and $N_2H^+$ line emission in other clustered star forming regions will be useful in understanding whether this trend is specific to the Oph Cores or a frequent feature of the higher density objects typically found in clustered star forming environments. These data call into question the utility of these lines as tracers of dense material. Previous conclusions based on low-resolution maps of other regions may require modification when high-resolution data of these regions become available.

The lack of correspondence between $NH_3$ and $N_2H^+$ emission was the impetus for further observations of molecules expected to be prevalent in regions dominated by high levels of depletion, including deuterated $N_2H^+$ ($N_2D^+$) and singly-deuterated $H_3^+$ ($H_2D^+$). $H_2D^+$ in particular is expected to become increasingly abundant in regions where nearly *all* heavy species (i.e., species containing elements more massive than H or He) are missing from the gas phase. Based on the results of Chapters 2 and 3, relatively strong $H_2D^+$ emission was thus expected to be found towards the Oph B2 continuum peak, where $NH_3$ and $N_2H^+$ were shown to be under-abundant. Again, the observations presented in Chapter 4 produced unexpected results, with the deuterated species abundant only in the northern half of the B2 Core, with no local maxima at the continuum emission peak. In contrast to the $NH_3$ and $N_2H^+$ results, however, no clear abundance trend with increasing $H_2$ column density was found for either $H_2D^+$ or $N_2D^+$, and instead the deuterated species' abundances appear anticorrelated with proximity to an embedded protostar.

Several questions have been raised by this dissertation. First, what is the dominant cause of the differing distributions of these dense gas tracers? The preceding chapters

suggest no single factor can fully explain the results. Consequently, a combination of factors, including both depletion and the impact of embedded protostars on the deuterium chemistry, is likely required. In recent years, models of the physical and chemical evolution of isolated star-forming cores have made great progress in matching observations of starless cores, and consequently probing the density, temperature, kinematics and chemical structure of the objects. A next step will be to evolve these models towards more complex, cluster forming environments, where simple assumptions (such as sphericity, or the formation of a protostar at the core centre only) are at best first order approximations. Additionally, studies of the impact of depletion and protostellar formation on 'clumpy' gas, rather than a smooth distribution, are likely needed in these environments, given the large number of small-scale objects found in Oph B in both continuum (Motte et al. 1998; Johnstone et al. 2000b) and molecular line emission (described in Chapters 2 and 3).

Second, how well can we understand the physical conditions of clustered star forming regions without observing *maps* of emission from the species we expect trace dense gas? These results show that the distribution of $NH_3$ and $N_2H^+$ in the clustered Ophiuchus environment are not well-matched to the continuum emission, as has been typically found in more isolated environments. Single-pointing studies which observe these tracers at the continuum peaks are thus uninformed as to whether the molecular line emission accurately traces the conditions at the assumed gas densities, while calculated abundances may not be representative of the entire core if determined at one location only.

Third, how do embedded protostars impact the dense gas chemistry, and over what size scales? The anticorrelation between deuterated species abundance and protostellar proximity suggests the embedded protostars are able to reverse the trend of enhanced deuterium fractionation in cold, dense gas over linear extents greater than expected from chemical models of isolated cores. In this study, it is unclear what the mechanism for this impact is, given the relatively low temperatures determined through $NH_3$ observations in Chapter 2 which suggest the gas is not warm enough to stop the deuterium enhancement directly or through destruction of $H_2D^+$ by CO evaporated from dust grains. The recent emphasis on deuterium chemistry in literature, and the advances in detector technology within the past decade that have allowed observations of some deuterated species (such as $H_2D^+$) for the first time, ensure that these questions will remain a focus of star formation chemistry studies.

## 5.2 Future initiatives in star formation studies

In the near future, new surveys on existing telescopes, enhanced telescope abilities and new facilities will impact greatly star formation research. Here, I discuss briefly several initiatives which are complementary to the work presented in this dissertation, including the James Clerk Maxwell Telescope (JCMT) Gould Belt Legacy Survey, the K-band Focal Plane Array (KFPA) at the Green Bank Telescope, the expanded Very Large Array (EVLA), and the Atacama Large Millimeter Array (ALMA).

### 5.2.1 Large scale mapping

#### JCMT Gould Belt Legacy Survey

The JCMT Gould Belt Legacy Survey (GBLS), first introduced in Chapter 1, is an ongoing systematic observational survey of the nearby ($d < 500\,\mathrm{pc}$) star-forming clouds in emission from CO and its isotopologues $C^{17}O$ and $C^{18}O$, as well as $450\,\mu\mathrm{m}$ and $850\,\mu\mathrm{m}$ continuum emission. The survey takes advantage of two new instruments at the JCMT designed for mapping emission over large areas: the HARP-B array (described in Chapter 4) and the SCUBA-2 widefield continuum array, currently being commissioned at the telescope. The survey has several science goals, including mapping of the structure of the clouds and embedded cores to moderate resolution over large scales. This survey can thus serve as a finder chart for followup mapping of $NH_3$ and $N_2H^+$ emission in nearby clouds to resolve some of the questions raised above. In addition to providing kinematic information at moderate ($\sim 10^3\,\mathrm{cm}^{-3}$) densities, the CO portion of the survey will also enable the calculation of the CO depletion factor across dense cores. This will help inform chemical models of more complex environments, in which the CO depletion factor is an important parameter. In conjunction with $N_2H^+$ and $N_2D^+$ observations, like those presented in Chapter 4, measurements of the CO depletion will enable detailed calculations of the core electron density, which is an important input both for chemical models and analysis of the timescale on which dense cores may collapse in the presence of a magnetic field.

Surveys such as the GBLS will help push detailed studies of dense environments, such as those presented here, beyond single regions to large-scale studies of the dense

gas across multiple molecular clouds. Followup research will be aided by new technologies and facilities.

#### The Green Bank Telescope K-band Focal Plane Array

The $NH_3$ maps presented in Chapter 2 were observed at the GBT using the telescope's current instrument operating at 23 GHz, the K-band receiver. With a single pixel, large-scale mapping is currently time prohibitive. For example, the observations presented in Chapter 2 required 48 hours of telescope time and covered regions only a few arcminutes on a side. The K-band Focal Plane Array (KFPA) is a focal plane array of seven pixels operating at the same frequency is currently in development at the GBT, and will greatly reduce mapping times of $NH_3$ in molecular clouds. The high sensitivity of the 100 m diameter dish combined with the KFPA will enable large-scale studies complementary to surveys such as the JCMT GBLS, allowing the detailed characterization of the physical distribution, dynamics and chemical constitution across clustered star forming cores. The array is projected to be completed in early 2010.

### 5.2.2 Astronomical facilities and upgrades

#### The Expanded VLA

The VLA, consisting of 27 movable 25 m diameter radio antennas, was formally dedicated in 1980. The Expanded VLA (EVLA) is a nearly completed project to increase the sensitivity and spectral capability of the VLA through receiver upgrades and the introduction of the new, next generation Wideband Interferometric Digital Architecture (WIDAR) correlator. The WIDAR correlator was built by the National Research Council of Canada (NRC) Dominion Radio Astronomical Observatory (DRAO). Early science testing of the EVLA with the WIDAR correlator will begin in spring 2010. The enhanced spectral capability will allow observations of $NH_3$, for example, to be performed at high spectral resolution over a wide bandwidth, removing the difficulties presented by the current relatively poor spectral resolution and bandwidth, discussed in Chapter 2 and analysed in Appendix A. In addition, the greater sensitivity will allow better maps of $NH_3$ emission over dense cores to be made in shorter periods of

time, enabling further study of the distribution of dense, cluster-forming cores over multiple regions.

### The Atacama Large Millimeter Array

Currently under construction, the Atacama Large Millimeter Array (ALMA) will revolutionize submillimetre and millimetre high resolution astronomy. Planned to incorporate up to 80 antennas (most 12 m in diameter), ALMA will provide unprecedented sensitivity at small angular resolution, matching or exceeding that of the Hubble Space Telescope (up to 0.005″) at its longest baselines and highest frequencies. With a relatively small field of view, ALMA will not be a survey instrument, but will instead complement single dish telescopes, e.g., through followup observations of small scale structure, and radio facilities operating at longer wavelengths. The frequency bands visible using the initial seven receivers cover a range of interesting molecular transitions for the study of chemistry in star forming environments, including those of many singly- and multiply-deuterated species. For example, detailed, high resolution studies of $N_2H^+$, $N_2D^+$, $H_2D^+$ and $D_2H^+$ emission from star forming regions will be possible with ALMA in a few short years. Commissioning of the first telescopes on-site has already begun and early science is expected to commence in 2011.

# Appendix A

# Determining Physical Parameters from HFS Line Fitting Results

## A.1 Kinetic Temperature

Since the metastable states across $K$-ladders are coupled only by collisions, and if we neglect the upper ($J \neq K$) non-metastable states, then the populations of molecules in the metastable states can be described by the Boltzmann equation.

$$\frac{n(J',K')}{n(J,K)} = \frac{g(J',K')}{g(J,K)} \exp\left(-\frac{\Delta E(J',K';J,K)}{T_{rot}(J',K';J,K)}\right) \tag{A.1}$$

where $T_{rot}(J',K';J,K)$ is the rotational temperature relating the populations in the $(J,K)$ and $(J',K')$ states, and $\Delta E(J',K';J,K)$ is the energy difference between the two states. For $(J',K') = (2,2)$ and $(J,K) = (1,1)$, $\Delta E(2,2;1,1)/k = -41.5\,\mathrm{K}$. The state statistical weights, $g(J,K)$ and $g(J',K')$, are equal to 3 and 5 respectively for the $NH_3$ (1,1) and (2,2) states (Ho & Townes 1983). Assuming the molecular cloud is homogenous such that $n(J',K') \,/\, n(J,K) = N(J',K') \,/\, N(J,K)$, we can solve for $T_{rot}(2,2;1,1)$ using

$$T_{rot}^{21} = T_{rot}(2,2;1,1) = -41.5\left[\ln\left(-\frac{0.283}{\tau(1,1,m)}\frac{\Delta\nu(2,2)}{\Delta\nu(1,1)}\right.\right. \times \left.\left.\ln\left[1-\frac{\Delta T_A(2,2,m)}{\Delta T_A(1,1,m)}\left(1-\exp(-\tau(1,1,m))\right)\right]\right)\right]^{-1} \quad \text{(A.2)}$$

where $\Delta T_A(1,1,m)$ and $\Delta T_A(2,2,m)$ are the antenna temperatures of the main component of the (1,1) and (2,2) transitions, respectively, $\tau(1,1,m)$ is the opacity of the (1,1) line summed over the main component only, and we assume that the line widths $\Delta\nu(1,1) = \Delta\nu(2,2)$. We then calculate the gas kinetic temperature $T_K$ from the rotational temperature following the updated result given by Tafalla et al. (2004) in their Appendix B:

$$T_K = \frac{T_{rot}^{21}}{1-\frac{T_{rot}^{21}}{42}\ln[1+1.1\exp(-16/T_{rot}^{21})]} \quad \text{(A.3)}$$

## A.2 Column Density

The pyramidal molecule $NH_3$ can be found in two distinct species, ortho- and para-$NH_3$, which describe the possible orientations of the hydrogen spins. In ortho-$NH_3$, all three hydrogen spins are parallel, and $K = 3n$, where $n$ is an integer. In para-$NH_3$, the spin of one hydrogen atom is anti-parallel to the other two, and $K \neq 3n$. Transformation of one type to the other are not allowed via normal radiative or collisional interactions. Observations of $NH_3$ (1,1) and (2,2) emission therefore probe only the opacity (and hence, column density) of para-$NH_3$, although we can estimate the total $NH_3$ column density (including both ortho- and para-$NH_3$) with assumptions about the ortho- to para-$NH_3$ ratio.

We calculate the column density of the lower $NH_3$ $(J,K)$ level, $N_l$, from the line opacity:

$$\int \tau \mathrm{d}\nu = \frac{g_u}{g_l}\frac{h\nu}{4\pi}\frac{c^2}{2h\nu^3}A_{ul}[1-\exp(-h\nu/kT_{ex})]N_l \quad \text{(A.4)}$$

where $g_u$ and $g_l$ are the statistical weights for the upper and lower inversion levels, $A_{ul}$ is the Einstein coefficient for spontaneous emission, and $T_{ex}$ is the excitation temperature of the transition. The integral $\int \tau \mathrm{d}\nu$ can be solved in terms of the FWHM line width $\Delta v$ by

$$\int \tau \mathrm{d}\nu = \sqrt{2\pi} \frac{\Delta v}{2\sqrt{2\ln 2}} \frac{\nu}{c} \tau. \tag{A.5}$$

$A_{ul}$ is given by

$$A_{ul} = \frac{64\pi^4 \nu^3}{3hc^3} |\mu^2| \tag{A.6}$$

where the non-zero matrix dipole elements are given by

$$|\mu_{ul}^2| = \frac{\mu^2 K^2}{J(J+1)} \tag{A.7}$$

for a symmetric top molecule like $NH_3$. For the $NH_3$ (1,1) inversion transition, the dipole moment $\mu = 1.468\,\mathrm{debye}$. The column density in the lower $N(J,K)$ inversion level $N_l$ is then

$$N_l = \frac{3h}{8\pi^3 \mu^2} \frac{J(J+1)}{K^2} \frac{\sqrt{\pi}}{2\sqrt{\ln 2}} \frac{1}{1 - \exp(-h\nu/kT_{ex})} \Delta v \tau \tag{A.8}$$

Since the $NH_3$ inversion state consists of two levels, we must include a two level partition function to solve for the total column density $N(J,K)$, such that

$$\frac{N(J,K)}{N_l} = \frac{n_{J,K}}{n_l} = \frac{g_l \exp(-E_l/kT_{ex})}{\sum_{i=0}^{1} g_i \exp(-E_i/kT_{ex})} \tag{A.9}$$

where

$$\sum_{i=0}^{1} g_i \exp(-E_i/kT_{ex}) = g_l \exp(-E_l/kT_{ex}) + g_u \exp(-E_l/kT_{ex}) \tag{A.10}$$

and the statistical weights $g_l = g_u$ for the upper and lower levels of the inversion transitions. Then we solve for $N(J,K)$

$$N(J,K) = [1 + \exp(-\Delta E/kT_{ex})]N_l \tag{A.11}$$

where $\Delta E = E_u - E_l = h\nu$. Finally,

$$N(J,K) = \frac{3h}{8\pi^3\mu^2}\frac{\sqrt{\pi}}{2\sqrt{\ln 2}}\frac{J(J+1)}{K^2}\frac{1+\exp(-h\nu/kT_{ex})}{1-\exp(-h\nu/kT_{ex})}\Delta v\tau \tag{A.12}$$

The total para-$NH_3$ column density $N(NH_3)$ can then be determined by calculating the value of the partition function $Z$ of the metastable states (Townes & Schawlow 1975):

$$Z = \sum_J (2J+1)\exp\frac{-h[BJ(J+1)+(C-B)K^2]}{kT_k}, \tag{A.13}$$

over $J = K = 1, 2, 4, 5, ...$, where the total para-$NH_3$ column is then $N(1,1) \times Z/Z(1,1)$. The values of the rotational constants B and C are 298117 MHz and 186726 MHz, respectively (Pickett et al. 1998).

We can estimate the total $NH_3$ column density by assuming an ortho- to para-$NH_3$ ratio. Since the lowest $NH_3$ inversion level is ortho-$NH_3$, we expect a large ortho- to para-$NH_3$ ratio if $NH_3$ is produced and equilibriated at low temperatures (Takano et al. 2000).

Alternatively, the total $NH_3$ column density $N(NH_3)$ can be determined by calculating the value of the partition function $Z$ of the metastable states:

$$Z = \sum_J (2J+1)S(J)\exp\frac{-h[BJ(J+1)+(C-B)J^2]}{kT_k}, \tag{A.14}$$

where the function $S(J)$ accounts for the extra statistical weight of the ortho- over para-$NH_3$ states, with $S(J) = 2$ for $J = 3, 6, 9, ...$ and $S(J) = 1$ for all other $J$ (the $(J,K) = (0,0)$ state, while an ortho-$NH_3$ state, lacks half of the inversion doublet due

to spin statistics and symmetry considerations (Ho & Townes 1983), and consequently $S(0) = 1$). This partition function effectively assumes the ortho-to-para ratio is thermalized at $T_k$.

## A.3 Consequences of 0.3 km s$^{-1}$ Velocity Resolution

To fit the hyperfine components of the $NH_3$ (1,1) inversion emission and obtain robust measurements of the opacity and excitation temperature of the line, we required an observational bandwidth wide enough to contain the main and at least two satellite components of the line. To meet this requirement, we were able to obtain velocity resolution across the band of only 0.3 km s$^{-1}$ due to the present correlator capabilities at the VLA. Here, we investigate the effect of the relatively low spectral line resolution on our determined line widths and kinetic temperatures by creating model spectra, including random noise with an rms value equal to that in our observed spectra. The spectra are then convolved by a finite spectral resolution and resampled. We then fit the resulting spectra with our custom HFS routine.

$NH_3$ (1,1) spectra were modelled given an excitation temperature $T_{ex}$ and opacity $\tau$ typical of the regions observed, while the line width $\Delta v$ was varied. The line intensity at each velocity is then given by Equations 2.1 and 2.2. The amplitudes of the 21 components of the $NH_3$ (2,2) line were then determined in a similar manner, with the relative intensities of each component given by Kukolich (1967). The relative intensity of the (2,2) line at a given $T_K$ was determined using Equation A.2, by first calculating the associated rotational temperature $T_{rot}$ (reversing Equation A.3).

While the observational resolution does significantly impact some of the returned parameters, we show that the derived kinetic temperatures in this work are robust.

## A.4 Line widths

Figure A.1 plots the returned $\Delta v$ against that of the model spectrum for 0.1 km s$^{-1}$ and 0.3 km s$^{-1}$ resolution for a range of line widths. For both resolutions, the returned

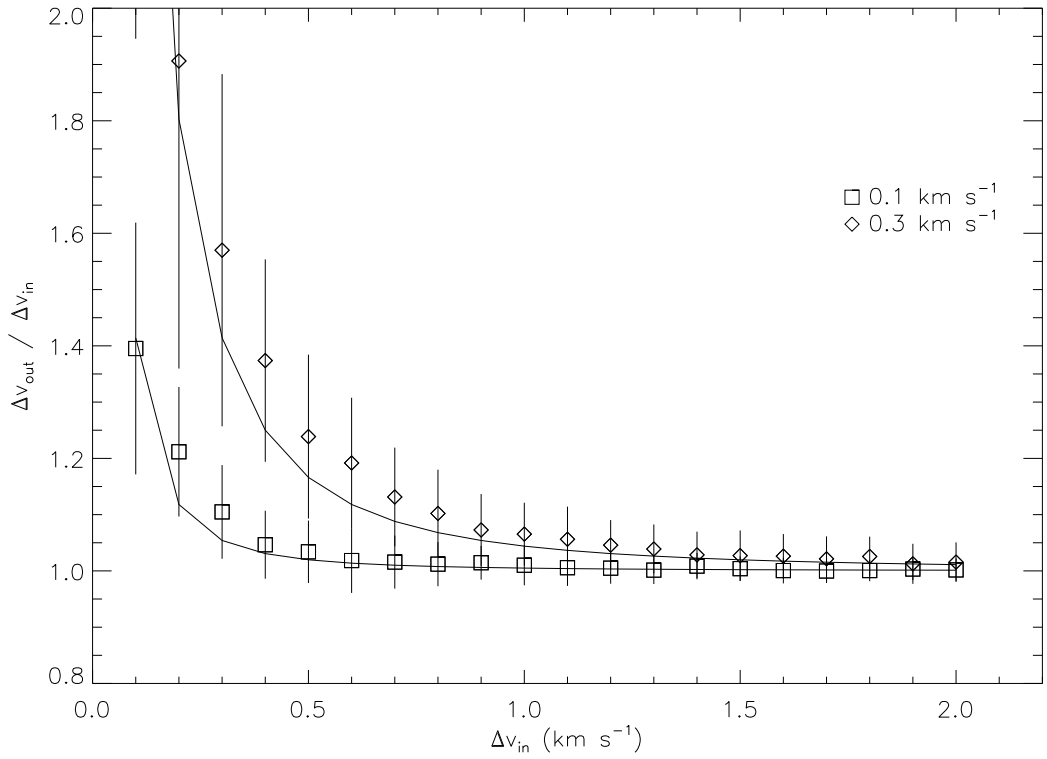


Figure A.1 Input versus recovered line widths determined by creating a model spectrum convolved to $0.1\,\mathrm{km\,s^{-1}}$ and $0.3\,\mathrm{km\,s^{-1}}$ velocity resolution and subsequently fitting with the $NH_3$ HFS routine. Solid lines show the expected observed line width $\Delta v_{obs} = \sqrt{\Delta v_{line} + \Delta v_{res}}$ for $0.1\,\mathrm{km\,s^{-1}}$ and $0.3\,\mathrm{km\,s^{-1}}$.

line width is greater than the actual for small values, with the $0.3\,\mathrm{km\,s^{-1}}$ resolution showing a significantly greater effect. The trends, however, follow that expected for addition in quadrature of the true line width and the resolution, i.e. $\Delta v_{obs} = \sqrt{\Delta v_{line} + \Delta v_{res}}$ with some additional offset at small values and larger scatter due to poor resolution. For the mean values found in this study, the corrected line widths consequently reflect the true line widths, but at small widths the corrected values still overestimate the true value. For this reason, we cannot accurately state the true widths of lines where returned (uncorrected) values $\Delta v \lesssim 0.35\,\mathrm{km\,s^{-1}}$, but do show that these uncorrected line widths are consistent with purely or nearly thermal values.

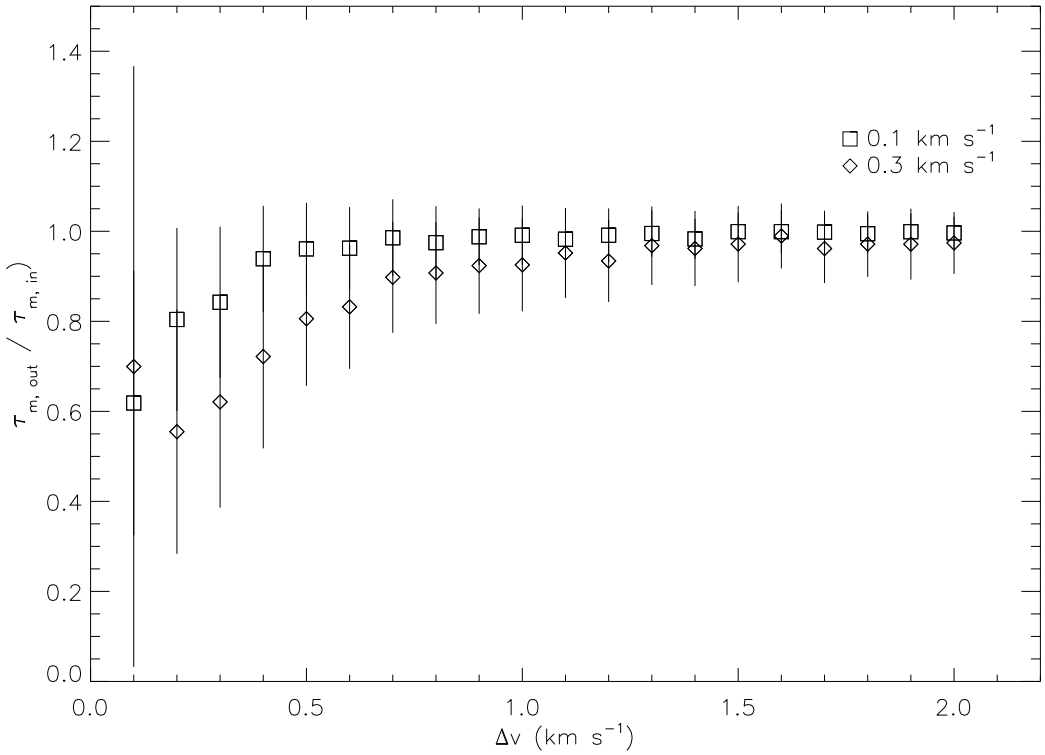


Figure A.2 Recovered versus input $NH_3$ (1,1) opacities as a function of line width $\Delta v$ for $0.1\,\mathrm{km\,s^{-1}}$ and $0.3\mathrm{km\,s^{-1}}$ velocity resolution. At small line widths, the returned opacities are significantly smaller than the true values.

## A.5 Opacity

Figure A.2 plots the returned opacity $\tau$ against that of the model spectrum for $0.1\,\mathrm{km\,s^{-1}}$ and $0.3\,\mathrm{km\,s^{-1}}$ resolution over a range of line widths. The relatively low spectral resolution of our observations has a significant impact on the returned opacity, with our fitting routine significantly underestimating the opacity by greater than 20% for line widths $\lesssim 0.7\,\mathrm{km\,s^{-1}}$. In addition, the scatter in the returned opacities is large at small line widths, and this affects the uncertainty in the calculated $NH_3$ column density, $N(NH_3)$, in §4.3. Since $N(NH_3)$ depends linearly on the opacity (see Equation 3.3), the uncertainty in the opacity dominates the uncertainty in the column density at small line widths. Since the column density also depends linearly on line width, however, and the returned line width at small values is greater than the true value by a similar relative amount, the returned column density is more accurate

than the uncertainties suggest.

## A.6 Kinetic Temperature

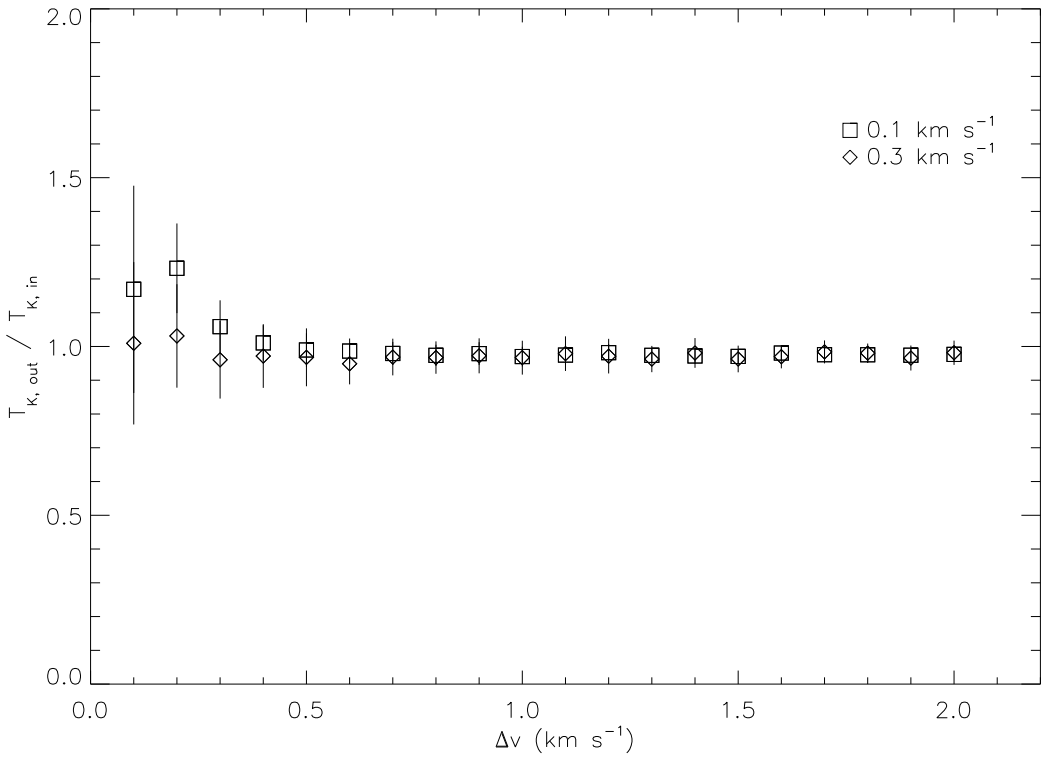


Figure A.3 Recovered versus input kinetic temperatures $T_K$ as a function of $NH_3$ (1,1) line width $\Delta v$ for $0.1\,\mathrm{km\,s^{-1}}$ and $0.3\,\mathrm{km\,s^{-1}}$ velocity resolution. Even at small line widths, the returned kinetic temperature closely agrees with the input value, with little scatter.

The results from the above tests show that at small $NH_3$ line widths, the returned line widths and opacities can vary significantly from the true values. Regardless, the returned kinetic temperatures from our $NH_3$ line fitting are robust, as shown in Figure A.3 (for $T_K = 15\,\mathrm{K}$). Even at small line widths ($\Delta v \lesssim 0.3\,\mathrm{km\,s^{-1}}$), the kinetic temperatures derived from the fits are accurate within uncertainties of the true $T_K$, with relatively little scatter. At the lowest temperatures found in the Oph cores, $T_K = 10\,\mathrm{K}$, the results are similar with slightly more scatter at the lowest line widths.

# Appendix B

# Calculating $N_2H^+$ column density

The optical depth at frequency $\nu$, $\tau_\nu$, can be expressed as

$$\tau_\nu = \frac{g_u}{g_l}\frac{h\nu_0}{4\pi}\frac{c^2}{2h\nu_0^3}A_{ul}\left(1-\exp(-h\nu/kT_{ex})\right)\frac{N_l}{\delta\nu} \tag{B.1}$$

where $g_u$ and $g_l$ are the statistical weights of the upper and lower levels of the transition, $\nu_0$ is the line centre frequency, $A_{ul}$ is the Einstein $A$ coefficient for spontaneous emission, $T_{ex}$ is the excitation temperature (assumed to be the same for all rotational levels), and $N_l$ is the column density of the lower level. For the $J+1 \rightarrow J$ transition of a linear rotor, $g_J = 2J+1$, and

$$A_{ul} = \frac{64\pi^4\nu^3}{3hc^3}|\mu_{ul}^2| \tag{B.2}$$

where

$$|\mu^2_{J+1\rightarrow J}| = \mu^2\frac{J+1}{2J+3} \tag{B.3}$$

are the non-zero dipole matrix elements. We let $\delta\nu = \nu\delta v/c$, apply a factor $(2\sqrt{\ln 2/\pi})^{-1}$ to account for a Gaussian line profile, and solve for $N_J$:

$$N_J = \frac{3h}{8\pi^3}\frac{\sqrt{\pi}}{2\sqrt{\ln 2}}\frac{1}{\mu^2}\frac{2J+1}{J+1}\frac{\tau\Delta v}{1-\exp(-h\nu/kT_{ex})} \tag{B.4}$$

The number of particles in level $J$, $n_J$, can be related to the total population, $n_{tot}$, via the Boltzmann equation. The column density ratio $N_J \,/\, N_{tot} = n_J \,/\, n_{tot}$, such that

$$\frac{N_J}{N_{tot}} = \frac{n_J}{n_{tot}} = \frac{g_J \exp(-E_J/kT_{ex})}{\sum_{l=0}^{\infty} g_l \exp(-E_l/kT_{ex})} \tag{B.5}$$

where $\sum_{l=0}^{\infty} g_l \exp(-E_l/kT_{ex})$ is the partition function, $Q_{rot}$. The total column density $N_{tot}$ can then be calculated from $N_J$:

$$N_{tot} = \frac{N_J Q_{rot}}{(2J+1)\exp(-E_J/kT_{ex})} \tag{B.6}$$

For a linear molecule, the partition function can be approximated by its integral:

$$Q_{rot} = \frac{kT_{ex}}{hB} + \frac{1}{3} \tag{B.7}$$

where $B$ is the rotational constant. Then

$$N_{tot} = \frac{3h}{8\pi^3}\frac{1}{\mu^2}\frac{\sqrt{\pi}}{2\sqrt{\ln 2}}\frac{1}{(J+1)\exp(-E_J/kT_{ex})}\left(\frac{kT_{ex}}{hB}+\frac{1}{3}\right)\frac{\Delta v\tau}{1-\exp(-h\nu/kT_{ex})} \tag{B.8}$$

For the $N_2H^+$ $J+1 \rightarrow J = 1-0$ transition, $\mu = 3.40\,\mathrm{dB}$ (Green et al. 1974), $B = 46.586702\,\mathrm{GHz}$ (Caselli et al. 1995) and $E_J = J(J+1)hB$.

# Bibliography

Aikawa, Y., Herbst, E., Roberts, H., & Caselli, P. 2005, ApJ, 620, 330

Aikawa, Y., Wakelam, V., Garrod, R. T., & Herbst, E. 2008, ApJ, 674, 984

Alves, J. F., Lada, C. J., & Lada, E. A. 2001, Nature, 409, 159

André, P., Belloche, A., Motte, F., & Peretto, N. 2007, A&A, 472, 519

Belloche, A. & André, P. 2004, A&A, 419, L35

Benson, P. J. & Myers, P. C. 1983, ApJ, 270, 589

Bergin, E. A., Alves, J., Huard, T., & Lada, C. J. 2002, ApJ, 570, L101

Bergin, E. A. & Langer, W. D. 1997, Astrophys. J., 486, 316

Bergin, E. A., Plume, R., Williams, J. P., & Myers, P. C. 1999, ApJ, 512, 724

Bergin, E. A. & Tafalla, M. 2007, ARA&A, 45, 339

Bisschop, S. E., Fraser, H. J., Oberg, K. I., van D ishoeck, E. F., & Schlemmer, S. 2006, astro-ph/0601082

Bonnor, W. B. 1956, MNRAS, 116, 351

Cambrésy, L. 1999, A&A, 345, 965

Casanova, S., Montmerle, T., Feigelson, E. D., & Andre, P. 1995, ApJ, 439, 752

Caselli, P., Benson, P. J., Myers, P. C., & Tafalla, M. 2002a, ApJ, 572, 238

Caselli, P., Myers, P. C., & Thaddeus, P. 1995, ApJ, 455, L77+

Caselli, P., van der Tak, F. F. S., Ceccarelli, C., & Bacmann, A. 2003, A&A, 403, L37

Caselli, P., Vastel, C., Ceccarelli, C., van der Tak, F. F. S., Crapsi, A., & Bacmann, A. 2008, A&A, 492, 703

Caselli, P., Walmsley, C. M., Terzieva, R., & Herbst, E. 1998, ApJ, 499, 234

Caselli, P., Walmsley, C. M., Zucconi, A., Tafalla, M., Dore, L., & Myers, P. C. 2002b, ApJ, 565, 331

—. 2002c, ApJ, 565, 344

Chen, X., Launhardt, R., Bourke, T. L., Henning, T., & Barnes, P. J. 2008, ApJ, 683, 862

Chini, R. 1981, A&A, 99, 346

Codella, C., Welser, R., Henkel, C., Benson, P. J., & Myers, P. C. 1997, A&A, 324, 203

Crapsi, A., Caselli, P., Walmsley, C. M., Myers, P. C., Tafalla, M., Lee, C. W., & Bourke, T. L. 2005, ApJ, 619, 379

Crapsi, A., Caselli, P., Walmsley, C. M., Tafalla, M., Lee, C. W., Bourke, T. L., & Myers, P. C. 2004, A&A, 420, 957

Crapsi, A., Caselli, P., Walmsley, M. C., & Tafalla, M. 2007, A&A, 470, 221

Daniel, F., Cernicharo, J., & Dubernet, M.-L. 2006, ApJ, 648, 461

Daniel, F., Cernicharo, J., Roueff, E., Gerin, M., & Dubernet, M. L. 2007, ApJ, 667, 980

de Geus, E. J., de Zeeuw, P. T., & Lub, J. 1989, A&A, 216, 44

de Gregorio-Monsalvo, I., Gómez, J. F., Suárez, O., Kuiper, T. B. H., Rodríguez, L. F., & Jiménez-Bailón, E. 2006, ApJ, 642, 319

Di Francesco, J., André, P., & Myers, P. C. 2004, ApJ, 617, 425

Di Francesco, J., Evans, II, N. J., Caselli, P., Myers, P. C., Shirley, Y., Aikawa, Y., & Tafalla, M. 2007, in Protostars and Planets V, ed. B. Reipurth, D. Jewitt, & K. Keil, 17–32

Di Francesco, J., Hogerheijde, M. R., Welch, W. J., & Bergin, E. A. 2002, AJ, 124, 2749

Di Francesco, J., Johnstone, D., Kirk, H., MacKenzie, T., & Ledwosinska, E. 2008, ApJS, 175, 277

Di Francesco, J., Myers, P. C., Wilner, D. J., Ohashi, N., & Mardones, D. 2001, ApJ, 562, 770

Dore, L., Caselli, P., Beninati, S., Bourke, T., Myers, P. C., & Cazzoli, G. 2004, A&A, 413, 1177

Draine, B. T. & Lee, H. M. 1984, Astrophys. J., 285, 89

Elias, J. H. 1978, ApJ, 224, 453

Emerson, D. T. & Graeve, R. 1988, Astron. & Astrophys., 190, 353

Emprechtinger, M., Caselli, P., Volgenau, N. H., Stutzki, J., & Wiedner, M. C. 2009, A&A, 493, 89

Enoch, M. L., Evans, N. J., Sargent, A. I., & Glenn, J. 2009, ApJ, 692, 973

Enoch, M. L., Evans, II, N. J., Sargent, A. I., Glenn, J., Rosolowsky, E., & Myers, P. 2008, ApJ, 684, 1240

Enoch, M. L., Glenn, J., Evans, II, N. J., Sargent, A. I., Young, K. E., & Huard, T. L. 2007, ApJ, 666, 982

Enoch, M. L., Young, K. E., Glenn, J., Evans, II, N. J., Golwala, S., Sargent, A. I., Harvey, P., Aguirre, J., Goldin, A., Haig, D., Huard, T. L., Lange, A., Laurent, G., Maloney, P., Mauskopf, P., Rossinot, P., & Sayers, J. 2006, ApJ, 638, 293

Evans, N. J., Dunham, M. M., Jørgensen, J. K., Enoch, M. L., Merín, B., van Dishoeck, E. F., Alcalá, J. M., Myers, P. C., Stapelfeldt, K. R., Huard, T. L., Allen, L. E., Harvey, P. M., van Kempen, T., Blake, G. A., Koerner, D. W., Mundy, L. G., Padgett, D. L., & Sargent, A. I. 2009, ApJS, 181, 321

Flower, D. R., Pineau Des Forêts, G., & Walmsley, C. M. 2006, A&A, 456, 215

Fontani, F., Caselli, P., Bourke, T. L., Cesaroni, R., & Brand, J. 2008, A&A, 477, L45

Fontani, F., Caselli, P., Crapsi, A., Cesaroni, R., Molinari, S., Testi, L., & Brand, J. 2006, A&A, 460, 709

Foster, J. B., Rosolowsky, E. W., Kauffman, J., Pineda, J. E., Borkin, M. A., Caselli, P., Myers, P. C., & Goodman, A. A. 2009, ArXiv e-prints

Friesen, R. K., Di Francesco, J., Shimajiri, Y., & Takakuwa, S. 2009a, ApJ, submitted

Friesen, R. K., Di Francesco, J., Shirley, Y. L., & Myers, P. C. 2009b, ApJ, 697, 1457

Fuller, G. A. & Myers, P. C. 1993, ApJ, 418, 273

Gerin, M., Pearson, J. C., Roueff, E., Falgarone, E., & Phillips, T. G. 2001, ApJ, 551, L193

Goldsmith, P. F., Bergin, E. A., & Lis, D. C. 1997, ApJ, 491, 615

Goldsmith, P. F. & Langer, W. D. 1978, ApJ, 222, 881

Gould, B. A. 1879, Resultados del Observatorio Nacional Argentino, 1

Grasdalen, G. L., Strom, K. M., & Strom, S. E. 1973, ApJ, 184, L53+

Green, S., Montgomery, Jr., J. A., & Thaddeus, P. 1974, ApJ, 193, L89

Gurney, M., Plume, R., & Johnstone, D. 2008, PASP, 120, 1193

Harju, J., Juvela, M., Schlemmer, S., Haikala, L. K., Lehtinen, K., & Mattila, K. 2008, ArXiv e-prints, 802

Hatchell, J., Richer, J. S., Fuller, G. A., Qualtrough, C. J., Ladd, E. F., & Chandler, C. J. 2005, A&A, 440, 151

Herschel, J. F. W. S. 1847, Results of astronomical observations made during the years 1834, 5, 6, 7, 8, at the Cape of Good Hope; being the completion of a telescopic survey of the whole surface of the visible heavens, commenced in 1825 (London, Smith, Elder and co., 1847.)

Hildebrand, R. H. 1983, Quart. Jour. Royal Astron. Society, 24, 267

Ho, P. T. P. & Townes, C. H. 1983, ARA&A, 21, 239

Hotzel, S., Harju, J., Lemke, D., Mattila, K., & Walmsley, C. M. 2001, A&A, 372, 302

Hotzel, S., Harju, J., & Walmsley, C. M. 2004, A&A, 415, 1065

Jijina, J., Myers, P. C., & Adams, F. C. 1999, ApJS, 125, 161

Johnstone, D. & Bally, J. 2006, ApJ, 653, 383

Johnstone, D., Di Francesco, J., & Kirk, H. 2004, ApJ, 611, L45

Johnstone, D., Fich, M., Mitchell, G. F., & Moriarty-Schieven, G. 2001, ApJ, 559, 307

Johnstone, D., Matthews, H., & Mitchell, G. F. 2006, ApJ, 639, 259

Johnstone, D., Wilson, C. D., Moriarty-Schieven, G., Giannakopoulou-Creighton, J., & Gregersen, E. 2000a, ApJS, 131, 505

Johnstone, D., Wilson, C. D., Moriarty-Schieven, G., Joncas, G., Smith, G., Gregersen, E., & Fich, M. 2000b, ApJ, 545, 327

Jørgensen, J. K., Johnstone, D., Kirk, H., Myers, P. C., Allen, L. E., & Shirley, Y. L. 2008, ApJ, 683, 822

Jørgensen, J. K., Schöier, F. L., & van Dishoeck, E. F. 2005, Astron. & Astrophys., 435, 177

Kamazaki, T., Saito, M., Hirano, N., Umemoto, T., & Kawabe, R. 2003, ApJ, 584, 357

Keto, E., Rybicki, G. B., Bergin, E. A., & Plume, R. 2004, ApJ, 613, 355

Kirk, H., Johnstone, D., & Di Francesco, J. 2006, ApJ, 646, 1009

Knude, J. & Hog, E. 1998, A&A, 338, 897

Kukolich, S. G. 1967, Physical Review, 156, 83

Lada, C. J., Bergin, E. A., Alves, J. F., & Huard, T. L. 2003, ApJ, 586, 286

Lada, C. J. & Lada, E. A. 2003, ARA&A, 41, 57

Lada, C. J., Lada, E. A., Clemens, D. P., & Bally, J. 1994, ApJ, 429, 694

Lai, S.-P. & Crutcher, R. M. 2000, ApJS, 128, 271

Lai, S.-P., Velusamy, T., Langer, W. D., & Kuiper, T. B. H. 2003, AJ, 126, 311

Larsson, B., Liseau, R., Bergman, P., Bernath, P., Black, J. H., Booth, R. S., Buat, V., Curry, C. L., Encrenaz, P., Falgarone, E., Feldman, P., Fich, M., Florén, H. G., Frisk, U., Gerin, M., Gregersen, E. M., Harju, J., Hasegawa, T., Johansson, L. E. B., Kwok, S., Lecacheux, A., Liljeström, T., Mattila, K., Mitchell, G. F., Nordh, L. H., Olberg, M., Olofsson, G., Pagani, L., Plume, R., Ristorcelli, I., Sandqvist, A., Schéele, F. v., Tothill, N. F. H., Volk, K., Wilson, C. D., & Hjalmarson, Å. 2003, A&A, 402, L69

Lee, J.-E., Bergin, E. A., & Evans, N. J. 2004, Astrophys. J., 617, 360

Lee, J.-E., Di Francesco, J., Bourke, T. L., Evans, II, N. J., & Wu, J. 2007, ApJ, 671, 1748

Linsky, J. L., Draine, B. T., Moos, H. W., Jenkins, E. B., Wood, B. E., Oliveira, C., Blair, W. P., Friedman, S. D., Gry, C., Knauth, D., Kruk, J. W., Lacour, S., Lehner, N., Redfield, S., Shull, J. M., Sonneborn, G., & Williger, G. M. 2006, ApJ, 647, 1106

Lis, D. C., Roueff, E., Gerin, M., Phillips, T. G., Coudert, L. H., van der Tak, F. F. S., & Schilke, P. 2002, ApJ, 571, L55

Liseau, R., Larsson, B., Brandeker, A., Bergman, P., Bernath, P., Black, J. H., Booth, R., Buat, V., Curry, C., Encrenaz, P., Falgarone, E., Feldman, P., Fich, M., Florén, H., Frisk, U., Gerin, M., Gregersen, E., Harju, J., Hasegawa, T., Hjalmarson, Å., Johansson, L., Kwok, S., Lecacheux, A., Liljeström, T., Mattila, K., Mitchell, G., Nordh, L., Olberg, M., Olofsson, G., Pagani, L., Plume, R., Ristorcelli, I., Sandqvist, A., Schéele, F. v., Serra, G., Tothill, N., Volk, K., & Wilson, C. 2003, A&A, 402, L73

Loinard, L., Torres, R. M., Mioduszewski, A. J., & Rodríguez, L. F. 2008, ApJ, 675, L29

Lombardi, M., Lada, C. J., & Alves, J. 2008, A&A, 480, 785

Loren, R. B. 1989, ApJ, 338, 902

Loren, R. B., Wootten, A., & Wilking, B. A. 1990, Astrophys. J., 365, 269

Lynds, B. T. 1962, ApJS, 7, 1

Mac Low, M.-M. & Klessen, R. S. 2004, Reviews of Modern Physics, 76, 125

Mamajek, E. E. 2008, Astronomische Nachrichten, 329, 10

Mangum, J. G., Wootten, A., & Mundy, L. G. 1992, ApJ, 388, 467

McKee, C. F. 1989, ApJ, 345, 782

Mestel, L. & Spitzer, Jr., L. 1956, MNRAS, 116, 503

Miettinen, O., Harju, J., Haikala, L. K., Kainulainen, J., & Johansson, L. E. B. 2009, ArXiv e-prints

Millar, T. J., Bennett, A., & Herbst, E. 1989, ApJ, 340, 906

Millar, T. J. & Herbst, E. 1990, A&A, 231, 466

Motte, F., Andre, P., & Neri, R. 1998, A&A, 336, 150

Myers, P. C. 1998, ApJ, 496, L109+

Myers, P. C., Benson, P. J., & Ho, P. T. P. 1979, ApJ, 233, L141

Nutter, D., Ward-Thompson, D., & André, P. 2006, MNRAS, 368, 1833

Ohishi, M., Irvine, W. M., & Kaifu, N. 1992, in IAU Symposium, Vol. 150, Astrochemistry of Cosmic Phenomena, ed. P. D. Singh, 171–+

Ossenkopf, V. & Henning, T. 1994, Astron. & Astrophys., 291, 943

Pagani, L., Daniel, F., & Dubernet, M.-L. 2009, A&A, 494, 719

Palau, A., Estalella, R., Girart, J. M., Ho, P. T. P., Zhang, Q., & Beuther, H. 2007, A&A, 465, 219

Pickett, H. M., Poynter, R. L., Cohen, E. A., Delitsky, M. L., Pearson, J. C., & Muller, H. C. P. 1998, "J. Quant. Spect. & Rad. Trans.", 82, 293

Pollack, J. B., Hollenbach, D., Beckwith, S., Simonelli, D. P., Roush, T., & Fong, W. 1994, Astrophys. J., 421, 615

Pon, A., Plume, R., Friesen, R. K., Di Francesco, J., Matthews, B., & Bergin, E. A. 2009, ApJ, 698, 1914

Ramanlal, J. & Tennyson, J. 2004, MNRAS, 354, 161

Rathborne, J. M., Lada, C. J., Muench, A. A., Alves, J. F., & Lombardi, M. 2008, ApJS, 174, 396

Rosolowsky, E. W., Pineda, J. E., Foster, J. B., Borkin, M. A., Kauffmann, J., Caselli, P., Myers, P. C., & Goodman, A. A. 2008a, ApJS, 175, 509

Rosolowsky, E. W., Pineda, J. E., Kauffmann, J., & Goodman, A. A. 2008b, ApJ, 679, 1338

Roueff, E., Tiné, S., Coudert, L. H., Pineau des Forêts, G., Falgarone, E., & Gerin, M. 2000, A&A, 354, L63

Sastry, K. V. L. N., Helminger, P., Herbst, E., & De Lucia, F. C. 1981, Chem. Phys. Lett., 84, 286

Sault, R. J., Teuben, P. J., & Wright, M. C. H. 1995, in Astronomical Society of the Pacific Conference Series, Vol. 77, Astronomical Data Analysis Software and Systems IV, ed. R. A. Shaw, H. E. Payne, & J. J. E. Hayes, 433–+

Schöier, F. L., van der Tak, F. F. S., van Dishoeck, E. F., & Black, J. H. 2005, A&A, 432, 369

Schuster, K.-F., Boucher, C., Brunswig, W., Carter, M., Chenu, J.-Y., Foullieux, B., Greve, A., John, D., Lazareff, B., Navarro, S., Perrigouard, A., Pollet, J.-L., Sievers, A., Thum, C., & Wiesemeyer, H. 2004, A&A, 423, 1171

Shirley, Y. L., Evans, II, N. J., & Rawlings, J. M. C. 2002, ApJ, 575, 337

Shirley, Y. L., Evans, II, N. J., Rawlings, J. M. C., & Gregersen, E. M. 2000, ApJS, 131, 249

Shu, F. H., Adams, F. C., & Lizano, S. 1987, ARA&A, 25, 23

Shull, J. M. & Beckwith, S. 1982, ARA&A, 20, 163

Smith, H., Buckle, J., Hills, R., Bell, G., Richer, J., Curtis, E., Withington, S., Leech, J., Williamson, R., Dent, W., Hastings, P., Redman, R., Wooff, B., Yeung, K., Friberg, P., Walther, C., Kackley, R., Jenness, T., Tilanus, R., Dempsey, J., Kroug, M., Zijlstra, T., & Klapwijk, T. M. 2008, in Society of Photo-Optical Instrumentation Engineers (SPIE) Conference Series, Vol. 7020, Society of Photo-Optical Instrumentation Engineers (SPIE) Conference Series

Stamatellos, D., Whitworth, A. P., & Ward-Thompson, D. 2007, MNRAS, 379, 1390

Stanke, T., Smith, M. D., Gredel, R., & Khanzadyan, T. 2006, A&A, 447, 609

Stark, R., van der Tak, F. F. S., & van Dishoeck, E. F. 1999, ApJ, 521, L67

Steer, D. G., Dewdney, P. E., & Ito, M. R. 1984, Astron. & Astrophys., 137, 159

Stutzki, J. & Guesten, R. 1990, ApJ, 356, 513

Suzuki, H., Yamamoto, S., Ohishi, M., Kaifu, N., Ishikawa, S.-I., Hirahara, Y., & Takano, S. 1992, ApJ, 392, 551

Swift, J. J., Welch, W. J., Di Francesco, J., & Stojimirović, I. 2006, ApJ, 637, 392

Tafalla, M., Myers, P. C., Caselli, P., & Walmsley, C. M. 2004, A&A, 416, 191

Tafalla, M., Myers, P. C., Caselli, P., Walmsley, C. M., & Comito, C. 2002, ApJ, 569, 815

Tafalla, M., Santiago-García, J., Myers, P. C., Caselli, P., Walmsley, C. M., & Crapsi, A. 2006, A&A, 455, 577

Takano, S., Nakai, N., Kawaguchi, K., & Takano, T. 2000, PASJ, 52, L67

Testi, L. & Sargent, A. I. 1998, ApJ, 508, L91

Townes, C. H. & Schawlow, A. L. 1975, Microwave Spectroscopy (New York: Dover Publications Inc)

van Dishoeck, E. F., Phillips, T. G., Keene, J., & Blake, G. A. 1992, A&A, 261, L13

Vastel, C., Caselli, P., Ceccarelli, C., Phillips, T., Wiedner, M. C., Peng, R., Houde, M., & Dominik, C. 2006, ApJ, 645, 1198

Visser, R., van Dishoeck, E. F., Doty, S. D., & Dullemond, C. P. 2009, A&A, 495, 881

Vrba, F. J. 1977, AJ, 82, 198

Vrba, F. J., Strom, K. M., Strom, S. E., & Grasdalen, G. L. 1975, ApJ, 197, 77

Walmsley, C. M., Flower, D. R., & Pineau des Forêts, G. 2004, A&A, 418, 1035

Walmsley, C. M. & Ungerechts, H. 1983, A&A, 122, 164

Walsh, A. J., Myers, P. C., Di Francesco, J., Mohanty, S., Bourke, T. L., Gutermuth, R., & Wilner, D. 2007, ApJ, 655, 958

Ward-Thompson, D., André, P., Crutcher, R., Johnstone, D., Onishi, T., & Wilson, C. 2007a, in Protostars and Planets V, ed. B. Reipurth, D. Jewitt, & K. Keil, 33–46

Ward-Thompson, D., Di Francesco, J., Hatchell, J., Hogerheijde, M. R., Nutter, D., Bastien, P., Basu, S., Bonnell, I., Bowey, J., Brunt, C., Buckle, J., Butner, H., Cavanagh, B., Chrysostomou, A., Curtis, E., Davis, C. J., Dent, W. R. F., van Dishoeck, E., Edmunds, M. G., Fich, M., Fiege, J., Fissel, L., Friberg, P., Friesen, R., Frieswijk, W., Fuller, G. A., Gosling, A., Graves, S., Greaves, J. S., Helmich, F., Hills, R. E., Holland, W. S., Houde, M., Jayawardhana, R., Johnstone, D., Joncas, G., Kirk, H., Kirk, J. M., Knee, L. B. G., Matthews, B., Matthews, H., Matzner, C., Moriarty-Schieven, G. H., Naylor, D., Padman, R., Plume, R., Rawlings, J. M. C., Redman, R. O., Reid, M., Richer, J. S., Shipman, R., Simpson, R. J., Spaans, M., Stamatellos, D., Tsamis, Y. G., Viti, S., Weferling, B., White, G. J., Whitworth, A. P., Wouterloot, J., Yates, J., & Zhu, M. 2007b, PASP, 119, 855

Wilking, B. A., Gagné, M., & Allen, L. E. Star Formation in the $\rho$ Ophiuchi Molecular Cloud (ASP Monograph Publications), 351–+

Wilking, B. A. & Lada, C. J. 1983, ApJ, 274, 698

Wilking, B. A., Meyer, M. R., Robinson, J. G., & Greene, T. P. 2005, AJ, 130, 1733

Williams, J. P., Bergin, E. A., Caselli, P., Myers, P. C., & Plume, R. 1998, ApJ, 503, 689

Williams, J. P., de Geus, E. J., & Blitz, L. 1994, ApJ, 428, 693

Williams, J. P. & Myers, P. C. 2000, ApJ, 537, 891

Wilson, R. W., Jefferts, K. B., & Penzias, A. A. 1970, Astrophys. J. Letters, 161, L43+

Womack, M., Ziurys, L. M., & Wyckoff, S. 1992, ApJ, 387, 417

Wu, Y., Zhang, Q., Yu, W., Miller, M., Mao, R., Sun, K., & Wang, Y. 2006, A&A, 450, 607

Young, K. E., Enoch, M. L., Evans, II, N. J., Glenn, J., Sargent, A., Huard, T. L., Aguirre, J., Golwala, S., Haig, D., Harvey, P., Laurent, G., Mauskopf, P., & Sayers, J. 2006, ApJ, 644, 326